THESE DE DOCTORAT DE

L'UNIVERSITE DE RENNES 1
COMUE UNIVERSITE BRETAGNE LOIRE

ECOLE DOCTORALE N° 601
Mathématiques et Sciences et Technologies
de l'Information et de la Communication
Spécialité : Signal, Image, Vision

Par
Bastien RIGAUD

Radiothérapie adaptative guidée par l'imagerie anatomique

Thèse présentée et soutenue à Rennes, le 7 novembre 2018
Unité de recherche : LTSI – INSERM U1099
Thèse N° :

Rapporteurs avant soutenance :

Caroline Petitjean	MCU, Université de Rouen
David Sarrut	DR CNRS, Centre Léon Bérard, Lyon

Composition du Jury :

Président :	Yohan Payan	DR CNRS, Université Grenoble Alpes
Examinateurs :	Caroline Petitjean	MCU, Université de Rouen
	David Sarrut	DR CNRS, Centre Léon Bérard, Lyon
	Yohan Payan	DR CNRS, Université Grenoble Alpes
	Renaud De Crevoisier	PU/PH, Université de Rennes
	Antoine Simon	MCU, Université de Rennes
Dir. de thèse :	Renaud De Crevoisier	PU/PH, Université de Rennes
Co-dir. de thèse :	Antoine Simon	MCU, Université de Rennes

REMERCIEMENTS

Ces travaux de thèse ont fait l'objet d'une forte collaboration avec de nombreuses personnes que j'aimerais remercier.

Dans un premier temps je souhaiterais remercier les membres de mon jury. Merci à Caroline Petitjean et David Sarrut d'avoir accepté de rapporter les travaux de ma thèse. Merci aussi à Yohan Payan de bien avoir accepté d'être examinateur de mes travaux.

Ces remerciements s'adressent tout particulièrement à mes directeurs de thèse, Renaud de Crevoisier et Antoine Simon. Merci à Antoine Simon de m'avoir accompagné tout au long de ces trois dernières années et de m'avoir fait confiance. Son calme et son expertise ont été des qualités précieuses pour l'aboutissement de ces travaux. Merci à Renaud de Crevoisier pour ses compétences, sa détermination et sa passion qui ont permis de dynamiser ces trois années de travail.

Merci à Oscar Acosta qui m'a fait confiance et m'a fait découvrir le domaine du traitement de l'image appliqué au domaine de la santé.

Je tiens à remercier Kristy Brock et Guillaume Cazoulat pour avoir accepté de m'accueillir au sein de leur laboratoire à Houston et de m'avoir fait confiance. Je retiens d'excellents souvenirs de cette mobilité de thèse, à la fois professionnels et personnels. J'espère que cette collaboration pourra perdurer.

Je souhaite remercier les trois générations de doctorants que j'ai pu rencontrer au cours de mon activité au sein du LTSI. Mes pensées vont d'en un premier temps à Frédéric et Mohamed avec qui j'ai passé d'excellents moments aussi bien professionnels que personnels. Mes pensées vont ensuite à Pablo, Vivien, Auréline, aux trois Mathieu (ils se reconnaitront), Richard, Sophie, Karim, Mahmoud, Jérémie, Gaël, Jean Charles et Nawras.

Je remercie les gens du CEM avec qui j'ai eu l'occasion de partager des moments de travail, merci à Joël Castelli, Maxime, Loïg, Khemara pour ces plus ou moins courtes collaborations. Ce fut un plaisir.

Merci à mes collègues du MD Anderson, Molly, Brian, Andrea, Anando. My french accent may come back soon !

Je tiens à remercier mes amis qui m'ont accompagné pendant cette aventure. Camille, Anthony, Pitchounou, Yann, Bertrand, Amandine, Marion, Anne-Laure et Johan. Cette thèse est dédicacée à toi, Camille, « binôme de compétition » avec lequel j'espère avoir l'opportunité de retravailler et de continuer à rouler encore longtemps. FOUPOUDAV.

Je remercie mes parents, mon frangin, mes grands-parents qui restent tous très proche de mon cœur malgré la distance. Je remercie ma belle-famille pour leur soutien.

Finalement, cette thèse s'adresse à ma future femme, Morgane, qui a su me soutenir dans toutes les épreuves (les bonnes et les moins bonnes) de ces 5 dernières années.

RESUME

Dans le contexte du traitement du cancer du col de l’utérus localement avancé, le traitement standard repose sur une radiothérapie en parallèle à une chimiothérapie et une curiethérapie. La radiothérapie externe se déroule en deux phases, une phase de planification du traitement faite à partir d’une unique acquisition scanner et une phase de délivrance quotidienne de ce traitement. Cependant, il existe de fortes variations anatomiques de la cible tumorale qui s’explique notamment par le remplissage des organes voisins (volume vésical et rectal) et par la fonte tumorale. De ce fait, la planification initiale ne correspond plus à la configuration anatomique en cours de traitement. Cette différence peut engendrer une sous-couverture de la cible clinique ainsi qu’une sur-couverture des organes à risque, augmentant les risques de récidive et de toxicité pour ces patientes.

L’objectif de cette thèse est donc de développer des stratégies optimisées de radiothérapie adaptative personnalisées permettant de prendre en compte et de compenser l’incidence de ces déformations anatomiques. Les images acquises lors de la planification et de la délivrance du traitement jouant alors un rôle central, ceci passe par le développement de méthodes de recalage, de fusion et d’analyse d’images ainsi que d’outils d’aide à la décision.

Les travaux de thèse ont permis la définition de deux nouvelles stratégies de traitement de radiothérapie externe : (1) Une stratégie reposant sur le concept d’une librairie évolutive permettant d’exploiter l’anatomie de la patiente en cours de traitement pour enrichir une librairie préexistante ; (2) Une stratégie de librairie modélisée à partir d’un scanner de planification unique reposant sur l’analyse des déformations d’une population. De plus, dans l’objectif d’une estimation de la dose délivrée sur l’ensemble du traitement (radiothérapie externe et curiethérapie), une étude est proposée pour la mise en correspondance des anatomies avec et sans applicateur de curiethérapie. Cette dernière repose la définition et l’évaluation des méthodes de recalage déformable standards et biomécaniques pour la déformation de dose.

Les résultats, reposant notamment sur des critères géométriques, montrent que les approches proposées permettent d’assurer, pour toutes les patientes, une bonne couverture de la cible, tout en limitant l’irradiation des organes sains et donc, à terme, des meilleurs résultats cliniques.

Mots clés : Col de l’utérus, radiothérapie adaptive, recalage déformable, modèle statistique de forme

TABLE DES MATIERES

Résumé 4

Table des matières 6

Acronymes 9

Introduction 12

Références 15

1 Contexte 16

1.1 Introduction 17

1.2 Cancer du col de l'utérus 17

1.2.1 Anatomie de l'utérus 17

1.2.2 Epidémiologie 18

1.2.3 Cause 19

1.2.4 Classification 19

1.2.5 Vaccination et dépistage 20

1.2.6 Bilan initial 21

1.3 Traitement des cancers du col de l'utérus 23

1.3.1 Radiothérapie externe 24

1.3.2 Curiethérapie 28

1.3.3 Effets secondaires du traitement 32

1.4 Problématique de la variabilité anatomique 33

1.4.1 Quantification des incertitudes anatomiques 33

1.4.2 Impact sur la dose délivrée 35

1.4.3 Prise en compte des incertitudes géométriques 36

1.5 Objectifs de la thèse 40

1.6 Références 41

2 Recalage déformable pour la radiothérapie : principe, méthodes, applications et évaluation 48

2.1 Introduction 49

2.2 Article : "Deformable image registration for radiation therapy: principle, methods, applications, and evaluation" 50

2.2.1 Introduction 51

2.2.2 Principle of deformable image registration 52

2.2.3 Classic registration methods used in radiotherapy 56

2.2.4 DIR applications in RT 59

2.2.5 DIR evaluation 68

2.2.6 Conclusion 75

2.2.7 References 76

2.3 Discussion : recalage déformable pour les cancers du col de l’utérus 93

2.3.1 Recalage déformable pour la propagation des contours 93

2.3.2 Recalage déformable pour la radiothérapie adaptative 94

2.4 Conclusion 97

2.5 Références 98

3 Librairie évolutive guidée par l’imagerie CBCT pour l’IMRT des cancers du col utérin 102

3.1 Introduction 103

3.2 Article : “CBCT-guided evolutive library for cervical adaptive IMRT” 105

3.2.1 Introduction 107

3.2.2 Materials and methods 108

3.2.3 Results 115

3.2.4 Discussion 123

3.2.5 Conclusion 126

3.2.6 References 127

3.3 Discussion 131

3.4 Conclusion 135

3.5 Références 136

4 Modèle statistique de forme pour la modélisation d’une librairie de plans de traitement 138

4.1 Introduction 139

4.2 Article : “Statistical shape model to generate a planning library for cervical adaptive radiotherapy” 140

4.2.1 Introduction 141

4.2.2 Methods 143

4.2.3 Evaluation 150

4.2.4 Discussion and Conclusion 157

4.2.5 References 159

4.3 Discussion 162

4.3.1 Limites et perspectives 162

4.4 Extension au cancer de la vessie 164

4.5 Conclusion 168

4.6 Références 169

5 Recalage déformable biomécanique pour la curiethérapie des cancers du col utérin 172
5.1 Introduction 173
5.1.1 Principe de base des modèles biomécaniques 174
5.1.2 Méthode des éléments finis 175
5.2 Article : "Technical Note: Biomechanical model-based deformable image registration to solve extreme position variation in a commercial treatment planning system" 177
5.2.1 Introduction 179
5.2.2 Materials and methods 179
5.2.3 Registration methods description 181
5.2.4 Registration methods evaluation 182
5.2.5 Results 182
5.2.6 Discussion 186
5.2.7 Conclusion 186
5.2.8 References 187
5.3 Article : "Deformable image registration for dose mapping between external beam radiotherapy and brachytherapy for cervical cancer" 188
5.3.1 Introduction 189
5.3.2 Materials and methods 191
5.3.3 Results 198
5.3.4 Discussion 208
5.3.5 Conclusion 210
5.3.6 References 211
5.4 Discussion 216
5.5 Conclusion 217
5.6 Références 218
Synthèse et conclusion 220
Références 224
Liste des publications 225

ACRONYMES

Acronyme	Définition française	Définition anglaise
AAPM	Association américaine des physiciens médicaux	*American association of physicists in medicine*
ACVD		*Approximated centroidal Voronoi diagrams*
ADN	Acide désoxyribonucléique	*Deoxyribonucleic acid*
ANACONDA	Algorithme de déformation contraint par l'anatomie	*ANAtomically CONstrained Deformation Algorithm*
AP	Antéro-postérieur	*Antero-posterior*
ART	Radiothérapie adaptative	*Adaptive radiation therapy*
BT	Curiethérapie	*Brachytherapy*
CBCT	Imagerie volumétrique par faisceau conique	*Cone beam computed tomography*
CCS	Système de coordonnée commun	*Common coordinate system*
CPD		*Coherent point drift*
CT	Tomodensitométrie (TDM)	*Computed tomography*
CTV	Volume de la cible clinique	*Clinical target volume*
DDM		*Distance discordance metric*
DIR	Recalage déformable d'images	*Deformable image registration*
DMR	Recalage déformable de maillages	*Deformable mesh registration*
DSC	Coefficient de similarité de Dice	*Dice similarity score*
DTA		*Distance to agreement*
DVF	Champ de déformation	*Deformation vector field*
DVH	Histogramme dose-volume	*Dose volume histogram*
EB	Vessie vide	*Empty bladder*
EBRT	Radiothérapie externe	*External beam radiation therapy*
EQD2	Dose équivalente à un traitement fractionné de 2 Gy	*Equivalent dose to a 2 Gy fraction treatment*
ESTRO	Société Européenne de Radiothérapie et d'Oncologie	*European Society for Radiotherapy and Oncology*
FB	Vessie pleine	*Full bladder*
FDG	Fluorodésoxyglucose	*Fluorodeoxyglucose*
FEM	Méthode des éléments finis	*Finite element model*
FEA	Analyse des éléments finis	*Finite element analysis*
FFD		*Free-form deformation*
FIGO	Fédération Internationale de Gynécologie et d'Obstétrique	
FOV	Champ de vue	*Field of view*
GEC	Groupe Européen de Curiethérapie	
GeoD	Distance géodésique	*Geodesic distance*
GPU	Processeur graphique	*Graphic processing unit*
GTV	Volume de la tumeur brute	*Gross tumor volume*
Gy	Gray	*Gray*
HAS	Haute Autorité de la Santé	
H&N	Tête et cou	*Head and neck*
HCSP	Haut Conseil de la Santé Publique	
HD	Distance de Hausdorff	*Hausdorff distance*
HDR	Débit de dose élevé	*High dose rate*

HR-CTV	Volume de la cible clinique à haut risque	*High risk clinical target volume*
HU	Unité Hounsfield	*Hounsfield unit*
IB	Vessie intermédiaire	*Intermediate bladder*
ICCP		*International Cancer Control Partnership*
ICE		*Inverse consistency error*
IGRT	Radiothérapie guidée par l'image	*Image guided radiation therapy*
InVS	Institut de Veille Sanitaire	
IR-CTV	Volume de la cible clinique à risque intermédiaire	*Intermediate risk clinical target volume*
ITV	Volume cible joint	*Internal target volume*
IMRT	Radiothérapie par modulation d'intensité (RCMI)	*Intensity-modulated radiation therapy*
LACC	Cancer des col de l'utérus localement avancés	*Locally advanced cervical carcinoma*
LDR	Débit de dose faible	*Low dose rate*
LINAC	Accélérateur linéaire	*Linear accelerator*
LR	Latérale, gauche-droite	*Left-right*
MATAD		*Mean absolute triangle area difference*
MNND		*Mean nearest neighbor distance*
MRI	Imagerie par résonance magnétique (IRM)	*Magnetic resonance imaging*
MVCT		*Megavoltage computed tomography*
OAR	Organe à risqué	*Organ at risk*
PCA	Analyse en composantes principales (ACP)	*Principal component analysis*
PDR	Débit de dose pulsé	*Pulsed dose rate*
PET	Tomographie par émission de positons	*Positron emission tomography*
PTV	Volume de traitement prévisionnel	*Planning target volume*
RR	Recalage rigide	*Rigid registration*
RC3D	Radiothérapie conformationnelle 3D	*3D conformal radiotherapy*
RT	Radiothérapie	*Radiation therapy*
SFBR	Registration basée sur les caractéristiques	*Salient feature-based registration*
SC	Contexte de forme	*Shape context*
SI	Supéro-inférieur	*Superior-inferior*
SIMPLE		*Selective and iterative method for performance level estimation*
SSM	Model statistique de forme	*Statistical shape model*
STAPLE		*Simultaneous truth and performance level estimation*
ToU	Point du fond utérin	*Top of the uterus*
TPS	Système de planification de traitement	*Treatment planning systems*
TPS-RPM	Correspondance de points robuste par spline plaque mince	*Thin plate spline robust-point matching*
TNM	Tumeur, ganglion, métastase	*Tumor, node, metastasis*
TRE		*Target registration error*
US	Ultrason	*Ultrasound*
VMAT	Radiothérapie à modulation d'intensité volumétrique par Arc Thérapie	*Volumetric modulated arc therapy (*VMAT)
VOI	Volume d'intérêt	*Volume of interest*
VPH	Virus papillome humain	*Human papillomavirus*

INTRODUCTION

Le cancer du col de l'utérus touche environ 3000 femmes en France chaque année, causant 1400 décès [1]. A l'échelle mondiale, il représente le quatrième cancer chez la femme, avec 6.6% des nouveaux cas, soit 570 000 cas et 311 000 décès. Son incidence est particulièrement élevée dans les pays en développement (par ex. 40 cas pour 100 000 femmes en Afrique de l'Est, contre 6.8 en Europe de l'Ouest). Le nombre de nouveaux cas est de plus en diminution dans les pays industrialisés grâce à la mise en place d'un dépistage anticipé et de deux vaccins qui visent 70% des virus papillomes humains, qui sont la première cause du cancer du col de l'utérus.

Le traitement recommandé pour les cancers du col de l'utérus localement avancés, c'est-à-dire les tumeurs non limitées au col, consiste en une radiothérapie externe en parallèle à une chimiothérapie, suivie d'une curiethérapie. La radiothérapie externe consiste en l'irradiation de la cible clinique, qui comprend le col, l'utérus et l'atteinte vaginale, par un rayonnement externe. La curiethérapie repose quant à elle sur la mise en place d'un dispositif médical permettant l'irradiation locale de la tumeur résiduelle.

La radiothérapie externe repose sur deux étapes, une étape de planification et une phase de délivrance du traitement. La planification est réalisée à partir d'une image de tomodensitométrie (TDM) permettant de représenter l'anatomie du pelvis de la patiente. Sur cette TDM, la cible clinique et les organes à risque voisins (rectum, vessie, cavité péritonéale…) sont délinéés afin de permettre l'optimisation d'une balistique de traitement qui est utilisée pour les 5 semaines de traitement. Pour la curiethérapie, une opération chirurgicale en ambulatoire permet l'insertion d'un applicateur au sein de l'anatomie, au contact de la tumeur. Comme pour la radiothérapie externe, une image de planification est acquise, avec l'applicateur, pour permettre la délinéation des organes et la planification de la dose de traitement. La curiethérapie est ensuite réalisée sur quelques séances et délivre une dose importante dans la tumeur résiduelle tout en limitant l'irradiation des organes voisins.

Grâce aux évolutions technologiques des dispositifs d'irradiation et d'imagerie, la précision de ces deux traitements a été grandement améliorée et permet de délivrer des distributions de doses aux formes complexes afin de mieux cibler la tumeur tout en épargnant au maximum les organes sains. Cependant, optimisés suivant l'anatomie de la patiente représentée par les images de planification (avec généralement une unique image acquise pour chaque traitement), ces traitements ne prennent pas en compte les modifications anatomiques qui sont susceptibles de se produire entre la planification et les séances de délivrance de la dose. En effet, la position et la forme de la cible clinique peuvent être modifiées, notamment en fonction du remplissage des organes voisins mais aussi en fonction de la réponse au traitement (réduction du volume tumoral). Par exemple, l'utérus étant positionné juste au-dessus de la vessie, le niveau de remplissage de cette dernière peut avoir un impact considérable sur sa position et sa forme. De ce fait, la dose de planification optimisée sur une anatomie acquise en début de traitement peut ne pas correspondre à la dose réellement délivrée, avec un risque de sous-dosage de la tumeur et de surdosage des organes sains, et un impact clinique avec une augmentation des risques de récidive du cancer et d'apparition d'effets secondaires.

La prise en compte de ces variations anatomiques est donc indispensable afin d'assurer un traitement optimal. Une première approche repose sur l'utilisation de marges, afin d'augmenter la taille du volume traité pour améliorer la couverture de la cible, avec toutefois une augmentation de l'irradiation des organes sains. Une autre approche, plus complexe, repose sur l'utilisation de plusieurs plans de traitement (au lieu d'un unique plan utilisé en standard), afin d'adapter le traitement en fonction de l'anatomie de la patiente lors des différences séances d'irradiation. Cette approche est dite « radiothérapie adaptative ». Pour les cancers du col de l'utérus, la stratégie adaptative la plus utilisée repose sur une librairie de plans de traitement. Puisque le volume vésical influe la position de l'utérus [2], plusieurs images TDM sont acquises à la planification avec des volumes de vessie variables (de vide à pleine) [3,4]. Différentes planifications peuvent être alors générées, qui seront choisies à chaque séance de traitement en fonction de l'anatomie du jour [5]. Si cette approche a montré une amélioration de la couverture tumorale [6,7], elle est limitée pour les patientes dont l'utérus, non-mobile à la planification, devient mobile en cours de traitement.

Les déformations anatomiques peuvent être estimées à partir des images acquises, grâce à des méthodes de recalage déformable qui permettent l'estimation d'un champ de déformation. Plusieurs méthodes de recalage déformable ont été développées dans la littérature pour des applications spécifiques en termes de population étudiée, d'objectif, d'organes et d'images considérés. Cependant, aucune méthode de référence n'a été définie pour le col de l'utérus, ce qui complique le développement et l'évaluation de nouvelles stratégies adaptatives.

Les objectifs de cette thèse sont donc d'améliorer la prise en compte des variations anatomiques importantes survenant au cours du traitement des cancers du col de l'utérus. Ceci passe par la proposition et l'évaluation de nouvelles stratégies de radiothérapie adaptative et le développement d'outils de traitement d'images, notamment de recalage, permettant leur mise en œuvre. Ces approches optimisées doivent être comparées aux approches classiques de la littérature afin de quantifier leur bénéfice potentiel.

Ce manuscrit de thèse commence par présenter le contexte clinique du cancer du col de l'utérus, son traitement standard, ainsi que la problématique des incertitudes géométriques. Les quatre chapitres suivants reposent sur des articles soumis (chapitres 2 et 5) ou publiés (chapitres 3 et 4).

Le deuxième chapitre propose une étude de la littérature sur les techniques de recalage déformable d'images dans le contexte de la radiothérapie, externe et par curiethérapie. L'objectif est de présenter de manière didactique le principe du recalage déformable ainsi que les principales méthodes utilisées en radiothérapie. Leurs principales applications sont aussi présentées, ainsi que les approches d'évaluation. Ce chapitre s'achève sur une section se concentrant sur les méthodes de recalage utilisées dans le contexte des cancers du col de l'utérus.

Les deux chapitres suivants proposent des nouvelles stratégies de radiothérapie adaptative pour les cancers du col de l'utérus.

Décrite dans le chapitre 3, la première stratégie proposée, appelée « librairie évolutive » repose sur une librairie de plans de traitement qui puisse être enrichie grâce aux images acquises pendant le traitement. Cette approche est comparée aux principales stratégies alternatives.

Dans le chapitre 4, une stratégie adaptative reposant sur une analyse de population est présentée et évaluée. Cette stratégie repose sur une étape de recalage déformable pour mettre en correspondance une cohorte de patientes et sur une analyse populationnelle afin d'extraire les déformations dominantes, avant de les propager sur l'anatomie d'une nouvelle patiente. Son objectif est de modéliser, dès la planification, une librairie de plans de traitement pour anticiper les déformations les plus probables.

Le chapitre 5 s'intéresse à la deuxième partie du traitement, la curiethérapie. Son objectif est de quantifier les déformations anatomiques induites par l'insertion de l'applicateur qui permet la délivrance de la dose de curiethérapie. Afin de propager cette dose vers une anatomie de référence sans applicateur, une approche de recalage déformable reposant sur un modèle biomécanique est proposée. L'approche est évaluée et comparée à des méthodes classiques et des outils commerciaux. Ce dernier chapitre a fait l'objet d'un travail en collaboration, dans le cadre d'une mobilité, avec le *Morfeus Lab* situé au *MD Anderson Cancer Center, The University of Texas, Houston*.

Ces travaux de cette thèse ont été financés par la Ligue contre le Cancer et Rennes Métropole.

RÉFÉRENCES

1. (GCO) TGCO. Estimating the world cancer burden: Globocan 2018.

2. Ahmad R, Hoogeman MS, Bondar M, Dhawtal V, Quint S, De Pree I, Mens JW, Heijmen BJ. Increasing treatment accuracy for cervical cancer patients using correlations between bladder-filling change and cervix–uterus displacements: Proof of principle. *Radiotherapy and oncology* 2011;98:340-346.

3. Bondar L, Hoogeman M, Mens JW, Dhawtal G, De Pree I, Ahmad R, Quint S, Heijmen B. Toward an individualized target motion management for imrt of cervical cancer based on model-predicted cervix–uterus shape and position. *Radiotherapy and Oncology* 2011;99:240-245.

4. Bondar M, Hoogeman M, Mens J, Quint S, Ahmad R, Dhawtal G, Heijmen B. Individualized nonadaptive and online-adaptive intensity-modulated radiotherapy treatment strategies for cervical cancer patients based on pretreatment acquired variable bladder filling computed tomography scans. *International Journal of Radiation Oncology* Biology* Physics* 2012;83:1617-1623.

5. Heijkoop ST, Langerak TR, Quint S, Bondar L, Mens JWM, Heijmen BJ, Hoogeman MS. Clinical implementation of an online adaptive plan-of-the-day protocol for nonrigid motion management in locally advanced cervical cancer imrt. *Int J Radiat Oncol Biol Phys* 2014;90:673-679.

6. Seppenwoolde Y, Stock M, Buschmann M, Georg D, Bauer-Novotny K-Y, Pötter R, Georg P. Impact of organ shape variations on margin concepts for cervix cancer art. *Radiotherapy and Oncology* 2016.

7. van de Schoot AJ, de Boer P, Visser J, Stalpers LJ, Rasch CR, Bel A. Dosimetric advantages of a clinical daily adaptive plan selection strategy compared with a non-adaptive strategy in cervical cancer radiation therapy. *Acta Oncologica* 2017;56:667-674.

1 CONTEXTE

1 Contexte 16
  1.1 Introduction 17
  1.2 Cancer du col de l'utérus 17
    1.2.1 Anatomie de l'utérus 17
    1.2.2 Epidémiologie 18
    1.2.3 Cause 19
    1.2.4 Classification 19
    1.2.5 Vaccination et dépistage 20
    1.2.6 Bilan initial 21
  1.3 Traitement des cancers du col de l'utérus 23
    1.3.1 Radiothérapie externe 24
    1.3.2 Curiethérapie 28
    1.3.3 Effets secondaires du traitement 32
  1.4 Problématique de la variabilité anatomique 33
    1.4.1 Quantification des incertitudes anatomiques 33
    1.4.2 Impact sur la dose délivrée 35
    1.4.3 Prise en compte des incertitudes géométriques 36
  1.5 Objectifs de la thèse 40
  1.6 Références 41

1.1 INTRODUCTION

Ce chapitre a pour objectif de présenter le contexte clinique dans lequel a évolué cette thèse. La première partie présente l'anatomie du pelvis féminin avec le col de l'utérus, le vagin, l'utérus et les organes voisins. Ensuite, l'incidence du cancer du col de l'utérus, ses causes et son diagnostic sont décrits. Ce chapitre présente alors le traitement de référence proposé aux patientes atteintes d'un cancer du col de l'utérus localement avancé, en détaillant principalement la radiothérapie externe (*External Beam Radiation Therapy*, EBRT) et la curiethérapie (*Brachytherapy*, BT), qui font l'objet de ces travaux. Ce chapitre s'achève sur les problématiques liées aux modifications anatomiques (variabilité anatomique) survenant en cours de traitement et sur les objectifs de ces travaux.

1.2 CANCER DU COL DE L'UTÉRUS

1.2.1 ANATOMIE DE L'UTERUS

L'anatomie du pelvis féminin comprend le vagin, l'utérus (avec le col utérin et le corps de l'utérus), la vessie et l'urètre, le rectum et le canal anal ainsi que le sigmoïde qui rejoint la cavité péritonéale (*cf.* Figure 1-1).

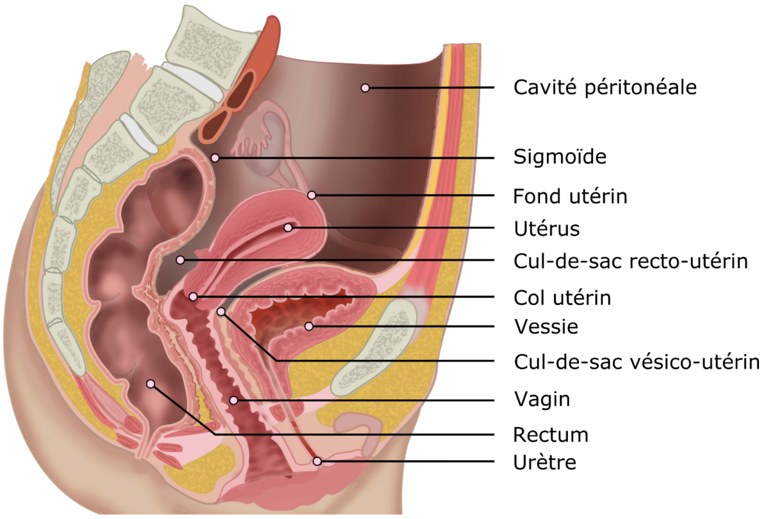

Figure 1-1 : Vue sagittale de l'anatomie du pelvis féminin

L'utérus est l'organe de la gestation dans lequel se développe l'œuf fécondé. Pendant la grossesse, il augmente de volume pour contenir le fœtus et ses annexes (le placenta, cordon ombilical et les membranes), le temps du développement du bébé. Après l'accouchement, cet organe retrouve quasiment sa forme initiale.

L'utérus est un organe musculaire creux avec une paroi épaisse, positionné au centre du pelvis féminin, entre la vessie (en antérieur) et le rectum (en postérieur, *cf.* Figure 1-1). De chaque côté on trouve la séparation avec le rectum et la vessie, que l'on appelle respectivement le cul-de-sac recto-utérin et cul-de-sac vésico-utérin. L'utérus peut être divisé en deux parties au niveau de son rétrécissement, l'isthme utérin, qui sépare le corps de l'utérus (partie haute) et le col de l'utérus (partie basse, *cf.* Figure 1-2) :

- Le corps de l'utérus est de forme conique plate avec une partie ventrale (côté vessie) et dorsale (côté rectum). Le corps de l'utérus est composé d'une partie musculaire (le myomètre), d'une cavité de 3 à 6 ml et d'une muqueuse tapissant l'intérieur de cette cavité (l'endomètre). Au niveau du fond utérin (partie supérieure), on retrouve de chaque côté les cornes utérines qui intègrent les trompes de Fallope, de fins canaux qui rejoignent les ovaires.
- Le col de l'utérus est de forme cylindrique et divisé en deux portions, la portion supra-vaginale qui prolonge le corps utérin et la portion intra-vaginale. Au voisinage de la portion supra-vaginale se trouvent, de chaque côté, des structures tissulaires fibreuses fixant l'utérus latéralement (les paramètres). La portion intra-vaginale se présente comme un bouchon muqueux, percée en son milieu par le canal endocervical, permettant de relier la cavité utérine à la cavité vaginale (*cf*. Figure 1-2, endocol et exocol).

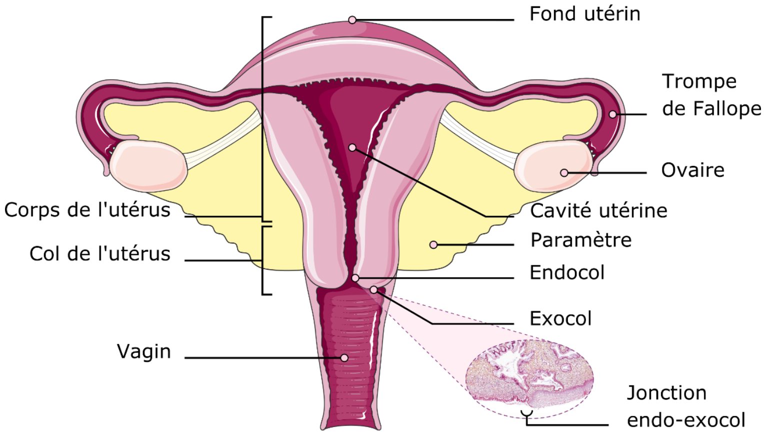

Figure 1-2 : Anatomie de l'appareil reproducteur féminin (vue de face)

1.2.2 EPIDEMIOLOGIE

D'après l'Institut de Veille Sanitaire (InVS), le nombre de nouveaux cas de cancer du col de l'utérus rapportés en France en 2015 est estimé à 2797 pour un nombre de décès de 1102 [1]. Le cancer du col de l'utérus est en diminution en France depuis les années 1980 (-2.5% en moyenne par an). Un dépistage, annuel dans un premier temps puis trisannuel, est recommandé aux femmes de plus de 20 ans depuis les années 1990. Au niveau mondial, le nombre de nouveaux cas par an est estimé à plus de 500 000. L'incidence du cancer du col de l'utérus est géographiquement très hétérogène, touchant notamment les pays en voie de développement. D'après l'Alliance des Ligues francophones Africaines et Méditerranéennes contre le cancer (ALIAM), le nombre de cancers du col de l'utérus en Afrique francophone (21 pays) en 2012 était de 21511 pour un nombre de décès de 14736 [2].

Le cancer du col de l'utérus est la 4ème cause de cancer chez la femme dans le monde. En France, il est le 12ème cancer le plus commun et la 10ème cause de mortalité par cancer. Il est à noter que les cancers gynécologiques représentent 19% des cancers dans le monde (sur un total de 5.1 millions de cas estimé en 2002) [3]. Ces cancers regroupent les cancers du col de l'utérus (20%), du corps de l'utérus (endomètre) (44%), des ovaires (31%), du vagin (<4%) et de la vulve (<4%) [4].

1.2.3 CAUSE

La principale cause du cancer du col de l'utérus est une infection persistante du Virus Papillome Humain (VPH) qui se transmet par contact sexuel [5]. Cette infection est souvent transitoire et devient indétectable dans 90% des cas à 2 ans. L'utilisation du préservatif n'empêche pas cette infection mais en diminue les risques. Environ 80% des femmes seront infectées au moins une fois par ce type de virus au cours de leur vie. Dans certains cas, pour environ 10% des femmes infectées, le virus s'installe pendant plusieurs années au niveau de la muqueuse du col de l'utérus, à la jonction entre l'endocol et l'exocol (*cf*. Figure 1-2). Le virus peut alors provoquer des lésions précancéreuses qui risquent, sur une durée de 10 à 15 ans, d'évoluer vers un cancer. Une centaine de VPH existent, parmi lesquels 13 sont cancérogènes. L'implication du VPH16 et VPH18 dans les cancers du col est de 70.7% dans le monde et de 81.8% en France.

Même si le VPH est responsable de l'apparition du cancer du col de l'utérus dans 99.7% des cas, d'autres facteurs peuvent favoriser le développement de celui-ci, avec notamment : les rapports sexuels à un âge précoce, la multiplicité des partenaires, le tabagisme [6], l'utilisation prolongée de contraceptifs hormonaux [7], l'immunosuppression ou encore d'autres infections comme la Chlamydia Trachomatis ou le virus de l'herpès génital.

1.2.4 CLASSIFICATION

Le cancer du col de l'utérus peut être caractérisé suivant plusieurs classifications cliniques. Les principales classifications sont les suivantes : la classification de la Fédération Internationale de Gynécologie et d'Obstétrique (FIGO), la classification « *Tumor, Node, Metastasis* » (TNM, pour « tumeur, ganglions, métastases »), la classification du *MD Anderson Cancer Center* et la classification de l'Institut Gustave-Roussy. Ces classifications cliniques ne prennent pas en compte les résultats issus des examens d'imagerie médicale. La plus utilisée est la classification FIGO, qui existe depuis 1958 et a été définie d'après la classification en 4 stades de la *League of Nations* en 1929 [8]. Depuis, la classification FIGO a été révisée 7 fois jusqu'à 2009 [9].

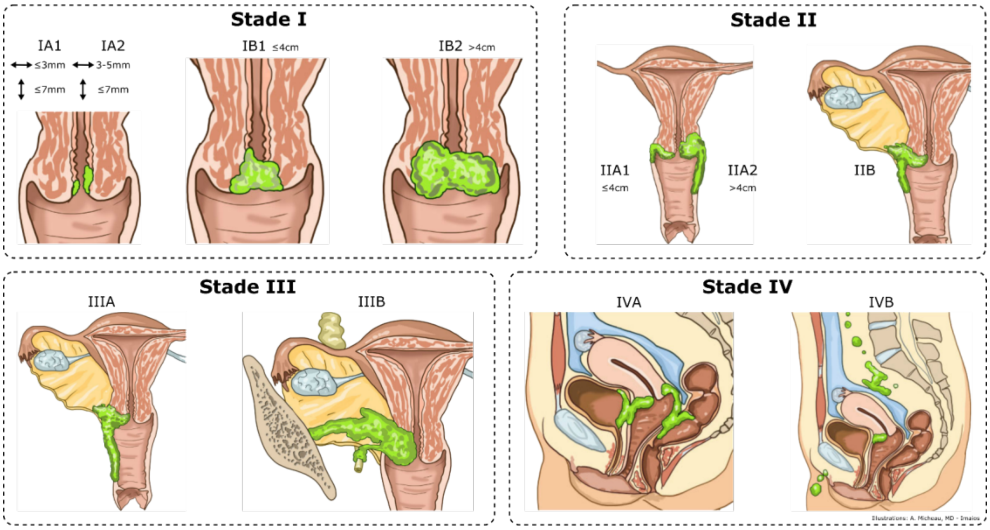

Figure 1-3 : Stades cliniques des cancers invasifs du col de l'utérus selon les recommandations de la FIGO (adapté de [10])

La classification FIGO caractérise les cancers gynécologiques en fonction du stade de la tumeur. Pour le cancer du col de l'utérus, le stade 0 correspond aux lésions précancéreuses locales, le stade I aux cancers localisés, les stades II à IVA aux tumeurs localement avancées et le stade IVB aux tumeurs métastatiques (*cf*. Figure 1-3 et Tableau 1-1).

Tableau 1-1 : Classification des cancers invasifs du col de l'utérus selon les recommandations de la FIGO

Stade	Description du stade clinique du cancer
0	Carcinome in situ
I	Carcinome limité au col
IA	Carcinome invasif préclinique. Toute lésion macroscopique est un stade IB
IA1	Invasion du stroma (tissu de soutien) ≤ 3 mm en profondeur et ≤ 7 mm horizontalement
IA2	Invasion du stroma entre 3 et 5 mm en profondeur et ≤ 7 mm horizontalement
IB	Tumeur limitée au col mais supérieure au stade IA2 ou macroscopique
IB1	Tumeur limitée au col ≤ 4 cm
IB2	Tumeur limitée au col > 4 cm
II	Tumeur dépassant le col et sans prolifération à la paroi pelvienne ni premier tiers du vagin
IIA	Sans envahissement du paramètre
IIB	Avec envahissement du paramètre
III	Prolifération à la paroi pelvienne ou au premier tiers du vagin
IIIA	Lésion atteignant le tiers inférieur du vagin sans atteinte de la paroi pelvienne
IIIB	Lésion atteignant la paroi pelvienne
IV	Tumeur dépassant le pelvis ou atteignant la vessie ou le rectum
IVA	Lésion atteignant la vessie ou le rectum
IVB	Métastase à distance

1.2.5 VACCINATION ET DEPISTAGE

Depuis 2006, deux vaccins prophylactiques recombinants sont utilisés en France, qui visent 70% des VPH cancérogènes. Cette vaccination est proposée à toutes les jeunes femmes de 11-14 ans et jusqu'à 19 ans en rattrapage. Ce chiffre est ramené à 9 ans dans le cas de patientes ayant subi une greffe, de par le risque accru d'immunosuppression. D'après un rapport du Haut Conseil de la Santé Publique (HCSP) [11], le taux de vaccination du VPH en France reste trop faible, avec un taux de 14% de femmes vaccinées en 2014, contre 80% au Royaume-Uni. Le taux de protection du vaccin contre les virus visés est proche de 100%, cependant, ce dernier n'est pas efficace si l'infection a eu lieu avant l'injection. De plus, il est encore trop tôt pour avoir un retour sur le taux de protection à long terme, inconnue après 5 ans. C'est pourquoi, dans l'intérêt de réduire l'incidence de ce cancer, un plan de dépistage a été mis en place, combinant la vaccination des jeunes femmes et un dépistage régulier.

Le dépistage du cancer du col de l'utérus, réalisé par un médecin, a pour objectif de confirmer l'absence ou la présence de lésions ou cellules précancéreuses. Il repose sur le frottis cervico-utérin, qui est un test cytologique (c'est-à-dire d'étude des cellules), une inspection visuelle des organes génitaux externes et l'examen au spéculum du col de l'utérus. Dans le cas de deux dépistages annuels négatifs successifs, celui-ci devient trisannuel. D'après la Haute Autorité de la Santé (HAS) [12], en France, le taux de dépistage du cancer du col de l'utérus a été estimé à 58% entre 2007 et 2009. Il est considéré que seulement 8% des femmes âgées entre 25 et 65 ans ont un suivi régulier adéquat.

1.2.6 BILAN INITIAL

Dans le cas d'un dépistage positif (frottis cervico-utérin anormal) ou dans le cas de symptômes (par ex. incontinence urinaire avec brûlure, écoulements sanguins, écoulements de type infectieux, douleurs lombaire ou pelvienne), des examens sont effectués pour définir un diagnostic. Un bilan initial de la maladie est fait si le diagnostic est positif.

1.2.6.1 Examen clinique

L'examen clinique a pour objectif de définir le stade de la tumeur et repose sur un examen gynécologique complet. Celui-ci comprend un examen au speculum afin de définir la taille de la tumeur et d'évaluer la prolifération macroscopique de la lésion au vagin. Un toucher vaginal est réalisé pour examiner les cloisons recto-vaginale et vésico-vaginale. De plus, un toucher rectal est réalisé afin d'examiner le cul-de-sac recto-utérin, le rétrécissement de l'utérus (l'isthme utérin) et les paramètres.

1.2.6.2 Examen d'histopathologie

L'examen d'histopathologie est indispensable afin d'apporter un diagnostic définitif. Pour ce faire, une opération chirurgicale est nécessaire afin d'extraire une pièce de la lésion. En cas de petite lésion, une biopsie peut être réalisée dans la région observée par l'assistance d'une colposcopie. Lorsque la biopsie n'est pas possible par manque d'accès visuel, une ablation d'un fragment du col utérin en forme de cône, au niveau de la jonction de l'exocol et de l'endocol, est réalisée (la conisation).

L'examen anatomopathologique de la pièce de la lésion précise alors le type histologique, le caractère invasif et le grade de différentiation de la tumeur (par ex. bas grade différencié, ou haut grade différencié ou indifférencié). Deux principaux types de cancers du col de l'utérus sont rencontrés. Le carcinome épidermoïde, représentant environ 85% des cancers du col de l'utérus, se développe au niveau de la surface du col (revêtement épithélial du col). L'adénocarcinome, représentant environ les 15% restant, se développe au niveau des tissus glandulaires du col (épithélium glandulaire du col) [13].

1.2.6.3 Examen d'imagerie

L'examen d'imagerie a comme objectif de quantifier le volume de la tumeur initiale, l'extension locorégionale et d'évaluer le statut ganglionnaire. La classification FIGO encourage l'usage d'examens d'imageries, si disponible, afin de renforcer la précision du diagnostic.

Pour les lésions de petites tailles, l'imagerie n'est pas obligatoire. Cependant, dans le cas de lésions macroscopiques bien définies, elle est recommandée pour évaluer la taille de la tumeur, l'atteinte exacte aux paramètres et la prolifération de la tumeur dans la zone pelvienne et aux ganglions.

1.2.6.3.1 Imagerie IRM

L'Imagerie par Résonance Magnétique (IRM ou *Magnetic Resonance Imaging*, MRI) permet, par l'observation des propriétés des atomes d'hydrogène, de générer des images 2D ou 3D non invasives du corps humain. Les plus utilisées dans le contexte de la détection de cancers sont les images avec séquences T1 et T2, qui permettent d'observer le contraste entre les tissus et au sein d'un même tissu, respectivement.

Dans le cadre du diagnostic du cancer du col de l'utérus, les recommandations pour l'acquisition d'IRM sont les suivantes [14] :

- Acquisition à séquence pondérée T2, parallèle et perpendiculaire au col de l'utérus qui permet l'évaluation de la taille de la tumeur initiale et son extension aux organes adjacents (*cf*. Figure 1-4) ;
- Acquisition à séquence pondérée T1 de grand champ qui permet l'évaluation de l'extension du cancer aux ganglions lymphatiques. De plus, une image pondérée de diffusion peut être acquise ;
- Acquisition avec un produit de contraste, à base de gadolinium, qui peut aider à la visualisation des petites lésions inférieures à 2 cm.

L'IRM semble la plus adaptée pour enrichir le diagnostic et correctement définir le stade de la tumeur. Il a en effet été montré que les performances de sensibilité et de spécificité de l'IRM comparées à la tomodensitométrie (TDM ou *Computed Tomography*, CT) étaient globalement meilleures [15].

1.2.6.3.2 Imagerie TEP/TDM

L'imagerie de Tomographie par Emission de Positons (TEP) au fluorodésoxyglucose (18F-FDG) permet l'acquisition d'une image fonctionnelle, puisqu'elle traduit l'activité des cellules en termes de consommation de glucose, notamment les cellules tumorales (*cf*. Figure 1-4). Dans la majorité des cas, cet examen est acquis simultanément avec une TDM non contrastée qui n'a pas d'objectif diagnostic mais permet une correction de l'atténuation des photons. Cette image, acquise coupe par coupe, représente la densité des tissus en unité Hounsfield (*Hounsfield Unit*, HU) de -1000 pour l'air à +1000 pour l'os dense, en passant par -50 pour la graisse et 0 pour l'eau.

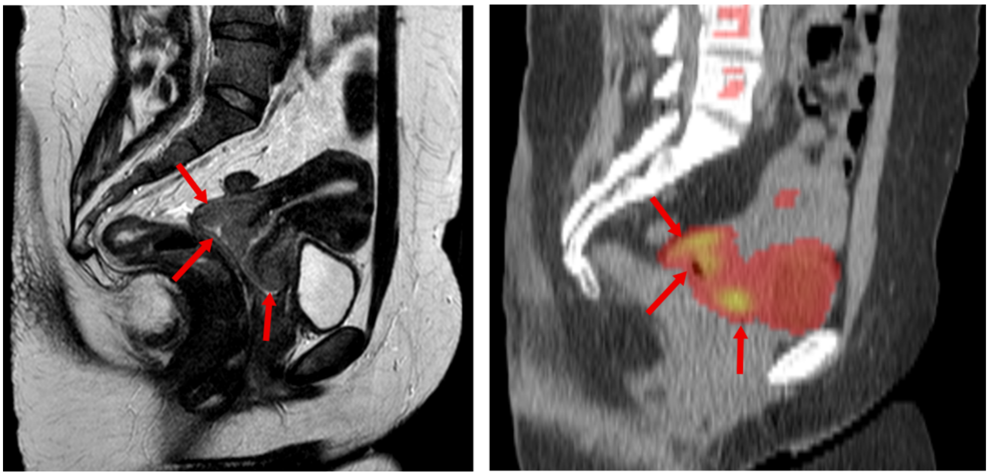

Figure 1-4 : Imagerie IRM (à gauche) et TEP/TDM (à droite) de diagnostic pour une patiente atteinte d'un carcinome épidermoïde stade FIGO IIb (aucun signe d'extension aux ganglions lymphatiques à la TEP ; vessie marquée de par l'accumulation du radio-traceur dans l'urine)

Même si les performances de ces modalités d'imagerie sont différentes pour évaluer le stade et l'extension du cancer, la complémentarité de ces informations offre un diagnostic qui permet de sélectionner un traitement adapté. La biopsie des ganglions sentinelles (pelviens et para-aortiques) reste la méthode de diagnostic la plus précise pour le statut ganglionnaire [16,17].

Ce bilan initial permet de définir la tumeur macroscopique (*Gross Tumor Volume*, GTV).

1.3 TRAITEMENT DES CANCERS DU COL DE L'UTÉRUS

Plusieurs options de traitement sont recommandées en fonction du stade de la tumeur. Ces différentes options peuvent être une simple surveillance, une (colpo)-hystérectomie ou une radiothérapie externe couplée à une chimiothérapie suivie d'une curiethérapie seule.

L'hystérectomie ou colpo-hystérectomie est un geste chirurgical qui a comme objectif de retirer l'utérus et, parfois, les paramètres et les ganglions lymphatiques du pelvis. En fonction du pronostic, il est possible de procéder à une chirurgie conservatrice qui ne retire que le col de l'utérus et les ganglions lymphatiques pelviens. Dans ce dernier cas, la grossesse est encore possible après convalescence.

La chimiothérapie est un traitement médicamenteux qui est souvent prescrit en parallèle à la radiothérapie externe. Ce traitement est délivré par voie sanguine et est constitué d'une dose de cisplatine. L'objectif de ce traitement est de détruire les cellules qui se divisent vite (par ex. les cellules sanguines, les cellules malignes…) en provoquant leur apoptose, le suicide cellulaire. Ce traitement étant global, il a pour rôle de détruire les cellules qui se sont éloignées du cœur de la tumeur diagnostiquée et qui pourraient se propager sur d'autres organes sains. De plus, le cisplatine peut agir comme un « radiosensibilisant » qui améliore l'efficacité de la radiothérapie externe [18].

En fonction de la classification FIGO du cancer, les différentes options sont :

- Stade 0 :
  - Surveillance simple si la tumeur était suffisamment petite pour être retirée chirurgicalement au moment de la biopsie ;
  - Chirurgie si la patiente accepte l'hystérectomie (c'est-à-dire ablation de l'utérus).
- Stades IA et IB1 :
  - Colpo-hystérectomie élargie (ablation de l'utérus, du tiers supérieur du vagin et des paramètres) ;
  - Radiochirurgie qui consiste en une curiethérapie et une colpo-hystérectomie élargie ;
  - Radiothérapie qui associe une radiothérapie externe et une curiethérapie. En cas d'extension aux ganglions, une chimiothérapie (radiochimiothérapie concomitante) est ajoutée.
- A partir du stage IB2 :
  - Radiochimiothérapie concomitante qui associe une radiothérapie externe, une chimiothérapie, suivie d'une curiethérapie ;
  - Une hystérectomie est faite à l'issue de ce traitement, si besoin.

La radiothérapie externe et la curiethérapie sont présentées dans les sections 1.3.1 et 1.3.2, respectivement.

La délivrance du traitement par radiochimiothérapie et curiethérapie doit se faire en moins de 8 semaines au total. En effet, il a été prouvé qu'un traitement court conduit à un meilleur contrôle de la tumeur et peut améliorer le taux de survie des patientes [19,20]. La première partie du traitement par radiochimiothérapie a pour but de réduire la taille de la tumeur initiale. La deuxième partie du traitement par curiethérapie va permettre de traiter la tumeur résiduelle. La combinaison de ces deux traitements est souvent proposée car elle a montré une augmentation de 21% du taux de survie à 5 ans des patientes atteintes d'un cancer de stade IIIB [21]. De plus, l'efficacité de la curiethérapie dépend beaucoup de celle de la radiothérapie, une tumeur résiduelle trop importante à l'instant de la curiethérapie pouvant conduire à un sous-dosage de celle-ci [22]. Le taux de survie à 5 ans après une récurrence de ce type de cancer est inférieure à 5% [23].

1.3.1 RADIOTHERAPIE EXTERNE

1.3.1.1 Principe du traitement

La radiothérapie externe (*External Beam Radiation Therapy,* EBRT) représente la première partie du traitement de référence des cancers du col utérin localement avancés, en parallèle avec la chimiothérapie. Ce traitement est délivré à la patiente par un accélérateur linéaire de particules (*LINear ACcelerator*, LINAC) (*cf.* Figure 1-5). Ce LINAC va permettre de délivrer des faisceaux ionisants ciblés vers la tumeur. Les particules chargées peuvent être des photons de haute énergie (*Megavolt*, MV) ou des électrons (*Mega electronvolt*, MeV). Cette irradiation va détruire l'ADN des cellules pour bloquer leur multiplication de manière à provoquer leur apoptose. Pour traiter la tumeur, les faisceaux sont délivrés depuis l'extérieur du corps de la patiente en traversant les tissus sains. C'est la convergence de ces faisceaux qui va permettre de délivrer la dose nécessaire au volume cible. Cette dose s'exprime en Gray (Gy) et représente l'énergie délivrée dans une masse (1J/Kg). Pour protéger les organes sains aux alentours de la tumeur, le traitement est fractionné, c'est-à-dire délivré en plusieurs séances, appelées « fractions de traitement ». Pour le traitement des cancers du col utérin, la patiente est généralement traitée 5 jours par semaine pendant 5 semaines. La vitesse de réparation des cellules saines étant plus élevée que pour les cellules cancéreuses, ce fractionnement permet de laisser du temps aux cellules saines de se régénérer. Tout au long du traitement, une diminution de la quantité de cellules cancéreuses par rapport aux cellules saines doit être observée, correspondant à la fonte tumorale.

Un traitement par radiothérapie externe repose sur deux étapes principales : la planification et la délivrance du traitement.

Figure 1-5 : Accélérateur linéaire (*VersaHD*, *Elekta*, Stockholm, Suède)

1.3.1.2 Planification du traitement

La première étape de la radiothérapie est la planification du traitement. Cette planification est réalisée grâce à une image TDM représentant l'anatomie de la patiente. Cette étape de planification se divise en deux parties : la délinéation des organes et l'optimisation dosimétrique.

1.3.1.2.1 Délinéation des organes

La délinéation de la cible clinique et des organes à risque (*Organs at Risk*, OAR) se fait généralement manuellement sur l'image TDM, coupe par coupe, avec, dans certains cas, des outils d'assistance afin de réduire la charge de travail. Les images IRM, si disponibles, peuvent aider à cette délinéation.

Les volumes de la cible et des OAR pour la radiothérapie externe des cancers du col de l'utérus sont les suivants (*cf.* Figure 1-6) :

- Cible clinique (*Clinical Target Volume*, CTV) :
    - CTV_T (T : *tumor*) : Cible clinique correspondant à la tumeur du col de l'utérus. De par la prolifération microscopique des cellules cancéreuses invisibles à l'imagerie, ce volume comprend systématiquement le col et le corps de l'utérus. Le vagin et les paramètres sont ajoutés à ce volume pour les tumeurs supérieures au stade FIGO II (*cf*. Figure 1-3) ;
    - CTV_N (N : *nodal*) : Cible clinique correspondant à l'extension aux ganglions ;
    - PTV *(Planning Target Volume,* PTV*)* : Volume cible prévisionnel correspondant au CTV (combinant le CTV_N et le CTV_T) dilaté par une marge isotropique ou anisotropique (*cf*. section 1.4.3.1).
- Organes à risque :
    - Vessie : poche urinaire dont la base est située entre l'os du pubis et le col de l'utérus ;
    - Rectum : Volume compris entre l'anus et le premier coude du sigmoïde ;
    - Sigmoïde : Volume en forme de « S », horizontal, compris entre le rectum et la cavité péritonéale ;
    - Cavité péritonéale : Volume englobant les intestins à partir de la fin du sigmoïde ;
    - Moelle spinale : Système nerveux de la zone coccygienne ;
    - Têtes fémorales : Volume osseux au contact du bassin.

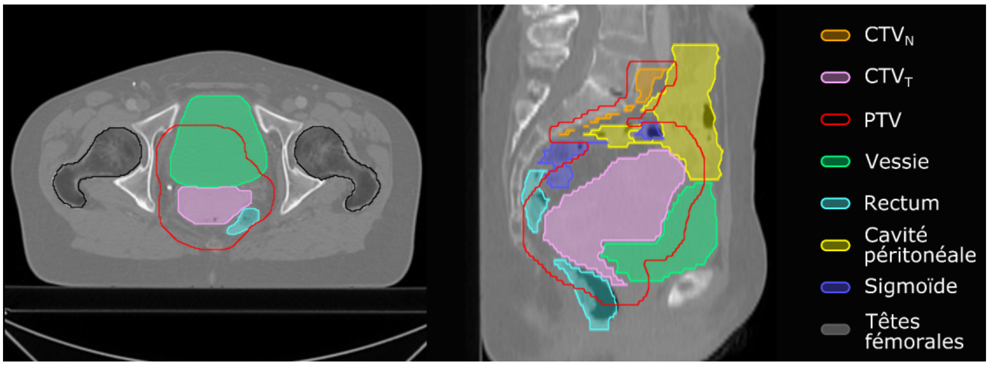

Figure 1-6 : Vue axiale (à gauche) et sagittale (à droite) de la délinéation des volumes cibles et des principaux organes sains pour une TDM de planification de radiothérapie externe

1.3.1.2.2 *Optimisation dosimétrique*

La planification de dose est réalisée, par les physiciens médicaux ou les dosimétristes, suivant l'image TDM et à l'aide des délinéations. La balistique de traitement est optimisée grâce à un système de planification de traitement (*Treatment Planning System*, TPS). L'objectif de cette optimisation est double. Elle doit assurer la délivrance de la dose prescrite par le radiothérapeute dans le PTV, mais doit aussi épargner au maximum les OAR. Une méthode dite de « planification inverse » est couramment utilisée. Elle optimise une fonction de coût correspondant à l'écart entre la dose calculée et les contraintes identifiées par le dosimétriste. L'algorithme ajuste les paramètres correspondant à chaque faisceau (par ex. la position des lames du collimateur, *cf.* Figure 1-8). Pour chaque scénario, la dose reçue par les organes est simulée en fonction des paramètres de la balistique et des densités électroniques des tissus, fournies par l'image TDM.

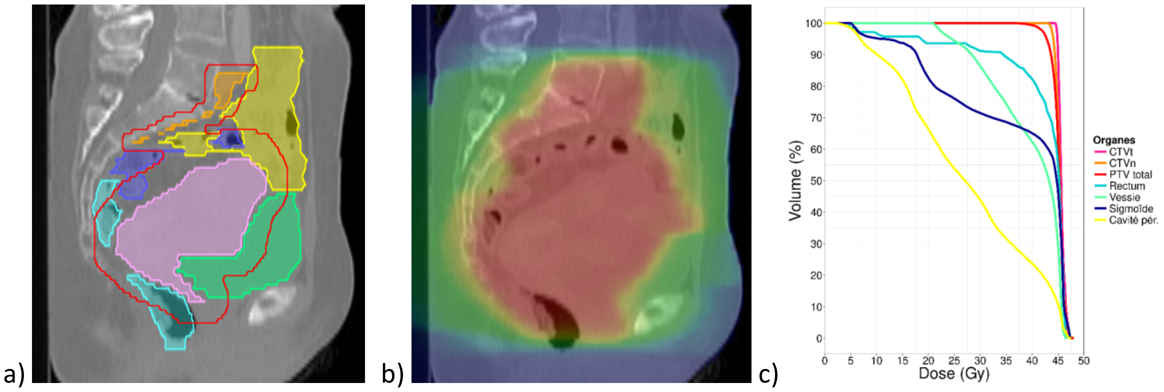

Figure 1-7 : Illustration des Histogrammes Dose-Volume (HDV) (c) de la dose (b) calculée sur la TDM à l'aide des délinéations (a). L'HDV représente le volume de l'organe qui reçoit une dose au moins égale à la dose lue en abscisse.

La prescription de référence en France pour les cancers du col de l'utérus est de 45 Gy, délivrée en 25 factions de 1.8 Gy, à raison de cinq fractions par semaine. En fonction de l'extension ganglionnaire, la dose prescrite est augmentée à 55 Gy (*boost*). Elles sont définies par le *Radiation Therapy Oncology Group* (RTOG 0418) [24].

Les objectifs et contraintes de dose, qui peuvent être en partie visualisés à partir des Histogrammes Dose-Volume (HDV, *cf.* Figure 1-7), sont :

- Cible clinique :
    - Dose totale : 45 Gy au PTV
    - 95% du PTV doit recevoir au moins 95% de la dose prescrite (42.75 Gy)
    - 1.8 cm^3 du PTV peut recevoir au maximum 110% de la dose prescrite (49.5 Gy)
    - Augmentation de dose (*boost*) : 55 Gy au PTV_N (correspondant au CTV_N)
- Organes à risque :
    - Vessie, rectum, sigmoïde :
        - Dose médiane inférieure à 40 Gy
        - Dose maximale dans 2% du volume inférieure à 49 Gy
    - Cavité péritonéale :
        - Dose médiane inférieure à 30 Gy
        - Dose maximale dans 2% du volume inférieure à 49 Gy
        - Volume recevant 15 Gy inférieur à 200 cm^3
        - Volume recevant 35 Gy inférieur à 300 cm^3
    - Têtes fémorales :
        - Dose dans 15% du volume inférieure à 30 Gy

1.3.1.3 Délivrance du traitement

La délivrance du traitement se fait en suivant un schéma fractionné. A chaque séance, la patiente est positionnée, par le manipulateur, à l'aide de tatouages qui permettent de définir un positionnement global sous le LINAC. A partir d'une imagerie 2D (kV ou mV) ou 3D, un repositionnement de la patiente est effectué par déplacement de la table, déterminé suivant l'anatomie osseuse. L'imagerie 3D est communément une imagerie embarquée de type *Cone Beam Computed Tomography* (CTBCT) [25]. Dans certains centres, le repositionnement de la patiente peut être réajusté par l'utilisation de marqueurs anatomiques implantés au niveau des tissus du col de l'utérus (par ex. grain d'or ou marqueurs à base de polymère) [26,27]. Une fois la patiente correctement positionnée sous le LINAC, la balistique planifiée peut être délivrée.

Pour contraindre la forme du faisceau d'irradiation à la forme de la cible clinique, et donc réduire l'impact aux organes sains, les accélérateurs linéaires modernes intègrent un collimateur multi-lames (*cf.* Figure 1-8). La première technologie à utiliser ces collimateurs multi-lames est la Radiothérapie Conformationnelle 3D (RC3D) où chaque faisceau a la même intensité. De nouvelles techniques, comme l'*Intensity Modulated Radiation Therapy* (IMRT) ou la radiothérapie à modulation d'intensité volumétrique par Arc Thérapie (*Volumetric Modulated Arc Therapy,* VMAT) permettent, en jouant sur l'intensité des faisceaux, de suivre des volumes cibles complexes (jusqu'à des formes concaves) et donc de mieux épargner les organes sains. Les moyennes et hautes doses aux OARs sont réduites par l'IMRT par rapport aux techniques conformationnelles [28]. Ces diminutions permettent de réduire le risque de toxicité aux organes sains [29-33], tout en réduisant le temps d'irradiation [34].

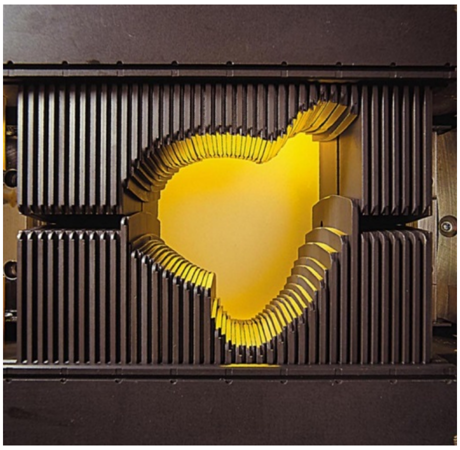

Figure 1-8 : Collimateur multi-lames (*Varian, Palo Alto, California, United States*)

1.3.2 CURIETHERAPIE

1.3.2.1 Principe du traitement

La curiethérapie (*Brachytherapy*, BT) représente la deuxième étape du traitement de référence pour les cancers du col utérin localement avancés. Elle a comme objectif de traiter la tumeur résiduelle après radiothérapie externe. Contrairement à la radiothérapie externe, qui traite le volume cible par un rayonnement externe au corps de la patiente, la curiethérapie est locale. La dose est délivrée par des matériaux radioactifs comme l'iridium ou le césium par contact physique avec la tumeur résiduelle. Cette tumeur résiduelle est évaluée par une IRM afin de guider la procédure de curiethérapie. La curiethérapie est recommandée à partir des tumeurs IB2.

Afin de délivrer la dose prescrite, plusieurs étapes sont nécessaires, qui peuvent varier suivant les matériels utilisés et les centres cliniques. Dans un premier temps, le type d'applicateur est choisi par le médecin en fonction de l'anatomie de la patiente. Pour les applicateurs qui combinent un tandem et un anneau/ovoïdes (*cf*. Figure 1-9), un moule vaginal personnalisé est fabriqué. Celui-ci va permettre d'immobiliser l'applicateur de sources radioactives, on parle alors de curiethérapie endocavitaire. Les sources radioactives sont envoyées par un « projecteur de sources » au travers de fins cathéters. Ces cathéters sont placés précisément au contact de ou dans la tumeur afin de délivrer la dose prescrite. Dans le cas d'une prolifération aux paramètres, des cathéters supplémentaires permettent d'atteindre cette zone, on parle alors de curiethérapie interstitielle. La mise en place de l'applicateur est faite par un geste chirurgical sous anesthésie générale. Après cette mise en place, une image est de nouveau acquise (TDM ou IRM) afin d'observer la position de l'applicateur et la non perforation de l'utérus par celui-ci. Cette image permet aussi de calculer la dose de planification, qui est à la fois spatiale et temporelle. En effet, pendant les séances de curiethérapie, les sources radioactives sont projetées au travers des cathéters pendant des durées définies par la planification de dose. Du fait de cette délivrance locale, la curiethérapie permet de délivrer une dose élevée dans la tumeur tout en limitant l'irradiation des OAR.

Plusieurs types de curiethérapie existent :

- Curiethérapie à bas débit de dose (*Low Dose Rate*, LDR) : diffusion de sources radioactives de césium en continu. La patiente est hospitalisée, allongée, pendant une durée de 2 à 6 jours. Ce type de traitement n'est plus délivré en France ;
- Curiethérapie à débit de dose pulsé (*Pulsed Dose Rate*, PDR) : diffusion de sources radioactives d'iridium sur un intervalle de 15 à 30 min par heure, pendant plusieurs heures. La forme de la dose est ajustée à la tumeur par le temps de présence et la position de chaque source au sein du cathéter ;
- Curiethérapie à haut débit de dose (*High Dose Rate*, HDR) : diffusion de sources radioactives d'iridium, plus fortes que celles utilisées en PDR, pendant quelques minutes. La délivrance du traitement se fait sur plusieurs séances (2 à 6 séances réparties en une ou plusieurs semaines). Plusieurs IRM peuvent être acquises.

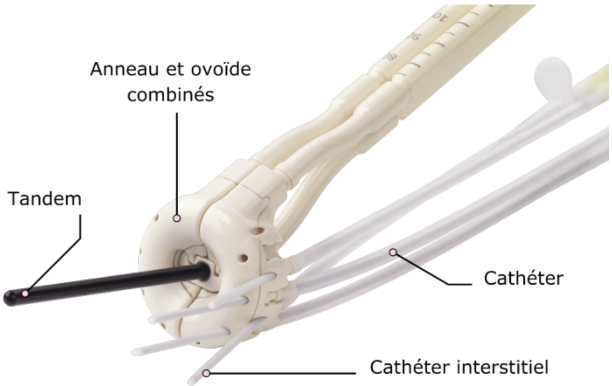

Figure 1-9 : Applicateur hybride (anneau et ovoïde) avec tandem (*Advanced Gynecological Applicator* Venezia™, Elekta, Stockholm, Suède)

1.3.2.2 Planification du traitement

L'arrivée des applicateurs compatibles TDM et IRM pour la curiethérapie endocavitaire a permis d'améliorer la personnalisation du traitement pour les patientes à partir des années 2000. Depuis l'apparition de la planification de dose 3D sur imagerie volumique [35], le Groupe Européen de Curiethérapie (GEC) et la Société Européenne de Radiothérapie et d'Oncologie (*European Society for Radiotherapy and Oncology*, ESTRO), s'efforce, au sein du GEC-ESTRO, de diffuser des recommandations de traitement. Ces recommandations permettent de définir un consensus de délinéation [36] et de dose [37] afin d'avoir une homogénéité des planifications et des traitements entre centres et de permettre leur comparaison.

1.3.2.2.1 Délinéation des organes

La planification de dose se fait sur un TPS dédié qui requiert une délinéation précise des organes et de la cible clinique sur l'IRM acquise entre l'EBRT et la BT (pour la définition de la tumeur résiduelle, qui est le nouveau GTV) et sur l'image acquise après insertion de l'applicateur au bloc opératoire, pour une description anatomique dans les conditions de traitement. De plus, cela permet au TPS de modéliser la position des cathéters pour optimiser la dosimétrie.

Les volumes de la cible et des OAR pour la curiethérapie des cancers du col de l'utérus sont les suivants (*cf.* Figure 1-10) :

- Cible clinique
  - Tumeur macroscopique (GTV) à l'instant de l'IRM de diagnostic, avant la radiothérapie externe : GTV_D ;
  - Volume du GTV après la radiochimiothérapie, juste avant la curiethérapie : GTV_C ;
  - Volume du CTV à haut risque de récidive au moment de la curiethérapie (*High Risk CTV*, HR-CTV). Le HR-CTV comprend le GTV_C, le col de l'utérus et l'extension de la tumeur ;
  - Volume du CTV à risque intermédiaire de récidive au moment de la curiethérapie (*Intermediate Risk* CTV, IR-CTV). Ce volume représente le HR-CTV avec une marge entre 5 et 15 mm en fonction de la taille de la tumeur.
- Organes à risque : Vessie, rectum, sigmoïde, cavité péritonéale.

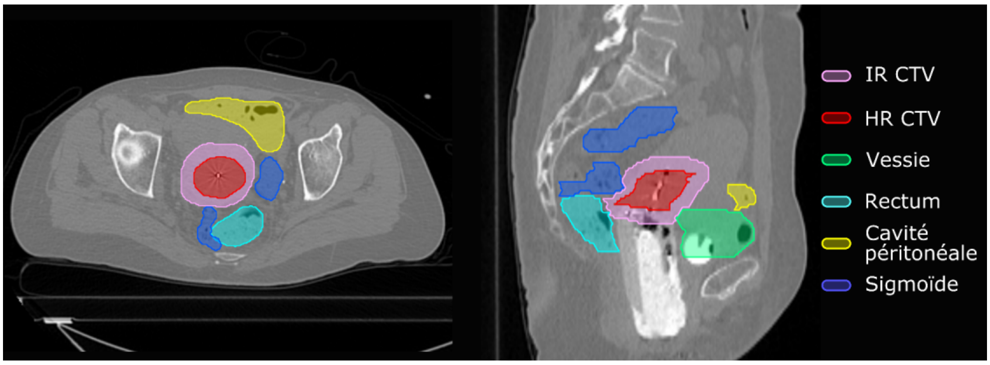

Figure 1-10 : Vue axiale (à gauche) et sagittale (à droite) de la délinéation des volumes cibles et des principaux organes sains pour une TDM de planification de curiethérapie

Pour les traitements par curiethérapie fractionnés (PDR ou HDR), le volume cible peut-être redéfini en cas de fonte tumorale importante ou de déplacement de l'applicateur. Dans ce cas, une replanification est envisagée et requiert un repositionnement de l'applicateur ainsi que l'acquisition d'une nouvelle image de planification (IRM ou TDM).

1.3.2.2.2 Optimisation dosimétrique

La dose de curiethérapie est optimisée sur la TDM ou l'IRM de la patiente avec l'applicateur en place. La dose est optimisée manuellement par l'intermédiaire des outils du TPS et de la reconstruction de l'applicateur [38]. Le physicien médical a la possibilité de « dessiner » l'isodose (non recommandé) ou de définir les temps de pause pour générer une dose qui respecte au mieux les objectifs et contraintes de prescription (recommandé). Afin d'assurer la comparaison des valeurs de doses délivrées entre la radiothérapie externe et la curiethérapie, les doses sont exprimées en dose équivalente à un traitement fractionné de 2 Gy (*Equivalent Dose in 2 Gy Fractions*, EQD2). Un modèle, dit « linéaire quadratique » est utilisé pour calculer l'EQD2. Ses paramètres sont $\alpha/\beta=10$ Gy et $\alpha/\beta=3$ Gy pour la tumeur et les OAR, respectivement [39,40]. Puisque la dose de curiethérapie est localement très élevée, il est important de définir des contraintes strictes. Malgré les avancées technologiques, un point spécifique, noté « A », reste un objectif de prescription de dose, d'après le *Manchester system* [41]. Ce point se situe à 2 cm perpendiculairement aux sources du tandem et de l'anneau de l'applicateur et illustre la propagation du gradient de dose par les sources.

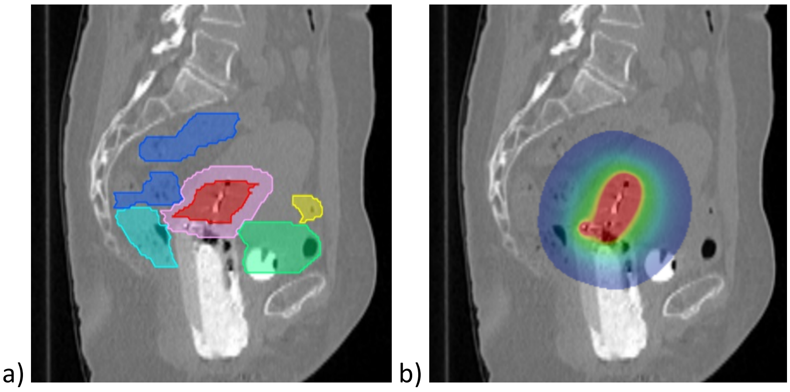

Figure 1-11 : Illustration de la dose de curiethérapie (b), calculée en fonction du dispositif (moule vaginale, applicateur, anneau, tandem et cathéters) et à l'aide des délinéations (a)

D'après le GEC-ESTRO [37], une curiethérapie endocavitaire HDR doit être délivrée à 40 Gy_{EQD2}. Aux Etats Unis, elle est souvent délivrée en 5 séances de 6 Gy [42]. Les objectifs de dose aux OAR prennent en compte le pire scénario possible en supposant que 2 cm^3 des OAR aient reçu le maximum de la dose de radiothérapie externe prescrite (45 Gy).

En prenant en compte le total des deux traitements (EBRT et BT), les contraintes et objectifs de dose de la BT doivent respecter les contraintes suivantes (*cf.* Figure 1-11) :

- Cible clinique (Gy en EQD2 $\alpha/\beta=10$ Gy) :
  - 90% du HR-CTV doit recevoir au moins 84 Gy ;
  - 90% du IR-CTV doit recevoir au moins 60 Gy ;
  - La dose au point A doit être supérieure à 80 Gy.
- Organes à risque (Gy en EQD2 $\alpha/\beta=3$ Gy) :
  - La D_{2cc} de la vessie doit recevoir moins de 90 Gy ;
  - Les D_{2cc} du rectum et du sigmoïde doivent recevoir moins de 70 Gy.

L'analyse des critères suivants est importante pour la comparaison des planifications entre séances, patients et études :

- Cible clinique (GTV_B, HR-CTV et IR-CTV, Gy en EQD2 α/β=10 Gy) :
    - Dose reçue par 100% du volume ;
    - Volume absolu recevant 85 Gy ;
    - Volume absolu recevant 60 Gy ;
    - Volume en pourcentage recevant 100% de la dose de prescription ;
    - Présence ou non de l'applicateur dans ces valeurs.
- Organes à risque (vessie, rectum, sigmoïde et cavité péritonéale, Gy en EQD2 α/β=3 Gy) :
    - Dose reçue par les volumes les plus exposés (D_{2cc}, D_{1cc} et $D_{0.1cc}$).

1.3.2.3 Délivrance du traitement

La délivrance de la curiethérapie est variable en fonction de l'expérience des centres et de la stratégie de traitement utilisée. Pour une curiethérapie LDR, elle se fait en chambre spéciale ou la patiente est consciente mais isolée avec le projecteur de sources contenant le matériau radioactif. Un manipulateur place les cathéters, guidés par l'applicateur déjà mis en place, au contact de la tumeur. A la fin du traitement, le dispositif est retiré. Pour une curiethérapie PDR ou HDR, l'applicateur peut être gardé entre chaque séance. Ce dernier permet de repositionner les cathéters à la séance suivante dans les conditions de la planification et sans anesthésie. Un examen d'imagerie peut être réalisé afin de vérifier que l'applicateur n'a pas bougé. En cas de réinsertion de l'applicateur ou de modification anatomique importante (par ex. fonte tumorale due à la réponse au traitement), une replanification du traitement peut être envisageable. Les avantages de la curiethérapie HDR sont une non-exposition aux sources par le personnel soignant, un traitement plus reproductible et une meilleure optimisation de la dose [43-45].

1.3.3 EFFETS SECONDAIRES DU TRAITEMENT

Ce traitement des cancers du col utérin localement avancés n'est pas sans effet secondaire. En effet, les rayons devant traverser des tissus sains pour atteindre la tumeur, la radiothérapie externe peut provoquer de la toxicité aux organes sains, suite à leur irradiation prolongée. Ces effets secondaires peuvent être directement liés à la localisation de forts gradients de dose ou à une dose moyenne trop élevée dans l'ensemble de l'organe. On peut parler d'effet secondaire immédiat (par ex. fatigue, diarrhées, inflammation des muqueuses, rougeurs, diminution de la pilosité) ou tardif (par ex. incontinence, saignement, sécheresse) quand ils apparaissent plusieurs mois après le traitement. Comparé à la RC3D, l'IMRT permet de réduire le volume intestinal recevant une dose supérieure à 40 Gy (V40 Gy) [46]. Cette réduction a permis de réduire l'incidence des complications intestinales aigües de grade 3 de 26% tout en conservant ou améliorant le contrôle tumoral et le taux de survie global. Par ailleurs, la V40 reçue par la moelle osseuse est prédictive de la toxicité hématologique [47].

De plus, différents outils sont disponibles pour interroger les patientes sur leur ressentis par rapport au traitement. Par exemple, le questionnaire QLQ-C30 permet de quantifier l'état de santé général de la patiente avant, pendant et après le traitement (par ex. fatigue, nausée, insomnie…) [48]. Un questionnaire plus spécifique, le QLQ-CX24, permet de quantifier les effets secondaires pour les patientes traitées pour un cancer du col de l'utérus (fonctions sexuelles…) [49]. A partir de ces questionnaires, une étude de 742 patientes a montré l'évolution de la qualité de vie avant et après traitement [50]. Dans cette étude, la qualité de vie, dégradée avant traitement, est améliorée à partir de 6 mois jusqu'à être similaire à celle d'une cohorte de femmes sans cancer. Cette qualité de vie semble évoluer rapidement au cours du traitement. Le remplissage des questionnaires chaque semaine permet de mieux suivre l'apparition et l'évolution des effets secondaires et pourrait permettre de mieux comprendre leur cause [51].

1.4 PROBLÉMATIQUE DE LA VARIABILITÉ ANATOMIQUE

Le traitement par radiothérapie externe est optimisé suivant une anatomie fixe mais délivré en une série de fractions. Cependant les organes cibles et les OAR subissent des déplacements et déformations au cours du temps, et donc au cours du traitement. Cette variabilité anatomique constitue une difficulté majeure pour la délivrance d'une dose élevée dans une cible précise. Cette problématique est d'autant plus importante que les techniques modernes de traitement permettent de mieux cibler des formes complexes grâce à des distributions de dose avec de forts gradients. Ces techniques sont donc très sensibles aux variations anatomiques puisqu'un faible déplacement peut se traduire par une variation de dose élevée.

Cette section présente cette problématique de la variabilité anatomique et son impact sur les traitements par radiothérapie externe des cancers du col de l'utérus. Cette section présente ensuite les différentes stratégies proposées afin de prendre en compte cette variabilité anatomique.

1.4.1 QUANTIFICATION DES INCERTITUDES ANATOMIQUES

La région pelvienne est, par nature, sujette à de fortes variations anatomiques. La position du CTV (col et corps de l'utérus) peut notamment être modifiée suivant le remplissage du rectum et de la vessie (*cf*. Figure 1-12). Cette variation anatomique peut survenir entre les fractions de traitement (inter-fractions) ou pendant une fraction de traitement (intra-fraction). La dose délivrée risque alors de différer de la dose planifiée, avec des conséquences sur le résultat du traitement (diminution du contrôle de la tumeur, augmentation des effets secondaires).

Une revue de la littérature par Jadon *et al* en 2014 [52] résume les études qui ont observé le déplacement du CTV (39 études dont 12 conférences). Les mouvements inter-fractions moyens du col de l'utérus ont été rapportés entre 2.3 et 16 mm dans la direction Antéro-Postérieure (AP), 2.7 et 8 mm dans la direction Supéro-Inférieure (SI) et 0.3 et 10 mm dans la direction latérale (*Left-Right*, LR). Certaines études ont rapporté des valeurs extrêmes, jusqu'à 25 mm en AP, 36 mm en SI et 23 mm en LR [53,54]. De plus, il a été rapporté que le mouvement de l'utérus était plus important que celui du col de l'utérus. Des déplacements du fond utérin jusqu'à 48 mm en AP, 36 mm en SI et 28 mm en LR ont été rapportés [55,56]. Des déplacements du centroïde du CTV ont été rapportés jusqu'à 18.9 mm et 15.3 mm dans les directions AP et SI, respectivement [57]. Les mouvements du CTV en intra-fraction sont largement inférieurs. Ils ont été rapportés entre 0.1 et 3 mm, avec une incidence d'un déplacement supérieur à 5 mm dans seulement 3% des cas [58]. Ces résultats ont été confirmés dans une étude récente sur 16 patientes avec CBCT quotidiens acquis en début et fin de fractions [59].

Ces déplacements du col de l’utérus et de l’utérus sont principalement liés aux déformations des organes voisins [60]. Il a été montré que le déplacement du col de l’utérus dans la direction AP est corrélé au volume et au diamètre du rectum [61]. Le déplacement de l’utérus dans la direction SI a quant à lui été corrélé au volume de la vessie, à la fois à partir d’observations inter-fractions [61-63] et intra-fraction [59].

La réponse à la radiochimiothérapie fait partie des déformations importantes que peut subir le GTV, notamment pendant les premières semaines du traitement. Une diminution moyenne du GTV a été mesurée à 46% (jusqu’à 100%) à 30 Gy. En considérant l’ensemble du volume du col de l’utérus (comprenant le GTV), la diminution moyenne a été évaluée à 63% (jusqu’à 87%) à la fin du traitement par radiothérapie externe [54,64,65].

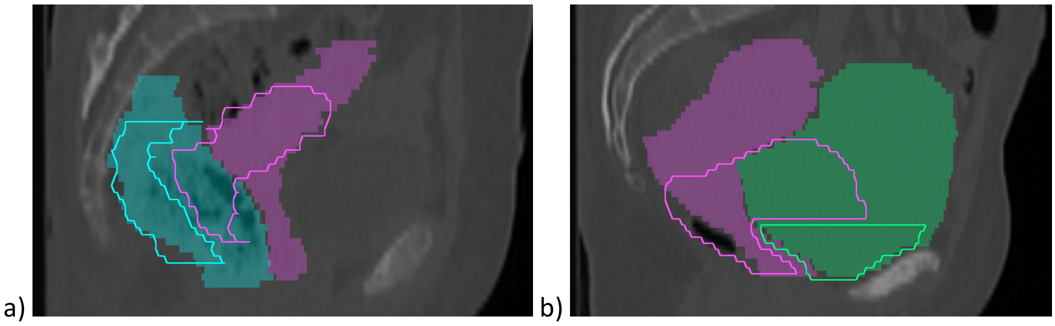

Figure 1-12 : Illustration des déformations du CTV (rose) par rapport (a) au rectum (bleu) et (b) à la vessie (vert) pour deux patientes. Chaque image représente la TDM de planification avec les contours de planification (plein) et les contours d’une séance de EBRT (ligne).

1.4.2 IMPACT SUR LA DOSE DELIVREE

Ces incertitudes géométriques peuvent avoir un impact dosimétrique, et notamment résulter en une diminution de la dose reçue par la cible et une augmentation de celle reçue par les OAR. Cette impact dosimétrique peut être quantifié : (i) soit à la séance, en évaluant, pour des fractions données, la couverture dosimétrique des structures d'intérêt ; (ii) soit sur l'ensemble du traitement, ce qui nécessite une quantification des déformations anatomiques pour pouvoir propager les doses vers une anatomie de référence. Afin d'effectuer cette quantification des déformations anatomiques, des méthodes de recalage déformable (*Deformable Image Registration*, DIR) ont été développées et exploitées durant les dernières années [66]. Ces méthodes permettent de calculer une transformation non-linéaire, représentée par un champ de vecteurs de déformation (*Deformation Vector Field,* DVF), mettant en correspondance une image à déformer avec une image de référence. Il est alors possible de mettre en correspondance les différentes images issues du traitement avec l'image de planification et de déformer la dose de chaque séance vers l'anatomie de référence. Ces doses déformées peuvent être comparées, point à point, ou sommées afin d'avoir une estimation de la dose totale délivrée pendant le traitement. Cette dose délivrée estimée peut enfin être comparée à la dose de planification pour évaluer l'impact dosimétrique des modifications anatomiques.

Grâce à ce type d'approches, quelques études se sont donc penchées sur la quantification de l'impact dosimétrique de la variabilité anatomique pendant l'EBRT. Elles sont présentées par le Tableau 1-2.

Tableau 1-2 : Etudes évaluant l'impact dosimétrique de la variabilité anatomique

Etude	Nb ptts	Dose	Marge (mm)	Images	Objectif	Résultats
Buchali [63] Rad Onc, 1999	29	RC3D (50 Gy)	10	2 TDM de planification	Variation de dose aux OAR en fonction de leur volume (rectum et vessie vides/pleins).	- Diminution de la dose planifiée pour un volume de vessie vide ; - Pas de variation de dose au rectum.
Han [67] IJROBP, 2006	10	IMRT (50 Gy)	15	- 1 TDM de planification - 3 TDM /semaine	- Observation des indices des DVH pendant le traitement ; - Comparaison avec la planification.	- Sous-dosage de 3% entre la V40% et V97% du PTV ; - Variation de la V40%, V60% et V80% du petit intestin à la 3-4ème semaine (+20-30 cc).
Lim [68] IJROBP, 2009	20	1 RC3D et 2 IMRT (50 Gy)	20 ou 5	- 1 TDM/IRM de planification - 1 IRM /semaine	- Estimation de la dose cumulée par recalage déformable biomécanique ; - Comparaison avec la planification ; - Différentes marges et techniques (PTV 20 et 5 mm)	- Faible variation de la dose au GTV et CTV suivant les marges ; - Risque de sous-dosage du CTV pour une marge de 5 mm (-3.5 Gy pour une patiente) ; - Forte variation de la dose au OAR à l'échelle de l'individu (max 5% pour le rectum/vessie; max 20% pour sigmoïde).
Gobeli [69] Can Rad, 2015	10	IMRT (45 Gy)	10	- 3 TDM de planification - 2 CBCT /semaine	- Estimation de la dose cumulée par recalage déformable ; - Comparaison avec la planification.	- Sous-dosage moyen du CTV de 3.4 Gy pour la D98 ; - Surdosage de 2% pour la V40Gy du rectum ; - Surdosage de 6% pour la V35Gy de la cavité péritonéale.

Les différentes études de la littérature, comparant la dose délivrée aux organes avec la dose de planification, montrent une baisse de la dose au CTV. Cette variation augmente avec la réduction de la marge et peut être mesurée jusqu'à 3.4 Gy en moyenne pour la D98 [69]. A l'échelle de l'individu, une marge de PTV réduite (5 mm) augmente le risque de sous-dosage du CTV avec des valeurs rapportées jusqu'à -3.5 Gy par rapport à une dose de prescription de 50 Gy [68]. Les auteurs stipulent que ces sous-dosages étaient observés dans le cas de déplacements importants de l'utérus. Cet impact dosimétrique est observé pour les OAR avec notamment des variations de la V40Gy pour le rectum et la vessie et de la V35 pour la cavité péritonéale.

1.4.3 PRISE EN COMPTE DES INCERTITUDES GEOMETRIQUES

Ces variations dosimétriques peuvent avoir des conséquences sur l'issue du traitement, en termes de contrôle de la tumeur ou d'événements de toxicité. Si la radiothérapie guidée par l'image (*Image-Guided Radiotherapy*, IGRT) permet, par le repositionnement de la patiente, de compenser des déplacements globaux de la cible, elle ne permet pas de compenser les déformations [70,71]. Les principales techniques mises en œuvre pour tenter de limiter l'impact des variations anatomiques sont présentées dans cette section.

1.4.3.1 Adaptation des marges

Afin d'assurer la couverture de la tumeur au cours du traitement, la première stratégie repose sur une modification des marges du PTV. Ces marges sont utilisées pour augmenter la taille de la cible traitée et ainsi compenser différentes incertitudes sur la position et la forme de cette dernière (erreur de délinéation, de positionnement de la patiente, déformations…). Par une dilatation isotropique ou anisotropique du CTV, elles permettent de générer le PTV, volume cible qui sera effectivement utilisé pour la planification. L'objectif est donc de définir des marges pour prendre en compte les déformations du CTV. Il n'y a cependant pas de consensus sur le choix de la marge du PTV dans la littérature. Des marges isotropiques ont été rapportées, entre 3 et 15 mm [28,55,63,67,68,72-82]. La marge isotropique revenant le plus souvent dans la littérature est de 10 mm. Des marges anisotropiques ont aussi été utilisées, entre 15 et 24 mm dans la direction AP, 8 et 15 mm en SI, et entre 10 et 20 mm en LR [53,61,68,83-85]. Une étude disposant d'une cohorte de 50 patientes avec CBCT quotidiens a estimé une marge optimale, dite « populationnelle », pour assurer une probabilité de couverture du CTV supérieure à 95% [86]. Le PTV optimisé nécessitait une dilatation isotropique de 4.3 et 11.2 mm pour assurer 95% et 100% de couverture pendant le traitement, respectivement. Les mouvements inter-fractions du CTV étant de fortes amplitudes, l'utilisation de marges importantes est souvent conseillée afin d'assurer la couverture de la cible pour l'ensemble des patientes. De telles marges augmentent l'irradiation des OAR et limitent les bénéfices d'une distribution de dose précise permise par l'IMRT.

1.4.3.2 Définition d'un volume cible interne (ITV)

Dans le cas de cibles tumorales avec de fortes variations anatomiques, une stratégie repose sur la définition de volumes cibles englobant les positions potentielles de la cible à la planification. Ce volume cible est alors appelé « volume cible interne » (*Internal Target Volume*, ITV). Dans le cadre de l'utérus, de par la corrélation entre le volume de la vessie et la position de l'utérus, une stratégie repose sur l'acquisition de plusieurs images TDM suivant différents niveaux de remplissage de la vessie. Une fois les CTV délinéés sur chaque image, l'ITV est défini par l'union des différents CTV (*cf*. Figure 1-13). Si la couverture de la cible est grandement améliorée par cette approche, le volume traité augmente considérablement, se traduisant potentiellement par un surdosage important des OAR [76,81,87].

1.4.3.3 Librairie de plans de traitement

Les stratégies reposant sur l'augmentation des marges du PTV et sur l'utilisation d'un ITV montrent leurs limites pour assurer un compromis entre le contrôle de la tumeur et l'épargne des OAR. De ce fait, les approches de radiothérapie adaptatives ont été proposées, reposant sur la planification non plus d'un unique plan de traitement mais de plusieurs. Ainsi, de nombreuses études ont exploité la relation entre le volume vésical et la position de l'utérus [62] pour définir une stratégie dite de « librairie de plans de traitement ». Cette stratégie consiste en la définition d'une librairie de plans de traitement construite à partir de plusieurs TDM acquises, à la planification, suivant différents niveaux de remplissage de la vessie (*cf*. Figure 1-13).

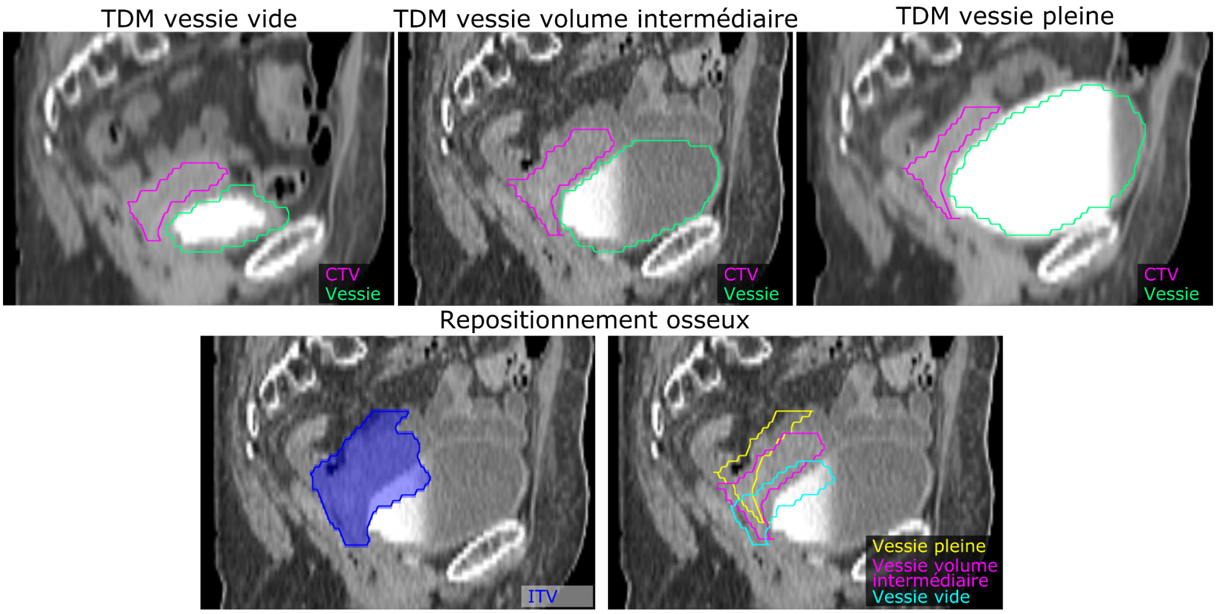

Figure 1-13 : Exemple de la stratégie ITV et de la librairie de plans de traitement générés à partir des 3 TDM avec volume de vessie vide, intermédiaire et plein

A partir de ces TDM, différents plans de traitement sont optimisés. Les CTV considérés sont soit directement ceux représentés dans les TDM, soit correspondent à des « sous-ITV » représentant une plage de déformation de la cible (par exemple deux sous-ITV pour couvrir les différentes positions potentielles entre vessie vide et pleine) [75]. Après définition de ces CTV, les dosimétries sont optimisées à partir des PTV correspondant, communément obtenus avec une marge 10 mm. Pendant le traitement, à chaque fraction, le CBCT permet au radiothérapeute de choisir le plan de la librairie qui offre la meilleure couverture du CTV de la fraction. La sélection du choix du plan de traitement est souvent faite visuellement, mais peut être envisagée à partir d'une mesure du volume vésical, par exemple par échographie [84].

Plusieurs études ont simulé et implémenté en clinique ce type de stratégie, avec différents choix quant au nombre d'images considérées, au mode de génération des PTV, aux valeurs de marges et aux approches d'évaluation. Elles sont synthétisées par le Tableau 1-3.

Parmi les études évaluant les performances d'une librairie de plans de traitement, le critère de comparaison était géométrique pour deux études [75,88] et dosimétrique pour quatre études [69,81,87,90]. La littérature montre qu'une implémentation de cette stratégie en routine clinique est possible. Cette stratégie a montré de bons résultats de couverture du CTV avec une marge de PTV de 10 mm. Par rapport à une stratégie standard, une épargne du rectum et de la cavité péritonéale est systématiquement observée. Dans certains cas, une augmentation de la couverture de la vessie peut être rapportée [90]. Pour l'implémentation clinique, Heijkoop *et al* [76] propose d'ajouter à la librairie de plans de traitement une planification RC3D calculée à partir de l'ITV de planification (généré à partir des 2 TDM) pour assurer la couverture du CTV lorsque des déformations trop importantes sont observées ou lorsque le CBCT du jour est inexploitable. Ce plan de secours risque cependant d'entraîner une dégradation de l'épargne des OAR. Des difficultés dans la sélection du plan de traitement peuvent en effet émerger dû à la qualité variable de l'imagerie embarquée CBCT. Buschmaan *et al* [87] ont montré une variation dans le choix du plan de traitement pour 14% des fractions d'une cohorte de 16 patientes. Cette variabilité a été observée pour des CBCT fortement bruités ou lorsque les plans de traitement se ressemblaient [91]. Un mois plus tard, avec l'expérience des utilisateurs, cette inconsistance était réduite à 7% des fractions sur la même cohorte. Ces stratégies complexes nécessitent donc une formation des équipes cliniques pour assurer une bonne implémentation.

Tableau 1-3 : Etudes evaluant les performances de la librairie de plans de traitement

Etude	Nb ptts	Imagerie	Méthode	Résultats
Bondar [88] Rad Onc, 2011	13	- 5 TDM de planification - 5 TDM à 40 Gy - Volume vessie variable	Définition d'un modèle de prédiction entre le volume de vessie et la position de l'utérus.	Erreur de prédiction du modèle inférieure à une marge de PTV à 10 mm.
Bondar [75] IJROBP, 2012	13	- 5 TDM de planification - 5 TDM à 40 Gy - Volume vessie variable	- Validation du modèle de [88] pour générer des sous-ITV et définir une librairie de plans de traitement ; - Comparaison aux stratégies de PTV populationnel.	Librairie de 2 sous-ITV permet de réduire la taille du PTV, d'assurer la couverture du CTV et de réduire la couverture des OAR (marge de 7 mm).
Heijkoop [76] IJROBP, 2014	64	- 2 TDM de planification (vessie vide et pleine) - CBCT quotidiens	- Validation clinique ; - Deux phases : Phase 1 : IMRT avec ITV et plan de secours RC3D (24 patientes) ; Phase 2 : librairie de plans de traitement (2 sous-ITV) et plan de secours (11 patients) ; - Pas d'évaluation dosimétrique.	- Implémentation clinique possible ; - Définition de deux groupes en fonction de la mobilité de l'utérus à la planification (seuil 2.5 cm) ;
Gobeli [69] Can Rad, 2014	10	- 3 TDM de planification (vessie vide, volume intermédiaire, pleine) - CBCT bihebdomadaires	- Simulation stratégie standard et librairie de plans de traitement ; - Comparaison planification et dose délivrée ; - Recalage déformable.	La librairie de plans de traitement permet : - Réduction des marges du PTV à 10 mm ; - Augmentation de la D98 du CTV ; - Epargne rectum et cavité péritonéale.
Seppenwoolde [81] Rad Onc, 2016	10	- 2 TDM de planification (vessie vide et pleine) - 3-5 CBCT/semaine	Comparaison de 3 stratégies : - Standard (2 marges de PTV) ; - ITV large ; - Librairie de plans de traitement issue de [76].	La librairie de plans de traitement améliore la couverture du CTV et l'épargne des OAR.
O'Reilly [89] Physica Med, 2016	10	- 1 TDM de planification - TDM quotidiens	- Librairie de plans de traitement basée sur un unique CTV mais différentes marges (5, 7, 10, 15, 20 et 25 mm) ; - Définition d'une librairie *online* (choix du plan à la séance) et *offline* (PTV 15 mm puis dégressif si besoin) ; - Evaluation par la sommation des doses équivalentes uniformes.	La librairie de PTV *offline* permet d'assurer une couverture du CTV satisfaisante par rapport à une stratégie standard (PTV 15 mm)
van de Schoot [90] Acta Onco, 2017	13	- 2 TDM de planification (vessie vide et pleine) - pré fraction CT hebdomadaire - post fraction CBCT quotidiens	Comparaison stratégie standard et librairie de plans de traitement (3 sous-ITV).	La librairie de plans de traitement améliore la couverture du CTV et l'épargne du rectum et cavité ; Surdosage de la vessie observée.
Buschmaan [87] ZMP, 2017	16	- 2 TDM de planification (vessie vide et pleine) - 1 IRM de planification (vessie variable) - CBCT quotidiens	- Comparaison stratégies ITV et librairie de plans de traitement ; - Evaluation sur indices des DVH.	Léger sous-dosage du CTV pour la librairie de plans de traitement (par rapport ITV) et épargne modeste des OAR.
Nováková [82] Rad Onc, 2017	14	- 2 TDM de planification (vessie vide et pleine) - CBCT quotidiens	Evaluation de la taille de la librairie de plans de traitement en fonction du mouvement de l'utérus.	Trois sous-ITV pour les patientes avec une mobilité supérieure à 3 mm à la planification.

1.4.3.4 Replanification en cours de traitement

L'équipe du *Princess Margaret Cancer Centre* (Toronto, Canada) a évalué le bénéfice de replanifications au cours du traitement, soit réalisées systématiquement [73], soit déclenchées suivant un critère visuel ou dosimétrique [72,74]. Par rapport à la stratégie standard, une stratégie de replanification hebdomadaire a permis l'augmentation de 73% à 100% du nombre de patientes avec une D98 supérieure à 95% de la dose prescrite pour le GTV et le CTV, avec une marge de PTV de 3 mm [74]. Cette stratégie nécessite cependant une replanification de la dose sur l'anatomie du jour, ce qui n'est pas actuellement envisageable en routine clinique. Sur la même cohorte, une stratégie reposant sur un repositionnement par rapport au CTV tumoral combiné à une replanification à mi-traitement permettait d'obtenir des résultats de couverture similaires avec une charge de travail réduite [74]. Afin de prendre en compte l'aspect aléatoire des déformations du CTV, une stratégie reposant sur une surveillance de la dose délivrée au GTV et au CTV, par recalage déformable biomécanique, a été proposée [72]. Une replanification était déclenchée si la D98 de la dose délivrée était inférieure à 98% et 95% de la dose prescrite au GTV et CTV, respectivement, toujours avec une marge de 3 mm. Plus de 50% des patientes a nécessité le déclenchement d'au moins une replanification.

Pour les stratégies reposant sur une ou plusieurs replanifications en cours de traitement, de faibles gains aux OAR ont été observés à l'échelle de la population. Cependant, de fortes variations ont été observées pour certaines patientes. Par rapport à une stratégie standard, seule la stratégie avec replanification à mi-traitement a permis une épargne significative des OAR.

1.5 OBJECTIFS DE LA THÈSE

Un des principaux enjeux de la radiothérapie, qui est le traitement de référence des cancers du col de l'utérus localement avancés, est la prise en compte de la variabilité anatomique rencontrée en cours de traitement. Il en résulte un risque de sous-dosage important de la cible clinique. Pour y répondre, différentes approches ont été proposées, avec notamment l'augmentation des marges, la génération d'un volume cible englobant différentes configurations anatomiques (ITV) ou l'utilisation de stratégies adaptatives, comme des replanifications en cours de traitement ou des librairies de plans de traitement. Cependant, les modalités de leur implémentation clinique, et de leur éventuelle combinaison, restent à préciser. Concernant la stratégie prometteuse des librairies de plans, le nombre de plans de traitement, les valeurs de marge, les critères de sélection des plans et la gestion des anatomies non-représentées dans la librairie restent notamment des questions ouvertes. L'évaluation de ces différentes approches sur une même cohorte doit aussi être menée, permettant d'évaluer l'apport potentiel de nouvelles stratégies. Enfin, leur combinaison avec la curiethérapie doit aussi être investiguée, ce qui passe tout d'abord par la possibilité d'évaluer précisément la dose reçue par les tissus lors de l'ensemble du traitement.

Les objectifs de cette thèse sont donc de proposer et d'évaluer des stratégies de radiothérapie adaptative améliorant la prise en compte des variations anatomiques au cours du traitement des cancers du col de l'utérus localement avancés. Les images acquises à la planification et lors du traitement doivent donc être exploitées de façon à améliorer la personnalisation du traitement, notamment grâce au développement de méthodes de recalage déformable permettant d'estimer les déformations des organes.

1.6 RÉFÉRENCES

1. Duport N. Données épidémiologiques sur le cancer du col de l'utérus. *Etats des connaissances-Actualisation* 2008.
2. ALIAM, Les cancers en afrique francophone, 2017.
3. Sankaranarayanan R, Ferlay J. Worldwide burden of gynaecological cancer: The size of the problem. *Best practice & research Clinical obstetrics & gynaecology* 2006;20:207-225.
4. Sancho-Garnier H. Epidémiologie des cancers gynécologiques: Utérus, ovaire, vulve, vagin. *Cancers gynécologiques pelviens Elsevier Masson, Paris* 2013:85-99.
5. Walboomers JM, Jacobs MV, Manos MM, Bosch FX, Kummer JA, Shah KV, Snijders PJ, Peto J, Meijer CJ, Munoz N. Human papillomavirus is a necessary cause of invasive cervical cancer worldwide. *The Journal of pathology* 1999;189:12-19.
6. Lacey JV, Frisch M, Brinton LA, Abbas FM, Barnes WA, Gravitt PE, Greenberg MD, Greene SM, Hadjimichael OC, McGowan L. Associations between smoking and adenocarcinomas and squamous cell carcinomas of the uterine cervix (united states). *Cancer Causes & Control* 2001;12:153-161.
7. Appleby P, Beral V, Berrington de González A, Colin D, Franceschi S, Goodhill A, Green J, Peto J, Plummer M, Sweetland S. International collaboration of epidemiological studies of cervical, cancer. Cervical cancer and hormonal contraceptives: Collaborative reanalysis of individual data for 16,573 women with cervical cancer and 35,509 women without cervical cancer from 24 epidemiological studies. *Lancet* 2007;370:1609-1621.
8. Heyman J. Atlas. *Illustrating the division of cancer of the uterine cervix into four stages according to the anatomoclinical extent of the growth(With illustrations by M Strandqvist) League of Nations Health Organization Soner, Stockholm* 1932:0.
9. Pecorelli S, Zigliani L, Odicino F. Revised figo staging for carcinoma of the cervix. *International Journal of Gynecology & Obstetrics* 2009;105:107-108.
10. Micheau A. Radiological classifications commonly used in medical imaging. In: Editor, editor^editors. Book Radiological classifications commonly used in medical imaging; 2009.
11. HCSP. Vaccination contre les infections à papillomavirus humains 2014.
12. HAS. Prévention du cancer du col de l'utérus actualisation du référentiel de pratiques de l'examen périodique de santé (eps)[internet]. *Haute Autorité de Santé* 2013:55.
13. HAS. Tumeur maligne, affection maligne du tissu lymphatique ou hématopoïétique, cancer invasif du col utérin [internet]. *Haute Autorité de Santé* 2010.
14. Balleyguier C, Sala E, Da Cunha T, Bergman A, Brkljacic B, Danza F, Forstner R, Hamm B, Kubik-Huch R, Lopez C. Staging of uterine cervical cancer with mri: Guidelines of the european society of urogenital radiology. *European radiology* 2011;21:1102-1110.
15. Bipat S, Glas AS, van der Velden J, Zwinderman AH, Bossuyt PM, Stoker J. Computed tomography and magnetic resonance imaging in staging of uterine cervical carcinoma: A systematic review. *Gynecologic oncology* 2003;91:59-66.
16. Selman TJ, Mann C, Zamora J, Appleyard T-L, Khan K. Diagnostic accuracy of tests for lymph node status in primary cervical cancer: A systematic review and meta-analysis. *Canadian Medical Association Journal* 2008;178:855-862.
17. Lai C-H, Huang K-G, Hong J-H, Lee C-L, Chou H-H, Chang T-C, Hsueh S, Huang H-J, Ng K-K, Tsai C-S. Randomized trial of surgical staging (extraperitoneal or laparoscopic) versus clinical staging in locally advanced cervical cancer☆*Gynecologic oncology* 2003;89:160-167.
18. Rose PG, Bundy BN, Watkins EB, Thigpen JT, Deppe G, Maiman MA, Clarke-Pearson DL, Insalaco S. Concurrent cisplatin-based radiotherapy and chemotherapy for locally advanced cervical cancer. *New England Journal of Medicine* 1999;340:1144-1153.
19. Petereit DG, Sarkaria JN, Chappell R, Fowler JF, Hartmann TJ, Kinsella TJ, Stitt JA, Thomadsen BR, Buchler DA. The adverse effect of treatment prolongation in cervical carcinoma. *International Journal of Radiation Oncology• Biology• Physics* 1995;32:1301-1307.

20. Lanciano RM, Pajak TF, Martz K, Hanks GE. The influence of treatment time on outcome for squamous cell cancer of the uterine cervix treated with radiation: A patterns-of-care study. *International Journal of Radiation Oncology• Biology• Physics* 1993;25:391-397.
21. Logsdon MD, Eifel PJ. Figo iiib squamous cell carcinoma of the cervix: An analysis of prognostic factors emphasizing the balance between external beam and intracavitary radiation therapy. *International Journal of Radiation Oncology• Biology• Physics* 1999;43:763-775.
22. Petereit DG, Sarkaria JN, Potter DM, Schink JC. High-dose-rate versus low-dose-rate brachytherapy in the treatment of cervical cancer: Analysis of tumor recurrence—the university of wisconsin experience. *International Journal of Radiation Oncology• Biology• Physics* 1999;45:1267-1274.
23. Petignat P, Roy M. Diagnosis and management of cervical cancer. *BMJ: British Medical Journal* 2007;335:765.
24. Jhingran A, Winter K, Portelance L, Miller B, Salehpour M, Gaur R, Souhami L, Small W, Berk L, Gaffney D. A phase ii study of intensity modulated radiation therapy (imrt) to the pelvic for post-operative patients with endometrial carcinoma (rtog 0418). *International Journal of Radiation Oncology• Biology• Physics* 2008;72:S16-S17.
25. Jaffray DA, Siewerdsen JH, Wong JW, Martinez AA. Flat-panel cone-beam computed tomography for image-guided radiation therapy. *International Journal of Radiation Oncology* Biology* Physics* 2002;53:1337-1349.
26. Yamamoto R, Yonesaka A, Nishioka S, Watari H, Hashimoto T, Uchida D, Taguchi H, Nishioka T, Miyasaka K, Sakuragi N. High dose three-dimensional conformal boost (3dcb) using an orthogonal diagnostic x-ray set-up for patients with gynecological malignancy: A new application of real-time tumor-tracking system. *Radiotherapy and oncology* 2004;73:219-222.
27. Langerak T, Mens JW, Quint S, Bondar L, Heijkoop S, Heijmen B, Hoogeman M. Cervix motion in 50 cervical cancer patients assessed by daily cone beam computed tomographic imaging of a new type of marker. *International Journal of Radiation Oncology* Biology* Physics* 2015;93:532-539.
28. van de Bunt L, Van der Heide UA, Ketelaars M, de Kort GA, Jürgenliemk-Schulz IM. Conventional, conformal, and intensity-modulated radiation therapy treatment planning of external beam radiotherapy for cervical cancer: The impact of tumor regression. *International Journal of Radiation Oncology* Biology* Physics* 2006;64:189-196.
29. Naik A, Gurjar O, Gupta K, Singh K, Nag P, Bhandari V. Comparison of dosimetric parameters and acute toxicity of intensity-modulated and three-dimensional radiotherapy in patients with cervix carcinoma: A randomized prospective study. *Cancer/Radiothérapie* 2016;20:370-376.
30. Vargo JA, Kim H, Choi S, Sukumvanich P, Olawaiye AB, Kelley JL, Edwards RP, Comerci JT, Beriwal S. Extended field intensity modulated radiation therapy with concomitant boost for lymph node–positive cervical cancer: Analysis of regional control and recurrence patterns in the positron emission tomography/computed tomography era. *International Journal of Radiation Oncology* Biology* Physics* 2014;90:1091-1098.
31. Gandhi AK, Sharma DN, Rath GK, Julka PK, Subramani V, Sharma S, Manigandan D, Laviraj M, Kumar S, Thulkar S. Early clinical outcomes and toxicity of intensity modulated versus conventional pelvic radiation therapy for locally advanced cervix carcinoma: A prospective randomized study. *International Journal of Radiation Oncology* Biology* Physics* 2013;87:542-548.
32. Portelance L, Chao KC, Grigsby PW, Bennet H, Low D. Intensity-modulated radiation therapy (imrt) reduces small bowel, rectum, and bladder doses in patients with cervical cancer receiving pelvic and para-aortic irradiation. *International Journal of Radiation Oncology• Biology• Physics* 2001;51:261-266.
33. Klopp AH, Yeung AR, Deshmukh S, Gil KM, Wenzel L, Westin SN, Gifford K, Gaffney DK, Small Jr W, Thompson S. Patient-reported toxicity during pelvic intensity-modulated radiation therapy: Nrg oncology–rtog 1203. *Journal of Clinical Oncology* 2018:JCO. 2017.2077. 4273.
34. Tamaki T, Hirai R, Igari M, Kumazaki Y, Noda S-e, Suzuki Y, Kato S. Dosimetric comparison of three-dimensional conformal radiotherapy versus volumetric-arc radiotherapy in cervical cancer

treatment: Applying the central-shielding principle to modern technology. *Journal of Radiation Research* 2018.

35. Jürgenliemk-Schulz IM, Tersteeg RJ, Roesink JM, Bijmolt S, Nomden CN, Moerland MA, de Leeuw AA. Mri-guided treatment-planning optimisation in intracavitary or combined intracavitary/interstitial pdr brachytherapy using tandem ovoid applicators in locally advanced cervical cancer. *Radiotherapy and Oncology* 2009;93:322-330.
36. Haie-Meder C, Pötter R, Van Limbergen E, Briot E, De Brabandere M, Dimopoulos J, Dumas I, Hellebust TP, Kirisits C, Lang S. Recommendations from gynaecological (gyn) gec-estro working group☆(i): Concepts and terms in 3d image based 3d treatment planning in cervix cancer brachytherapy with emphasis on mri assessment of gtv and ctv. *Radiotherapy and oncology* 2005;74:235-245.
37. Pötter R, Haie-Meder C, Van Limbergen E, Barillot I, De Brabandere M, Dimopoulos J, Dumas I, Erickson B, Lang S, Nulens A. Recommendations from gynaecological (gyn) gec estro working group (ii): Concepts and terms in 3d image-based treatment planning in cervix cancer brachytherapy—3d dose volume parameters and aspects of 3d image-based anatomy, radiation physics, radiobiology. *Radiotherapy and Oncology* 2006;78:67-77.
38. Hellebust TP, Kirisits C, Berger D, Pérez-Calatayud J, De Brabandere M, De Leeuw A, Dumas I, Hudej R, Lowe G, Wills R. Recommendations from gynaecological (gyn) gec-estro working group: Considerations and pitfalls in commissioning and applicator reconstruction in 3d image-based treatment planning of cervix cancer brachytherapy. *Radiotherapy and Oncology* 2010;96:153-160.
39. Lang S, Kirisits C, Dimopoulos J, Georg D, Pötter R. Treatment planning for mri assisted brachytherapy of gynecologic malignancies based on total dose constraints. *International Journal of Radiation Oncology• Biology• Physics* 2007;69:619-627.
40. Fowler JF. The linear-quadratic formula and progress in fractionated radiotherapy. *The British journal of radiology* 1989;62:679-694.
41. Tod M, Meredith W. Treatment of cancer of the cervix uteri—a revised “manchester method”. *The British journal of radiology* 1953;26:252-257.
42. Viswanathan AN, Beriwal S, Jennifer F, Demanes DJ, Gaffney D, Hansen J, Jones E, Kirisits C, Thomadsen B, Erickson B. American brachytherapy society consensus guidelines for locally advanced carcinoma of the cervix. Part ii: High-dose-rate brachytherapy. *Brachytherapy* 2012;11:47-52.
43. Orton CG, Seyedsadr M, Somnay A. Comparison of high and low dose rate remote afterloading for cervix cancer and the importance of fractionation. *International Journal of Radiation Oncology• Biology• Physics* 1991;21:1425-1434.
44. Lertsanguansinchai P, Lertbutsayanukul C, Shotelersuk K, Khorprasert C, Rojpornpradit P, Chottetanaprasith T, Srisuthep A, Suriyapee S, Jumpangern C, Tresukosol D. Phase iii randomized trial comparing ldr and hdr brachytherapy in treatment of cervical carcinoma. *International Journal of Radiation Oncology• Biology• Physics* 2004;59:1424-1431.
45. Patel FD, Sharma SC, Negi PS, Ghoshal S, Gupta BD. Low dose rate vs. High dose rate brachytherapy in the treatment of carcinoma of the uterine cervix: A clinical trial. *International Journal of Radiation Oncology• Biology• Physics* 1994;28:335-341.
46. Isohashi F, Mabuchi S, Yoshioka Y, Seo Y, Suzuki O, Tamari K, Yamashita M, Unno H, Kinose Y, Kozasa K. Intensity-modulated radiation therapy versus three-dimensional conformal radiation therapy with concurrent nedaplatin-based chemotherapy after radical hysterectomy for uterine cervical cancer: Comparison of outcomes, complications, and dose-volume histogram parameters. *Radiation Oncology* 2015;10:180.
47. Klopp AH, Moughan J, Portelance L, Miller BE, Salehpour MR, Hildebrandt E, Nuanjing J, D'Souza D, Souhami L, Small Jr W. Hematologic toxicity in rtog 0418: A phase 2 study of postoperative imrt for gynecologic cancer. *International Journal of Radiation Oncology* Biology* Physics* 2013;86:83-90.

48. Aaronson NK, Ahmedzai S, Bergman B, Bullinger M, Cull A, Duez NJ, Filiberti A, Flechtner H, Fleishman SB, de Haes JC. The european organization for research and treatment of cancer qlq-c30: A quality-of-life instrument for use in international clinical trials in oncology. *JNCI: Journal of the National Cancer Institute* 1993;85:365-376.
49. Greimel ER, Vlasic KK, Waldenstrom AC, Duric VM, Jensen PT, Singer S, Chie W, Nordin A, Radisic VB, Wydra D. The european organization for research and treatment of cancer (eortc) quality-of-life questionnaire cervical cancer module. *Cancer* 2006;107:1812-1822.
50. Kirchheiner K, Pötter R, Tanderup K, Lindegaard JC, Haie-Meder C, Petrič P, Mahantshetty U, Jürgenliemk-Schulz IM, Rai B, Cooper R. Health-related quality of life in locally advanced cervical cancer patients after definitive chemoradiation therapy including image guided adaptive brachytherapy: An analysis from the embrace study. *International Journal of Radiation Oncology* Biology* Physics* 2016;94:1088-1098.
51. Heijkoop S, Nout R, Quint S, Mens J, Heijmen B, Hoogeman M. Dynamics of patient reported quality of life and symptoms in the acute phase of online adaptive external beam radiation therapy for locally advanced cervical cancer. *Gynecologic oncology* 2017;147:439-449.
52. Jadon R, Pembroke C, Hanna C, Palaniappan N, Evans M, Cleves A, Staffurth J. A systematic review of organ motion and image-guided strategies in external beam radiotherapy for cervical cancer. *Clinical Oncology* 2014;26:185-196.
53. Lee CM, Shrieve DC, Gaffney DK. Rapid involution and mobility of carcinoma of the cervix. *International Journal of Radiation Oncology* Biology* Physics* 2004;58:625-630.
54. Beadle BM, Jhingran A, Salehpour M, Sam M, Iyer RB, Eifel PJ. Cervix regression and motion during the course of external beam chemoradiation for cervical cancer. *International Journal of Radiation Oncology* Biology* Physics* 2009;73:235-241.
55. Huh SJ, Park W, Han Y. Interfractional variation in position of the uterus during radical radiotherapy for cervical cancer. *Radiotherapy and oncology* 2004;71:73-79.
56. Lee JE, Han Y, Huh SJ, Park W, Kang MG, Ahn YC, Lim DH. Interfractional variation of uterine position during radical rt: Weekly ct evaluation. *Gynecologic oncology* 2007;104:145-151.
57. Tyagi N, Lewis JH, Yashar CM, Vo D, Jiang SB, Mundt AJ, Mell LK. Daily online cone beam computed tomography to assess interfractional motion in patients with intact cervical cancer. *International Journal of Radiation Oncology• Biology• Physics* 2011;80:273-280.
58. Mayr N, Koch R, Wang J, Sammet S, Montebello J, Gupta N, Grecula J, Wu D, Edwards S, Yuh W. 1060: Intra-fractional organ motion of the uterus and tumor in cervical cancer patients-implications for radiation therapy planning and delivery. *International Journal of Radiation Oncology• Biology• Physics* 2006;66:S164.
59. Heijkoop ST, Langerak TR, Quint S, Mens JWM, Zolnay AG, Heijmen BJ, Hoogeman MS. Quantification of intra-fraction changes during radiotherapy of cervical cancer assessed with pre-and post-fraction cone beam ct scans. *Radiotherapy and Oncology* 2015;117:536-541.
60. Eminowicz G, Motlib J, Khan S, Perna C, McCormack M. Pelvic organ motion during radiotherapy for cervical cancer: Understanding patterns and recommended patient preparation. *Clinical Oncology* 2016.
61. Taylor A, Powell ME. An assessment of interfractional uterine and cervical motion: Implications for radiotherapy target volume definition in gynaecological cancer. *Radiotherapy and Oncology* 2008;88:250-257.
62. Ahmad R, Hoogeman MS, Bondar M, Dhawtal V, Quint S, De Pree I, Mens JW, Heijmen BJ. Increasing treatment accuracy for cervical cancer patients using correlations between bladder-filling change and cervix–uterus displacements: Proof of principle. *Radiotherapy and oncology* 2011;98:340-346.
63. Buchali A, Koswig S, Dinges S, Rosenthal P, Salk J, Lackner G, Böhmer D, Schlenger L, Budach V. Impact of the filling status of the bladder and rectum on their integral dose distribution and the movement of the uterus in the treatment planning of gynaecological cancer. *Radiotherapy and oncology* 1999;52:29-34.

64. Chen W, Bai P, Pan J, Xu Y, Chen K. Changes in tumor volumes and spatial locations relative to normal tissues during cervical cancer radiotherapy assessed by cone beam computed tomography. *Technology in cancer research & treatment* 2017;16:246-252.
65. Lim K, Chan P, Dinniwell R, Fyles A, Haider M, Cho Y-B, Jaffray D, Manchul L, Levin W, Hill RP. Cervical cancer regression measured using weekly magnetic resonance imaging during fractionated radiotherapy: Radiobiologic modeling and correlation with tumor hypoxia. *International Journal of Radiation Oncology* Biology* Physics* 2008;70:126-133.
66. Sotiras A, Davatzikos C, Paragios N. Deformable medical image registration: A survey. *Medical Imaging, IEEE Transactions on* 2013;32:1153-1190.
67. Han Y, Shin EH, Huh SJ, Lee JE, Park W. Interfractional dose variation during intensity-modulated radiation therapy for cervical cancer assessed by weekly ct evaluation. *International Journal of Radiation Oncology* Biology* Physics* 2006;65:617-623.
68. Lim K, Kelly V, Stewart J, Xie J, Cho Y-B, Moseley J, Brock K, Fyles A, Lundin A, Rehbinder H. Pelvic radiotherapy for cancer of the cervix: Is what you plan actually what you deliver? *International Journal of Radiation Oncology* Biology* Physics* 2009;74:304-312.
69. Gobeli M, Simon A, Getain M, Leseur J, Lahlou E, Lafond C, Dardelet E, Williaume D, Rigaud B, de Crevoisier R. Benefit of a pretreatment planning library-based adaptive radiotherapy for cervix carcinoma? *Cancer radiotherapie* 2015;19:471-478.
70. Ríos I, Vásquez I, Cuervo E, Garzón Ó, Burbano J. Problems and solutions in igrt for cervical cancer. *Reports of Practical Oncology & Radiotherapy* 2018.
71. Lucia F, Schick U, Pradier O, Espenel S, de Crevoisier R, Chargari C. Radiothérapie guidée par l'image des cancers gynécologiques. *Cancer/Radiothérapie* 2018.
72. Lim K, Stewart J, Kelly V, Xie J, Brock KK, Moseley J, Cho Y-B, Fyles A, Lundin A, Rehbinder H. Dosimetrically triggered adaptive intensity modulated radiation therapy for cervical cancer. *International Journal of Radiation Oncology* Biology* Physics* 2014;90:147-154.
73. Stewart J, Lim K, Kelly V, Xie J, Brock KK, Moseley J, Cho Y-B, Fyles A, Lundin A, Rehbinder H. Automated weekly replanning for intensity-modulated radiotherapy of cervix cancer. *International Journal of Radiation Oncology* Biology* Physics* 2010;78:350-358.
74. Oh S, Stewart J, Moseley J, Kelly V, Lim K, Xie J, Fyles A, Brock KK, Lundin A, Rehbinder H, Milosevic M, Jaffray D, Cho YB. Hybrid adaptive radiotherapy with on-line mri in cervix cancer imrt. *Radiother Oncol* 2014;110:323-328.
75. Bondar M, Hoogeman M, Mens J, Quint S, Ahmad R, Dhawtal G, Heijmen B. Individualized nonadaptive and online-adaptive intensity-modulated radiotherapy treatment strategies for cervical cancer patients based on pretreatment acquired variable bladder filling computed tomography scans. *International Journal of Radiation Oncology* Biology* Physics* 2012;83:1617-1623.
76. Heijkoop ST, Langerak TR, Quint S, Bondar L, Mens JWM, Heijmen BJ, Hoogeman MS. Clinical implementation of an online adaptive plan-of-the-day protocol for nonrigid motion management in locally advanced cervical cancer imrt. *Int J Radiat Oncol Biol Phys* 2014;90:673-679.
77. Langerak T, Heijkoop S, Quint S, Mens J-W, Heijmen B, Hoogeman M. Towards automatic plan selection for radiotherapy of cervical cancer by fast automatic segmentation of cone beam ct scans Medical image computing and computer-assisted intervention–miccai 2014: Springer; 2014. pp. 528-535.
78. Georg P, Georg D, Hillbrand M, Kirisits C, Pötter R. Factors influencing bowel sparing in intensity modulated whole pelvic radiotherapy for gynaecological malignancies. *Radiotherapy and oncology* 2006;80:19-26.
79. Taylor A, Powell M. Conformal and intensity-modulated radiotherapy for cervical cancer. *Clinical oncology* 2008;20:417-425.
80. Whelan B, Kumar S, Dowling J, Begg J, Lambert J, Lim K, Vinod SK, Greer PB, Holloway L. Utilising pseudo-ct data for dose calculation and plan optimization in adaptive radiotherapy. *Australasian Physical & Engineering Sciences in Medicine* 2015;38:561-568.

81. Seppenwoolde Y, Stock M, Buschmann M, Georg D, Bauer-Novotny K-Y, Pötter R, Georg P. Impact of organ shape variations on margin concepts for cervix cancer art. *Radiotherapy and Oncology* 2016.
82. Nováková E, Heijkoop S, Quint S, Zolnay A, Mens J, Godart J, Heijmen B, Hoogeman M. What is the optimal number of library plans in art for locally advanced cervical cancer? *Radiotherapy and Oncology* 2017.
83. Kaatee RS, Olofsen MJ, Verstraate MB, Quint S, Heijmen BJ. Detection of organ movement in cervix cancer patients using a fluoroscopic electronic portal imaging device and radiopaque markers. *International Journal of Radiation Oncology* Biology* Physics* 2002;54:576-583.
84. Ahmad R, Hoogeman MS, Quint S, Mens JW, de Pree I, Heijmen BJ. Inter-fraction bladder filling variations and time trends for cervical cancer patients assessed with a portable 3-dimensional ultrasound bladder scanner. *Radiotherapy and oncology* 2008;89:172-179.
85. van de Bunt L, Jürgenliemk-Schulz IM, de Kort GA, Roesink JM, Tersteeg RJ, van der Heide UA. Motion and deformation of the target volumes during imrt for cervical cancer: What margins do we need? *Radiotherapy and Oncology* 2008;88:233-240.
86. Khan A, Jensen LG, Sun S, Song WY, Yashar CM, Mundt AJ, Zhang F-q, Jiang SB, Mell LK. Optimized planning target volume for intact cervical cancer. *International Journal of Radiation Oncology* Biology* Physics* 2012;83:1500-1505.
87. Buschmann M, Majercakova K, Sturdza A, Smet S, Najjari D, Daniel M, Pötter R, Georg D, Seppenwoolde Y. Image guided adaptive external beam radiation therapy for cervix cancer: Evaluation of a clinically implemented plan-of-the-day technique. *Zeitschrift für Medizinische Physik* 2017.
88. Bondar L, Hoogeman M, Mens JW, Dhawtal G, De Pree I, Ahmad R, Quint S, Heijmen B. Toward an individualized target motion management for imrt of cervical cancer based on model-predicted cervix–uterus shape and position. *Radiotherapy and Oncology* 2011;99:240-245.
89. O'Reilly FH, Shaw W. A dosimetric evaluation of igart strategies for cervix cancer treatment. *Physica Medica: European Journal of Medical Physics* 2016;32:1360-1367.
90. van de Schoot AJ, de Boer P, Visser J, Stalpers LJ, Rasch CR, Bel A. Dosimetric advantages of a clinical daily adaptive plan selection strategy compared with a non-adaptive strategy in cervical cancer radiation therapy. *Acta Oncologica* 2017;56:667-674.
91. Gobeli M, Rigaud B, Charra-Brunaud C, Renard S, De Rauglaudre G, Beneyton V, Racadot S, Peignaux K, Leseur J, Williaume D. Po-1078: Cbct guided adaptive radiotherapy for cervix cancer: Uncertainty of the choice of the plan of the day. *Radiotherapy and Oncology* 2018;127:S606-S607.

2 RECALAGE DEFORMABLE POUR LA RADIOTHERAPIE : PRINCIPE, METHODES, APPLICATIONS ET EVALUATION

2 Recalage déformable pour la radiothérapie : principe, méthodes, applications et évaluation 48

2.1 Introduction....49

2.2 Article : "Deformable image registration for radiation therapy: principle, methods, applications, and evaluation"....50

2.2.1 Introduction....51

2.2.2 Principle of deformable image registration....52

2.2.3 Classic registration methods used in radiotherapy....56

2.2.4 DIR applications in RT....59

2.2.5 DIR evaluation....68

2.2.6 Conclusion....75

2.2.7 References....76

2.3 Discussion : recalage déformable pour les cancers du col de l'utérus....93

2.3.1 Recalage déformable pour la propagation des contours....93

2.3.2 Recalage déformable pour la radiothérapie adaptative....94

2.4 Conclusion....97

2.5 Références....98

2.1 INTRODUCTION

La déformation d'organes survenant à la planification et en cours de traitement étant l'une des principales difficultés auxquelles la radiothérapie (RT) moderne doit faire face, l'utilisation des méthodes de recalage déformable a connu un développement important pour différentes applications. Cet outil commence depuis peu à être manipulé par des cliniciens. Cependant, sa complexité et son effet « boîte noire » limitent souvent son utilisation.

Comme présenté dans le chapitre 1 (section 1.4.1), les organes de la région pelvienne subissent des déformations importantes au cours du traitement. Ces déformations ont un impact non-négligeable sur la précision du traitement et ont besoin d'être quantifiées. Le recalage déformable est une méthode qui permet d'estimer un champ de déformations entre deux images. Cette approche permet d'assister de nombreuses applications en RT comme la propagation de contours réalisés sur une image de référence vers des images à délinéer, la quantification des déformations anatomiques entre les différentes images du traitement ou encore l'estimation de la distribution de dose totale délivrée en propageant les doses de chaque séance du traitement vers l'anatomie de planification. L'intérêt du recalage déformable est donc crucial puisqu'il permet d'assister le traitement pour des applications fastidieuses (par ex. le contourage des organes) ou de l'enrichir d'informations importantes (par ex. la quantification des déformations et le suivi de dose). Ce deuxième chapitre a donc pour but de présenter le recalage déformable dans le contexte de la radiothérapie.

L'objectif est tout d'abord de présenter de manière didactique le principe du recalage déformable et les principales méthodes utilisées dans le cadre de la RT. Ensuite, les différentes applications qui nécessitent l'apport de ces méthodes sont présentées, en ne se limitant pas aux cancers du col de l'utérus. Bien que les méthodes de recalage déformable se soient grandement améliorées pendant les dernières années, la question de leur évaluation reste centrale. De ce fait, la dernière partie de ce chapitre porte sur les méthodes d'évaluation des performances du recalage déformable. Enfin, une discussion complémentaire se concentre sur les études qui utilisent le recalage déformable dans le contexte des cancers du col utérin.

Ces travaux correspondent à un article, intitulée « *Deformable image registration for radiation therapy: principle, methods, applications, and evaluation* », resoumis après révision majeure dans le journal *Acta Oncologica* en mars 2018 et reproduit ci-dessous.

2.2 ARTICLE : "DEFORMABLE IMAGE REGISTRATION FOR RADIATION THERAPY: PRINCIPLE, METHODS, APPLICATIONS, AND EVALUATION"

Bastien Rigaud *MSc* (1, 2) *, Antoine Simon *PhD* (1, 2), Joël Castelli *MD, MSc* (1, 2, 3), Caroline Lafond *PhD* (1, 2, 3), Oscar Acosta *PhD* (1, 2), Pascal Haigron *PhD* (1, 2), Guillaume Cazoulat *PhD* (4), and Renaud De Crevoisier *MD, PhD* (1, 2, 3) *

1. Université de Rennes 1, LTSI, Campus de Beaulieu, Rennes, F-35042
2. INSERM, U1099, Campus de Beaulieu, Rennes, F-35042
3. Centre Eugene Marquis, Radiotherapy Department, Rennes, F-35000
4. Department of Imaging Physics, The University of Texas MD Anderson Cancer Center, Houston, TX 77030, USA

Abstract

Background

Deformable image registration (DIR) is increasingly used in the field of radiation therapy (RT), to account for anatomical deformations. The aims of this paper are to describe the principle of DIR, the DIR methods used in RT, the main applications of DIR in RT and DIR evaluation methods.

Methods

An electronic search of articles published in PubMed and Science Direct was performed from January 2000 to January 2018. Our search was restricted to articles that report data obtained from humans written in English and addressing DIR methods for RT. A total of 192 articles were selected, among the 2616 identified in the electronic search, based on didactic considerations.

Results

DIR is an iterative process searching for geometric correspondence between a "moving" and a "fixed" images. The DIR workflow can be divided into two main steps: preprocessing and registration loop. The most frequently used DIR methods in RT are the following: Demons, free-form deformation, salient points-based methods and, more recently, the biomechanical model approach.

At the planning, DIR can be used for organ delineation, deformation-based model planning target volume definition, functional planning and MRI-based dose calculation. In image-guided RT, DIR can be used for contour propagation and dose calculation on the per-treatment imaging. DIR can also be used to accumulate the dose from fraction to fraction, both in external beam RT and brachytherapy and in adaptive RT for dose monitoring. In case of re-irradiation, DIR can also be useful to guide the second irradiation. Finally, DIR can be used for toxicity prediction via voxel-wise population analysis. Due to DIR uncertainties, many DIR evaluation methods have been proposed, generally focused on geometric metrics.

Conclusions

DIR played a crucial role in a large field of RT applications, from planning to toxicity prediction; however, it must be accurately evaluated mainly for dosimetric applications.

2.2.1 INTRODUCTION

Deformable image registration (DIR) is the estimation of the geometric transformation between two images to map them onto a common coordinate system (CCS). It is qualified as deformable, or non-linear, since the observed objects are submitted not only to a rigid transformation (*i.e.* translation and/or rotation) but also to deformations (*e.g.* shrinking or stretching).

DIR has increasingly been studied for radiation therapy (RT) applications, and its integration in clinical practice is currently the object of intensive research effort, as testified to by the AAPM “Task Group 132 for DIR recommendations for quality assurance and quality control in clinical practice” [1]. This is primarily accounted for by the increasing number of acquired images, along with the development of multimodal imaging for planning, image-guided RT (IGRT) and adaptive RT (ART) during treatment delivery as well as by advances in image processing. Indeed, at the planning, DIR is a particularly attractive tool to assist the segmentation by the use of an atlas-based model and for fusion in the case of multimodal imaging. Moreover, DIR can be used to improve the dose targeting, with a posteriori information, from population analysis. During fractionated treatment, in both external beam RT and brachytherapy (BT), one clinical challenge is to manage organ deformations. These deformations are caused by different factors, for example, patient motion, breathing, weight loss, tumour and organ at risk (OAR) shrinkage or organ filling. If not corrected, these anatomical variations occurring at intra- or inter-fraction may lead to tumour underdosage and OAR overdosage, thus increasing the risk of recurrence or toxicity [2,3]. In this context, DIR has been proposed to monitor the deformations. DIR can, thus, propagate planning segmentations to per-treatment images. DIR can be then used to estimate and monitor the cumulated dose in a deformable anatomical structure. DIR has also been used for toxicity prediction within a voxel-based analysis framework. Thus, it allows the identification of specific organ subregions that are associated with high risk of toxicity.

First, this paper presents the principle, difficulties and classic methods of DIR in RT (supplementary material). Second, the applications of DIR in RT are detailed: at the planning to improve segmentation; during the treatment for IGRT, BT, ART and re-irradiation; and for toxicity prediction. Since DIR is subject to uncertainties, the last part of the paper is focused on DIR evaluation methods. This paper does not include rigid registration (*i.e.* limited to global translation and rotation), which is routinely used, for example, in IGRT for tumour repositioning.

We performed an electronic search of articles published in PubMed and Science Direct, from January 2000 to January 2018, using the following keywords: ("DIR" OR "deformable image registration" OR "elastic registration" OR "non-rigid registration") AND ("radiotherapy" OR "radiation therapy"). Our search was restricted to articles that report data obtained from humans written in English and addressing DIR methods for external beam RT (EBRT) and BT. A total of 2616 articles were identified from the electronic search. Since this paper is not an exhaustive review, 190 articles were selected based on didactic considerations to present the most often used methods and the main clinical applications.

2.2.2 PRINCIPLE OF DEFORMABLE IMAGE REGISTRATION

DIR is an iterative process searching for the geometric correspondence between a “moving” and a “fixed” images. Figure 2-1 presents the classical DIR workflow, which can be divided in two main steps: preprocessing (Step 1) and registration loop (Step 2). At each iteration of the registration loop, or optimization, the geometric transformation is updated and the moving image deformed accordingly. The goal is to find the transformation that corresponds to the optimal value of a metric comparing the fixed and transformed moving images (*i.e.* a similarity measure).

This process can be expressed by the following formula:

$$\hat{T} = \underset{T}{\operatorname{argmin}}\, C\left[I_{fixed}, T\left(I_{moving}\right)\right] \tag{2-1}$$

where $\hat{T}$ (Step 2a) represents the resulting transformation that minimizes the cost function C based on the metric (Step 2b) comparing the fixed image (I_{fixed}) and the transformed moving image $T(I_{\text{moving}})$. “argmin” represents the optimization process which updates the transformation T to minimize C (Step 2c) until the convergence criteria are reached (*e.g.* maximum number of iterations or metric convergence) (Step 2d).

In the remainder of this section, we briefly describe each one of these steps. For more details, the reader may refer to DIR reviews [4-7] or software libraries implementing DIR methods [8,9].

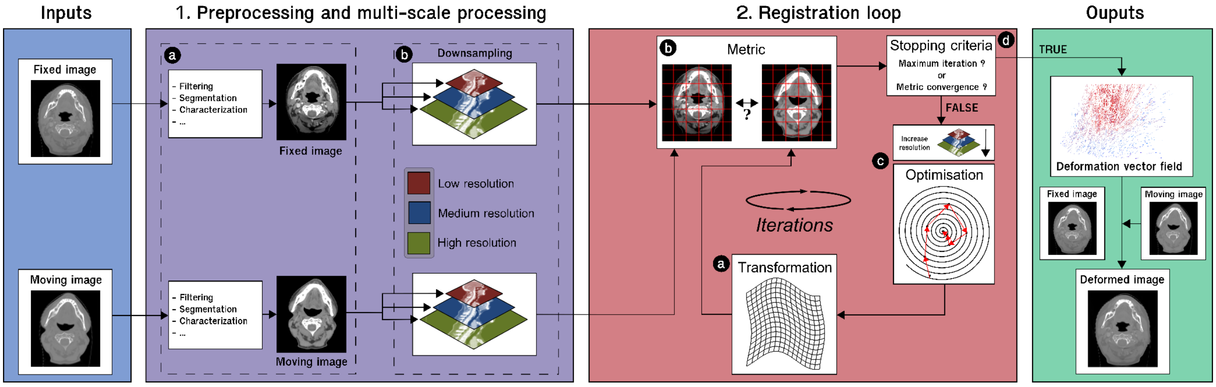

Figure 2-1 : General process of deformable image registration

The deformable image registration workflow is divided into two steps: In the preprocessing step, the input images can be improved either by increasing intensity contrast, segmenting regions of interest or extracting features (e.g. salient points, calcification, or metabolic information) (1a). Multi-scale images can be computed with multiple image resolutions downsampled from the original resolution or blurred images by using increasing smoothing filters (1b). In the second step, the registration loop is launched. At each iteration, the geometric transformation (2a) is updated and the moving image is deformed accordingly. The goal is to find the transformation corresponding to the optimal value of the metric (2b) comparing the fixed image and the transformed moving image. The optimal transformation parameters, obtained by optimization (2c) until the stopping criteria (2d), enable generation of a deformation vector field (DVF) that warps the moving image to match the fixed image

2.2.2.1 Step 1: Preprocessing and multi-scale processing

2.2.2.1.1 Preprocessing (Figure 2-1.1a)

Preprocessing the input images is useful for focusing the registration process on the information presented in both images. This can be performed by extracting some specific features, either manually or automatically, such as salient anatomical points (*e.g*. nose tip, vessel bifurcation, calcification) or implanted markers, which will be used to guide the registration (*cf*. section 2.2.3.3). The similarity between the images can also be improved by cropping or filtering them. Cropping the images enables them to be limited to common anatomical structures. This can also be achieved by automatically or manually segmenting a desired subpart of the images, such as the considered organs. Filtering the images can also improve the intensity consistency between both images, such as using a gradient filter to extract organ contours [10] or a sigmoid filter. Intensity correction or even the simulation of one imaging modality from another (*e.g.* computed tomography [CT] / cone beam CT [CBCT] registration) can also facilitate the comparison of the images [11]. Where applicable, the segmented regions can also be processed to describe their structure, *e.g*. using Euclidean distance maps [12-15] or Laplacian diffusion [16-18]. In some cases, segmented regions can be used to preprocess the underlying image and thus increase point correspondence between both images, *e.g*. by removing bowel gas [19-23] or applicator [24].

2.2.2.1.2 Multi-scale image description (Figure 2-1.1b)

The value of using a multi-scale or pyramidal outlook for image registration is to control the granularity of the registered information. Indeed, registration is an iterative process that needs both effective initialization and efficient optimization to tend to a unique solution within reasonable computation time. The aim of the multi-scale approach is therefore to decompose this process into multiple simpler tasks, starting from the coarsest information then refining the result by considering more and more details. Thus, from coarse-to-fine resolution, large-to-small (*i.e.* mostly linear-to-non-linear) deformations can be quantified, respectively at the boundary conditions of each level of registration. The multi-scale description of an image is based on its down-sampling to provide different levels of detail, from the finest (original image) to the coarsest. Optimization using multi-resolution is described in section 2.2.2.2.3.

2.2.2.2 Step 2: Registration loop

2.2.2.2.1 Transformation (Figure 2-1.2a)

Transformation aims to deform the moving image to make it correspond as closely as possible to the fixed image. When considering DIR, the transformation is generally represented as a deformation vector field (DVF), *i.e*. a set of vectors, defined on the fixed image space, with a displacement vector corresponding to each voxel. This transformation maps each voxel of the fixed image to the corresponding position in the moving image.

Generally, the transformations are method-dependent. Two main classes of transformations are used (*cf*. Figure 2-2): parametric and non-parametric. In the parametric method, the transformation is based on a limited number of control points, defined either regularly (*e.g*. using an overlying grid) or arbitrarily (*e.g*. using salient points). The non-parametric method is directly based on a DVF defined on each voxel. In this case, in order to generate realistic deformations, the DVF is smoothed to regularize it, *e.g*. prevent discontinuities like physically unrealistic deformations. Fluid or elastic deformations are then simulated [25].

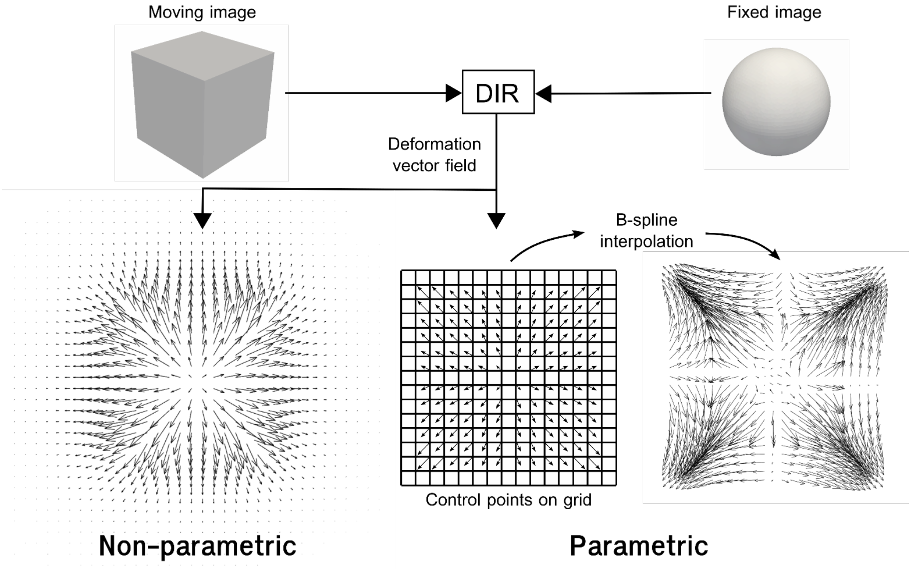

Figure 2-2 : Example of DVF from a non-parametric (Demons) and parametric method (free-form deformation)

The non-parametric method is directly based on a DVF defined on each voxel, while the parametric method uses a limited number of points (*e.g.* using an overlying grid with equidistant fixed points or using arbitrary salient points). DIR: Deformable image registration; DVF: Deformation vector field

2.2.2.2.2 Measure of similarity or metric (Figure 2-1.2b)

The metric measures the similarity between the fixed and transformed images. The choice of metric is crucial since this is the criterion that guides the optimization of the geometric transformation. The literature presents a very large number of metrics and their variants, which can be divided into two main groups. Feature-based metrics use geometric characteristics (*e.g*. points, curves, surfaces, or volumes) previously extracted in both images (*cf*. Step 1a - preprocessing), generally relying on the geometric distance (*e.g*. Euclidean) between identical characteristics in both images. Intensity-based metrics, on the other hand, directly use voxel intensity. In the context of mono-modality registration, the sum of squared differences (assuming one given voxel has the same intensity in both images) and the cross-correlation coefficient (assuming a linear relationship between the intensities in both images) [26] are the most often used metrics. In multimodality registration, metrics based on statistic similarity are preferred, such as mutual information [27] measuring the statistical relationship of the intensities between the two images. Multi-metric approaches can be also used to guide the process [4].

To compare the intensities of the fixed and deformed images, they have to be defined at the same locations. Thus, the intensities of the deformed image are generally interpolated at the voxel location in the fixed image. For example, a linear interpolation provides a smooth result by combining the neighboring intensities.

2.2.2.2.3 Optimization and multi-scale approach (Figure 2-1.2c)

The role of the optimizer is to adjust the geometric transformation in order to improve the metric value (increase or decrease the value, depending on the definition of the metric). The more complex the desired transformation, the larger the research space. Several optimization methods have been considered in the literature. The most classical optimizer is the gradient descent where the optimum is iteratively searched for by locally following the direction corresponding to the negative of the gradient of the metric values (*i.e*. the direction downwards). A rigorous setting of the gradient step is crucial to optimize computation time and stability. Recently, adaptive approaches have managed to iteratively modify this “searching” step in the optimization space. Different optimization methods have been derived from the classical gradient descent, considering other mathematical aspects (*e.g*. approximation of the derivative, random selection) [28].

The multi-scale approach proves useful for stabilizing the optimization. Starting from the lowest resolution, the transformation is optimized and initializes the optimization at higher resolutions until the highest has been reached (*cf*. Figure 2-1.1b). This procedure aims at simplifying the optimization process so as to facilitate the search for the optimum value. Thus, the problem-solving capacity generally becomes more efficient and faster.

2.2.2.2.4 Algorithm convergence (stopping criteria) and DVF generation (Figure 2-1.2d)

The optimization loops until a stopping criterion is reached. Two main stopping criteria can be used and combined: the number of iterations and the metric value convergence. Setting a maximum number of iterations prevents the optimization from looping indefinitely. Finally, the DVF is built from the “optimal” transformation and sampled on the fixed image coordinates. This DVF, representing the correspondence of the fixed image to the moving image domain, can be used to deform the moving image anatomy and spatially-linked information (delineations, dose).

2.2.2.3 Difficulties for DIR

DIR methods encounter difficulties depending on the image characteristics. Noise adds intensity information that is not related to patient anatomy, thus misleading DIR methods. Artefacts caused by either image acquisition (*e.g*. distortion, aliasing, motion) or patient prosthesis (resulting to distortions or star-burst artefacts) disturb the image intensities. Different fields of view (FOV) between the two images can likewise hamper their alignment and restrict the DVF to where they intersect [29].

The estimation of the deformation between two images is inherently an ill-posed problem, meaning that the solution is not unique. Indeed, based on the image intensity, a given point in a homogeneous region may be mapped to multiple points (non-unicity of the solution, *cf*. Figure 2-3d). Thereby, physical properties of the tissues or deformation vector field characteristics should be considered in order to estimate coherent transformations. Several constraints (*e.g*. manual landmarks) can be exploited to guide the estimation of the DVF [30].

DIR methods may encounter difficulties depending on organ or tissue characteristics. For some anatomical areas, sliding between tissues may occur (*e.g.* between the lungs and thoracic cage, *cf.* Figure 2-3a) [31]. More complex regularization methods (*e.g*. combination of transformations of different organs) have been proposed [32-38] in order to handle these situations.

Furthermore, the same tissues should always be present in both images, yet matter disappearance or appearance can occur, creating a challenge, *e.g*. gas appearance or disappearance in the bowel (*cf.* Figure 2-3b) or tumour shrinkage. This may require specific methods to be implemented (*e.g.* preprocessing to identify and remove gas [23]), or otherwise the estimated DVF results in unrealistic deformations.

The last difficulty with DIR methods consists in achieving good parametrization of the registration process based on the context (*e.g*. localization, application, imaging modality), with the aim to obtain good convergence of the optimization. For example, local large deformations can be difficult to estimate (*cf*. Figure 2-3c) due to inappropriate metric or optimization parameters. If the optimization gradient step is too small or large, the process can either converge to local minima, never converge, or converge very slowly. To deal with these large deformations, each organ can be registered separately based on their delineations. All organ DVFs can thereafter be fused to generate a global DVF (*e.g*. using weighting by distance) [12,39].

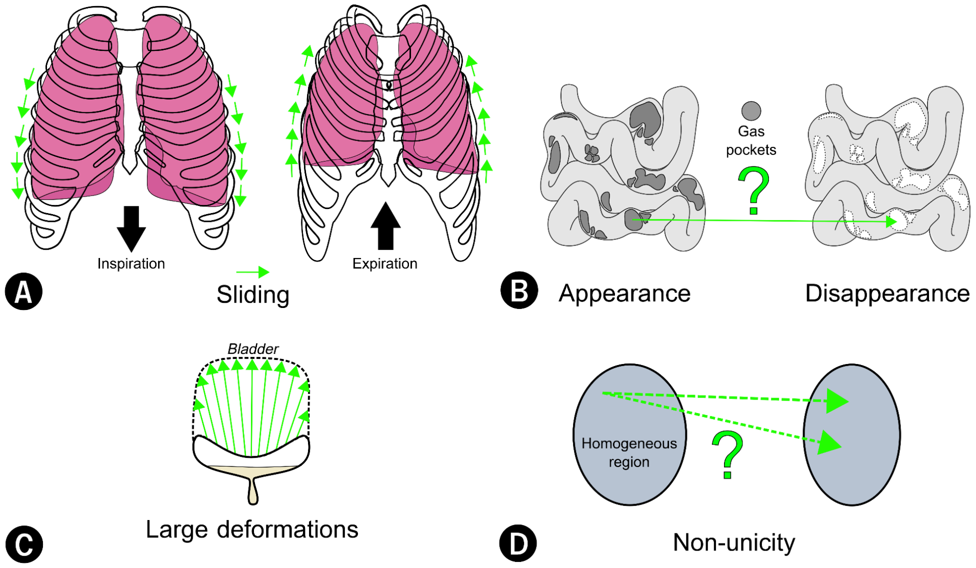

Figure 2-3 : Illustration of the main difficulties for DIR methods

Organ sliding resulting to deformation vector field (DVF) topology discontinuities (A); Matter appearance/disappearance over time (B); Large local deformations (C); Non-unicity of the DVF where different correspondences can be associated for one point in a homogenous region (D)

2.2.3 CLASSIC REGISTRATION METHODS USED IN RADIOTHERAPY

Several DIR methods using the general workflow detailed above have been proposed in the literature, with the most commonly-used in radiotherapy presented below (*cf*. Table 2-1).

2.2.3.1 Demons registration

One of the most popular DIR method is the Demons algorithm [40], which is a non-parametric method since that the displacement of each voxel is computed. The regularization is simply performed by smoothing the DVF at each iteration. The Demons DVF corresponds to a “force” directed in accordance with the intensity differences between the two images. This method actually corresponds to minimizing the intensity difference between images using a gradient descent [25]. Thus, the algorithm is adapted to images with the same intensity range (*i.e*. same imaging modality). Otherwise, intensity correspondences can be adjusted by preprocessing [41] or iterative correction [42]. Since the first proposed algorithm by Thirion [40], Demons registration has progressively been improved, especially in terms of convergence, by integrating an “active” force that also considers the moving image gradient [43], and DVF invertibility (*i.e*. nonsingularity), called diffeomorphism [44].

2.2.3.2 Free-form deformation

Free-form deformation (FFD) [45] is a generic parametric method relying on estimating the transformation based on a limited set of control points defined by a regular grid that is superimposed on the image. The vector displacements are iteratively optimized according to the metric. A dense DVF is then obtained by B-spline interpolation [45]. Splines are smooth functions used for coarse vector interpolation based on control points. The FFD model has the advantage of providing a smooth deformation with only few parameters. As shown by Zagorchev [46], who evaluated multiple transformation functions, the control points used for the parametric methods should be homogeneously distributed and limited in number. In multi-resolution approaches, the parameters are up-sampled using B-spline to represent the transformation in the higher scale. A recent method enriched the B-spline basis function during this up-sampling process in order to integrate desired discontinuities, such as sliding [47].

2.2.3.3 Geometric approaches: salient points-based registration

Contrary to the previous methods which are directly based on image intensities, the geometric approach consists of extracting anatomical or geometric salient points or surfaces in order to characterize the structures to be registered. This is particularly useful when both images exhibit very different intensities, such as when registering different imaging modalities (*e.g*. CT with magnetic resonance imaging [MRI]). Salient feature-based registration (SFBR) is a common geometric approach involving three steps: (i) salient features are extracted and refined using filtering, down-sampling, intensity, or topology analysis; (ii) the salient points of both images are matched using similarity of neighborhoods; (iii) a dense DVF is then estimated by interpolating the salient point pairs (*e.g*. with basis- or thin-plate splines [48]).

Geometric methods can also be based on morphing transformation [49]. Other methods use multiple-attribute extraction for inter- and intra-modality registration in variant cases [50,51]. Manual landmark-based approaches can similarly be used, though involve heavy workloads, since many landmarks have to be considered for a precise DVF to be generated [52].

2.2.3.4 Biomechanical model

Biomechanical model-based registration is inspired by the physical properties of the registered organs. Considering two images to register, a finite element model (FEM) of the considered organ(s) to be deformed is generated from segmentations. These properties can be divided into three main groups with varying complexity: (i) linear elastic modeling considers that the material returns to its original position after being stressed. Properties of the soft tissue are then represented by Hooke's law, which is defined by two constants: the modulus of elasticity (Young's modulus) and compression parameter (Poisson's ratio); (ii) the hyperelastic model considers soft tissues to be rubber-like material adopting non-linear behavior based on the strain-energy density and the material stretchiness; (iii) the viscoelastic model takes into consideration both viscous and elastic properties, with a time-dependent strain. After selecting the mechanical law, the corresponding parameter values have to be set. Since it is generally impossible to identify these values for each individual patient, some generic values are usually used. Next, boundary conditions are assigned between both images, corresponding to prescribed displacements (*e.g.* resulting from a previous DIR). Finally, a finite element analysis (*i.e.* numerical optimization) is performed and aimed to extract the resulting displacement, stress, and strain of each element of the meshes.

2.2.3.5 Hybrid methods

Hybrid methods have recently been proposed to take advantage of different DIR approaches. Their goal is to improve regularization, precision, and rapidity. The hybrid process can be applied either during optimization, by generating a DVF from different information (*e.g.* intensities, structures, landmarks), or afterward, by fusing the different DVFs resulting from the different methods. The idea is to compensate for errors introduced by each algorithm [53-62]. Another approach consists in constraining the update of the demons' DVF by the gradient of the salient points-based registration, with the aim to reduce the discontinuity provided by the largest deformations [63].

The main idea behind the principle of DIR is not evolving, yet more complex and advanced methods have emerged. In conclusion, there is no "universal" DIR method that proves efficient in all situations. Depending on image modality, image quality, anatomical localization, deformation magnitude, and patient anatomy, a variety of specific methods have been proposed. Certain challenges are particularly prohibitive for certain methods, like the consideration of very large deformations, tissue sliding or matter appearance/disappearance. For this purpose, both research and commercial applications are leaning towards hybrid and biomechanical models.

Table 2-1 : Principle, advantages, and drawbacks of various deformable image registration approaches

Transformation type (example)	Principle	Advantages	Drawbacks
Geometric (Salient points-based registration)	Extraction of homologous structures; Registration of these structures	Computation performance (marginal iterative optimization) Controllable environment	Difficulty finding corresponding landmarks Not always fully automatic (may need segmentations)
Parametric(Free-form deformation)	Deformation based on parameters optimized according to the intensity information	Highly customizable Compatibility with metrics Possibility of defining constraints	Parameters need by-application settings that can induce bad matching or low convergence performance
Non-parametric (Demons)	Deformation defined on each voxel optimized according to the intensity information	Rapidity to converge Simple customization	Low mapping in cases involving large deformation (local evaluation)
Biomechanical model	Deformation based on biomechanical laws	Realistic deformation Complex deformation Biomechanical soft tissue properties	Intra-individual registration Accurate delineations needed Good customization required (elasticity, constraints, and boundaries)

2.2.4 DIR APPLICATIONS IN RT

The following sections introduce the primary DIR applications in the RT workflow, along with their clinical benefits and limits.

2.2.4.1 DIR at the planning: atlas-based segmentation, multimodal image fusion, PTV definition, functional imaging and MRI-based dose calculation

The first step of treatment planning is the delineation of organs of interest. This delineation is based on computed tomography (CT) images, yet it can involve multimodal imaging. This task can be time-consuming, reaching 2.5 hours, for example, in the head and neck (H&N) [64].

2.2.4.1.1 Atlas-based segmentation

To perform automatic segmentation, atlas-based methods rely on DIR between the image to segment and the images of an atlas for which the associated delineations are known. The atlas consists of a single image template [65] or several templates (multi-atlas, typically 15-30 images, depending on the tumour localisation) [66], from patients with representative anatomy and organ delineations validated by experts. The first step consists of identifying the most similar template image in terms of the image intensities, specific characteristics (*e.g.* patient gender, age, weight) or anatomical features (*e.g.* organ size, centroid position, orientation) [67]. The DIR transformation between the template image and the image targeted for segmentation is then estimated and applied to the template delineations, to propagate the contours onto the new subject anatomy.

Finally, the radiation oncologist must verify these contours and correct them if necessary. Atlas-based segmentation methods are useful for organ delineation, although they are not appropriate for the segmentation of tumours. The tumours exhibit different shape characteristics and image features for different patients. Moreover, selecting the right template proves especially crucial. The more representative the template is of the considered image, the simpler and less prone to error the transformation. To reduce the uncertainties, the selection of a unique template can be replaced by the use of multiple templates [68-70]. In the latter case, the final segmentations over the multiple propagated contours can be obtained by averaging or majority vote [71], using the STAPLE (simultaneous truth and performance level estimation) [72] or the SIMPLE (selective and iterative method for performance level estimation) methods [73].

In total, having demonstrated their ability to provide segmentations of a quality comparable to expert delineations [69,70,74-76], while also reducing intra- and inter-observer delineation variability and decreasing the delineation time (*e.g.* up to 40% reduction for H&N [76]), atlas-based segmentation methods are currently proposed in several treatment planning systems (TPS) [77,78] and routinely used in clinics.

2.2.4.1.2 Multimodal image fusion

Morphological and functional images, considered to be diagnostic images, also play a crucial role in RT planning. These multimodal images must be therefore fused to combine the associated information in a CCS. For example, magnetic resonance imaging (MRI) and fluorodeoxyglucose-positron emission tomography (FDG-PET) are used for their abilities to improve the tumour delineation [79-81]. However, delineation could prove to be especially complex due to anatomical deformations or body position variations that are observed at image acquisition, which thus renders “standard” rigid registration impossible. For prostate delineation, MRI enables to clearly define the prostate contour as well as tumour volumes, whereas CT often overestimates this organ volume and does not show the tumour [82]. DIR methods have therefore been proposed to propagate the delineation of the prostate from MRI to CT, using a free-form deformation (FFD) (*cf.* section 2.2.3.2) [83] or finite-element model (FEM) (*cf.* section 2.2.3.4) [53] DIR methods. In cervical cancer, DIR has been used to propagate the prebrachytherapy MRI to the planning CT. The resulting propagated high-risk clinical target volume (HR-CTV) was shown to be smaller in MRI than in CT [84]. In H&N cancer, DIR has also been used to propagate the gross tumour volume (GTV) from the diagnostic position MRI to the planning CT, thus improving the accuracy of the GTV delineation [85]. Still in H&N, DIR has been used to propagate CT/ FDG-PET or MRI/ FDG-PET to the planning CT [86-88]. Finally, in lung cancer, DIR has been used to deform the static CT to the 4D MRI using a hybrid DIR method (*cf.* section 2.2.3.5) to generate a 4D CT for RT planning [60].

2.2.4.1.3 DIR for deformation-based model PTV definition and functional planning

DIR has been proposed to quantify the mobility and deformation of organs within a population of patients. DIR enables to quantify the deformations, either at an intra-patient scale (*e.g.* using 4D CT or early per-treatment imaging) or at an inter-patient scale (*e.g.* using planning or per-treatment imaging), thus generating a population-based deformation model. This model can then be used for a given patient, to define the planning target volume (PTV) margins, dose coverage probability and functional imaging-based planning. In prostate cancer, inter- and intra-patient anatomies have been put in correspondence, using DIR, to build a statistical deformable motion model. By accumulating the dominant deformations of the model, a population-based PTV could be defined, not only based on prostate displacements such as in a “standard” approach population-based PTV [89] but also in accounting for deformations [90]. In rectal cancer, the same method was applied [91]. The population-based PTV significantly improved OAR sparing compared to uniform and nonuniform CTV-to-PTV margins. In cervical cancer, a DIR-based model has been generated to simulate different treatment scenarios and assess the dose coverage probability of the CTV and OAR [92]. In lung cancer, DIR was used to estimate the deformation vector field (DVF) between either each breathing phase of the 4D CT or only the exhale/inhale images into a CCS, to generate functional imaging maps [93-96]. These maps were then used to guide the intensity-modulated RT (IMRT) dose planning and spare functional regions, especially for patients who have high-functional lung adjacent to the PTV [97].

2.2.4.1.4 DIR for MRI-based dose calculation

With the development of the MRI-linear accelerator (LINAC), the dose calculation of the MRI appears to be especially crucial [98-102]. Atlas-based approaches have been designed to generate, from a single MRI, a pseudo-CT (*i.e*. a virtual image that mimics CT densities on the MRI anatomy) on which a dose distribution can be calculated. The considered atlas consists of pairs of associated CT and MRI images. The template MRI can be deformed towards the new patient MRI. This deformation can be therefore used to propagate the electronic densities of the template CT on the new patient MRI space, thus providing a pseudo-CT. Studies on prostate [103,104] and H&N [105] have demonstrated that pseudo-CT images exhibit low Hounsfield unit differences compared with ground truth CT images.

2.2.4.2 DIR in IGRT: contour propagation and fraction dose estimation

2.2.4.2.1 DIR for contour propagation

Three-dimensional per-treatment imaging (*e.g.* CT, cone-beam CT (CBCT) or MRI) is routinely employed for tumour positioning under the LINAC. Per-treatment imaging can additionally be exploited, using DIR, to characterise anatomical deformations and their impact on the fraction dose. DIR has thus been proposed to propagate delineations from the planning CT to the per-treatment imaging (Figure 2-4). A DIR transformation is computed between the planning CT and per-treatment image, thus providing a DVF. The DVF is then used to propagate the planning CT delineations to the per-treatment image. An expert must then validate and, if necessary, correct the delineations. For example, in prostate cancer, a non-parametric (cf. section 2.2.3.1) or FFD DIR method has been used to propagate the delineation from the planning CT to the per-treatment images (CT or CBCT) [19,61,106-110]. Compared to rigid registration, DIR improved the accuracy of the organ delineation, achieving an increase of Dice similarity score (DSC) [111] (*cf.* section 2.2.5.2).The largest or complex deformations observed in the bladder and the rectum are, however, not usually fully handled by these DIR methods and, thus, still need manual corrections [109,112]. Specific geometric approaches based on a B-spline interpolated transformation from previously extracted salient points have therefore been developed and improved the registration, achieving over 90% accordance with manual contours [113,114]. In cervical carcinoma, B-spline-based registration with an organ-shape constraint was also applied to propagate the contours from planning to per-treatment MRI. This method resulted in a DSC of approximately 0.85 for the bladder and uterus and, thus, is comparable to expert delineation [115]. Another FFD method, which is constrained with a prior knowledge of the deformations, was employed for inter-patient and multimodal DIR, to generate one MRI atlas [116]. However, large and complex deformations between inter-patient cervix-uterus shapes were also poorly handled by this DIR method, and thus manual correction was required [117]. In image-guided BT, DIR has been used to propagate the high risk-CTV (HR-CTV) and OAR from fraction-to-fraction MRIs, thus showing clinically acceptable dose uncertainties [118]. In H&N cancer, intra-patient DIR has been used to propagate the planning contour to the per-treatment CTs [110,119-121] and CBCTs [122-124]. Still in H&N, when propagating the contours from the pre-treatment MRI to the end of the treatment MRI, DIR provided a contour error around the voxel size (2 mm) and a DSC around 0.8 [125]. In total, DIR was always more accurate than rigid registration, with a mean DSC increase of 0.12-0.15 and better target registration error (TRE) (3 mm on average). In lung cancer and upper-abdominal malignancies, manual tumour delineation on each phase of the 4D CT results in a potential waste of time and inter-observation variability [126]. DIR, by enabling the GTV propagation between the 4D CT phases [127-134], reduced the delineation time by a factor of 2 (from 40 min to 18 min) [127,128]. The propagated GTV delineations were similar than the manual delineations [135], with a reported DSC superior to 0.76, which is similar to the reported intra-physician variation score [127,130]). However, a physician was still needed to check and correct the propagated delineations.

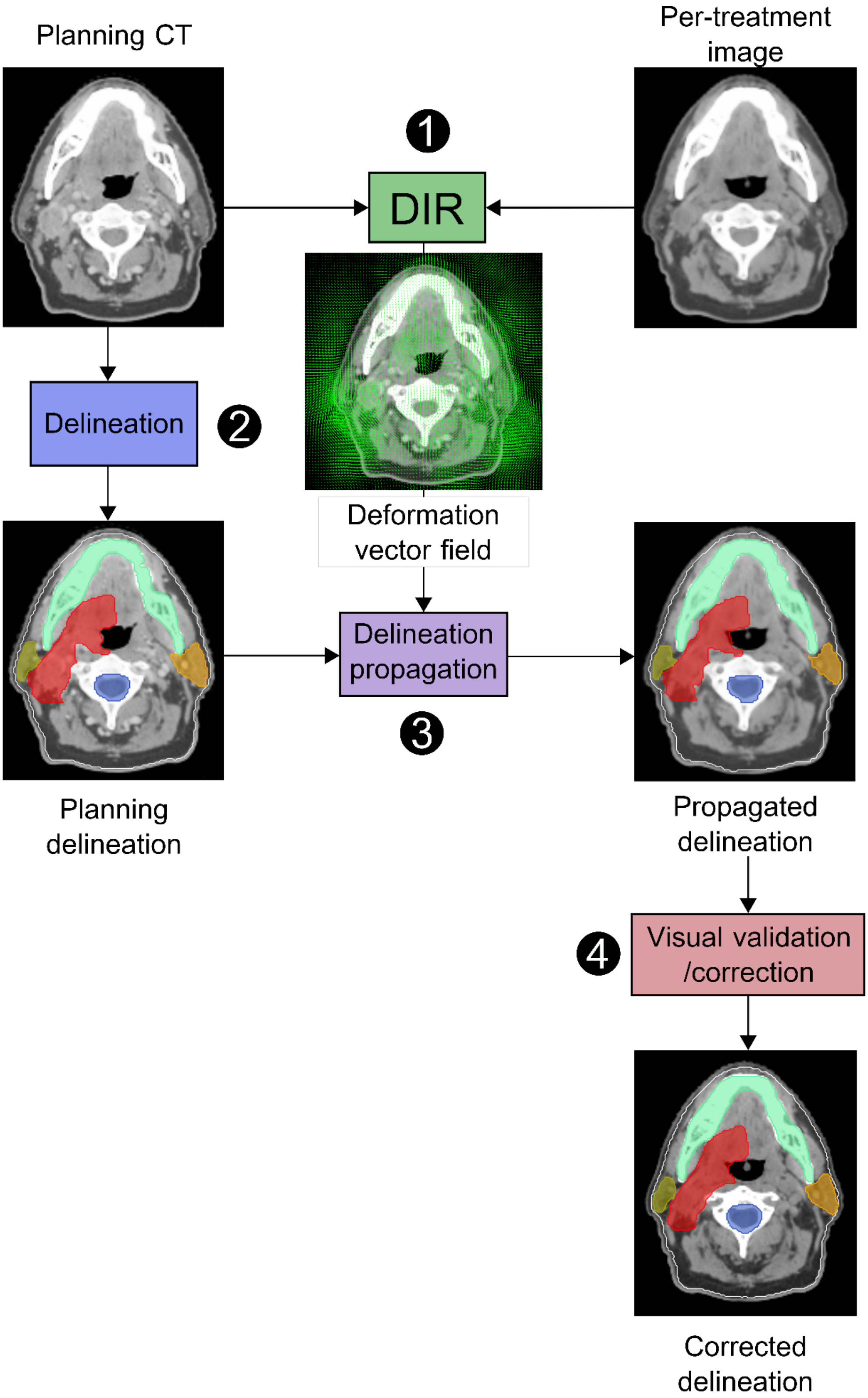

Figure 2-4 : Workflow of delineation propagation from the planning CT to per-treatment image (head-and-neck)

The planning delineations are propagated by means of the deformation vector field estimated by DIR. The propagated delineations are validated by the physician and corrected if needed DIR: Deformable image registration

2.2.4.2.2 DIR for fraction dose calculation

If the planning contours can be effectively propagated to the per-treatment images, the delivered fraction dose could be more difficult to estimate. Indeed, the planned dose distribution might not correspond to the delivered fraction dose distribution due to anatomical variations. In cases that involve large external contour variations and electronic density variations, the dose must be recalculated. When irradiating prostate cancer, the hypothesis of dose invariance (*i.e*. when the dose map remains globally constant between the planning and the fraction) has been validated, except for in the event of large appearance/disappearance of rectal gas or large external contour variations [136,137] (*cf.* section 2.2.2.3). When irradiating locally advanced H&N cancer, due to weight loss and tumour and parotid gland shrinking, dose recalculation is needed. Thus, an image that represents the anatomy of the day with reliable electronic densities is required. DIR has been therefore proposed to propagate the Hounsfield unit from the planning CT to the per-treatment imaging (*e.g*. CBCT or megavoltage CT (MVCT)) (*i.e.* generating a pseudo-CT), which allow to finally calculate the fraction dose distribution [138].

In H&N cancer, several studies have evaluated the accuracy of DIR to generate the pseudo-CT in term of the electronic density difference and dose calculation (*i.e.* dose difference and gamma index) [122,139-143]. The dose uncertainties were small and considered to be “clinically acceptable”. However, CBCT or MVCT proves to be challenging for DIR methods due to their inherent noise, low contrast, and limited field of view (FOV). Thus, preprocessing could be necessary to compute the dose on a corrected/modified CBCT [139,140,144,145] (*cf.* section 2.2.2.1.1).

2.2.4.3 DIR in ART for dose accumulation

2.2.4.3.1 Justification and principle of DIR for fraction doses accumulation

A crucial issue in RT is estimating the cumulated dose over the fractions, either for reporting the delivered dose or for comparison with the planning dose (dose monitoring), to trigger, for example, re-planning. Indeed, in EBRT, the dose-volume histograms (DVH) cannot be simply added when considering deformable structures [146-151]. Local anatomical variations should be accounted for to map the fraction doses to a CCS before summation. DIR has therefore been proposed to perform this mapping (Figure 2-5). With the same approach as contour propagation from planning CT to per-treatment images, the DVF between the planning CT and per-treatment image can be applied to deform the fraction dose toward the planning anatomy. The deformed fraction doses, thus propagated into a CCS, can then be summed. Figure 2-6ab illustrates the difference between the direct addition of the DVH and the use of DIR to accumulate the DVH while using a numerical phantom of the pelvis. This significant difference, thus, emphasises the need for a DIR-based method to accumulate the doses. In BT, the direct addition of the DVHs overestimated the delivered dose compared to a more appropriate DIR approach [22,152-156].

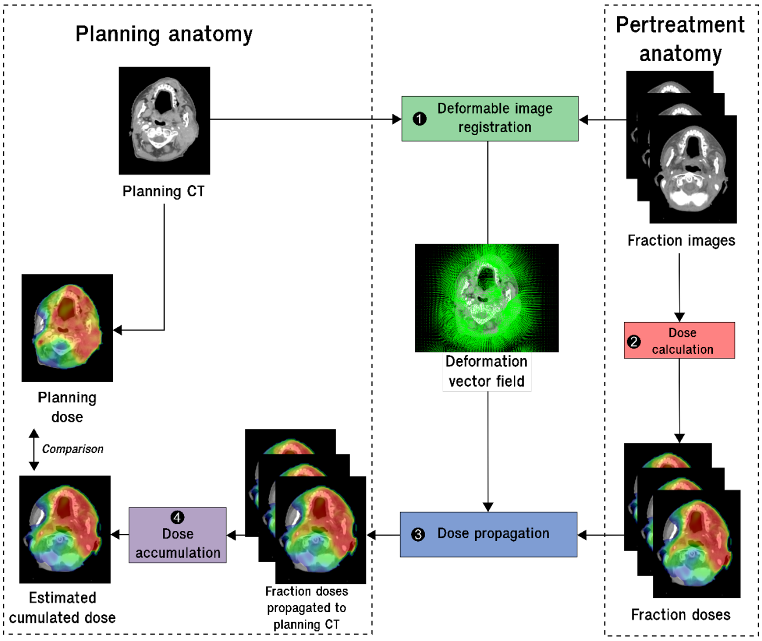

Figure 2-5 : Workflow of cumulated dose estimation by deformable image registration

Step 1: A deformable image registration is computed between the per-treatment images and the planning CT image. Step 2: The fraction doses are calculated from the per-treatment images with the same treatment parameters as the planning. Step 3: the fraction dose distributions are propagated to the planning CT by means of the resulting deformation vector fields. Step 4: The propagated dose distributions are summed to compute the cumulated dose on the planning CT. The planned dose can be compared to the estimated cumulated dose

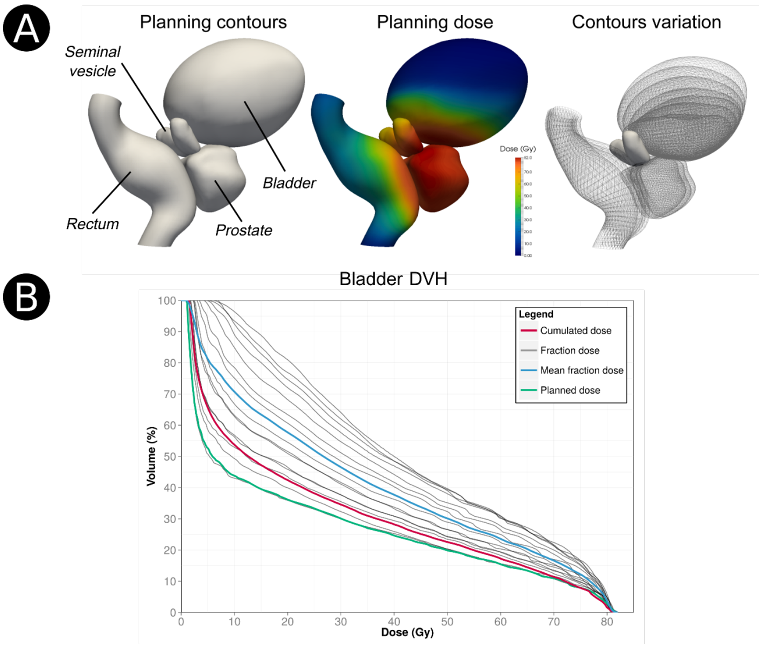

Figure 2-6 : Cumulated DVH should not be estimated as the mean fraction DVH

A pelvic numerical phantom [157] was designed (A) to compare dose accumulation using ground truth accumulated dose (in red) and DVH averaging (in blue) in the bladder for prostate cancer irradiation. The fraction dose DVHs are in grey (normalized to the total dose). The ground truth accumulated dose was obtained by propagating the fraction doses to the planning using the reference DVF resulting from biomechanical laws (*cf.* section 2.2.3.4). The cumulated dose appears superior to the planned dose. The mean fraction dose overestimates the dose received by the bladder. DVH: Dose volume histogram

After the DVF estimation, two approaches can be considered to propagate the dose according to the DVF. The first is to linearly interpolate the dose on the spatial grid of the fixed image, which carries the drawback of not considering the physical properties of the tissues in terms of the dose absorption [158]. The second approach consists of considering the tissue density when recalculating the deformed dose. Moreover, dose propagation methods should follow the principle of energy conservation [159]. Monte Carlo-based dose propagation has proven to be efficient for regions that have heterogeneous electronic densities (*e.g.* the lungs) [160,161], while linear interpolation-based dose propagation can be used for homogeneous regions (*e.g.* the pelvis).

2.2.4.3.2 Clinical applications of DIR for fraction doses accumulation in EBRT, BT and re-irradiation

DIR enables to accumulate the doses during EBRT and/or BT and, in case of re-irradiation, in a large number of tumour localisations. In prostate cancer, due to OAR deformations, differences between the planning and cumulated dose have been quantified [162-164]. The mean dose difference has been reported to be 7 Gy for the bladder and 2 Gy for the rectum [162]. The use of DIR has also allowed to quantify the rectal dose decrease when using a rectal balloon (70% of patients showed a decrease of more than 5% in the normal tissue complication probability, NTCP) [163]. Moreover, DIR can be used to accumulate the rectal dose of EBRT and high dose rate (HDR)-BT [165]. This dose was found to be superior when using DIR, compared to the direct addition of the DVH. In bladder cancer, DIR has been used to accumulate the treatment dose on the planning anatomy and, therefore, to compare several ART strategies [166]. In cervical cancer, the use of DIR to accumulate the EBRT doses did not show large differences compared to the planned dose for the target, although, large dose differences have been observed for the OARs [167-169]. In HDR-BT, DIR can also be useful to accumulate the fraction doses due to the large deformations as a result of organs filling and intracavity applicator insertion [24,152,170-172]. Moreover, DIR has been used to deform the EBRT planning CT anatomy towards the planning CT/MRI anatomy at the time of BT [173], which allows to estimate the cumulated received dose to the rectum and bladder [156,174]. However, uncertainties on this dose accumulation are linked to the DIR accuracy and the EBRT technique (*i.e.* steep dose gradient) [22,175,176]. The clinical benefit of DIR in this context, therefore, must be evaluated [155]. In H&N cancer, weight loss along with tumour and parotid gland shrinking during treatment can lead to large differences between planned and delivered doses. DIR methods estimated a mean overdose that exceeds 3 Gy for at least 30% (up to 60%) of parotid glands [64,177-181]. In lung cancer, due to breathing, the accumulated dose can first be quantified for each individual fraction. Using biomechanical model-based DIR on planning 4D CT and per-treatment 4D CBCT of 10 breathing phases, the average dose difference between the accumulated and planned dose of dmin (minimum dose to 0.5 cm^3 of the tumour) was quantified as 0.8 Gy and superior to 2 Gy for 3/10 patients [57]. Other studies in lung cancer have investigated the dose accumulation, which showed large variations to the OARs [182] and none to the target [135].

Finally, DIR has been used in the case of re-irradiation to propagate the dose of the first planning to the re-irradiation planning, such as in H&N, brain, liver, mediastinum and lung cancer [146,148,183]. DIR appears, therefore, especially helpful for guiding the radiation oncologist in irradiating the recurrence, while avoiding increased toxicity. However, the use of DIR in this situation appears challenging due to the large anatomical difference, especially when related to matter (dis)appearance between the two treatments.

2.2.4.4 DIR for toxicity prediction via voxel-wise population analysis

DIR can also be applied to investigate the local relationships between the dose and the side-effects by analysing the dose at finer scales via voxel-wise population analysis, thus revealing local differences across individuals. These methods are inspired from the voxel-based morphometry (VBM) [184]. In its standard form, VBM assesses the differences between groups at each voxel and relates them to different covariates (*e.g.* age, gender, diagnosis, cognitive scores). As mentioned before, the studies that were undertaken in toxicity studies have allowed the identification of more predictive subregions within the organs [185-188]. The dose mapping to a CCS remains a central question and can be obtained via a parametric representation of the anatomy in a spherical coordinate system, as in [185,189], or can be more precisely computed through tailored DIR, as proposed in [18]. Voxel-based methods require, however, different steps, as shown in Figure 2-7: (i) the mapping of a population of individuals in terms of their anatomy by DIR onto an anatomical template (steps 1, 2); (ii) the propagation of dose distributions according to the obtained DVFs (step 3); (iii) a local statistical analysis of the dose-effect relationship (step 4) that allows to finally identify anatomical subregions that are at high risk of toxicity.

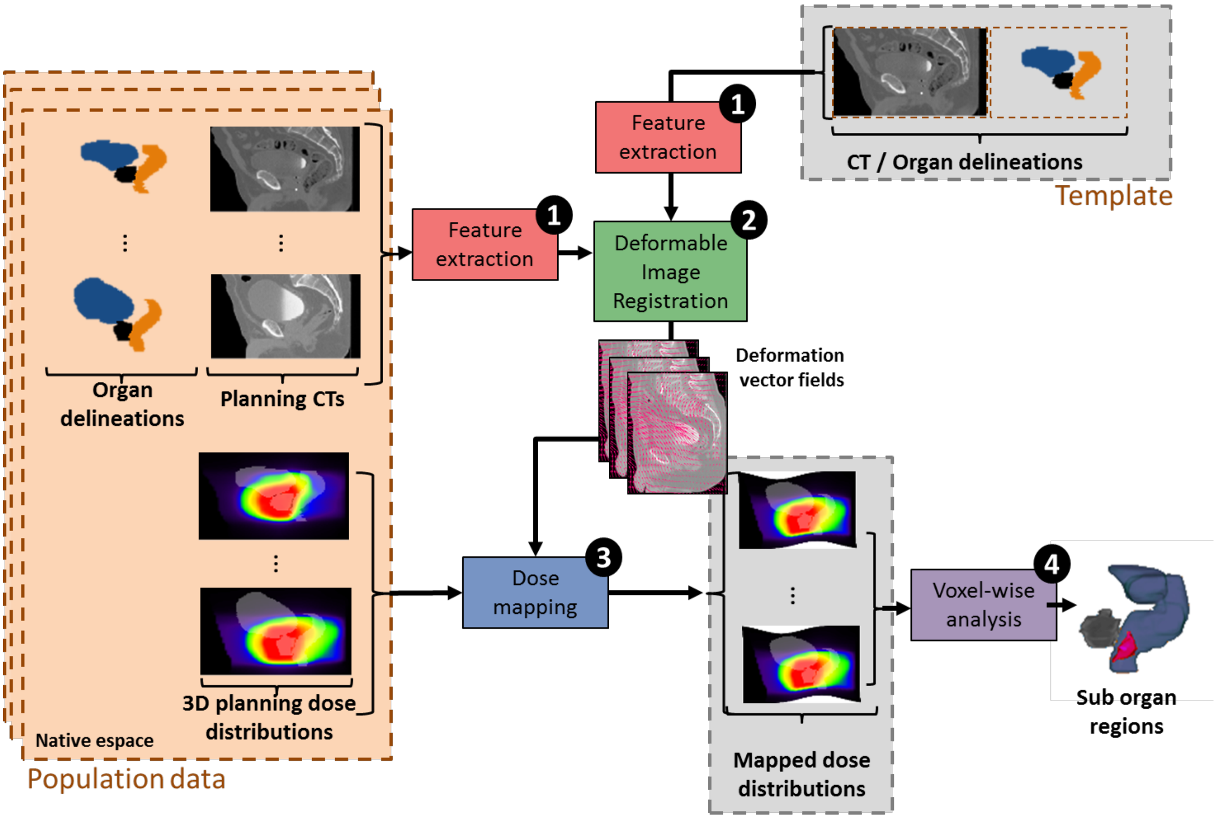

Figure 2-7 : Workflow of voxel-based analysis, using deformable image registration, for patient toxicity prediction

Step 1: Feature extraction is done on the population data and anatomical template (*i.e.* preprocessing); Step 2: A DIR method is used to compute the inter-individual deformation vector fields (DVF). Step 3: The resulting DVFs are used to propagate the 3D planning dose distributions of the population on the anatomical template coordinate system; Step 4: A local statistical analysis of dose-effect relationship is performed

In prostate cancer IMRT, DIR allows to identify the antero-inferior part of the anorectum as highly predictive of rectal bleeding [186,187]. This subregion was found to receive a significantly higher dose (up to 6.8 Gy) for patients with toxicity symptoms compared to non-toxic patients. In H&N cancer, an inter-patient DIR was also used to compare the local dose of patients with or without acute disphagya. Two subregions (cricopharyngeus muscle and cervical oesophagus) were found with a significant difference in terms of the received dose (superior to 10 Gy) [190]. Finally, in lung cancer, DIR was used to perform voxel-by-voxel analysis to assess the relationship between a local received dose and lung injury [191]. For each patient, a probability model was developed to represent the risk of severe lung injury by the received dose. Moreover, the peripheral medial-basal portion of the lungs was found to receive a higher mean dose for the patients with lung damage [192].

In total, the identified anatomical subregions can be used for patient toxicity prediction and/or specific OAR definition, and must be particularly spared at the time of planning to decrease the toxicity.

2.2.4.5 Uncertainties and perspectives of DIR in RT

DIR is validated in routine treatment for delineation at the planning and per-treatment contour propagation [1]. Its accuracy appears to be similar to the inter-observer variability in prostate and H&N localisation [110,193]. However, due to the limited number of dosimetric studies and the absence of published clinical studies, the use of DIR for dose accumulation is still under evaluation and cannot be used directly in clinical practice [64,194]. Indeed, the use of DIR for dose accumulation is subject to uncertainties that are linked to multiple parameters, such as the DIR algorithm's performance (*cf.* section 2.2.3), the lack of contrast between images, the conservation of mass, the tissue sliding and the dose mapping method (linear interpolation or Monte-Carlo). DIR algorithm performances have been compared to achieve dose accumulation in several anatomical localisations [119,149,180,195-199]. If volume of interest based metrics (*cf.* section 2.2.5.2) can testify to the dose accumulation uncertainties [197,199], the dose mapping error, however, is still hardly quantifiable [198].

In total, to improve the DIR accuracy, a number of commercial software now provide the ability to drive the DVF using contours [18,62] or corresponding points [200]. For this purpose, specific tools, developed in academic institutions, are imported to commercial RT TPS [62,201]. DIR algorithms are, therefore, still under development to better meet clinical needs, with improvements such as accounting for the different imaging modalities between the planning and treatment delivery [30,195], the need for near-real time algorithms with graphic processing unit (GPU)-based frameworks [62,202-205], and the anatomical properties simulated by finite element models [206-209]. Finally, in the context of MRI-LINAC, DIR allows the propagation of the tumour contour from the planning MRI to the per-treatment 2D cine MRI [210,211], which could be used for gating the treatment beam.

2.2.5 DIR EVALUATION

The clinical application of DIR requires precise quantification of the uncertainties related to the DIR algorithms. Several complementary DIR evaluation methods have been published in the literature.

2.2.5.1 Visual evaluation

The most natural way to evaluate DIR performance is to visually compare the reference and deformed images. Multiple visualisation methods exist, and they are usually based on fusing the reference with the deformed images (*cf*. Figure 2-8a). For example, checkerboards enable verification of the contour alignment. In addition, the overlay of one image on another with a coloured transparency effect enables showing the salient information in each image, while evaluating the alignment. When considering image registration using the same modality, absolute image intensity differences reveal the areas that have large intensity differences, which are thus sources of potential misregistration. In addition, visualising the DVF, overlapped on the images as a 2D vector or a deformed grid, can help to detect local irregularities (*i.e.* vector/grid folding) [212]. Modern tools tend to integrate and render these visual information into a single framework to ease the DIR evaluation [213].

While all of these evaluation methods are simple and qualitative, they suffer from not being able to quantify the uncertainties and detecting small uncertainties (*e.g.* below 2 mm) [214].

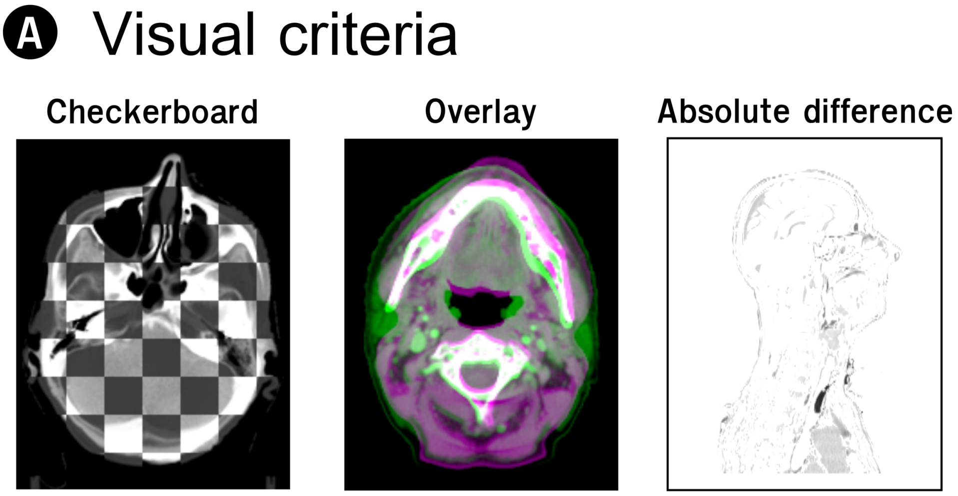

Figure 2-8 : (A) Visual inspection between the fixed and deformed images can be performed using a checkerboard, overlay, and absolute difference

2.2.5.2 Segmentation comparison

A standard quantitative evaluation method is based on a comparison between the reference contours, which is usually delineated by experts, and the propagated (*i.e.* deformed) contours. For each considered organ, the contour of the moving image is propagated using the estimated DVF, and then, it is compared to the fixed image reference contour. This comparison is performed using either overlap-based or surface distance-based scores. Figure 2-9b illustrates the most classic scores. The DSC [111] is the most commonly used score in the literature, followed by the Jaccard index [215] and the overlap coefficient [216], with all three considering the relationship between the union and the intersection of the two delineations. These scores range from a value of zero, which corresponds to no overlap and thus is a poor registration result, to one, which corresponds to a perfect overlap and thus a good result. These values could prove difficult to interpret given that they are dependent on the organ volumes (*e.g.* the DSC must be higher for larger volumes such as for the lung compared to a smaller volume such as for the prostate).

The Hausdorff distance measures the maximum Euclidean distance between two contours, which is defined by considering, for each point of one delineation's surface, the closest point on the second delineation's surface [217]. The mean distance to agreement (DTA) corresponds to the mean of the distances between the points of one structure to another [218].

The drawbacks of these delineation-based scores are as follows: rotation errors between structures are hardly quantifiable, and the size of the evaluated delineations could exert a significant influence. When manual delineations are performed, intra- and inter-observer variability should be accounted for [79,107,219,220]. Surface-based scores, compared to volume-based scores, were shown to better assess the local uncertainties, but not enough to be able to quantify the DIR accuracy [221]. Moreover, a surface representation could be more accurate since it does not rely on the underlying image resolution, especially for small segmentations [222,223]. Last, given that they are based on a global matching between two regions, these delineation-based scores do not characterise the local DVF accuracy. Therefore, they do work when used for delineation propagation, but not in applications where the local accuracy is required, such as dose monitoring.

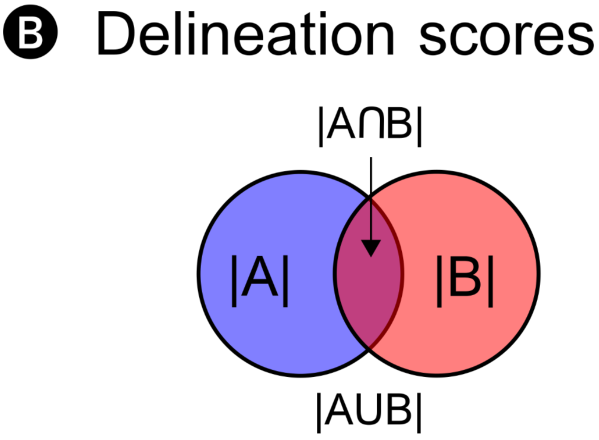

$$\boldsymbol{DSC} = 2\times\frac{|\boldsymbol{A} \cap \boldsymbol{B}|}{|\boldsymbol{A}| + |\boldsymbol{B}|}$$

$$\boldsymbol{JACCARD} = 2\times\frac{|\boldsymbol{A} \cap \boldsymbol{B}|}{|\boldsymbol{A}| \cup |\boldsymbol{B}|}$$

$$\boldsymbol{OVERLAP} = \frac{|\boldsymbol{A} \cap \boldsymbol{B}|}{\min\,(|\boldsymbol{A}|, |\boldsymbol{B}|)}$$

$$\boldsymbol{HD} = \max\{\boldsymbol{d}(\boldsymbol{A},\boldsymbol{B}), \boldsymbol{d}(\boldsymbol{B},\boldsymbol{A})\}$$

$$\boldsymbol{where:}\ \boldsymbol{d}(\boldsymbol{X},\boldsymbol{Y}) = \max_{\boldsymbol{x}\in \boldsymbol{X}}(\min_{\boldsymbol{y}\in \boldsymbol{Y}}\|\boldsymbol{x}-\boldsymbol{y}\|)$$

Figure 2-9 : (B) The fixed image delineations and the deformed image delineations can be compared using similarity coefficient (*e.g.* DSC). |X| denotes the volume of the region X

2.2.5.3 Point-to-point error

The point-to-point error measures the distance between a point that is propagated by the DVF and a ground truth point. Landmarks are either placed manually in the images by an expert or implanted (gold markers) to provide information on the "true" displacement, thus enabling the TRE to be measured (*cf.* Figure 2-10c) [224,225]. Manually or automatically determined landmarks have previously been used, such as the centre of mass of the parotid glands for H&N, gold markers for prostate, and the top of the uterus and midline of the bladder in cervical cancer [226]. For example, in H&N, 14 landmarks have been used to evaluate the accuracy of 10 DIR methods. The TRE of inter-individual variability appeared to be similar to the DIR performance [119,227]. For the parotid gland, the mean error was approximately 2 mm [119]. Nevertheless, using landmarks has demonstrated that DIR cannot be used for tumours due to their complex deformations and matter disappearance [228,229].

Although evaluation methods based on manual landmarks enable a local evaluation of the DVF, they rely on the ability to identify landmarks in the images. This process could prove to be very time-consuming [230] and challenging owing to the poor contrast in soft tissues, homogeneous intensity regions, artefacts, or poor image resolution. More sophisticated approaches based on feature extraction (*cf.* section 2.2.3.3) can extract a large number of landmarks with the aim of reducing both the uncertainties and workload [231,232].

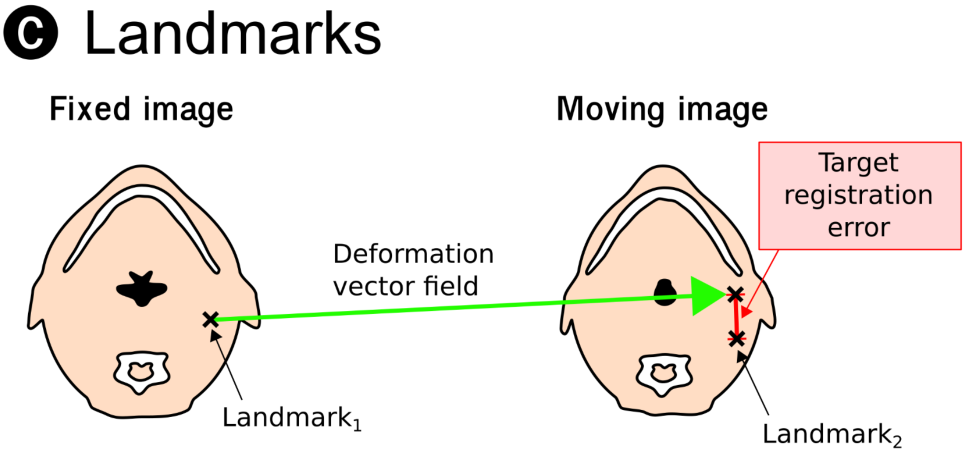

Figure 2-10 : (C) Manually placed landmarks can also be used to provide point-to-point accuracy. The distance between the landmark and the point propagated by the DVF is used as the metric (TRE)

2.2.5.4 Deformation vector field (DVF) evaluation

The DVF analysis allows us to characterise the local or global behaviour of the deformation. For example, the DVF consistency can thus be measured by comparing the results of two deformations that have different paths. Indeed, the DIR methods do not, at all times, ensure inverse consistency, *i.e.* the results differ according to the order in which the images are registered. This metric is termed as the inverse consistency error (ICE) or transitivity error (TE) when there are two or more considered images, respectively [233-236]. The ICE and TE are defined as the Euclidean distance between the points mapped by the forward and reverse transformations. Figure 2-11d represents the transitivity, which is illustrated by a registration of an image “1” toward an image “2”, and then “3”, which should be equivalent to the registration of the image “1” toward the image “3”. Following a similar idea, the distance discordance metric (DDM) measures the backward distances of the distributed voxels from multiple registered images to a single fixed image [237,238]. This metric allows to quantify the local uncertainties/variability of DIR based on at least four observations.

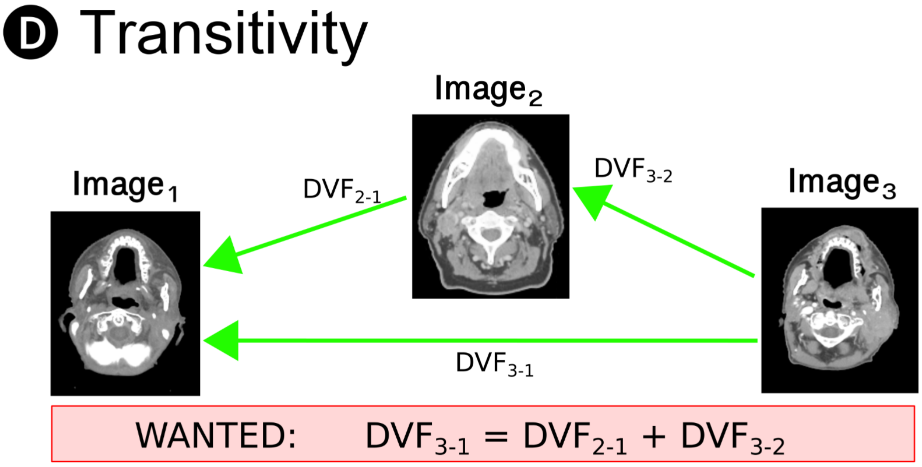

Figure 2-11 : (D) Transitivity of the DIR method can be evaluated by comparing the DVF generated by different paths

Another measurement method is based on the Jacobian matrix, which is computed from the DVF of the neighbourhood of any given point. The determinant of this matrix testifies to the voxel-wise volumetric change according to the DVF. A Jacobian determinant with a value superior to one represents a volume expansion and inferior to one represents compression. A Jacobian determinant with a value below or equal to zero corresponds to self-folding that results from the crossing of the vectors of the DVF, primarily due to poor regularisation of the DVF. This circumstance implies that the fixed image would not be recovered by the inverse transformation [239]. Figure 2-12e represents a schematic vision of the Jacobian determinant in the context of vector crossing.

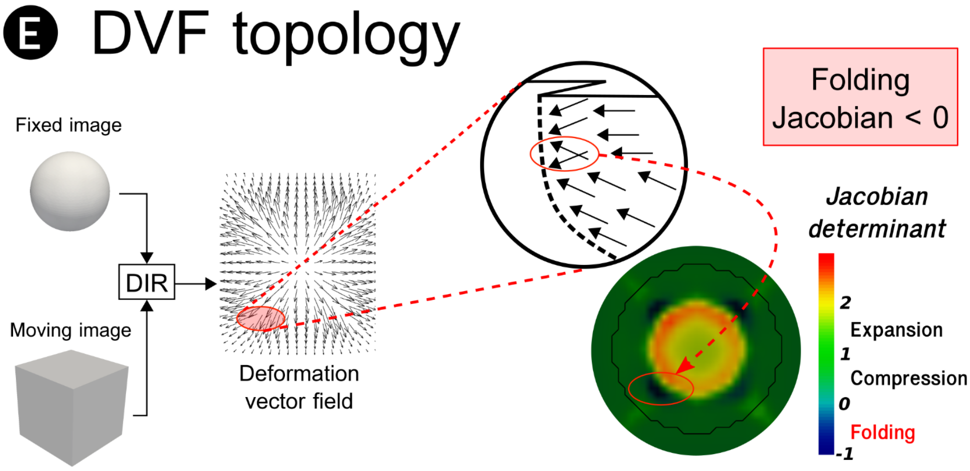

Figure 2-12 : (E) DVF topology analysis (*e.g.* using Jacobian determinant) enables crossed vectors, highly non-linear regions, and discontinuity to be detected. Considering the Jacobian values, the dark blue spot (Jacobian determinant <0) is the region where folding occurs due to crossed vectors

The harmonic energy measures the local DVF deviation based on an affine transformation, with its value inversely related to the DVF smoothness [240]. Similarly, another proposed method measures the unbalanced energy produced by the DVF at each node of an organ mesh by considering the material heterogeneity in terms of the elasticity (*i.e*. Young modulus, *cf*. section 2.2.3.4) [241,242]. A value is then assigned to each node and each corresponding voxel of the image, which represents the error induced by the DVF in terms of the precision and energy preservation.

In total, the evaluation of the local DVF behaviour enables detecting irregularities that can lessen the deformed image quality. Such metrics have been measured for dose warping; they reveal ambiguity to assess the accumulated dose [236] and should be used to validate DIR for this purpose [243]. While interpreting the results proves to be often complex, this characterisation does not testify to the local accuracy of the DIR method.

2.2.5.5 Physical and numerical phantoms

The previous evaluation criteria have the main limitation that they are not based on a reference DVF, and thereby, they focus the evaluation on some restricted criteria (global matching of specific regions, local matching of some specific points, specific characteristics of the DVF). On the other hand, phantoms can be used to represent an anatomy with known deformations. These ground-truth deformations can be employed for comparison with the deformations estimated by a DIR algorithm (*cf*. Figure 2-13f). Two types of deformable phantoms are currently available: physical and numerical phantoms.

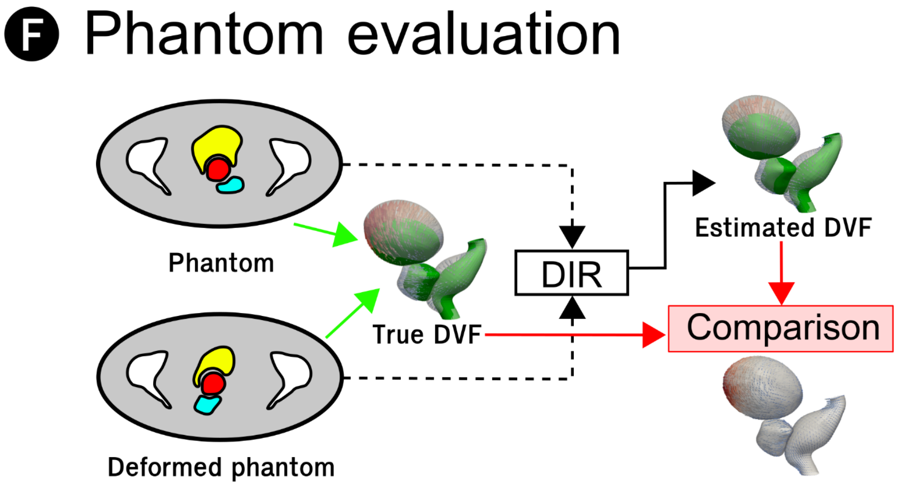

Figure 2-13 : (F) DIR DVF can be compared to ground truth DVF generated by phantoms

Physical deformable phantoms are real phantoms that are scanned before and after deformation. Their aim is to represent different shapes, either mimicking human organs or not. Basic shapes can be simulated by using balloons, sponges [244,245], porcine bladders [246,247], or deformable gels [248,249], 3D printed or not [175,250]. More complex shapes can be represented by combining different materials to represent an anthropomorphic phantom in which each material provides a particular X-ray attenuation [244,250-253]. The flexibility of the materials combined with a physical constraint (*e.g.* the insertion of a balloon) allows for the phantom to be deformed [251]. The ground-truth deformations are usually measured using radiopaque [247,250,254] or nonradiopaque markers visible by optical camera [251-253,255]. A cadaver has also been employed to simulate different anatomical deformations [256]. Last, while enriching the phantom setup with radiosensitive gels [248,249] or diodes [251], dose monitoring applications can be evaluated in terms of dosimetric accuracy [250,257,258]. Such phantoms are especially useful for "end-to-end" tests.

On the other hand, numerical phantoms rely on the design of numerical objects and the simulation of their deformation (*cf*. Figure 2-6a). The geometry of the phantom is based on the images or set of delineations from a real patient or on typical geometry. It is deformed, either manually, based on biomechanical laws [157,162,245,259], or using a model of deformations (*e.g.* cardiac or respiratory movements) [260], providing the reference DVF. Finally, the corresponding images must be simulated. Once the whole workflow has been implemented, an infinite number of configurations can be simulated with respect to realistic behaviour.

In both cases, whereas physical or numerical phantoms are powerful tools, they are still difficult to build and limited when complex human shapes, realistic clinical behaviour (*e.g.* treatment response), and tissue heterogeneity must be represented [253]. Many steps of physical or numerical phantom generation can indeed be challenging. For physical phantoms, the quality of the phantom images and the nature of the deformations are limited by the choice of materials. For numerical phantoms, the choice of the biomechanical properties of each organ could prove to be challenging and time-consuming. Phantoms can, however, provide information on selecting the most adequate algorithm depending on the clinical site [261]. Numerical phantoms are especially appropriate for evaluating DIR due to their possibility of simulating anthropomorphic geometries, having potential high complexity of the simulated deformations, and having the ability to control the resulting image quality (noise, artefact) [1]. Moreover, they can easily be shared among clinical centres. For example, the IMSIMQA™ (OSL, UK) software provides a library of numerical phantoms that have configurable deformations [262,263]. Open-source phantom libraries are also available online [264-266], which facilitates the evaluation of commercial or homemade DIR algorithms [59,267,268].

2.2.5.6 Issues in the choice of the DIR evaluation method

While there is an increasing number of publications that compare the performance of different DIR methods (commercial or homemade) for RT applications [119,180,263,269-276], one of the main challenges that faces DIR evaluation is its adaptation to each considered application. For example, dose monitoring requires low point-to-point error, whereas delineation propagation often requires only good correspondence between the organ boundaries. Moreover, DIR evaluation for dose monitoring must include dosimetric indices, since any given geometric error could cause different dosimetric errors depending on the dose gradient (high dosimetric errors in cases of high-dose gradients) [58]. A perfect point-to-point matching is likely an unreachable goal considering the material, such as the voxel size, artefacts, and realistic deformation constraints. Due to the large number of DIR methods, standard evaluation criteria must be defined and generalised [263,277]. The development of numerical phantoms is a first step in this direction to compare and validate DIR methods, in particular for dose accumulation. Moreover, challenge datasets are available online to evaluate and compare various homemade DIR methods [264-266,278,279]. More advanced techniques, such as neural networks, could also be used for the quantification of DIR performance [280]. However, a number of particular situations will always defeat the DIR methods. Thus, even after a thorough evaluation study, each individual registration should be evaluated. For this purpose, while DVF analysis can be used as a first step, it should be followed, ultimately, by visual evaluation.

2.2.6 CONCLUSION

Although great progress has been accomplished in the development of DIR in RT, it still must gain in maturity to enable its exploitation in the clinical workflow. DIR in RT is complex, in terms of both methods and applications. As recently recommended by the AAPM TG132 [1], DIR can be used at the planning stage and during IGRT for autosegmentation and multimodality fusion to reduce the delineation workload, especially given the increasing number of images generated for each patient. Using DIR for assessing the accumulated dose could be the answer to a so far unmet clinical need, namely, the need to estimate the potential deviation from the planned dose. It also enables a comparison of different RT strategies, mainly ART, in terms of the delivered dose. Nevertheless, DIR must be used with caution since this more complex application implies high local accuracy. Indeed, DIR evaluation must consider both geometrical and dosimetric metrics, which thus requires sophisticated dedicated tools, such as numerical phantoms. Moreover, a consensus on the evaluation method and criteria is first needed to assess its potential contribution in the clinical workflow. However, given that each considered situation is unique (patient anatomy, image noise, and so on), the evaluation must also be performed at an individual scale.

2.2.7 REFERENCES

1. Brock KK, Mutic S, McNutt TR, Li H, Kessler ML. Use of image registration and fusion algorithms and techniques in radiotherapy: Report of the aapm radiation therapy committee task group no. 132. *Medical Physics* 2017.
2. de Crevoisier R, Tucker SL, Dong L, Mohan R, Cheung R, Cox JD, Kuban DA. Increased risk of biochemical and local failure in patients with distended rectum on the planning ct for prostate cancer radiotherapy. *International Journal of Radiation Oncology• Biology• Physics* 2005;62:965-973.
3. Guckenberger M, Pohl F, Baier K, Meyer J, Vordermark D, Flentje M. Adverse effect of a distended rectum in intensity-modulated radiotherapy (imrt) treatment planning of prostate cancer. *Radiotherapy and oncology* 2006;79:59-64.
4. Pluim JP, Fitzpatrick JM. Image registration. *Medical Imaging, IEEE Transactions on* 2003;22:1341-1343.
5. Sotiras A, Davatzikos C, Paragios N. Deformable medical image registration: A survey. *Medical Imaging, IEEE Transactions on* 2013;32:1153-1190.
6. Maintz JA, Viergever MA. A survey of medical image registration. *Medical image analysis* 1998;2:1-36.
7. Brock KK. Image processing in radiation therapy: CRC Press; 2013.
8. Klein S, Staring M, Murphy K, Viergever MA, Pluim JP. Elastix: A toolbox for intensity-based medical image registration. *Medical Imaging, IEEE Transactions on* 2010;29:196-205.
9. Ibanez L, Schroeder W, Ng L, Cates J. The itk software guide 2003.
10. Pluim JP, Maintz JA, Viergever MA. Image registration by maximization of combined mutual information and gradient information. Medical Image Computing and Computer-Assisted Intervention–MICCAI 2000. Springer. 2000. pp. 452-461.
11. Wein W, Brunke S, Khamene A, Callstrom MR, Navab N. Automatic ct-ultrasound registration for diagnostic imaging and image-guided intervention. *Medical image analysis* 2008;12:577-585.
12. Dréan G, Acosta O, Simon A, De Crevoisier R, Haigron P. Inter-individual organ-driven ct registration for dose mapping in prostate cancer radiotherapy. Biomedical Imaging (ISBI), 2012 9th IEEE International Symposium on. IEEE. 2012. pp. 370-373.
13. Reaungamornrat S, Liu W, Wang A, Otake Y, Nithiananthan S, Uneri A, Schafer S, Tryggestad E, Richmon J, Sorger J. Deformable image registration for cone-beam ct guided transoral robotic base-of-tongue surgery. *Physics in medicine and biology* 2013;58:4951.
14. Danielsson P-E. Euclidean distance mapping. *Computer Graphics and image processing* 1980;14:227-248.
15. Maurer CR, Qi R, Raghavan V. A linear time algorithm for computing exact euclidean distance transforms of binary images in arbitrary dimensions. *IEEE Transactions on Pattern Analysis and Machine Intelligence* 2003;25:265-270.
16. Dréan G, Acosta O, Ospina J, Voisin C, Rigaud B, Simon A, Haigron P, de Crevoisier R. How to identify rectal sub-regions likely involved in rectal bleeding in prostate cancer radiotherapy. IX International Seminar on Medical Information Processing and Analysis. International Society for Optics and Photonics. 2013. pp. 89220L-89220L-89229.
17. Jones SE, Buchbinder BR, Aharon I. Three-dimensional mapping of cortical thickness using laplace's equation. *Human brain mapping* 2000;11:12-32.
18. Drean G, Acosta O, Lafond C, Simon A, de Crevoisier R, Haigron P. Interindividual registration and dose mapping for voxelwise population analysis of rectal toxicity in prostate cancer radiotherapy. *Med Phys* 2016;43:2721-2730.
19. Gao S, Zhang L, Wang H, de Crevoisier R, Kuban DD, Mohan R, Dong L. A deformable image registration method to handle distended rectums in prostate cancer radiotherapy. *Medical physics* 2006;33:3304-3312.

20. Foskey M, Davis B, Goyal L, Chang S, Chaney E, Strehl N, Tomei S, Rosenman J, Joshi S. Large deformation three-dimensional image registration in image-guided radiation therapy. *Physics in Medicine and Biology* 2005;50:5869.
21. Yang D, Chaudhari SR, Goddu SM, Pratt D, Khullar D, Deasy JO, El Naqa I. Deformable registration of abdominal kilovoltage treatment planning ct and tomotherapy daily megavoltage ct for treatment adaptation. *Medical physics* 2009;36:329-338.
22. Teo B-K, Millar LPB, Ding X, Lin LL. Assessment of cumulative external beam and intracavitary brachytherapy organ doses in gynecologic cancers using deformable dose summation. *Radiotherapy and Oncology* 2015;115:195-202.
23. Davis B, Foskey M, Rosenman J, Goyal L, Chang S, Joshi S. Automatic segmentation of intra-treatment ct images for adaptive radiation therapy of the prostate. *Medical Image Computing and Computer-Assisted Intervention–MICCAI 2005* 2005:442-450.
24. Zhen X, Chen H, Yan H, Zhou L, Mell LK, Yashar CM, Jiang S, Jia X, Gu X, Cervino L. A segmentation and point-matching enhanced efficient deformable image registration method for dose accumulation between hdr ct images. *Physics in Medicine & Biology* 2015;60:2981.
25. Pennec X, Cachier P, Ayache N. Understanding the “demon’s algorithm”: 3d non-rigid registration by gradient descent. Medical Image Computing and Computer-Assisted Intervention–MICCAI’99. Springer. 1999. pp. 597-605.
26. Svedlow M, McGillem CD, Anuta PE. Image registration: Similarity measure and preprocessing method comparisons. *IEEE Transactions on Aerospace and Electronic Systems* 1978:141-150.
27. Wells WM, Viola P, Atsumi H, Nakajima S, Kikinis R. Multi-modal volume registration by maximization of mutual information. *Medical image analysis* 1996;1:35-51.
28. Klein S, Staring M, Pluim JP. Evaluation of optimization methods for nonrigid medical image registration using mutual information and b-splines. *IEEE Transactions on Image Processing* 2007;16:2879-2890.
29. Zhen X, Yan H, Zhou L, Jia X, Jiang SB. Deformable image registration of ct and truncated cone-beam ct for adaptive radiation therapy. *Physics in Medicine & Biology* 2013;58:7979.
30. Cazoulat G, Simon A, Dumenil A, Gnep K, De Crevoisier R, Acosta O, Haigron P. Surface-constrained nonrigid registration for dose monitoring in prostate cancer radiotherapy. *IEEE Transactions on Medical Imaging* 2014;33:1464-1474.
31. Al-Mayah A, Moseley J, Velec M, Hunter S, Brock K. Deformable image registration of heterogeneous human lung incorporating the bronchial tree. *Medical physics* 2010;37:4560-4571.
32. Staring M, Klein S, Pluim JP. A rigidity penalty term for nonrigid registration. *Medical physics* 2007;34:4098-4108.
33. Delmon V, Rit S, Pinho R, Sarrut D. Registration of sliding objects using direction dependent b-splines decompositionthis work was presented in part at the 4th international workshop on pulmonary image analysis during the medical image computing and computer assisted intervention (miccai) in toronto, canada (2011). *Physics in medicine and biology* 2013;58:1303.
34. Papież BW, Heinrich MP, Fehrenbach J, Risser L, Schnabel JA. An implicit sliding-motion preserving regularisation via bilateral filtering for deformable image registration. *Medical image analysis* 2014;18:1299-1311.
35. Vandemeulebroucke J, Bernard O, Kybic J, Clarysse P, Sarrut D. Automatic motion mask extraction for deformable registration of the lungs. XVIth International Conference on the Use of Computers in Radiation Therapy, Amsterdam. 2010.
36. Wu Z, Rietzel E, Boldea V, Sarrut D, Sharp GC. Evaluation of deformable registration of patient lung 4dct with subanatomical region segmentations. *Medical physics* 2008;35:775-781.
37. Schmidt-Richberg A, Ehrhardt J, Werner R, Handels H. Slipping objects in image registration: Improved motion field estimation with direction-dependent regularization. International Conference on Medical Image Computing and Computer-Assisted Intervention. Springer. 2009. pp. 755-762.

38. Heinrich MP, Jenkinson M, Brady M, Schnabel J. Discontinuity preserving regularisation for variational optical-flow registration using the modified lp norm. *Medical Image Analysis for the Clinic: A Grand Challenge* 2010:185-194.
39. Vásquez Osorio EM, Kolkman-Deurloo IKK, Schuring-Pereira M, Zolnay A, Heijmen BJ, Hoogeman MS. Improving anatomical mapping of complexly deformed anatomy for external beam radiotherapy and brachytherapy dose accumulation in cervical cancer. *Medical physics* 2015;42:206-220.
40. Thirion J-P. Image matching as a diffusion process: An analogy with maxwell's demons. *Medical image analysis* 1998;2:243-260.
41. Nithiananthan S, Schafer S, Uneri A, Mirota DJ, Stayman JW, Zbijewski W, Brock KK, Daly MJ, Chan H, Irish JC. Demons deformable registration of ct and cone-beam ct using an iterative intensity matching approach. *Medical physics* 2011;38:1785-1798.
42. Zhen X, Gu X, Yan H, Zhou L, Jia X, Jiang SB. Ct to cone-beam ct deformable registration with simultaneous intensity correction. *Physics in medicine and biology* 2012;57:6807.
43. Wang H, Dong L, O'Daniel J, Mohan R, Garden AS, Ang KK, Kuban DA, Bonnen M, Chang JY, Cheung R. Validation of an accelerated 'demons' algorithm for deformable image registration in radiation therapy. *Physics in medicine and biology* 2005;50:2887.
44. Vercauteren T, Pennec X, Perchant A, Ayache N. Diffeomorphic demons: Efficient non-parametric image registration. *NeuroImage* 2009;45:S61-S72.
45. Rueckert D, Sonoda LI, Hayes C, Hill DL, Leach MO, Hawkes DJ. Nonrigid registration using free-form deformations: Application to breast mr images. *Medical Imaging, IEEE Transactions on* 1999;18:712-721.
46. Zagorchev L, Goshtasby A. A comparative study of transformation functions for nonrigid image registration. *Image Processing, IEEE Transactions on* 2006;15:529-538.
47. Hua R, Pozo JM, Taylor ZA, Frangi AF. Multiresolution extended free-form deformations (xffd) for non-rigid registration with discontinuous transforms. *Medical Image Analysis* 2017;36:113-122.
48. Allaire S, Pekar V, Breen S, Hope A, Jaffray D. Th-c-aud c-02: Automatic extraction of salient interest points in 3d images for contour propagation in igrt. *Medical Physics* 2008;35:2972-2972.
49. Vemuri BC, Ye J, Chen Y, Leonard CM. Image registration via level-set motion: Applications to atlas-based segmentation. *Medical image analysis* 2003;7:1-20.
50. Ou Y, Sotiras A, Paragios N, Davatzikos C. Dramms: Deformable registration via attribute matching and mutual-saliency weighting. *Medical image analysis* 2011;15:622-639.
51. Staring M, Van Der Heide U, Klein S, Viergever M, Pluim JP. Registration of cervical mri using multifeature mutual information. *Medical Imaging, IEEE Transactions on* 2009;28:1412-1421.
52. Paganelli C, Peroni M, Baroni G, Riboldi M. Quantification of organ motion based on an adaptive image-based scale invariant feature method. *Medical physics* 2013;40.
53. Zhong H, Wen N, Gordon JJ, Elshaikh MA, Movsas B, Chetty IJ. An adaptive mr-ct registration method for mri-guided prostate cancer radiotherapy. *Physics in medicine and biology* 2015;60:2837.
54. Samavati N, Velec M, Brock K. A hybrid biomechanical intensity based deformable image registration of lung 4dct. *Physics in medicine and biology* 2015;60:3359.
55. Cazoulat G, Owen D, Matuszak MM, Balter JM, Brock KK. Biomechanical deformable image registration of longitudinal lung ct images using vessel information. *Physics in medicine and biology* 2016;61:4826-4839.
56. Li M, Castillo E, Zheng X-L, Luo H-Y, Castillo R, Wu Y, Guerrero T. Modeling lung deformation: A combined deformable image registration method with spatially varying young's modulus estimates. *Medical physics* 2013;40:081902.
57. Samavati N, Velec M, Brock KK. Effect of deformable registration uncertainty on lung sbrt dose accumulation. *Medical physics* 2016;43:233-240.
58. Qin A, Liang J, Han X, O'Connell N, Yan D. The impact of deformable image registration methods on dose warping. *Medical physics* 2018.

59. Takayama Y, Kadoya N, Yamamoto T, Ito K, Chiba M, Fujiwara K, Miyasaka Y, Dobashi S, Sato K, Takeda K. Evaluation of the performance of deformable image registration between planning ct and cbct images for the pelvic region: Comparison between hybrid and intensity-based dir. *Journal of radiation research* 2017;58:567-571.
60. Yang Y, Teo SK, Van Reeth E, Tan C, Tham I, Poh C. A hybrid approach for fusing 4d-mri temporal information with 3d-ct for the study of lung and lung tumor motion. *Medical physics* 2015;42:4484-4496.
61. Kim J, Kumar S, Liu C, Zhong H, Pradhan D, Shah M, Cattaneo R, Yechieli R, Robbins JR, Elshaikh MA. A novel approach for establishing benchmark cbct/ct deformable image registrations in prostate cancer radiotherapy. *Physics in Medicine & Biology* 2013;58:8077.
62. Weistrand O, Svensson S. The anaconda algorithm for deformable image registration in radiotherapy. *Medical physics* 2015;42:40-53.
63. Zhang L, Wen Y. Log-demons with driving force for large deformation image registration. Neural Networks (IJCNN), 2016 International Joint Conference on. IEEE. 2016. pp. 3052-3059.
64. Castelli J, Simon A, Louvel G, Henry O, Chajon E, Nassef M, Haigron P, Cazoulat G, Ospina J, Jegoux F, Benezery K, de Crevoisier R. Impact of head and neck cancer adaptive radiotherapy to spare the parotid glands and decrease the risk of xerostomia. *Radiat Oncol* 2015;10:6.
65. Bondiau P-Y, Malandain G, Chanalet S, Marcy P-Y, Habrand J-L, Fauchon F, Paquis P, Courdi A, Commowick O, Rutten I. Atlas-based automatic segmentation of mr images: Validation study on the brainstem in radiotherapy context. *International Journal of Radiation Oncology* Biology* Physics* 2005;61:289-298.
66. Han X, Hoogeman MS, Levendag PC, Hibbard LS, Teguh DN, Voet P, Cowen AC, Wolf TK. Atlas-based auto-segmentation of head and neck ct images. International Conference on Medical Image Computing and Computer-assisted Intervention. Springer. 2008. pp. 434-441.
67. Acosta O, Mylona E, Le Dain M, Voisin C, Lizee T, Rigaud B, Lafond C, Gnep K, de Crevoisier R. Multi-atlas-based segmentation of prostatic urethra from planning ct imaging to quantify dose distribution in prostate cancer radiotherapy. *Radiotherapy and Oncology* 2017;125:492-499.
68. Ramus L, Malandain G. Multi-atlas based segmentation: Application to the head and neck region for radiotherapy planning. MICCAI Workshop Medical Image Analysis for the Clinic-A Grand Challenge. 2010. pp. 281-288.
69. Acosta O, Simon A, Monge F, Commandeur F, Bassirou C, Cazoulat G, De Crevoisier R, Haigron P. Evaluation of multi-atlas-based segmentation of ct scans in prostate cancer radiotherapy. Biomedical Imaging: From Nano to Macro, 2011 IEEE International Symposium on. IEEE. 2011. pp. 1966-1969.
70. Dowling JA, Fripp J, Chandra S, Pluim JPW, Lambert J, Parker J, Denham J, Greer PB, Salvado O. Fast automatic multi-atlas segmentation of the prostate from 3d mr images Prostate cancer imaging. Image analysis and image-guided interventions: Springer; 2011. pp. 10-21.
71. Rohlfing T, Brandt R, Menzel R, Maurer CR. Evaluation of atlas selection strategies for atlas-based image segmentation with application to confocal microscopy images of bee brains. *NeuroImage* 2004;21:1428-1442.
72. Warfield SK, Zou KH, Wells WM. Simultaneous truth and performance level estimation (staple): An algorithm for the validation of image segmentation. *IEEE transactions on medical imaging* 2004;23:903-921.
73. Langerak TR, van der Heide UA, Kotte AN, Viergever MA, Van Vulpen M, Pluim JP. Label fusion in atlas-based segmentation using a selective and iterative method for performance level estimation (simple). *IEEE transactions on medical imaging* 2010;29:2000-2008.
74. Langerak T, Heijkoop S, Quint S, Mens J-W, Heijmen B, Hoogeman M. Towards automatic plan selection for radiotherapy of cervical cancer by fast automatic segmentation of cone beam ct scans Medical image computing and computer-assisted intervention–miccai 2014: Springer; 2014. pp. 528-535.

75. Acosta O, Dowling J, Drean G, Simon A, De Crevoisier R, Haigron P. Multi-atlas-based segmentation of pelvic structures from ct scans for planning in prostate cancer radiotherapy Abdomen and thoracic imaging: Springer; 2014. pp. 623-656.
76. Daisne J-F, Blumhofer A. Atlas-based automatic segmentation of head and neck organs at risk and nodal target volumes: A clinical validation. *Radiation Oncology* 2013;8:154.
77. La Macchia M, Fellin F, Amichetti M, Cianchetti M, Gianolini S, Paola V, Lomax AJ, Widesott L. Systematic evaluation of three different commercial software solutions for automatic segmentation for adaptive therapy in head-and-neck, prostate and pleural cancer. *Radiation Oncology* 2012;7:160.
78. Isambert A, Dhermain F, Bidault F, Commowick O, Bondiau P-Y, Malandain G, Lefkopoulos D. Evaluation of an atlas-based automatic segmentation software for the delineation of brain organs at risk in a radiation therapy clinical context. *Radiotherapy and oncology* 2008;87:93-99.
79. Rasch C, Steenbakkers R, van Herk M. Target definition in prostate, head, and neck. *Seminars in Radiation Oncology* 2005;15:136-145.
80. Geets X, Daisne JF, Tomsej M, Duprez T, Lonneux M, Gregoire V. Impact of the type of imaging modality on target volumes delineation and dose distribution in pharyngo-laryngeal squamous cell carcinoma: Comparison between pre- and per-treatment studies. *Radiother Oncol* 2006;78:291-297.
81. Farina E, Ferioli M, Castellucci P, Farina A, Rambaldi GZ, Cilla S, Cammelli S, Fanti S, Morganti AG. 18f-fdg-pet-guided planning and re-planning (adaptive) radiotherapy in head and neck cancer: Current state of art. *Anticancer research* 2017;37:6523-6532.
82. Seppälä T, Visapää H, Collan J, Kapanen M, Beule A, Kouri M, Tenhunen M, Saarilahti K. Converting from ct-to mri-only-based target definition in radiotherapy of localized prostate cancer. *Strahlentherapie und Onkologie* 2015;191:862-868.
83. Sabater S, del Rosario Pastor-Juan M, Berenguer R, Andres I, Sevillano M, Lozano-Setien E, Jimenez-Jimenez E, Rovirosa A, Sanchez-Prieto R, Arenas M. Analysing the integration of mr images acquired in a non-radiotherapy treatment position into the radiotherapy workflow using deformable and rigid registration. *Radiotherapy and Oncology* 2016;119:179-184.
84. Tait LM, Hoffman D, Benedict S, Valicenti R, Mayadev JS. The use of mri deformable image registration for ct-based brachytherapy in locally advanced cervical cancer. *Brachytherapy* 2016;15:333-340.
85. Chuter R, Prestwich R, Bird D, Scarsbrook A, Sykes J, Wilson D, Speight R. The use of deformable image registration to integrate diagnostic mri into the radiotherapy planning pathway for head and neck cancer. *Radiotherapy and Oncology* 2017;122:229-235.
86. Leibfarth S, Mönnich D, Welz S, Siegel C, Schwenzer N, Schmidt H, Zips D, Thorwarth D. A strategy for multimodal deformable image registration to integrate pet/mr into radiotherapy treatment planning. *Acta oncologica* 2013;52:1353-1359.
87. Hwang AB, Bacharach SL, Yom SS, Weinberg VK, Quivey JM, Franc BL, Xia P. Can positron emission tomography (pet) or pet/computed tomography (ct) acquired in a nontreatment position be accurately registered to a head-and-neck radiotherapy planning ct? *Int J Radiat Oncol Biol Phys* 2009;73:578-584.
88. Ireland RH, Dyker KE, Barber DC, Wood SM, Hanney MB, Tindale WB, Woodhouse N, Hoggard N, Conway J, Robinson MH. Nonrigid image registration for head and neck cancer radiotherapy treatment planning with pet/ct. *Int J Radiat Oncol Biol Phys* 2007;68:952-957.
89. Van Herk M. Errors and margins in radiotherapy. Seminars in radiation oncology. Elsevier. 2004. pp. 52-64.
90. Thörnqvist S, Hysing LB, Zolnay AG, Söhn M, Hoogeman MS, Muren LP, Heijmen BJ. Adaptive radiotherapy in locally advanced prostate cancer using a statistical deformable motion model. *Acta Oncologica* 2013;52:1423-1429.
91. Bondar L, Intven M, Burbach JM, Budiarto E, Kleijnen J-P, Philippens M, van Asselen B, Seravalli E, Reerink O, Raaymakers B. Statistical modeling of ctv motion and deformation for imrt of early-

stage rectal cancer. *International Journal of Radiation Oncology* Biology* Physics* 2014;90:664-672.

92. Tilly D, van de Schoot AJ, Grusell E, Bel A, Ahnesjö A. Dose coverage calculation using a statistical shape model—applied to cervical cancer radiotherapy. *Physics in Medicine and Biology* 2017;62:4140.
93. Kipritidis J, Hugo G, Weiss E, Williamson J, Keall PJ. Measuring interfraction and intrafraction lung function changes during radiation therapy using four-dimensional cone beam ct ventilation imaging. *Medical physics* 2015;42:1255-1267.
94. Guerrero T, Sanders K, Castillo E, Zhang Y, Bidaut L, Pan T, Komaki R. Dynamic ventilation imaging from four-dimensional computed tomography. *Physics in Medicine & Biology* 2006;51:777.
95. Yamamoto T, Kabus S, Klinder T, Lorenz C, Von Berg J, Blaffert T, Loo Jr BW, Keall PJ. Investigation of four-dimensional computed tomography-based pulmonary ventilation imaging in patients with emphysematous lung regions. *Physics in Medicine & Biology* 2011;56:2279.
96. Guerrero T, Sanders K, Noyola-Martinez J, Castillo E, Zhang Y, Tapia R, Guerra R, Borghero Y, Komaki R. Quantification of regional ventilation from treatment planning ct. *International Journal of Radiation Oncology• Biology• Physics* 2005;62:630-634.
97. Yamamoto T, Kabus S, Von Berg J, Lorenz C, Keall PJ. Impact of four-dimensional computed tomography pulmonary ventilation imaging-based functional avoidance for lung cancer radiotherapy. *International Journal of Radiation Oncology• Biology• Physics* 2011;79:279-288.
98. Freyhardt P, Hartwig T, De Bucourt M, Maurer M, Renz D, Gebauer B, Hamm B, Teichgräber UK, Streitparth F. Mr-guided facet joint injection therapy using an open 1.0-t mri system: An outcome study. *European radiology* 2013;23:3296-3303.
99. Van Heijst TC, Den Hartogh MD, Lagendijk JJ, van den Bongard HD, Van Asselen B. Mr-guided breast radiotherapy: Feasibility and magnetic-field impact on skin dose. *Physics in medicine and biology* 2013;58:5917.
100. Lagendijk JJ, Raaymakers BW, van Vulpen M. The magnetic resonance imaging–linac system. Seminars in radiation oncology. Elsevier. 2014. pp. 207-209.
101. Lambert J, Greer PB, Menk F, Patterson J, Parker J, Dahl K, Gupta S, Capp A, Wratten C, Tang C. Mri-guided prostate radiation therapy planning: Investigation of dosimetric accuracy of mri-based dose planning. *Radiotherapy and Oncology* 2011;98:330-334.
102. Owrangi AM, Greer PB, Glide-Hurst CK. Mri-only treatment planning: Benefits and challenges. *Physics in Medicine and Biology* 2018.
103. Dowling JA, Lambert J, Parker J, Salvado O, Fripp J, Capp A, Wratten C, Denham JW, Greer PB. An atlas-based electron density mapping method for magnetic resonance imaging (mri)-alone treatment planning and adaptive mri-based prostate radiation therapy. *International Journal of Radiation Oncology* Biology* Physics* 2012;83:e5-e11.
104. Chen S, Quan H, Qin A, Yee S, Yan D. Mr image-based synthetic ct for imrt prostate treatment planning and cbct image-guided localization. *Journal of applied clinical medical physics* 2016;17:236-245.
105. Burgos N, Cardoso MJ, Guerreiro F, Veiga C, Modat M, McClelland J, Knopf A-C, Punwani S, Atkinson D, Arridge SR. Robust ct synthesis for radiotherapy planning: Application to the head and neck region. International Conference on Medical Image Computing and Computer-Assisted Intervention. Springer. 2015. pp. 476-484.
106. König L, Derksen A, Papenberg N, Haas B. Deformable image registration for adaptive radiotherapy with guaranteed local rigidity constraints. *Radiation Oncology* 2016;11:122.
107. Gardner SJ, Wen N, Kim J, Liu C, Pradhan D, Aref I, Cattaneo II R, Vance S, Movsas B, Chetty IJ. Contouring variability of human-and deformable-generated contours in radiotherapy for prostate cancer. *Physics in medicine and biology* 2015;60:4429.
108. Thor M, Bentzen L, Elstrøm UV, Petersen JB, Muren LP. Dose/volume-based evaluation of the accuracy of deformable image registration for the rectum and bladder. *Acta Oncologica* 2013;52:1411-1416.

109. Thor M, Petersen JB, Bentzen L, Høyer M, Muren LP. Deformable image registration for contour propagation from ct to cone-beam ct scans in radiotherapy of prostate cancer. *Acta Oncologica* 2011;50:918-925.
110. Riegel AC, Antone JG, Zhang H, Jain P, Raince J, Rea A, Bergamo AM, Kapur A, Potters L. Deformable image registration and interobserver variation in contour propagation for radiation therapy planning. *Journal of applied clinical medical physics* 2016;17:347-357.
111. Dice LR. Measures of the amount of ecologic association between species. *Ecology* 1945;26:297-302.
112. Thörnqvist S, Petersen JB, Høyer M, Bentzen LN, Muren LP. Propagation of target and organ at risk contours in radiotherapy of prostate cancer using deformable image registration. *Acta Oncologica* 2010;49:1023-1032.
113. Chao M, Xie Y, Xing L. Auto-propagation of contours for adaptive prostate radiation therapy. *Physics in medicine and biology* 2008;53:4533.
114. Xie Y, Chao M, Lee P, Xing L. Feature-based rectal contour propagation from planning ct to cone beam ct. *Medical physics* 2008;35:4450-4459.
115. Lu C, Chelikani S, Jaffray D, Milosevic MF, Staib LH, Duncan JS. Simultaneous nonrigid registration, segmentation, and tumor detection in mri guided cervical cancer radiation therapy. *Medical Imaging, IEEE Transactions on* 2012;31:1213-1227.
116. Berendsen FF, Van Der Heide UA, Langerak TR, Kotte AN, Pluim JP. Free-form image registration regularized by a statistical shape model: Application to organ segmentation in cervical mr. *Computer Vision and Image Understanding* 2013;117:1119-1127.
117. Van Der Put R, Kerkhof E, Raaymakers B, Jürgenliemk-Schulz I, Lagendijk J. Contour propagation in mri-guided radiotherapy treatment of cervical cancer: The accuracy of rigid, non-rigid and semi-automatic registrations. *Physics in medicine and biology* 2009;54:7135.
118. Chapman CH, Polan D, Vineberg K, Jolly S, Maturen KE, Brock KK, Prisciandaro JI. Deformable image registration–based contour propagation yields clinically acceptable plans for mri-based cervical cancer brachytherapy planning. *Brachytherapy* 2018.
119. Rigaud B, Simon A, Castelli J, Gobeli M, Ospina Arango JD, Cazoulat G, Henry O, Haigron P, De Crevoisier R. Evaluation of deformable image registration methods for dose monitoring in head and neck radiotherapy. *Biomed Res Int* 2015;2015:726268.
120. Kumarasiri A, Siddiqui F, Liu C, Yechieli R, Shah M, Pradhan D, Zhong H, Chetty IJ, Kim J. Deformable image registration based automatic ct-to-ct contour propagation for head and neck adaptive radiotherapy in the routine clinical setting. *Medical physics* 2014;41.
121. Ramadaan IS, Peick K, Hamilton DA, Evans J, Iupati D, Nicholson A, Greig L, Louwe RJ. Validation of varian's smartadapt® deformable image registration algorithm for clinical application. *Radiation Oncology* 2015;10:73.
122. Veiga C, McClelland J, Moinuddin S, Lourenco A, Ricketts K, Annkah J, Modat M, Ourselin S, D'Souza D, Royle G. Toward adaptive radiotherapy for head and neck patients: Feasibility study on using ct-to-cbct deformable registration for "dose of the day" calculations. *Med Phys* 2014;41:031703.
123. Hou J, Guerrero M, Chen W, D'Souza WD. Deformable planning ct to cone-beam ct image registration in head-and-neck cancer. *Medical physics* 2011;38:2088-2094.
124. Hvid CA, Elstrøm UV, Jensen K, Alber M, Grau C. Accuracy of software-assisted contour propagation from planning ct to cone beam ct in head and neck radiotherapy. *Acta Oncologica* 2016;55:1324-1330.
125. Broggi S, Scalco E, Belli ML, Logghe G, Verellen D, Moriconi S, Chiara A, Palmisano A, Mellone R, Fiorino C. A comparative evaluation of 3 different free-form deformable image registration and contour propagation methods for head and neck mri: The case of parotid changes during radiotherapy. *Technology in cancer research & treatment* 2017;16:373-381.
126. Louie AV, Rodrigues G, Olsthoorn J, Palma D, Yu E, Yaremko B, Ahmad B, Aivas I, Gaede S. Inter-observer and intra-observer reliability for lung cancer target volume delineation in the 4d-ct era. *Radiotherapy and Oncology* 2010;95:166-171.

127. Gaede S, Olsthoorn J, Louie AV, Palma D, Yu E, Yaremko B, Ahmad B, Chen J, Bzdusek K, Rodrigues G. An evaluation of an automated 4d-ct contour propagation tool to define an internal gross tumour volume for lung cancer radiotherapy. *Radiotherapy and Oncology* 2011;101:322-328.
128. Speight R, Sykes J, Lindsay R, Franks K, Thwaites D. The evaluation of a deformable image registration segmentation technique for semi-automating internal target volume (itv) production from 4dct images of lung stereotactic body radiotherapy (sbrt) patients. *Radiotherapy and Oncology* 2011;98:277-283.
129. Rietzel E, Chen GT, Choi NC, Willet CG. Four-dimensional image-based treatment planning: Target volume segmentation and dose calculation in the presence of respiratory motion. *International Journal of Radiation Oncology* Biology* Physics* 2005;61:1535-1550.
130. van Dam IE, de Koste JRvS, Hanna GG, Muirhead R, Slotman BJ, Senan S. Improving target delineation on 4-dimensional ct scans in stage i nsclc using a deformable registration tool. *Radiotherapy and oncology* 2010;96:67-72.
131. Hardcastle N, Van Elmpt W, De Ruysscher D, Bzdusek K, Tomé WA. Accuracy of deformable image registration for contour propagation in adaptive lung radiotherapy. *Radiation Oncology* 2013;8:243.
132. Stützer K, Haase R, Lohaus F, Barczyk S, Exner F, Löck S, Rühaak J, Lassen-Schmidt B, Corr D, Richter C. Evaluation of a deformable registration algorithm for subsequent lung computed tomography imaging during radiochemotherapy. *Medical physics* 2016;43:5028-5039.
133. Hardcastle N, Hofman MS, Hicks RJ, Callahan J, Kron T, MacManus MP, Ball DL, Jackson P, Siva S. Accuracy and utility of deformable image registration in 68ga 4d pet/ct assessment of pulmonary perfusion changes during and after lung radiation therapy. *International Journal of Radiation Oncology• Biology• Physics* 2015;93:196-204.
134. Al-Ward SM, Kim A, McCann C, Ruschin M, Cheung P, Sahgal A, Keller BM. The development of a 4d treatment planning methodology to simulate the tracking of central lung tumors in an mri-linac. *Journal of applied clinical medical physics* 2017.
135. de Xivry JO, Janssens G, Bosmans G, De Craene M, Dekker A, Buijsen J, van Baardwijk A, De Ruysscher D, Macq B, Lambin P. Tumour delineation and cumulative dose computation in radiotherapy based on deformable registration of respiratory correlated ct images of lung cancer patients. *Radiotherapy and Oncology* 2007;85:232-238.
136. Sharma M, Weiss E, Siebers JV. Dose deformation-invariance in adaptive prostate radiation therapy: Implication for treatment simulations. *Radiotherapy and Oncology* 2012;105:207-213.
137. Simon A, Le Maitre A, Nassef M, Rigaud B, Castelli J, Acosta O, Haigron P, Lafond C, de Crevoisier R. Is dose deformation-invariance hypothesis verified in prostate igrt? *International Journal of Radiation Oncology • Biology • Physics*.
138. Moteabbed M, Sharp G, Wang Y, Trofimov A, Efstathiou J, Lu HM. Validation of a deformable image registration technique for cone beam ct-based dose verification. *Medical physics* 2015;42:196-205.
139. Arai K, Kadoya N, Kato T, Endo H, Komori S, Abe Y, Nakamura T, Wada H, Kikuchi Y, Takai Y. Feasibility of cbct-based proton dose calculation using a histogram-matching algorithm in proton beam therapy. *Physica Medica: European Journal of Medical Physics* 2017;33:68-76.
140. Kurz C, Kamp F, Park YK, Zöllner C, Rit S, Hansen D, Podesta M, Sharp GC, Li M, Reiner M. Investigating deformable image registration and scatter correction for cbct-based dose calculation in adaptive impt. *Medical physics* 2016;43:5635-5646.
141. Landry G, Dedes G, Zöllner C, Handrack J, Janssens G, de Xivry JO, Reiner M, Paganelli C, Riboldi M, Kamp F. Phantom based evaluation of ct to cbct image registration for proton therapy dose recalculation. *Physics in Medicine & Biology* 2014;60:595.
142. Landry G, Nijhuis R, Dedes G, Handrack J, Thieke C, Janssens G, Orban de Xivry J, Reiner M, Kamp F, Wilkens JJ. Investigating ct to cbct image registration for head and neck proton therapy as a tool for daily dose recalculation. *Medical physics* 2015;42:1354-1366.

143. Branchini M, Fiorino C, Dell'Oca I, Belli M, Perna L, Di Muzio N, Calandrino R, Broggi S. Validation of a method for “dose of the day” calculation in head-neck tomotherapy by using planning ct-to-mvct deformable image registration. *Physica Medica: European Journal of Medical Physics* 2017;39:73-79.
144. Onozato Y, Kadoya N, Fujita Y, Arai K, Dobashi S, Takeda K, Kishi K, Umezawa R, Matsushita H, Jingu K. Evaluation of on-board kv cone beam computed tomography–based dose calculation with deformable image registration using hounsfield unit modifications. *International Journal of Radiation Oncology• Biology• Physics* 2014;89:416-423.
145. Marchant TE, Joshi KD, Moore CJ. Accuracy of radiotherapy dose calculations based on cone-beam ct: Comparison of deformable registration and image correction based methods. *Physics in Medicine and Biology* 2018.
146. Boman E, Kapanen M, Pickup L, Lahtela S-L. Importance of deformable image registration and biological dose summation in planning of radiotherapy retreatments. *Medical Dosimetry* 2017.
147. Andersen E, Muren L, Sørensen TS, Noe KØ, Thor M, Petersen J, Høyer M, Bentzen L, Tanderup K. Bladder dose accumulation based on a biomechanical deformable image registration algorithm in volumetric modulated arc therapy for prostate cancer. *Physics in medicine and biology* 2012;57:7089.
148. Lee DS, Woo J-Y, Kim JW, Seong J. Re-irradiation of hepatocellular carcinoma: Clinical applicability of deformable image registration. *Yonsei medical journal* 2016;57:41-49.
149. Thor M, Andersen ES, Petersen JB, Sørensen TS, Noe KØ, Tanderup K, Bentzen L, Elstrøm UV, Høyer M, Muren LP. Evaluation of an application for intensity-based deformable image registration and dose accumulation in radiotherapy. *Acta Oncologica* 2014;53:1329-1336.
150. Kvinnsland Y, Muren LP, Dahl O. Evaluation of a new method for calculation of cumulative doses in the rectum wall using repeat ct scans. *Acta Oncologica* 2004;43:388-395.
151. Dale E, Hellebust TP, Skjønsberg A, Høgberg T, Olsen DR. Modeling normal tissue complication probability from repetitive computed tomography scans during fractionated high-dose-rate brachytherapy and external beam radiotherapy of the uterine cervix. *International Journal of Radiation Oncology• Biology• Physics* 2000;47:963-971.
152. Kobayashi K, Murakami N, Wakita A, Nakamura S, Okamoto H, Umezawa R, Takahashi K, Inaba K, Igaki H, Ito Y. Dosimetric variations due to interfraction organ deformation in cervical cancer brachytherapy. *Radiotherapy and Oncology* 2015;117:555-558.
153. Jamema SV, Mahantshetty U, Andersen E, Noe KØ, Sørensen TS, Kallehauge JF, Shrivastava SK, Deshpande DD, Tanderup K. Uncertainties of deformable image registration for dose accumulation of high-dose regions in bladder and rectum in locally advanced cervical cancer. *Brachytherapy* 2015;14:953-962.
154. Andersen ES, Noe KØ, Sørensen TS, Nielsen SK, Fokdal L, Paludan M, Lindegaard JC, Tanderup K. Simple dvh parameter addition as compared to deformable registration for bladder dose accumulation in cervix cancer brachytherapy. *Radiotherapy and Oncology* 2013;107:52-57.
155. van Heerden LE, Houweling AC, Koedooder K, van Kesteren Z, van Wieringen N, Rasch CR, Pieters BR, Bel A. Structure-based deformable image registration: Added value for dose accumulation of external beam radiotherapy and brachytherapy in cervical cancer. *Radiotherapy and Oncology* 2017;123:319-324.
156. Hayashi K, Isohashi F, Akino Y, Wakai N, Mabuchi S, Suzuki O, Seo Y, Ootani Y, Sumida I, Yoshioka Y. Estimation of the total rectal dose of radical external beam and intracavitary radiotherapy for uterine cervical cancer using the deformable image registration method. *Journal of radiation research* 2015;56:546-552.
157. Rubeaux M, Cazoulat G, Duménil A, Lafond C, Acosta O, De Crevoisier R, Simon A, Haigron P. Numerical phantom generation to evaluate non-rigid ct/cbct registration algorithms for prostate cancer radiotherapy. *Image-Guidance and Multimodal Dose Planning in Radiation Therapy* 2012:74.

158. Rosu M, Chetty IJ, Balter JM, Kessler ML, McShan DL, Ten Haken RK. Dose reconstruction in deforming lung anatomy: Dose grid size effects and clinical implications. *Medical physics* 2005;32:2487-2495.
159. Zhong H, Chetty IJ. Adaptive radiotherapy for nsclc patients: Utilizing the principle of energy conservation to evaluate dose mapping operations. *Physics in Medicine & Biology* 2017;62:4333.
160. Paganetti H, Jiang H, Adams JA, Chen GT, Rietzel E. Monte carlo simulations with time-dependent geometries to investigate effects of organ motion with high temporal resolution. *International Journal of Radiation Oncology* Biology* Physics* 2004;60:942-950.
161. Zhong H, Siebers JV. Monte carlo dose mapping on deforming anatomy. *Physics in medicine and biology* 2009;54:5815.
162. Nassef M, Simon A, Cazoulat G, Duménil A, Blay C, Lafond C, Acosta O, Balosso J, Haigron P, de Crevoisier R. Quantification of dose uncertainties in cumulated dose estimation compared to planned dose in prostate imrt. *Radiotherapy and Oncology* 2016;119:129-136.
163. Yu J, Hardcastle N, Jeong K, Bender ET, Ritter MA, Tomé WA. On voxel-by-voxel accumulated dose for prostate radiation therapy using deformable image registration. *Technology in cancer research & treatment* 2015;14:37-47.
164. Akino Y, Yoshioka Y, Fukuda S, Maruoka S, Takahashi Y, Yagi M, Mizuno H, Isohashi F, Ogawa K. Estimation of rectal dose using daily megavoltage cone-beam computed tomography and deformable image registration. *International Journal of Radiation Oncology• Biology• Physics* 2013;87:602-608.
165. Moulton CR, House MJ, Lye V, Tang CI, Krawiec M, Joseph DJ, Denham JW, Ebert MA. Accumulation of rectum dose-volume metrics for prostate external beam radiotherapy combined with brachytherapy: Evaluating deformably registered dose distribution addition using parameter-based addition. *Journal of medical imaging and radiation oncology* 2017;61:534-542.
166. Vestergaard A, Muren LP, Søndergaard J, Elstrøm UV, Høyer M, Petersen JB. Adaptive plan selection vs. Re-optimisation in radiotherapy for bladder cancer: A dose accumulation comparison. *Radiotherapy and Oncology* 2013;109:457-462.
167. Lim K, Kelly V, Stewart J, Xie J, Cho Y-B, Moseley J, Brock K, Fyles A, Lundin A, Rehbinder H. Pelvic radiotherapy for cancer of the cervix: Is what you plan actually what you deliver? *International Journal of Radiation Oncology* Biology* Physics* 2009;74:304-312.
168. Stewart J, Lim K, Kelly V, Xie J, Brock KK, Moseley J, Cho Y-B, Fyles A, Lundin A, Rehbinder H. Automated weekly replanning for intensity-modulated radiotherapy of cervix cancer. *International Journal of Radiation Oncology* Biology* Physics* 2010;78:350-358.
169. Oh S, Stewart J, Moseley J, Kelly V, Lim K, Xie J, Fyles A, Brock KK, Lundin A, Rehbinder H, Milosevic M, Jaffray D, Cho YB. Hybrid adaptive radiotherapy with on-line mri in cervix cancer imrt. *Radiother Oncol* 2014;110:323-328.
170. Christensen GE, Carlson B, Chao KC, Yin P, Grigsby PW, Nguyen K, Dempsey JF, Lerma FA, Bae KT, Vannier MW. Image-based dose planning of intracavitary brachytherapy: Registration of serial-imaging studies using deformable anatomic templates. *International Journal of Radiation Oncology• Biology• Physics* 2001;51:227-243.
171. Reniers B, Janssens G, de Xivry JO, Landry G, Verhaegen F. Dose distribution for gynecological brachytherapy with dose accumulation between insertions: Feasibility study. *Brachytherapy* 2016;15:504-513.
172. Ryckman JM, Shelton JW, Waller AF, Schreibmann E, Latifi K, Diaz R. Anatomic structure-based deformable image registration of brachytherapy implants in the treatment of locally advanced cervix cancer. *Brachytherapy* 2016;15:584-592.
173. Kim H, Huq MS, Houser C, Beriwal S, Michalski D. Mapping of dose distribution from imrt onto mri-guided high dose rate brachytherapy using deformable image registration for cervical cancer treatments: Preliminary study with commercially available software. *Journal of contemporary brachytherapy* 2014;6:178.

174. Abe T, Tamaki T, Makino S, Ebara T, Hirai R, Miyaura K, Kumazaki Y, Ohno T, Shikama N, Nakano T. Assessing cumulative dose distributions in combined radiotherapy for cervical cancer using deformable image registration with pre-imaging preparations. *Radiation Oncology* 2014;9:1.
175. Kadoya N, Miyasaka Y, Nakajima Y, Kuroda Y, Ito K, Chiba M, Sato K, Dobashi S, Yamamoto T, Takahashi N. Evaluation of deformable image registration between external beam radiotherapy and hdr brachytherapy for cervical cancer with a 3d-printed deformable pelvis phantom. *Medical physics* 2017;44:1445-1455.
176. Moulton CR, House MJ, Lye V, Tang CI, Krawiec M, Joseph DJ, Denham JW, Ebert MA. Registering prostate external beam radiotherapy with a boost from high-dose-rate brachytherapy: A comparative evaluation of deformable registration algorithms. *Radiation Oncology* 2015;10:254.
177. Lee C, Langen KM, Lu W, Haimerl J, Schnarr E, Ruchala KJ, Olivera GH, Meeks SL, Kupelian PA, Shellenberger TD. Assessment of parotid gland dose changes during head and neck cancer radiotherapy using daily megavoltage computed tomography and deformable image registration. *International Journal of Radiation Oncology* Biology* Physics* 2008;71:1563-1571.
178. Zhang P, Simon A, Rigaud B, Castelli J, Arango JDO, Nassef M, Henry O, Zhu J, Haigron P, Li B. Optimal adaptive imrt strategy to spare the parotid glands in oropharyngeal cancer. *Radiotherapy and Oncology* 2016;120:41-47.
179. Elstrøm UV, Wysocka BA, Muren LP, Petersen JB, Grau C. Daily kv cone-beam ct and deformable image registration as a method for studying dosimetric consequences of anatomic changes in adaptive imrt of head and neck cancer. *Acta oncologica* 2010;49:1101-1108.
180. Nobnop W, Chitapanarux I, Neamin H, Wanwilairat S, Lorvidhaya V, Sanghangthum T. Evaluation of deformable image registration (dir) methods for dose accumulation in nasopharyngeal cancer patients during radiotherapy. *Radiology and oncology* 2017;51:438-446.
181. Castelli J, Simon A, Rigaud B, Lafond C, Chajon E, Ospina J, Haigron P, Laguerre B, Loubière AR, Benezery K. A nomogram to predict parotid gland overdose in head and neck imrt. *Radiation Oncology* 2016;11:79.
182. Jung SH, Yoon SM, Park SH, Cho B, Park JW, Jung J, Park J-h, Kim JH, Do Ahn S. Four-dimensional dose evaluation using deformable image registration in radiotherapy for liver cancer. *Medical physics* 2013;40:011706.
183. Senthi S, Griffioen GH, de Koste JRvS, Slotman BJ, Senan S. Comparing rigid and deformable dose registration for high dose thoracic re-irradiation. *Radiotherapy and Oncology* 2013;106:323-326.
184. Ashburner J, Friston KJ. Voxel-based morphometry—the methods. *Neuroimage* 2000;11:805-821.
185. Heemsbergen WD, Al-Mamgani A, Witte MG, van Herk M, Pos FJ, Lebesque JV. Urinary obstruction in prostate cancer patients from the dutch trial (68 gy vs. 78 gy): Relationships with local dose, acute effects, and baseline characteristics. *International Journal of Radiation Oncology*Biology*Physics* 2010;78:19-25.
186. Acosta O, Drean G, Ospina JD, Simon A, Haigron P, Lafond C, De Crevoisier R. Voxel-based population analysis for correlating local dose and rectal toxicity in prostate cancer radiotherapy. *Physics in medicine and biology* 2013;58:2581.
187. Drean G, Acosta O, Ospina JD, Fargeas A, Lafond C, Correge G, Lagrange JL, Crehange G, Simon A, Haigron P, de Crevoisier R. Identification of a rectal subregion highly predictive of rectal bleeding in prostate cancer imrt. *Radiother Oncol* 2016;119:388-397.
188. Ospina JD, Commandeur F, Ríos R, Dréan G, Correa JC, Simon A, Haigron P, de Crevoisier R, Acosta O. A tensor-based population value decomposition to explain rectal toxicity after prostate cancer radiotherapy. In: Mori K, Sakuma I, Sato Y, Barillot C, Navab N, editors. Medical image computing and computer-assisted intervention – miccai 2013: 16th international conference, nagoya, japan, september 22-26, 2013, proceedings, part ii. Berlin, Heidelberg: Springer Berlin Heidelberg; 2013. pp. 387-394.

189. Witte MG, Heemsbergen WD, Bohoslavsky R, Pos FJ, Al-Mamgani A, Lebesque JV, van Herk M. Relating dose outside the prostate with freedom from failure in the dutch trial 68 gy vs. 78 gy. *International Journal of Radiation Oncology• Biology• Physics* 2010;77:131-138.
190. Monti S, Palma G, D'avino V, Gerardi M, Marvaso G, Ciardo D, Pacelli R, Jereczek-Fossa BA, Alterio D, Cella L. Voxel-based analysis unveils regional dose differences associated with radiation-induced morbidity in head and neck cancer patients. *Scientific Reports* 2017;7:7220.
191. Avanzo M, Barbiero S, Trovo M, Bissonnette J-P, Jena R, Stancanello J, Pirrone G, Matrone F, Minatel E, Cappelletto C. Voxel-by-voxel correlation between radiologically radiation induced lung injury and dose after image-guided, intensity modulated radiotherapy for lung tumors. *Physica Medica: European Journal of Medical Physics* 2017;42:150-156.
192. Palma G, Monti S, D'Avino V, Conson M, Liuzzi R, Pressello MC, Donato V, Deasy JO, Quarantelli M, Pacelli R. A voxel-based approach to explore local dose differences associated with radiation-induced lung damage. *International Journal of Radiation Oncology• Biology• Physics* 2016;96:127-133.
193. Jamema SV, Phurailatpam R, Paul SN, Joshi K, Deshpande D. Commissioning and validation of commercial deformable image registration software for adaptive contouring. *Physica Medica* 2018;47:1-8.
194. Zhong H, Guttmann D, Huang M, Geng H, Cheng C, Kong F, Machtay M, Brock K, Xiao Y. Evaluating the feasibility of applying deformable registration into adaptive therapy for nrg oncology rtog 1106. *International Journal of Radiation Oncology• Biology• Physics* 2017;99:E509-E510.
195. Veiga C, Lourenço AM, Mouinuddin S, Herk M, Modat M, Ourselin S, Royle G, McClelland JR. Toward adaptive radiotherapy for head and neck patients: Uncertainties in dose warping due to the choice of deformable registration algorithm. *Medical physics* 2015;42:760-769.
196. Fusella M, Giglioli FR, Fiandra C, Ragona R. Evaluation of dose recalculation vs dose deformation in a commercial platform for deformable image registration with a computational phantom. *Medical Dosimetry* 2017.
197. Abe Y, Kadoya N, Arai K, Takayama Y, Kato T, Kimura K, Ono T, Nakamura T, Wada H, Kikuchi Y. Effect of dir uncertainty on prostate passive-scattering proton therapy dose accumulation. *Physica Medica: European Journal of Medical Physics* 2017;39:113-120.
198. Zhong H, Siddiqui SM, Movsas B, Chetty IJ. Evaluation of adaptive treatment planning for patients with non-small cell lung cancer. *Physics in Medicine & Biology* 2017;62:4346.
199. Moriya S, Tachibana H, Kitamura N, Sawant A, Sato M. Dose warping performance in deformable image registration in lung. *Physica Medica: European Journal of Medical Physics* 2017;37:16-23.
200. Johnson PB, Padgett KR, Chen KL, Dogan N. Evaluation of the tool "reg refine" for user-guided deformable image registration. *Journal of applied clinical medical physics* 2016;17:158-170.
201. Velec M, Moseley JL, Svensson S, Hårdemark B, Jaffray DA, Brock KK. Validation of biomechanical deformable image registration in the abdomen, thorax and pelvis in a commercial radiotherapy treatment planning system. *Medical physics* 2017.
202. Qi XS, Santhanam A, Neylon J, Min Y, Armstrong T, Sheng K, Staton RJ, Pukala J, Pham A, Low DA. Near real-time assessment of anatomic and dosimetric variations for head and neck radiation therapy via graphics processing unit–based dose deformation framework. *International Journal of Radiation Oncology* Biology* Physics* 2015;92:415-422.
203. Sharp G, Kandasamy N, Singh H, Folkert M. Gpu-based streaming architectures for fast cone-beam ct image reconstruction and demons deformable registration. *Physics in medicine and biology* 2007;52:5771.
204. Gu X, Dong B, Wang J, Yordy J, Mell L, Jia X, Jiang SB. A contour-guided deformable image registration algorithm for adaptive radiotherapy. *Physics in medicine and biology* 2013;58:1889.
205. Østergaard Noe K, De Senneville BD, Elstrøm UV, Tanderup K, Sørensen TS. Acceleration and validation of optical flow based deformable registration for image-guided radiotherapy. *Acta Oncologica* 2008;47:1286-1293.

206. Brock KK, Dawson LA, Sharpe MB, Moseley DJ, Jaffray DA. Feasibility of a novel deformable image registration technique to facilitate classification, targeting, and monitoring of tumor and normal tissue. *International Journal of Radiation Oncology* Biology* Physics* 2006;64:1245-1254.
207. Al-Mayah A, Moseley J, Hunter S, Velec M, Chau L, Breen S, Brock K. Biomechanical-based image registration for head and neck radiation treatment. *Physics in medicine and biology* 2010;55:6491.
208. Polan DF, Feng M, Lawrence TS, Ten Haken RK, Brock KK. Implementing radiation dose-volume liver response in biomechanical deformable image registration. *International Journal of Radiation Oncology* Biology* Physics* 2017.
209. Hoda S, Hong Z, Hassan Bagher E, Wei L, Munther IA, Jian-Yue J, Feng-Ming K, Indrin JC, Hualiang Z. Utilization of a hybrid finite-element based registration method to quantify heterogeneous tumor response for adaptive treatment for lung cancer patients. *Physics in Medicine and Biology* 2018.
210. Mazur TR, Fischer-Valuck BW, Wang Y, Yang D, Mutic S, Li HH. Sift-based dense pixel tracking on 0.35 t cine-mr images acquired during image-guided radiation therapy with application to gating optimization. *Medical Physics* 2016;43:279-293.
211. Fast MF, Eiben B, Menten MJ, Wetscherek A, Hawkes DJ, McClelland JR, Oelfke U. Tumour auto-contouring on 2d cine mri for locally advanced lung cancer: A comparative study. *Radiotherapy and Oncology* 2017;125:485-491.
212. Rit S, Pinho R, Delmon V, Pech M, Bouilhol G, Schaerer J, Navalpakkam B, Vandemeulebroucke J, Seroul P, Sarrut D. Vv, a 4d slicer. Proceedings of the Fourth International Workshop on Pulmonary Image Analysis, Toronto, Canada. 2011. pp. 171-175.
213. Schlachter M, Fechter T, Jurisic M, Schimek-Jasch T, Oehlke O, Adebahr S, Birkfellner W, Nestle U, Bühler K. Visualization of deformable image registration quality using local image dissimilarity. *IEEE transactions on medical imaging* 2016;35:2319-2328.
214. Fitzpatrick JM, Hill DL, Shyr Y, West J, Studholme C, Maurer CR. Visual assessment of the accuracy of retrospective registration of mr and ct images of the brain. *Medical Imaging, IEEE Transactions on* 1998;17:571-585.
215. Jaccard P. Nouvelles recherches sur la distribution florale; 1908.
216. Crum WR, Camara O, Hill DL. Generalized overlap measures for evaluation and validation in medical image analysis. *Medical Imaging, IEEE Transactions on* 2006;25:1451-1461.
217. Huttenlocher DP, Klanderman G, Rucklidge WJ. Comparing images using the hausdorff distance. *Pattern Analysis and Machine Intelligence, IEEE Transactions on* 1993;15:850-863.
218. Chalana V, Kim Y. A methodology for evaluation of boundary detection algorithms on medical images. *IEEE transactions on medical imaging* 1997;16:642-652.
219. Foroudi F, Haworth A, Pangehel A, Wong J, Roxby P, Duchesne G, Williams S, Tai K. Inter-observer variability of clinical target volume delineation for bladder cancer using ct and cone beam ct. *Journal of medical imaging and radiation oncology* 2009;53:100-106.
220. Fiorino C, Reni M, Bolognesi A, Cattaneo GM, Calandrino R. Intra-and inter-observer variability in contouring prostate and seminal vesicles: Implications for conformal treatment planning. *Radiotherapy and oncology* 1998;47:285-292.
221. Ribeiro AS, Nutt DJ, McGonigle J. Which metrics should be used in non-linear registration evaluation? International Conference on Medical Image Computing and Computer-Assisted Intervention. Springer. 2015. pp. 388-395.
222. Wang J, Zhang Y, Zhang L, Dong L, Balter PA, Court LE, Yang J. Solving the “chinese postman problem” for effective contour deformation. *Medical physics* 2017.
223. Taha AA, Hanbury A. Metrics for evaluating 3d medical image segmentation: Analysis, selection, and tool. *BMC medical imaging* 2015;15:29.
224. Fitzpatrick JM, West JB, Maurer Jr CR. Predicting error in rigid-body point-based registration. *Medical Imaging, IEEE Transactions on* 1998;17:694-702.

225. Fitzpatrick JM, West JB. The distribution of target registration error in rigid-body point-based registration. *IEEE transactions on medical imaging* 2001;20:917-927.
226. Osorio EMV, Hoogeman MS, Bondar L, Levendag PC, Heijmen BJ. A novel flexible framework with automatic feature correspondence optimization for nonrigid registration in radiotherapy. *Medical physics* 2009;36:2848-2859.
227. Mencarelli A, van Beek S, van Kranen S, Rasch C, van Herk M, Sonke J-J. Validation of deformable registration in head and neck cancer using analysis of variance. *Medical physics* 2012;39:6879-6884.
228. Mencarelli A, van Kranen SR, Hamming-Vrieze O, van Beek S, Rasch CRN, van Herk M, Sonke J-J. Deformable image registration for adaptive radiation therapy of head and neck cancer: Accuracy and precision in the presence of tumor changes. *International Journal of Radiation Oncology* Biology* Physics* 2014;90:680-687.
229. Hoffmann C, Krause S, Stoiber EM, Mohr A, Rieken S, Schramm O, Debus J, Sterzing F, Bendl R, Giske K. Accuracy quantification of a deformable image registration tool applied in a clinical setting. *Journal of applied clinical medical physics* 2014;15:237-245.
230. Castillo R, Castillo E, Guerra R, Johnson VE, McPhail T, Garg AK, Guerrero T. A framework for evaluation of deformable image registration spatial accuracy using large landmark point sets. *Physics in medicine and biology* 2009;54:1849.
231. Yang D, Zhang M, Chang X, Fu Y, Liu S, Li HH, Mutic S, Duan Y. A method to detect landmark pairs accurately between intra-patient volumetric medical images. *Medical Physics* 2017.
232. Paganelli C, Peroni M, Riboldi M, Sharp GC, Ciardo D, Alterio D, Orecchia R, Baroni G. Scale invariant feature transform in adaptive radiation therapy: A tool for deformable image registration assessment and re-planning indication. *Physics in medicine and biology* 2013;58:287.
233. Christensen GE, Johnson HJ. Consistent image registration. *IEEE transactions on medical imaging* 2001;20:568-582.
234. Christensen GE, Johnson HJ. Invertibility and transitivity analysis for nonrigid image registration. *Journal of electronic imaging* 2003;12:106-118.
235. Christensen GE, Geng X, Kuhl JG, Bruss J, Grabowski TJ, Pirwani IA, Vannier MW, Allen JS, Damasio H. Introduction to the non-rigid image registration evaluation project (nirep). *Lecture Notes in Computer Science* 2006;4057:128-135.
236. Bender ET, Tomé WA. The utilization of consistency metrics for error analysis in deformable image registration. *Physics in Medicine & Biology* 2009;54:5561.
237. Saleh Z, Thor M, Apte AP, Sharp G, Tang X, Veeraraghavan H, Muren L, Deasy J. A multiple-image-based method to evaluate the performance of deformable image registration in the pelvis. *Physics in Medicine & Biology* 2016;61:6172.
238. Saleh ZH, Apte AP, Sharp GC, Shusharina NP, Wang Y, Veeraraghavan H, Thor M, Muren LP, Rao SS, Lee NY. The distance discordance metric—a novel approach to quantifying spatial uncertainties in intra-and inter-patient deformable image registration. *Physics in Medicine & Biology* 2014;59:733.
239. Ou Y, Ye DH, Pohl KM, Davatzikos C. Validation of dramms among 12 popular methods in cross-subject cardiac mri registration. WBIR. Springer. 2012. pp. 209-219.
240. Vercauteren T, Pennec X, Perchant A, Ayache N. Non-parametric diffeomorphic image registration with the demons algorithm. *Medical Image Computing and Computer-Assisted Intervention–MICCAI 2007* 2007:319-326.
241. Zhong H, Peters T, Siebers JV. Fem-based evaluation of deformable image registration for radiation therapy. *Physics in medicine and biology* 2007;52:4721.
242. Li S, Glide-Hurst C, Lu M, Kim J, Wen N, Adams JN, Gordon J, Chetty IJ, Zhong H. Voxel-based statistical analysis of uncertainties associated with deformable image registration. *Physics in medicine and biology* 2013;58:6481.
243. García-Mollá R, de Marco-Blancas N, Bonaque J, Vidueira L, López-Tarjuelo J, Perez-Calatayud J. Validation of a deformable image registration produced by a commercial treatment planning

system in head and neck. *Physica Medica: European Journal of Medical Physics* 2015;31:219-223.

244. Chang J, Suh TS, Lee DS. Development of a deformable lung phantom for the evaluation of deformable registration. *Journal of applied clinical medical physics* 2010;11:281-286.
245. Stanley N, Glide-Hurst C, Kim J, Adams J, Li S, Wen N, Chetty IJ, Zhong H. Using patient-specific phantoms to evaluate deformable image registration algorithms for adaptive radiation therapy. *Journal of applied clinical medical physics* 2013;14:177-194.
246. Chen H, Zhong Z, Liao Y, Pompoš A, Hrycushko B, Albuquerque K, Zhen X, Zhou L, Gu X. A non-rigid point matching method with local topology preservation for accurate bladder dose summation in high dose rate cervical brachytherapy. *Physics in medicine and biology* 2016;61:1217.
247. Wognum S, Heethuis S, Rosario T, Hoogeman M, Bel A. Validation of deformable image registration algorithms on ct images of ex vivo porcine bladders with fiducial markers. *Medical physics* 2014;41.
248. Yeo U, Taylor M, Supple J, Smith R, Dunn L, Kron T, Franich R. Is it sensible to “deform” dose? 3d experimental validation of dose-warping. *Medical physics* 2012;39:5065-5072.
249. Yeo U, Taylor M, Dunn L, Kron T, Smith R, Franich R. A novel methodology for 3d deformable dosimetry. *Medical physics* 2012;39:2203-2213.
250. Liao Y, Wang L, Xu X, Chen H, Chen J, Zhang G, Lei H, Wang R, Zhang S, Gu X. An anthropomorphic abdominal phantom for deformable image registration accuracy validation in adaptive radiation therapy. *Medical physics* 2017;44:2369-2378.
251. Graves YJ, Smith A-A, Mcilvena D, Manilay Z, Lai YK, Rice R, Mell L, Jia X, Jiang SB, Cerviño L. A deformable head and neck phantom with in-vivo dosimetry for adaptive radiotherapy quality assurance. *Medical physics* 2015;42:1490-1497.
252. Kirby N, Chuang C, Pouliot J. A two-dimensional deformable phantom for quantitatively verifying deformation algorithms. *Medical physics* 2011;38:4583-4586.
253. Kirby N, Chuang C, Ueda U, Pouliot J. The need for application-based adaptation of deformable image registration. *Medical physics* 2013;40.
254. Liu F, Hu Y, Zhang Q, Kincaid R, Goodman K, Mageras G. Evaluation of deformable image registration and a motion model in ct images with limited features. *Physics in medicine and biology* 2012;57:2539.
255. Singhrao K, Kirby N, Pouliot J. A three-dimensional head-and-neck phantom for validation of multimodality deformable image registration for adaptive radiotherapy. *Medical physics* 2014;41.
256. Nithiananthan S, Brock K, Daly M, Chan H, Irish J, Siewerdsen J. Demons deformable registration for cbct-guided procedures in the head and neck: Convergence and accuracy. *Medical physics* 2009;36:4755-4764.
257. Juang T, Das S, Adamovics J, Benning R, Oldham M. On the need for comprehensive validation of deformable image registration, investigated with a novel 3-dimensional deformable dosimeter. *International Journal of Radiation Oncology* Biology* Physics* 2013;87:414-421.
258. Velec M, Juang T, Moseley JL, Oldham M, Brock KK. Utility and validation of biomechanical deformable image registration in low-contrast images. *Practical radiation oncology* 2015;5:e401-e408.
259. Neylon J, Qi X, Sheng K, Staton R, Pukala J, Manon R, Low D, Kupelian P, Santhanam A. A gpu based high-resolution multilevel biomechanical head and neck model for validating deformable image registration. *Medical physics* 2015;42:232-243.
260. Segars W, Sturgeon G, Mendonca S, Grimes J, Tsui BM. 4d xcat phantom for multimodality imaging research. *Medical physics* 2010;37:4902-4915.
261. Nie K, Chuang C, Kirby N, Braunstein S, Pouliot J. Site-specific deformable imaging registration algorithm selection using patient-based simulated deformations. *Medical physics* 2013;40.
262. Loi G, Fusella M, Lanzi E, Cagni E, Garibaldi C, Iacoviello G, Lucio F, Menghi E, Miceli R, Orlandini LC. Performance of commercially available deformable image registration platforms for

contour propagation using patient-based computational phantoms: A multi-institutional study. *Medical physics* 2017.

263. Varadhan R, Karangelis G, Krishnan K, Hui S. A framework for deformable image registration validation in radiotherapy clinical applications. *Journal of applied clinical medical physics* 2013;14:192-213.
264. Vandemeulebroucke J, Sarrut D, Clarysse P. The popi-model, a point-validated pixel-based breathing thorax model. XVth international conference on the use of computers in radiation therapy (ICCR). 2007. pp. 195-199.
265. Castillo R, Castillo E, Fuentes D, Ahmad M, Wood AM, Ludwig MS, Guerrero T. A reference dataset for deformable image registration spatial accuracy evaluation using the copdgene study archive. *Physics in medicine and biology* 2013;58:2861.
266. Pukala J, Meeks SL, Staton RJ, Bova FJ, Mañon RR, Langen KM. A virtual phantom library for the quantification of deformable image registration uncertainties in patients with cancers of the head and neck. *Medical physics* 2013;40:111703.
267. Zhong H, Kim J, Chetty IJ. Analysis of deformable image registration accuracy using computational modeling. *Medical physics* 2010;37:970-979.
268. Pukala J, Johnson PB, Shah AP, Langen KM, Bova FJ, Staton RJ, Mañon RR, Kelly P, Meeks SL. Benchmarking of five commercial deformable image registration algorithms for head and neck patients. *Journal of applied clinical medical physics* 2016;17:25-40.
269. Castadot P, Lee JA, Parraga A, Geets X, Macq B, Grégoire V. Comparison of 12 deformable registration strategies in adaptive radiation therapy for the treatment of head and neck tumors. *Radiotherapy and oncology* 2008;89:1-12.
270. Hardcastle N, Tomé WA, Cannon DM, Brouwer CL, Wittendorp PW, Dogan N, Guckenberger M, Allaire S, Mallya Y, Kumar P. A multi-institution evaluation of deformable image registration algorithms for automatic organ delineation in adaptive head and neck radiotherapy. *Radiat Oncol* 2012;7:90.
271. Li X, Zhang Y, Shi Y, Wu S, Xiao Y, Gu X, Zhen X, Zhou L. Comprehensive evaluation of ten deformable image registration algorithms for contour propagation between ct and cone-beam ct images in adaptive head & neck radiotherapy. *PloS one* 2017;12:e0175906.
272. Kashani R, Hub M, Balter JM, Kessler ML, Dong L, Zhang L, Xing L, Xie Y, Hawkes D, Schnabel JA. Objective assessment of deformable image registration in radiotherapy: A multi-institution study. *Medical physics* 2008;35:5944-5953.
273. Kadoya N, Nakajima Y, Saito M, Miyabe Y, Kurooka M, Kito S, Fujita Y, Sasaki M, Arai K, Tani K. Multi-institutional validation study of commercially available deformable image registration software for thoracic images. *International Journal of Radiation Oncology• Biology• Physics* 2016;96:422-431.
274. Nie K, Pouliot J, Smith E, Chuang C. Performance variations among clinically available deformable image registration tools in adaptive radiotherapy—how should we evaluate and interpret the result? *Journal of applied clinical medical physics* 2016;17:328-340.
275. Yeo U, Supple J, Taylor M, Smith R, Kron T, Franich R. Performance of 12 dir algorithms in low-contrast regions for mass and density conserving deformation. *Medical physics* 2013;40.
276. Kadoya N, Fujita Y, Katsuta Y, Dobashi S, Takeda K, Kishi K, Kubozono M, Umezawa R, Sugawara T, Matsushita H. Evaluation of various deformable image registration algorithms for thoracic images. *Journal of radiation research* 2013;55:175-182.
277. Kierkels RG, den Otter LA, Korevaar EW, Langendijk JA, van der Schaaf A, Knopf A-C, Sijtsema NM. An automated, quantitative, and case-specific evaluation of deformable image registration in computed tomography images. *Physics in medicine and biology* 2017.
278. Murphy K, Van Ginneken B, Reinhardt JM, Kabus S, Ding K, Deng X, Cao K, Du K, Christensen GE, Garcia V. Evaluation of registration methods on thoracic ct: The empire10 challenge. *IEEE transactions on medical imaging* 2011;30:1901-1920.
279. Brock KK, Consortium DRA. Results of a multi-institution deformable registration accuracy study (midras). *International Journal of Radiation Oncology* Biology* Physics* 2010;76:583-596.

280. Neylon J, Min Y, Low DA, Santhanam A. A neural network approach for fast, automated quantification of dir performance. *Medical physics* 2017.

2.3 DISCUSSION : RECALAGE DÉFORMABLE POUR LES CANCERS DU COL DE L'UTÉRUS

Le recalage déformable est devenu un outil incontournable dans le contexte de la radiothérapie. Ses avantages sont multiples et les industriels continuent d'intégrer ce type de méthode dans leurs outils cliniques. Certains défis restent encore difficilement atteignables en fonction de la localisation anatomique et de l'application et il n'existe pas de méthode universelle adaptée à toutes les applications, localisations et modalités d'image. Les récentes études montrent un certain attrait vers des méthodes hybrides permettant d'obtenir à la fois des correspondances globales et locales reposant sur des propriétés biomécaniques (par ex. glissement entre les organes).

Dans le contexte des cancers du col utérin, le recalage déformable est un outil important puisque cette localisation montre de fortes variations anatomiques au cours du traitement. La forte amplitude et la complexité des déformations (par ex. glissement, fonte tumorale, gaz…) sont un réel défi pour le recalage [1]. De nombreuses études ont proposé l'usage du recalage pour la quantification des variations anatomiques aux différentes étapes des traitements par radiothérapie externe et curiethérapie [2], avec des problématiques différentes. Par rapport à la curiethérapie, des déformations plus importantes sont attendues au cours de la RT dues à un protocole plus souple (volumes des OAR variables, absence d'applicateur et de ballon de Foley…) et à la réponse au traitement. Cependant, la curiethérapie est aussi sujette à des variations anatomiques, notamment dues à l'insertion et à des déplacements de l'applicateur ainsi que des variations de volumes.

Les principales études utilisant le recalage déformable dans le contexte des cancers du col utérin sont décrites ci-dessous.

2.3.1 RECALAGE DEFORMABLE POUR LA PROPAGATION DES CONTOURS

Pour assister l'étape de délinéation des organes, le recalage déformable a été utilisé afin de mettre en correspondance, en intra-patiente, l'image de planification avec des images per-thérapeutiques ou, en inter-patientes, d'un atlas vers l'image à délinéer.

Pour le recalage intra-patiente, une méthode semi-automatique (*salient points-based registration*) par interpolation *B-spline* et guidée par l'information mutuelle [3] (*Mutual Information*, MI) a été proposée [4]. Cette méthode pouvait être initialisée à l'aide de marqueurs anatomiques (*landmarks)* placés au préalable par un expert et permettait de réduire l'erreur médiane entre les contours à 3.2 mm. Dans le même contexte, une version multidimensionnelle de l'information mutuelle, appliquée à des descripteurs calculés par dérivations de l'intensité, a été proposée [5]. Les résultats montrent un DSC autour de 0.8 pour l'ensemble des organes analysés (CTV, vessie, rectum). Une méthode hybride a été proposée, reposant sur une FFD simultanément guidée par une segmentation automatique par modèle statistique de forme et contrainte par le déterminant du Jacobien [6]. Cette méthode permettait d'améliorer significativement les résultats avec une correspondance finale en termes de superposition de volume supérieure à 90% pour la vessie et l'utérus.

Pour le recalage inter-patientes, une méthode hybride basée sur un modèle statistique de forme reposant sur une analyse en composantes principales (*Principal Components Analysis*, PCA) a été proposée [7]. La représentation des déformations dominantes du modèle permettait de contraindre le champ de déformations estimé par la FFD. La méthode améliore les résultats en termes de DSC et de distance de Hausdorff (*Hausdorff Distance*, HD) par rapport à une FFD classique, pour le CTV et la vessie. Cependant, les contours propagés correspondaient peu aux contours manuels, avec un DSC moyen à 0.53 pour le CTV. L'ensemble de ces études utilise l'IRM comme images per-thérapeutiques car elle offre un meilleur contraste et permet la définition du GTV. Considérant les images TDM, Bondar *et al* [8] ont évalué la propagation des contours par recalage déformable (méthode des Démons ou outil commercial) depuis un atlas, sur images TDM [9]. La méthode commerciale était efficace pour propager les contours de l'atlas vers les anatomies de la cohorte avec un DSC supérieur à 0.8. La méthode des Démons obtenait des résultats inférieurs.

Pour la curiethérapie, une méthode de recalage déformable commerciale, basée sur une FFD, a été utilisée pour propager les contours de la première séance vers quatre autres [10]. L'objectif était de réduire le temps de délinéation, à l'étape de l'optimisation de la dose, pour réduire la probabilité de déplacement de l'applicateur entre la planification et la délivrance. L'évaluation de cette méthode proposée a été faite avec des critères géométriques et dosimétriques, entre les contours manuels et propagés. Aucune différence significative n'a été observée entre les contours lorsque le volume de la vessie respectait la contrainte d'un volume inférieur à 100cc.

2.3.2 RECALAGE DEFORMABLE POUR LA RADIOTHERAPIE ADAPTATIVE

2.3.2.1 Planification de la radiothérapie externe

Dans un contexte de radiothérapie adaptative, le recalage déformable a été proposé pour assister l'étape de planification en considérant des images déjà délinéées. Dans de nombreuses études de l'équipe du *Erasmus Medical Center-Cancer Institute* (*Rotterdam, The Netherlands*), utilisent une méthode de recalage déformable de surface (*Thin Plate Spline Robust Point Matching*, TPS-RPM) qui repose sur une assignation des points par minimisation globale de correspondances, adaptatives, afin de définir une transformation TPS [11,12]. Elle a été utilisée pour mettre en correspondance les anatomies du col et de l'utérus, entre deux TDM de planification [13,14] pour générer les sous-ITV d'une librairie de plans de traitement [15-18]. Cette approche a été reprise par d'autres études [19,20].

Par ailleurs, le recalage déformable issu d'un TPS commercial a été utilisé pour définir un modèle statistique de forme intra- et inter-patientes reposant sur une PCA [21]. Cette méthode permettait de générer les probabilités de couverture dosimétrique du CTV et des OAR d'une nouvelle patiente au moment de la planification. Une pseudo dose délivrée était estimée en simulant des déformations aléatoires grâce au modèle.

2.3.2.2 Estimation de la dose délivrée en radiothérapie externe

Pour l'estimation de la dose délivrée, la majorité des études a utilisé une méthode exploitant des contours manuellement délinéés. Trois études [22-24], menées sur la même cohorte de patientes, ont utilisé une méthode de recalage déformable reposant sur le modèle biomécanique MORFEUS [25]. Tout d'abord, cette méthode nécessite la définition de conditions aux limites (déplacements point-à-point entre les surfaces des organes), estimés par une approche de recalage déformable de surface. Ensuite, un modèle en élément finis (*Finite Element Modeling*, FEM), représentant les organes par des maillages d'éléments finis tétraédrique, est généré. Finalement, l'étape d'analyse des éléments finis permet de calculer les contraintes appliquées à chaque élément interne des représentations volumiques du FEM, en fonction des conditions aux limites imposées et des propriétés matérielles définies (élasticité). Ces contraintes internes correspondent au champ de déformations dense. Ces études ne montrent aucune évaluation géométrique de la méthode pour cette localisation, bien qu'elle ait déjà montré de bonnes performances pour le pelvis masculin [26].

2.3.2.3 Estimation de la dose délivrée en curiethérapie

Plusieurs méthodes de recalage déformable ont été proposées et évaluées afin de mettre en correspondance les anatomies des différentes fractions de la BT vers l'anatomie de la planification, dans l'objectif d'estimer la dose délivrée. Pour cette application, la littérature propose trois méthodes de recalage basée sur l'intensité des images TDM, soit reposant sur les Démons [27,28] ou soit issue d'un outil commercial [29]. Puisque l'image TDM manque de contraste entre les tissus mous, les déformations ont été estimées à partir des contours manuellement délinéés pour deux de ces études [27,29]. Une approche automatisée a été proposée par [28], permettant la délinéation du dispositif de curiethérapie. Cette segmentation permettait d'initialiser les Démons par la méthode de la TPS-RPM et donc de s'abstenir des irrégularités d'intensité dues à la présence du dispositif.

Parmi les études de l'équipe de *Aarhus University Hospital* (*Denmark*), une approche biomécanique modélisant un modèle ressort/amortisseur suivant la loi de Hookes a été proposé pour recaler les surfaces de la vessie et du rectum [30-33]. Une méthode de mise en correspondance de points de surface par un modèle de mélange de gaussiennes et interpolée par une TPS [34] a été utilisé pour les mêmes organes [35]. Les deux approches montraient une bonne correspondance point-à-point avec une ICE autour de 2 mm.

L'objectif de l'ensemble de ces études était de comparer les indices des HDV de la dose délivrée estimée par recalage déformable ou par la méthode d'addition directe suivant les recommandations de l'ESTRO [36]. De fait, peu d'entre elles présentent une évaluation complète de la méthode de recalage. Uniquement deux études ont proposé une évaluation à partir d'un fantôme anatomique basée soit sur une patiente déformée synthétiquement [28] soit sur une représentation du rectum par un cylindre de différents diamètres [29].

2.3.2.4 Combinaison de la radiothérapie externe et de la curiethérapie

Enfin, le recalage déformable a été envisagé pour mettre en correspondance l'anatomie de la radiothérapie (sans applicateur) avec celle de la curiethérapie. L'intérêt de modéliser les déformations induites par la présence de l'applicateur et du ballon de Foley est de pouvoir mettre en correspondance les doses des différents traitements sur une anatomie commune. L'estimation de la dose totale délivrée permettrait d'aider à la compréhension et la prédiction de la toxicité locale des OAR [37]. Différentes méthodes ont été proposées pour cette application. Une méthode de recalage déformable, basée sur la mécanique des fluides couplée à une initialisation manuelle, a été développée pour recaler des images TDM délinéées avec et sans applicateur de curiethérapie [1]. Cette méthode a permis d'estimer des déformations jusqu'à 28 mm et d'assurer une bonne superposition des contours. Une méthode FFD, autorisant un recouvrement des vecteurs de déformation, a été proposée pour simuler la disparition de l'applicateur entre deux IRM (avant et après insertion) [38]. L'évaluation de cette méthode était limitée au DSC et au volume résiduel de l'applicateur présent après déformation. Une méthode utilisant la TPS-RPM à partir de points saillants extraits automatiquement a été proposée pour mettre en correspondance la TDM de planification de RT avec l'IRM de la BT pour analyser la dose totale au rectum [39]. Plus récemment, l'estimation des déformations de chaque organe, indépendamment par la méthode TPS-RPM, a été proposée [40]. Cette étude propose ensuite la combinaison de ces déformations indépendantes en un champ dense, grâce à une interpolation par plaque mince (*Thin Plate Spline*, TPS) qui conserve les discontinuités à l'interface des organes pour simuler les glissements. L'évaluation de cette approche a montré une bonne correspondance des marqueurs anatomiques (bifurcation de vaisseaux, ligne centrale de l'utérus, trompes de Fallope…), non considérés dans le recalage.

Pour la planification de la curiethérapie, la comparaison et la combinaison des traitements s'exprime classiquement en EQD2. La D90 et la D2cc doivent être rapportées pour le HR-CTV et les OAR car ils sont prédictifs du contrôle tumoral [41] et de la toxicité [42], respectivement. Les recommandations pour fusionner l'EBRT et la BT supposent alors une dose de planification d'EBRT uniforme, ce qui revient à additionner la prescription de radiothérapie externe du CTV aux OAR [36]. La dose de planification d'EBRT est donc propagée rigidement sur l'imagerie de planification de la BT, sans prendre en compte la correspondance locale des organes. Cependant, il a été montré que l'usage du recalage déformable pour cette propagation rapportait des valeurs plus importantes pour la D90 et la D2cc au HR-CTV et aux OAR, respectivement [43]. Deux études ont estimé la dose délivrée par l'ensemble du traitement à partir du recalage déformable [44,45]. Les études comprenaient 5 et 11 patientes. Les doses de chaque fraction (RC3D pour l'EBRT et HDR-BT) ont été déformées vers le premier scanner de la BT. Les résultats rapportent cette fois ci une surestimation des indices des DVH par la méthode d'addition directe comparés au recalage déformable, bien que non significative.

2.4 CONCLUSION

Au total, un grand nombre d'études de la littérature présentent différentes méthodes de recalage déformable qui ont été développées ou utilisées depuis un système commercial. Dans ce deuxième cas, la méthode de recalage exploitée n'est généralement pas explicitement décrite. Les variations entre les applications, les objectifs et les modalités d'image peuvent expliquer pourquoi aucune méthode de recalage déformable n'a été définie comme référence pour la localisation du col de l'utérus. Cependant, certaines similarités entre les méthodes existent en fonction des applications et des données de chaque étude.

La FFD est la méthode la plus souvent utilisée pour l'estimation des déformations intra-patiente avec un bon recouvrement global initial de l'anatomie et à partir de l'image IRM [4-6]. Elle est cependant très limitée pour quantifier des déformations inter-patientes [7] et n'est jamais proposée pour des applications sur images TDM. Pour des applications utilisant des images TDM, de par le manque de contraste de ce type d'images, la méthode des Démons est appliquée aux contours des organes [27] ou guidée par une étape de prétraitement [28]. Des méthodes proches sont implémentées dans des systèmes commerciaux et autorisent l'utilisation des contours manuels afin d'estimer des grandes déformations [21,29,46] Dans ce cas l'utilisation de modèles élastiques (par ex. TPS-RPM ou modèle de mélange de gaussiennes) [13,14,35,40] ou biomécaniques [22-24,30-33], a été privilégié.

Finalement, l'intérêt du recalage déformable est toujours en cours d'évaluation pour quantifier les déformations entre les deux parties du traitement, par exemple pour mettre en correspondances les anatomies avec et sans applicateur de curiethérapie. La complexité et l'amplitude de ces déformations rend leur évaluation difficile et limite les applications dosimétriques.

Considérant la littérature, différentes méthodes de recalage déformable seront proposées pour les différentes applications étudiées dans ces travaux de thèse, suivant l'objectif considéré et les données exploitées.

2.5 RÉFÉRENCES

1. Christensen GE, Carlson B, Chao KC, Yin P, Grigsby PW, Nguyen K, Dempsey JF, Lerma FA, Bae KT, Vannier MW. Image-based dose planning of intracavitary brachytherapy: Registration of serial-imaging studies using deformable anatomic templates. *International Journal of Radiation Oncology• Biology• Physics* 2001;51:227-243.
2. Ghose S, Holloway L, Lim K, Chan P, Veera J, Vinod SK, Liney G, Greer PB, Dowling J. A review of segmentation and deformable registration methods applied to adaptive cervical cancer radiation therapy treatment planning. *Artificial intelligence in medicine* 2015;64:75-87.
3. Studholme C, Hill DL, Hawkes DJ. An overlap invariant entropy measure of 3d medical image alignment. *Pattern recognition* 1999;32:71-86.
4. Van Der Put R, Kerkhof E, Raaymakers B, Jürgenliemk-Schulz I, Lagendijk J. Contour propagation in mri-guided radiotherapy treatment of cervical cancer: The accuracy of rigid, non-rigid and semi-automatic registrations. *Physics in medicine and biology* 2009;54:7135.
5. Staring M, Van Der Heide U, Klein S, Viergever M, Pluim JP. Registration of cervical mri using multifeature mutual information. *Medical Imaging, IEEE Transactions on* 2009;28:1412-1421.
6. Lu C, Chelikani S, Jaffray D, Milosevic MF, Staib LH, Duncan JS. Simultaneous nonrigid registration, segmentation, and tumor detection in mri guided cervical cancer radiation therapy. *Medical Imaging, IEEE Transactions on* 2012;31:1213-1227.
7. Berendsen FF, Van Der Heide UA, Langerak TR, Kotte AN, Pluim JP. Free-form image registration regularized by a statistical shape model: Application to organ segmentation in cervical mr. *Computer Vision and Image Understanding* 2013;117:1119-1127.
8. Bondar ML, Hoogeman M, Schillemans W, Heijmen B. Intra-patient semi-automated segmentation of the cervix–uterus in ct-images for adaptive radiotherapy of cervical cancer. *Physics in medicine and biology* 2013;58:5317.
9. Langerak T, Heijkoop S, Quint S, Mens J-W, Heijmen B, Hoogeman M. Towards automatic plan selection for radiotherapy of cervical cancer by fast automatic segmentation of cone beam ct scans Medical image computing and computer-assisted intervention–miccai 2014: Springer; 2014. pp. 528-535.
10. Chapman CH, Polan D, Vineberg K, Jolly S, Maturen KE, Brock KK, Prisciandaro JI. Deformable image registration–based contour propagation yields clinically acceptable plans for mri-based cervical cancer brachytherapy planning. *Brachytherapy* 2018.
11. Yang J. The thin plate spline robust point matching (tps-rpm) algorithm: A revisit. *Pattern Recognition Letters* 2011;32:910-918.
12. Chui H, Rangarajan A. A new point matching algorithm for non-rigid registration. *Computer Vision and Image Understanding* 2003;89:114-141.
13. Osorio EMV, Hoogeman MS, Bondar L, Levendag PC, Heijmen BJ. A novel flexible framework with automatic feature correspondence optimization for nonrigid registration in radiotherapy. *Medical physics* 2009;36:2848-2859.
14. Bondar L, Hoogeman MS, Osorio EMV, Heijmen BJ. A symmetric nonrigid registration method to handle large organ deformations in cervical cancer patients. *Medical physics* 2010;37:3760-3772.
15. Bondar L, Hoogeman M, Mens JW, Dhawtal G, De Pree I, Ahmad R, Quint S, Heijmen B. Toward an individualized target motion management for imrt of cervical cancer based on model-predicted cervix–uterus shape and position. *Radiotherapy and Oncology* 2011;99:240-245.
16. Bondar M, Hoogeman M, Mens J, Quint S, Ahmad R, Dhawtal G, Heijmen B. Individualized nonadaptive and online-adaptive intensity-modulated radiotherapy treatment strategies for cervical cancer patients based on pretreatment acquired variable bladder filling computed tomography scans. *International Journal of Radiation Oncology* Biology* Physics* 2012;83:1617-1623.
17. Heijkoop ST, Langerak TR, Quint S, Bondar L, Mens JWM, Heijmen BJ, Hoogeman MS. Clinical implementation of an online adaptive plan-of-the-day protocol for nonrigid motion

management in locally advanced cervical cancer imrt. *Int J Radiat Oncol Biol Phys* 2014;90:673-679.

18. Nováková E, Heijkoop S, Quint S, Zolnay A, Mens J, Godart J, Heijmen B, Hoogeman M. What is the optimal number of library plans in art for locally advanced cervical cancer? *Radiotherapy and Oncology* 2017.
19. Buschmann M, Majercakova K, Sturdza A, Smet S, Najjari D, Daniel M, Pötter R, Georg D, Seppenwoolde Y. Image guided adaptive external beam radiation therapy for cervix cancer: Evaluation of a clinically implemented plan-of-the-day technique. *Zeitschrift für Medizinische Physik* 2017.
20. Seppenwoolde Y, Daniel M, Furtado H, Georg D. Organ contour adaptor to create new structures to use for adaptive radiotherapy of cervix cancer using matlab bridge and 3dslicer/slicerrt. ICART/MICCAI Workshop Proceedings. 2015. pp. 66-72.
21. Tilly D, van de Schoot AJ, Grusell E, Bel A, Ahnesjö A. Dose coverage calculation using a statistical shape model—applied to cervical cancer radiotherapy. *Physics in Medicine and Biology* 2017;62:4140.
22. Lim K, Stewart J, Kelly V, Xie J, Brock KK, Moseley J, Cho Y-B, Fyles A, Lundin A, Rehbinder H. Dosimetrically triggered adaptive intensity modulated radiation therapy for cervical cancer. *International Journal of Radiation Oncology* Biology* Physics* 2014;90:147-154.
23. Stewart J, Lim K, Kelly V, Xie J, Brock KK, Moseley J, Cho Y-B, Fyles A, Lundin A, Rehbinder H. Automated weekly replanning for intensity-modulated radiotherapy of cervix cancer. *International Journal of Radiation Oncology* Biology* Physics* 2010;78:350-358.
24. Oh S, Stewart J, Moseley J, Kelly V, Lim K, Xie J, Fyles A, Brock KK, Lundin A, Rehbinder H, Milosevic M, Jaffray D, Cho YB. Hybrid adaptive radiotherapy with on-line mri in cervix cancer imrt. *Radiother Oncol* 2014;110:323-328.
25. Brock K, Sharpe M, Dawson L, Kim S, Jaffray D. Accuracy of finite element model-based multi-organ deformable image registration. *Medical physics* 2005;32:1647-1659.
26. Hensel JM, Ménard C, Chung PW, Milosevic MF, Kirilova A, Moseley JL, Haider MA, Brock KK. Development of multiorgan finite element-based prostate deformation model enabling registration of endorectal coil magnetic resonance imaging for radiotherapy planning. *International Journal of Radiation Oncology• Biology• Physics* 2007;68:1522-1528.
27. Ryckman JM, Shelton JW, Waller AF, Schreibmann E, Latifi K, Diaz R. Anatomic structure-based deformable image registration of brachytherapy implants in the treatment of locally advanced cervix cancer. *Brachytherapy* 2016;15:584-592.
28. Zhen X, Chen H, Yan H, Zhou L, Mell LK, Yashar CM, Jiang S, Jia X, Gu X, Cervino L. A segmentation and point-matching enhanced efficient deformable image registration method for dose accumulation between hdr ct images. *Physics in Medicine & Biology* 2015;60:2981.
29. Hayashi K, Isohashi F, Akino Y, Wakai N, Mabuchi S, Suzuki O, Seo Y, Ootani Y, Sumida I, Yoshioka Y. Estimation of the total rectal dose of radical external beam and intracavitary radiotherapy for uterine cervical cancer using the deformable image registration method. *Journal of radiation research* 2015;56:546-552.
30. Andersen ES, Noe KØ, Sørensen TS, Nielsen SK, Fokdal L, Paludan M, Lindegaard JC, Tanderup K. Simple dvh parameter addition as compared to deformable registration for bladder dose accumulation in cervix cancer brachytherapy. *Radiotherapy and Oncology* 2013;107:52-57.
31. Jamema SV, Mahantshetty U, Andersen E, Noe KØ, Sørensen TS, Kallehauge JF, Shrivastava SK, Deshpande DD, Tanderup K. Uncertainties of deformable image registration for dose accumulation of high-dose regions in bladder and rectum in locally advanced cervical cancer. *Brachytherapy* 2015;14:953-962.
32. Noe KØ, Tanderup K, Sørensen TS. Surface membrane based bladder registration for evaluation of accumulated dose during brachytherapy in cervical cancer. Biomedical Imaging: From Nano to Macro, 2011 IEEE International Symposium on. IEEE. 2011. pp. 1253-1256.
33. Andersen E, Muren L, Sørensen TS, Noe KØ, Thor M, Petersen J, Høyer M, Bentzen L, Tanderup K. Bladder dose accumulation based on a biomechanical deformable image registration

algorithm in volumetric modulated arc therapy for prostate cancer. *Physics in medicine and biology* 2012;57:7089.

34. Jian B, Vemuri BC. A robust algorithm for point set registration using mixture of gaussians. Computer Vision, 2005. ICCV 2005. Tenth IEEE International Conference on. IEEE. 2005. pp. 1246-1251.
35. Kobayashi K, Murakami N, Wakita A, Nakamura S, Okamoto H, Umezawa R, Takahashi K, Inaba K, Igaki H, Ito Y. Dosimetric variations due to interfraction organ deformation in cervical cancer brachytherapy. *Radiotherapy and Oncology* 2015;117:555-558.
36. Pötter R, Haie-Meder C, Van Limbergen E, Barillot I, De Brabandere M, Dimopoulos J, Dumas I, Erickson B, Lang S, Nulens A. Recommendations from gynaecological (gyn) gec estro working group (ii): Concepts and terms in 3d image-based treatment planning in cervix cancer brachytherapy—3d dose volume parameters and aspects of 3d image-based anatomy, radiation physics, radiobiology. *Radiotherapy and Oncology* 2006;78:67-77.
37. Chen J, Chen H, Zhong Z, Wang Z, Hrycushko B, Zhou L, Jiang S, Albuquerque K, Gu X, Zhen X. Investigating rectal toxicity associated dosimetric features with deformable accumulated rectal surface dose maps for cervical cancer radiotherapy. *Radiation Oncology* 2018;13:125.
38. Berendsen F, Kotte A, de Leeuw A, Jürgenliemk-Schulz I, Viergever M, Pluim J. Registration of structurally dissimilar images in mri-based brachytherapy. *Physics in Medicine & Biology* 2014;59:4033.
39. van Heerden LE, Houweling AC, Koedooder K, van Kesteren Z, van Wieringen N, Rasch CR, Pieters BR, Bel A. Structure-based deformable image registration: Added value for dose accumulation of external beam radiotherapy and brachytherapy in cervical cancer. *Radiotherapy and Oncology* 2017;123:319-324.
40. Vásquez Osorio EM, Kolkman-Deurloo IKK, Schuring-Pereira M, Zolnay A, Heijmen BJ, Hoogeman MS. Improving anatomical mapping of complexly deformed anatomy for external beam radiotherapy and brachytherapy dose accumulation in cervical cancer. *Medical physics* 2015;42:206-220.
41. Dimopoulos JC, Pötter R, Lang S, Fidarova E, Georg P, Dörr W, Kirisits C. Dose–effect relationship for local control of cervical cancer by magnetic resonance image-guided brachytherapy. *Radiotherapy and oncology* 2009;93:311-315.
42. Georg P, Kirisits C, Goldner G, Dörr W, Hammer J, Pötzi R, Berger D, Dimopoulos J, Georg D, Pötter R. Correlation of dose–volume parameters, endoscopic and clinical rectal side effects in cervix cancer patients treated with definitive radiotherapy including mri-based brachytherapy. *Radiotherapy and Oncology* 2009;91:173-180.
43. Kim H, Huq MS, Houser C, Beriwal S, Michalski D. Mapping of dose distribution from imrt onto mri-guided high dose rate brachytherapy using deformable image registration for cervical cancer treatments: Preliminary study with commercially available software. *Journal of contemporary brachytherapy* 2014;6:178.
44. Abe T, Tamaki T, Makino S, Ebara T, Hirai R, Miyaura K, Kumazaki Y, Ohno T, Shikama N, Nakano T. Assessing cumulative dose distributions in combined radiotherapy for cervical cancer using deformable image registration with pre-imaging preparations. *Radiation Oncology* 2014;9:1.
45. Kadoya N, Miyasaka Y, Nakajima Y, Kuroda Y, Ito K, Chiba M, Sato K, Dobashi S, Yamamoto T, Takahashi N. Evaluation of deformable image registration between external beam radiotherapy and hdr brachytherapy for cervical cancer with a 3d-printed deformable pelvis phantom. *Medical physics* 2017;44:1445-1455.
46. Teo B-K, Millar LPB, Ding X, Lin LL. Assessment of cumulative external beam and intracavitary brachytherapy organ doses in gynecologic cancers using deformable dose summation. *Radiotherapy and Oncology* 2015;115:195-202.

3 LIBRAIRIE EVOLUTIVE GUIDEE PAR L'IMAGERIE CBCT POUR L'IMRT DES CANCERS DU COL UTERIN

3 Librairie évolutive guidée par l'imagerie CBCT pour l'IMRT des cancers du col utérin 102

- 3.1 Introduction 103
- 3.2 Article : "CBCT-guided evolutive library for cervical adaptive IMRT" 105
  - 3.2.1 Introduction 107
  - 3.2.2 Materials and methods 108
  - 3.2.3 Results 115
  - 3.2.4 Discussion 123
  - 3.2.5 Conclusion 126
  - 3.2.6 References 127
- 3.3 Discussion 131
- 3.4 Conclusion 135
- 3.5 Références 136

3.1 INTRODUCTION

La littérature actuelle a proposé un ensemble de stratégies pour prendre en compte les variations anatomiques survenant en cours de traitement (*cf*. section 1.4.3) [1]. Ces stratégies sont notamment les approches standard reposant sur une unique planification avec des marges de PTV populationnelles, des librairies de plans de traitement générées à partir de plusieurs images TDM acquises avec des volumes de vessie variables et des replanifications en cours de traitement. Cependant, ces études sont hautement hétérogènes en termes de taille de cohorte, de définition des volumes d'intérêts, de nombre d'images utilisées et de marge du PTV. Il est donc difficile de comparer les approches proposées et de conclure sur la stratégie la plus adéquate.

Dans une étude antérieure [2], nous avons comparé une librairie de plans de traitement reposant sur l'acquisition de trois scanners de planification (suivant des volumes de vessie variables) à une stratégie standard, sur une cohorte de 10 patientes. Avec une marge du PTV réduite de 15 à 10 mm, les résultats ont montré un gain significatif de la couverture du CTV. Comme dans la littérature [3], cette étude confirme le potentiel de la librairie de plans de traitement pour assurer une couverture tumorale tout en réduisant les marges du PTV, permettant d'améliorer l'épargne du rectum et de la cavité péritonéale. Cependant, cette étude montre aussi les limites de cette approche lorsque l'anatomie de la séance est très différente de celles représentées dans la librairie. En effet, certaines Ces patientes présentent de ce fait un haut risque de sous-dosage du CTV.

L'exploitation des images acquises en cours de traitement peut donc être envisagée non seulement pour sélectionner le plan de traitement le plus adapté, mais aussi pour identifier une éventuelle baisse de la couverture de la cible et donc une mise à jour de la librairie. L'objectif de ce travail est donc de proposer une librairie de plans de traitement qui puisse être enrichie de l'anatomie issue des CBCT. Cette approche permettrait de bénéficier des avantages des stratégies déjà existantes, la librairie de plans de traitement et les replanifications déclenchées. De plus elle ne nécessite pas d'acquisitions supplémentaires puisque l'imagerie CBCT est indispensable pour le choix du plan de traitement optimal. Cependant, plusieurs questions se posent quant à l'implémentation d'une stratégie de ce type.

- Quels sont les instants et le nombre de replanification optimaux pour enrichir une librairie de plans de traitement ?
- Quelles sont les performances d'une telle librairie par rapport aux stratégies déjà existantes ?

Les objectifs de cette étude sont, dans un premier temps, de simuler les principales stratégies de la littérature (stratégie standard, replanification à mi-traitement, ITV et librairie de plans de traitement) afin d'apporter une conclusion quant à leur performance sur une même cohorte. Dans un second temps, l'imagerie embarquée CBCT sera exploitée pour enrichir la librairie de plans, dans le cadre d'une stratégie originale, appelée « librairie évolutive ».

Si l'implémentation de ces différentes stratégies de traitement ne nécessite pas d'étapes de recalage, leur évaluation repose en partie sur la mise en correspondance des anatomies des différentes patientes pour propager des cartes de couverture des organes (cible et OAR) et fournir une description synthétique de cette couverture. Pour cette étape, un recalage dense (défini en chaque voxel) est nécessaire pour propager l'ensemble de ces cartes. Nous nous sommes donc orientés vers un recalage par la méthode des Démons difféomorphiques. Etant donné le faible contraste entre les tissus mous dans les images TDM et CBCT, et puisque les délinéations des organes étaient disponibles, ce recalage a exploité des cartes de distance issues des délinéations des organes. Cette méthode a aussi été utilisée pour l'estimation de la dose délivrée suivant les différentes stratégies et marges de PTV pour la vessie et le rectum d'une patiente [4,5].

Ces travaux ont fait l'objet d'une publication, intitulée « *CBCT-guided evolutive library for cervical adaptive IMRT* », publiée dans le journal *Medical Physics* en 2018 et reproduite ci-dessous.

3.2 ARTICLE : "CBCT-GUIDED EVOLUTIVE LIBRARY FOR CERVICAL ADAPTIVE IMRT"

Bastien Rigaud *MSc* (1,2)*, Antoine Simon *PhD* (1,2), Maxime Gobeli *MD* (3), Caroline Lafond *MD, PhD* (1, 3), Julie Leseur *MD* (3), Anais Barateau *MSc* (1,2), Nicolas Jaksic *MD* (3), Joël Castelli *MD, MSc* (1,2,3), Danièle Williaume *MD* (3), Pascal Haigron *PhD* (1,2) and Renaud De Crevoisier *MD*, *PhD* (1,2,3)*

1. Université de Rennes 1, LTSI, Campus de Beaulieu, Rennes, F-35042
2. INSERM, U1099, Campus de Beaulieu, Rennes, F-35042
3. Centre Eugene Marquis, Radiotherapy Department, Rennes, F-35000

Abstract

Purpose

In the context of adaptive radiation therapy (ART) for locally advanced cervical carcinoma (LACC), this study proposed an original cone-beam computed tomography (CBCT)-guided "Evolutive library" and evaluated it against four other known radiotherapy (RT) strategies.

Material and methods

For 20 patients who underwent intensity-modulated radiation therapy (IMRT) for LACC, three planning CTs (with empty [EB], intermediate [IB], and full [FB] bladder volumes), a CT scan at 20 Gy and bi-weekly CBCTs for 5 weeks were performed. Five RT strategies were simulated for each patient: "Standard RT" was based on one IB planning CT; "internal target volume (ITV)-based RT" was an ITV built from the three planning CTs; "RT with one mid-treatment replanning (MidTtReplan)" corresponded to the standard RT with a replanning at 20 Gy; "Pretreatment library ART" using a planning library based on the three planning CTs; and the "Evolutive library ART", which was the "Pretreatment library ART" strategy enriched by including some CBCT anatomies into the library when the daily clinical target volume (CTV) shape differed from the ones in the library. Two planning target volume (PTV) margins of 7 and 10 mm were evaluated. All the strategies were geometrically compared in terms of the percentage of coverage by the PTV, for the CTV and the organs at risk (OAR) delineated on the CBCT. Inadequate coverage of the CTV and OARs by the PTV was also assessed using deformable image registration. The cumulated dose distributions of each strategy were likewise estimated and compared for one patient.

Results

The "Evolutive library ART" strategy involved a number of added CBCTs: 0 for 55%; 1 for 30%; 2 for 5%; and 3 for 10% of patients. Compared with the other four, this strategy provided the highest CTV geometric coverage by the PTV, with a mean (min – max) coverage of 98.5% (96.4 – 100) for 10 mm margins and 96.2% (93.0 – 99.7) for 7 mm margins ($p < 0.05$). Moreover, this strategy significantly decreased the geometric coverage of the bowel. CTV undercoverage by PTV occurred in the anterior and superior uterine regions for all strategies. The dosimetric analysis at 7 mm similarly demonstrated that the "Evolutive library ART" increased the $V_{42.75Gy}$ of the CTV by 27%, 20%, 13% and 28% compared with "Standard RT", "ITV-based RT", "MidTtReplan" and "Pretreatment library ART", respectively. The

dose to the bowel was also decreased by the “Evolutive library ART” compared with that by the other strategies.

Conclusion

The “Evolutive library ART” is a personalized ART strategy that comprises a pretreatment planning library of three CT scans, enriched for half of the patients by one to three per-treatment CBCTs. This original strategy increased both the CTV coverage and bowel sparing compared with all the other tested strategies and enables us to consider a PTV margin reduction.

3.2.1 INTRODUCTION

Intensity-modulated radiation therapy (IMRT) is increasingly used as a means to reduce normal tissue toxicity in cervical cancer, with or without treatment intensification, such as extended-field radiotherapy or concomitant boost radiotherapy [1-3]. Large intrapelvic intra- and inter-fraction anatomic variations may impede the benefits of IMRT. When occurring in steep-dose gradients around tight planning target volume (PTV) margins, these variations can expose patients to both tumour underdosage and organs at risk (OAR) overdosage [4-6]. Inter-fraction cervical displacements of up to 25 mm, 36 mm, and 23 mm have been reported in the anterior-posterior (AP), superior-inferior (SI), and left-right (LR) directions, respectively [7,8]. Moreover, uterus maximum displacements of 48 mm, 36 mm, and 28 mm have been reported in the AP, SI, and LR directions, respectively [9,10]. Uterine motion is mostly related to bladder filling, while vagina and cervix motion is linked to rectum filling [5,11-18]. Furthermore, large tumour regressions have been observed during treatment, with a mean decrease of 46% (up to 100%) of the gross cervical tumour volume achieved at 30 Gy [19] and 63% (up to 87%) of the cervix at the end of treatment [11,20,21].

Several strategies have previously been proposed to account for these anatomic variations. Defining an internal target volume (ITV) is a simple solution to overcome the risk of clinical target volume (CTV) underdosage, yet with the drawback of increasing OAR overdosage. Replanning at mid-treatment or following many fractions and weekly replannings have been proposed, with a deformable image registration (DIR)-based workflow [22-24]. Some authors have recently proposed adaptive radiation therapy (ART) based on a pretreatment planning library [15,25-29]. However, this approach may be limited in cases of cervix fixity at the planning or of per-treatment tumor shrinking. Nevertheless, these different strategies have not been compared in the same cohort. Moreover, no study has investigated the benefits of using per-treatment CTV shape variations to update a planning library into a tight-fitting planning library, with the aims of improving CTV coverage and OAR sparing [26].

Considering the use of ART for LACC, this work proposed an original strategy named the “cone-beam CT (CBCT)-guided evolutive library”. This strategy takes advantage of the CBCT images acquired during treatment to assess patient positioning and trigger per-treatment replannings, thereby optimizing the treatment library by considering both tumour deformation and shrinkage. This strategy was simulated and compared with four others: standard planning; ITV-based planning; mid-treatment replanning; and a pretreatment planning library.

3.2.2 MATERIALS AND METHODS

3.2.2.1 Patients, tumours, and treatment

This study enrolled 20 patients with a mean age of 51 years (range, 27-68). Stage distribution, according to the International Federation of Gynecology and Obstetrics (FIGO) classification [30], was as follows: IB2, n = 7; IIA-B, n = 9; IIIA-B, n = 3; and IVA, n = 1. Histology revealed squamous cell carcinoma in fifteen patients and adenocarcinoma in five. All patients were treated with a combination of external beam radiation therapy (EBRT) and pulse-dose-rate (PDR) brachytherapy (BT). PDR-BT was delivered in accordance with the GEC-ESTRO recommendations [31]. EBRT delivered a total dose of 45 Gy to the pelvis (supine position), at 1.8 Gy per fraction, using IMRT along with concomitant weekly cisplatin (40 mg/m^2). All patients provided signed informed consent.

3.2.2.2 Planning CTs and bi-weekly CBCT imaging

Each patient underwent three planning CTs (3 mm slice thickness, Big Bore Philips) at different bladder volumes: empty (EB); intermediate (IB); and full (FB). One hour prior to acquiring the first CT (IB-CT), the patients consumed 250 mL of water. The patients then consumed an additional 500 mL of water, and the FB CT was acquired 20 minutes later. The patients then emptied their bladders for the EB CT. Following the injection of intravenous contrast (IB only), CT images were obtained from the upper border of the L2 vertebral body to 3 cm below the ischial tuberosity. Before each treatment fraction, the IB procedure was reproduced.

CBCTs (2 mm slice thickness, XVI Elekta) were acquired on days 1, 2, and 3, then bi-weekly during the 5 weeks of treatment, with an average of 12 (range, 9 – 17) CBCTs acquired per patient. Patients underwent a supplementary IB CT at mid-treatment (20 Gy), without intravenous contrast medium injection. All CTs, CBCTs and RT fractions were performed with the patient in a supine position with personalized immobilization.

3.2.2.3 Region of interest delineation on CTs and CBCTs

The CTV included both the primary tumour site (CTV-T) and the regional lymphatics (CTV-N). The CTV-T included the cervical tumour and the uterus. In the event of vaginal involvement, it also included 2 cm below the most caudal tumour extension in addition to the parametria. The CTV-N included the common, external and internal iliac vessels, along with the obturator vessels and the presacral lymph nodes [32]. The inguinal lymph nodes were included in cases of lower vaginal involvement. The delineated OARs were the rectum, bladder, and bowel; the latter included the sigmoid colon. The sigmoid colon was not delineated because it was not individually distinguishable on CBCT.

One experienced radiation oncologist manually delineated the CTV-T and the OAR on all CT scans and CBCTs. The CTV-N was only delineated on the CT scans. All delineations were validated by a second experienced radiation oncologist. The “CTV-T” is simplified to “CTV” in this manuscript.

3.2.2.4 Definitions of RT/ART strategies and PTV margins

Five radiotherapy (RT) strategies were geometrically simulated for each patient (Figure 3-1).

(1) The standard RT was based on the planning CT with IB.

(2) The "ITV-based RT" used an ITV created by combining the delineated CTV from the three planning CT scans (EB, IB, and FB), following rigid bone registration of the two CT scans (EB and FB) to the IB CT scan. The ITV contour was smoothed by a Gaussian filter (standard deviation, 2 mm).

(3) The RT strategy with one mid-treatment replanning (named "MidTtReplan") corresponded to the standard RT with one additional replanning based on the CT acquired after the tumour received 20 Gy.

(4) The "Pretreatment library ART" was a PTV library defined from the three planning CTs. For daily treatment, one PTV was selected from the library. This PTV was the one that provided the maximum overlap (using the Sørensen-Dice similarity coefficient [DSC] [33]) between the CTV of the library and the daily CTV delineated in the CBCT, following rigid bone registration of the planning CT scans to the CBCT.

(5) The "Evolutive library ART" was an enriched version of this "Pretreatment library ART" and included new CTVs from the CBCTs in the pretreatment planning library, if the given CTV shape of the day differed from those in the library. Following each CBCT, if the overlap coefficients between the entire CTV library and the CTV of the day did not reach a defined threshold (*i.e.* the CTV shape of the day was not represented in the current library), the CBCT CTV was added to the library. Figure 3-2 illustrates the evolutive library-based ART strategy. Whether each CBCT CTV was included in the library depended upon the results of the similarity test. When a CBCT CTV was added to the library, it was considered available from the next fraction onwards. This strategy was thus off-line. All overlap coefficient thresholds were tested (range, 0.05-0.95).

3.2.2.5 Morphologic analysis

To quantify the movements represented in the pretreatment planning library, bladder volumes and CTV angles were measured on the planning CTs. The CTV angle was defined using three manually placed points at the top of the uterus, cervix, and vagina, as previously described [9,34]. Pearson's coefficient (r) was calculated to assess correlations between the CTV angle and the bladder volume.

During treatment, tumour shrinkage was quantified by calculating the volume of the CTV delineations on the planning CT and on the CBCTs. Vaginal displacement was also assessed by considering the displacement of a vaginal point defined as the centre of the inferior part (most inferior slice) of the CTV, after pelvic bone registration (Figure 3-3b). The average of this vaginal displacement per patient was computed. Pearson's coefficient was calculated to assess correlations between vaginal displacement and rectum coverage by the PTV.

Two PTV margins were used: 10 mm, considered to be the standard margin, and 7 mm to evaluate the ability of a narrow PTV to cover the target during treatment. PTVs were calculated by an isotropic expansion of the CTVs.

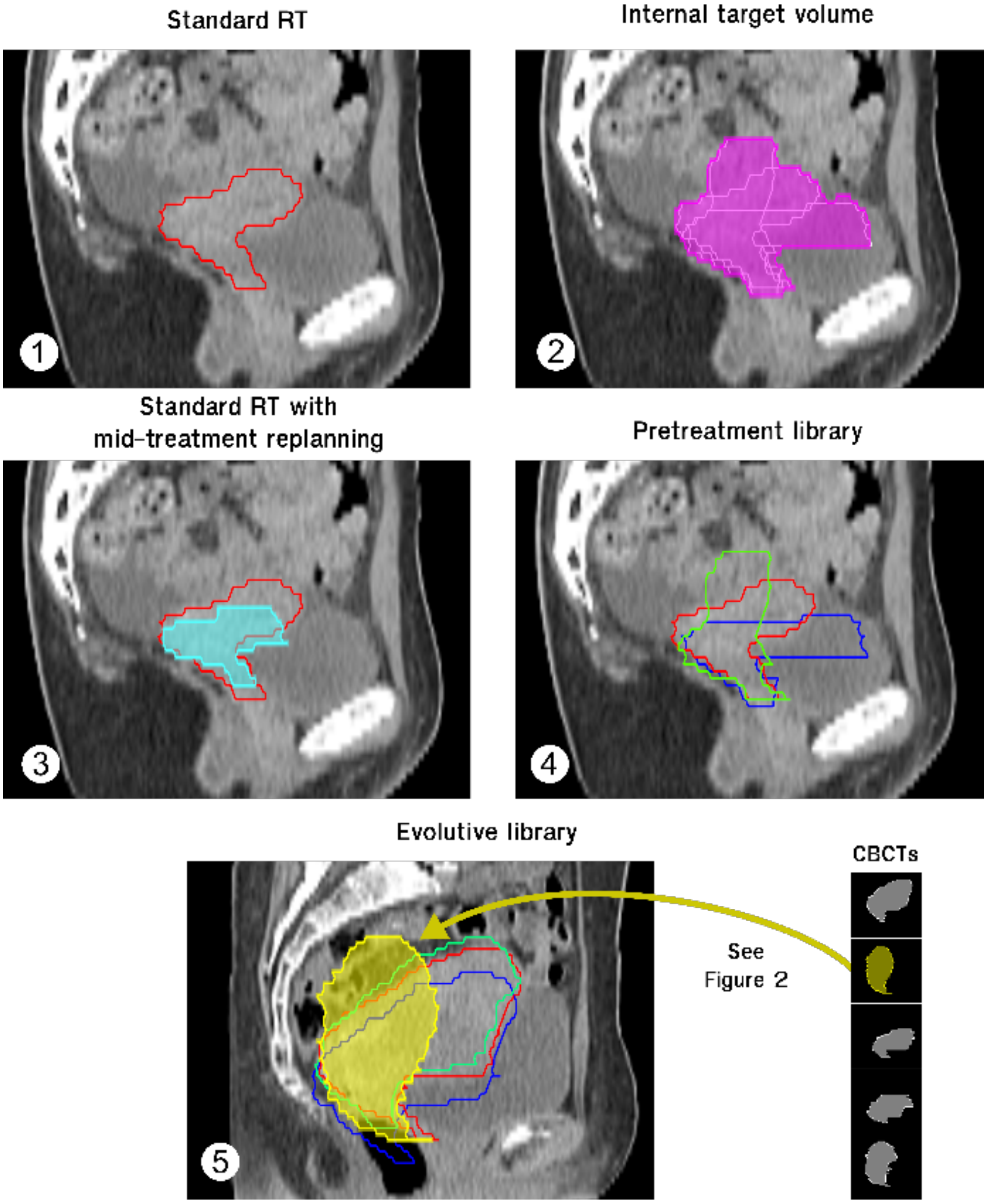

Figure 3-1 : Tested RT strategies in cervical IMRT

Each subfigure represents a simulated strategy: (1) Standard RT strategy, which uses the PTV defined on the intermediate bladder volume CT; (2) ITV-based RT strategy, using the PTV defined by the union of the three CTVs of the planning CTs with different bladder fillings (full [FB], intermediate [IB] and empty [EB]); (3) Standard RT strategy with an additional mid-treatment replanning at 20 Gy; (4) the pretreatment library strategy, which uses the best PTV of the three planning CTs at each treatment fraction; and (5) the evolutive library strategy, which is based on the pretreatment library that can be enriched by including CBCT anatomies (*cf*. Figure 3-2). The green, red and dark blue shapes represent the FB, IB and EB CTV, respectively. The pink shape represents the ITV. The light blue shape represents the CTV from the CT at 20 Gy. The yellow shape represents the CTV (delineated on a CBCT) added into the pretreatment library. CBCT: cone-beam CT; RT: radiotherapy

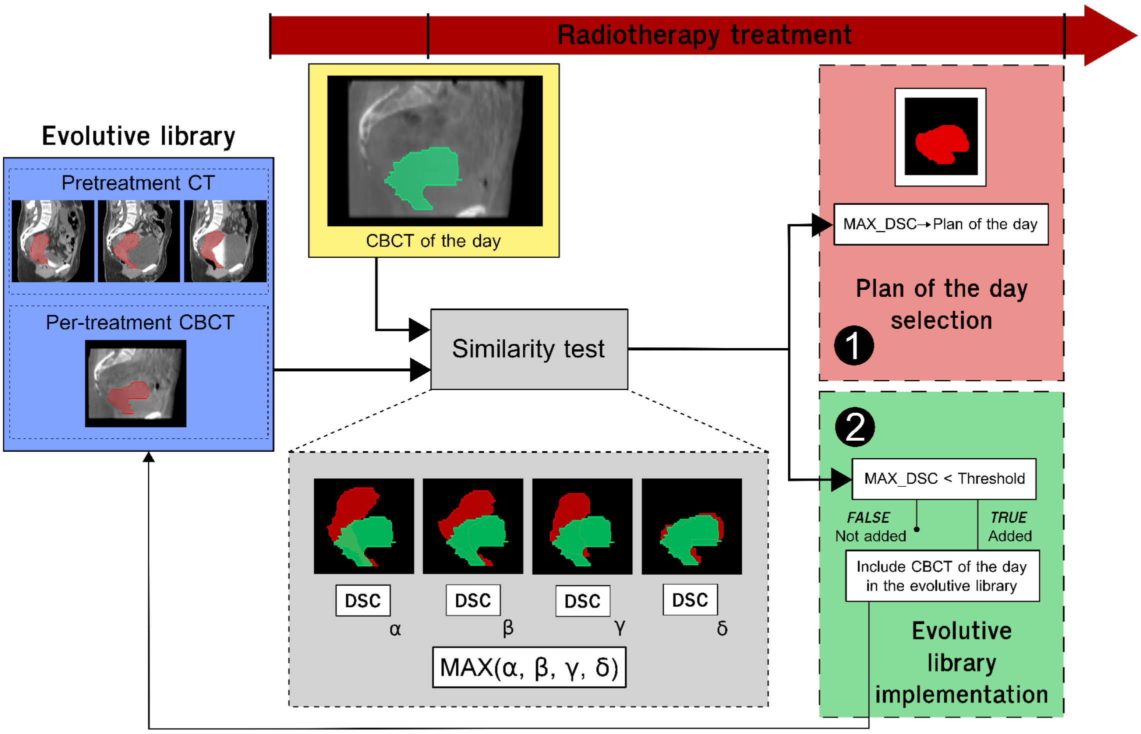

Figure 3-2 : Schema of the evolutive library strategy (5th scenario, see Figure 3-1). Whether a new CTV is included in the library depends on the result of the similarity test

The illustrated evolutive library is composed of the pretreatment library (3 CTVs) and one per-treatment CBCT replanning that was previously added. For each CBCT of the day, the similarity test calculated the DSC between the daily CBCT CTV and each of the evolutive library CTVs (resulting in this example of four values: α, β, ɣ, and δ). The maximum DSC (MAX_DSC) enabled the identification of the plan of the day (1) and informed whether the CTV of the day should be added to the evolutive library (2). The red shapes represent the CTVs from the evolutive library. The green shape represents the CTV from the considered daily CBCT. MAX_DSC: maximum Sørensen-Dice similarity coefficient; CBCT: cone-beam CT; CTV: clinical target volume

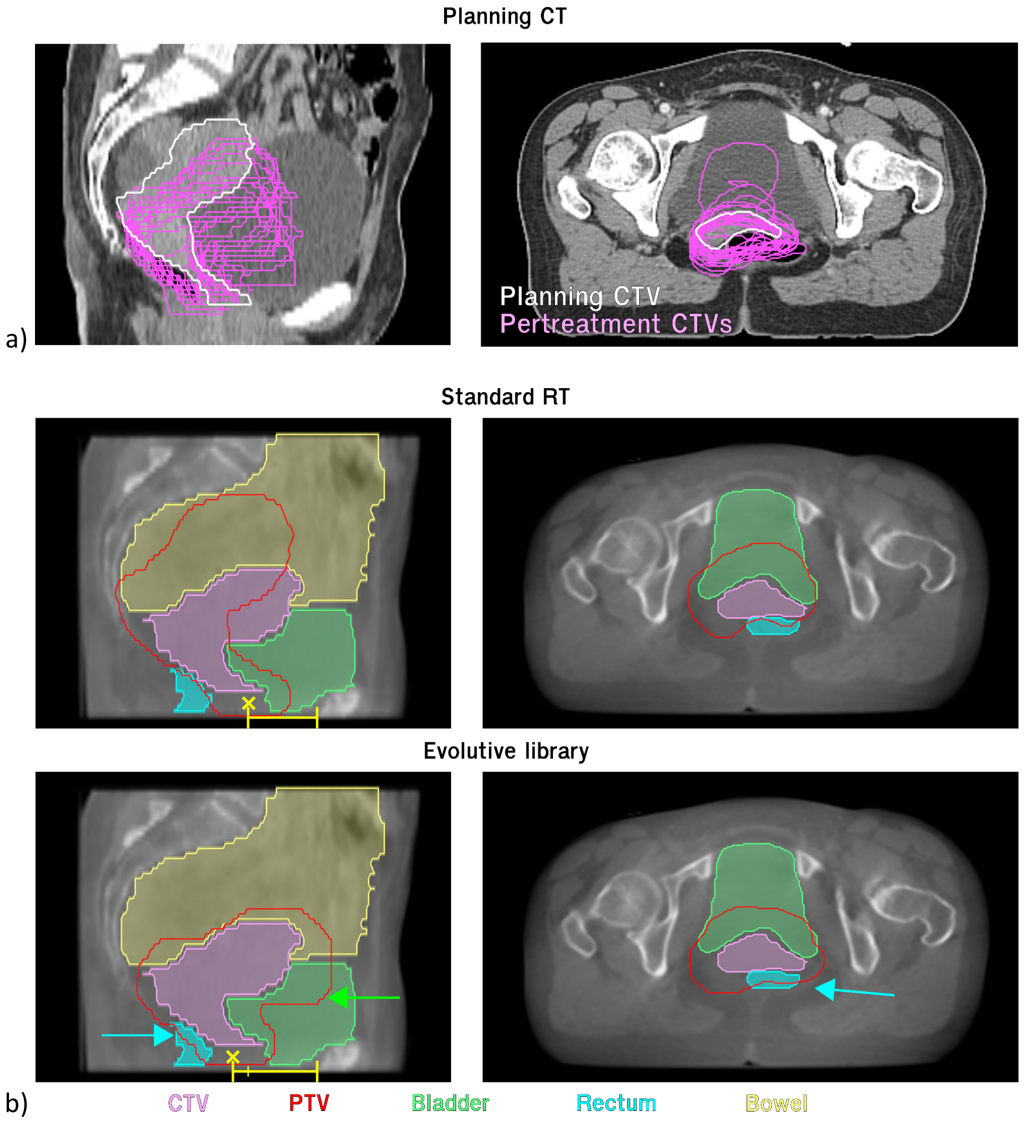

Figure 3-3 : Illustration for one patient of a) the per-treatment CTV deformations compared with the IB planning CT and b) the rectum and bladder overcoverage related to CTV coverage improvement when using the evolutive library

This figure shows: a) the per-treatment deformation of the CTV compared with the planning CTV; b) a CBCT of the day with the corresponding volumes of interest (CTV, bladder, rectum, and bowel). The red line represents the PTV of the day using either standard RT (upper row) or the evolutive library (lower row), in both cases with 10 mm PTV margins. The yellow cross represents the vagina point, which represents the posterior movement of the centre of the vagina towards the rectum. The blue and green arrows indicate rectum and bladder overcoverage, respectively, by the PTV due to improved CTV coverage obtained using the evolutive strategy. PTV: planning target volume; CTV: clinical target volume

3.2.2.6 Geometric evaluation of the five strategies

For the treatment simulations, the planning CT scans and the corresponding PTV were bone-registered to the per-treatment imaging (CBCT and mid-treatment CT). The different strategies were compared using a geometric criterion. The main endpoint was the "coverage" of the volumes of interest (VOI) by the PTV, which required calculation of the "overlapping volume" between the PTV and the VOI (CTV, bladder, rectum, or bowel). Coverage was defined as the ratio between the overlapping volume and the VOI volume. A total of 668 PTVs that evaluated the two margin values were computed (200 on the planning CTs; 468 on the per-treatment images). For each patient and each VOI, the mean coverage was calculated based on the patient's CBCTs (range, 9 – 17). The mean coverage values that corresponded to the different strategies were compared two by two using a non-parametric test (Wilcoxon signed-rank test). Each strategy was compared with the standard RT and the evolutive library strategy for each PTV margin.

To provide a spatial analysis of the coverage of the VOIs by the PTV, a probability map was generated that depicted overlapping between the PTV and the volumes of interest (CTV and OAR) (Figure 3-4). A unique template anatomy was first chosen in the cohort, corresponding to the IB CT scan with the median CTV volume (Stage III disease). Based on the contours of the VOIs, a rigid registration was first performed between the CBCTs of all the patients and the template, followed by deformable image registration (DIR) using the diffeomorphic Demons algorithm with a signed distance map [35,36]. The resulting deformation vector fields were used to propagate the overlapping volumes of the CBCT to the template. A map was thus generated, enabling visualization of the mean covered area of the CTV and the OARs for each patient. Finally, the mean of all patient maps was calculated for each RT strategy. DIR accuracy was estimated by calculating the Dice similarity coefficient (DSC). The mean (min – max) DSC values were 0.94 (0.93 – 0.95) for the CTV, 0.94 (0.91 – 0.95) for the rectum, 0.97 (0.96 – 0.98) for the bladder, and 0.97 (0.97 – 0.98) for the bowel.

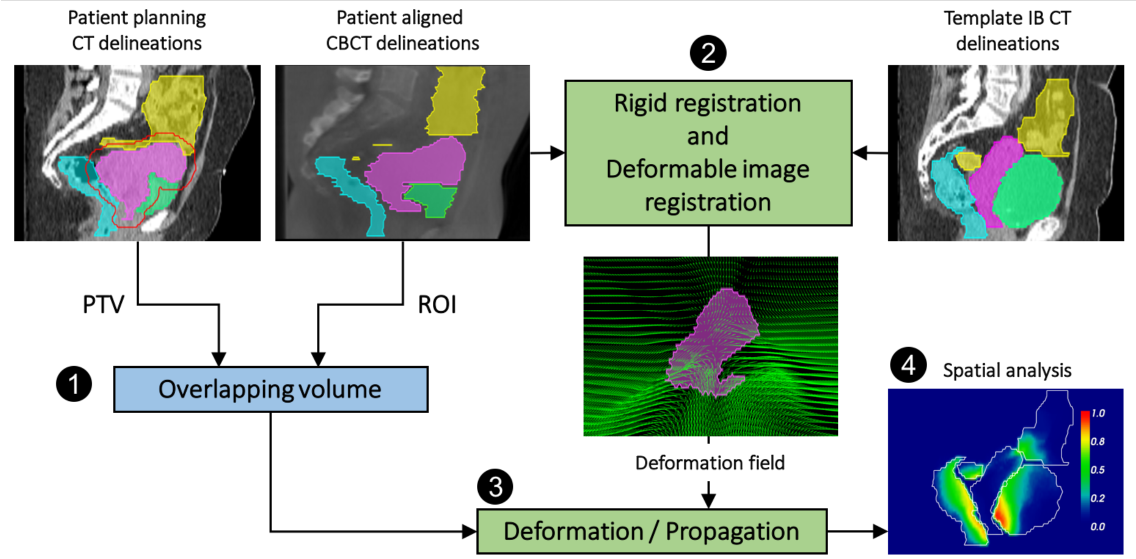

Figure 3-4 : Method for computing the overlapping probability map for each strategy

The template corresponded with the patient, within the whole cohort, with the median CTV volume in the intermediate volume bladder CT scan (Stage III disease). For each patient, CBCT delineations of the overlapping volume (coverage

volume of the CTV and OAR by the PTV) were extracted (Step 1). These volumes were propagated towards the template anatomy (Step 3) using contour-based deformable image registration, calculated between the CBCT anatomy and the template (Step 2). A map was generated that permitted the visualization of the mean covered area for CTV and OAR (Step 4). Finally, the means of all patient maps were calculated for each strategy (*cf.* Figure 3-8). PTV: planning target volume; ROI: region of interest; CBCT: cone-beam computed tomography; IB CT: intermediate bladder computed tomography; CTV: clinical target volume; OAR: organ at risk

3.2.2.7 Dosimetric evaluation of the five strategies

To illustrate the dosimetric impact of the five strategies, each strategy was simulated for a selected patient, and the associated dose distributions were calculated. The patient with the lowest coverage of the CTV by the PTV ("standard RT" strategy) was selected. Step and shoot IMRT plans were generated with the Pinnacle treatment planning system (v.9.10) using 7 coplanar 6-MV photons beams. The dose constraints recommended by RTOG 0418 were respected. A total of eight dose plans were computed for each PTV margin (7 and 10 mm): on each planning CT (EB, IB, and FB); on the CT at 20 Gy; on the IB planning CT with ITV; and on the per-treatment CBCTs included in the evolutive library (three CBCTs corresponding to the 1st, 2nd and 16th treatment fractions). The density overriding method was implemented to calculate the dose distribution on CT and CBCT images (water-air-bone: 0, -1000, 650 HU, respectively) [37]. Figure 3-5 shows the dose distributions, with a 7 mm PTV margin, of each corresponding image, along with the corresponding dose volume histograms (DVH). The field of view of the replanning CBCTs was extended in the cranial-caudal direction with the CT image that provided the most realistic body contour.

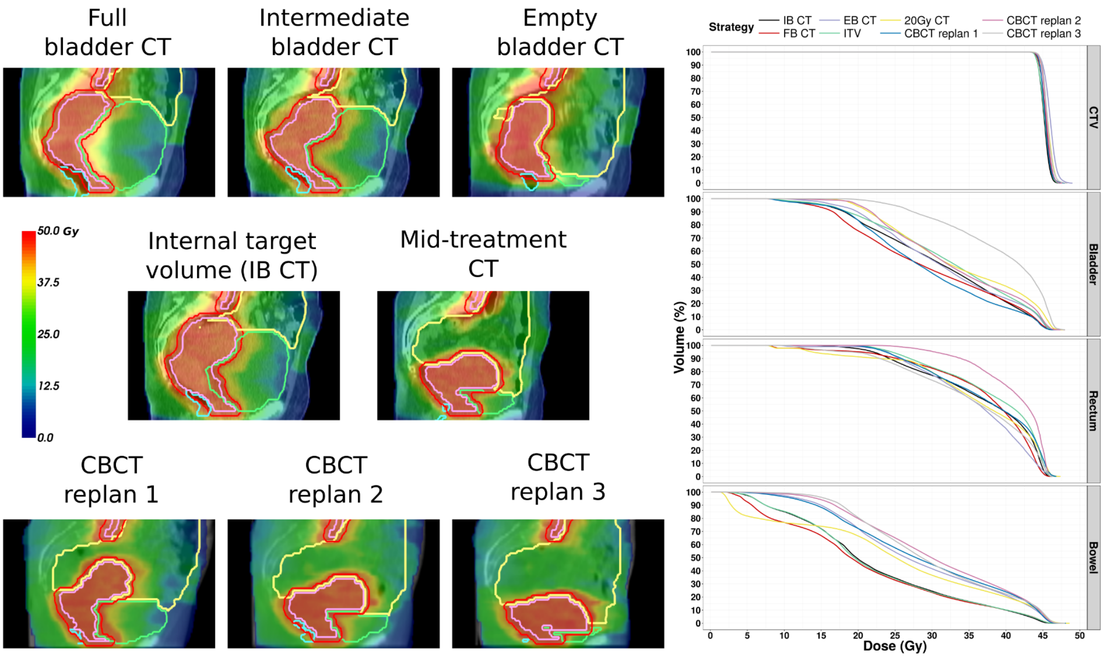

Figure 3-5 : Planned dose and DVH with 7 mm PTV margin on each image of the selected patient

The left side of the figure presents the computed dose distributions at each anatomic configuration (planning CTs, mid-treatment CT or replanning CBCT with each considered PTV). The right side presents the corresponding DVHs for each organ. The selected patient exhibited a large "intermediate" bladder volume that was manifest by a retroverted CTV on the planning CT, thus enabling adequate bowel sparing. Due to per-fraction bladder volume reduction and an anteverted

CTV, this bowel sparing was not maintained during treatment (Figure 3-3 a, b). IB CT: intermediate bladder computed tomography; EB CT: empty bladder CT; FB CT: full bladder CT; ITV: internal target volume; CBCT: cone-beam CT

To estimate the total received dose for each strategy, two approaches were considered. For the rectum and the bladder, a dose accumulation method based on deformable image registration was applied (with the method described in section 3.2.2.6). The fraction doses were then warped from the CBCT to the planning CT using the estimated deformation vector fields [38]. The warped doses were added together to obtain the cumulated dose, and the DVH was calculated. The DIR method's accuracy in assessing the cumulated dose, in terms of mean (min – max) DSC, was 0.93 (0.92 – 0.94) and 0.98 (0.95 – 0.98) for the rectum and bladder. For the CTV and the bowel, due to tissue disappearance/appearance, DIR-based dose accumulation was not appropriate to calculate [39,40], and the average DVH was thus computed. The following dosimetric indices were calculated to compare the strategies: the CTV (in %) receiving at least 42.75 Gy (95% of the prescribed dose) (V42.75); V40 (in %) of the rectum and the bladder; and V35 (in cc) of the bowel.

3.2.3 RESULTS

3.2.3.1 Morphologic analysis

The mean (min – max) CTV angles and bladder volumes were 79.7° (37.8 – 113.1°) and 50.5 cc (22.9 – 109.9 cc) for the EB CT scans, 80° (46.9 – 113.2°) and 209.7 cc (57.9 – 713.2 cc) for IB, and 85.2° (55.5 – 134.8°) and 282.6 cc (61.9 – 809.2 cc) for FB. The correlation between CTV angles and bladder volumes was low (r = 0.24; p = 0.06).

The mean (min – max) of the average vagina displacement per patient were -0.5 mm (-8.6 – 5.8 mm), -4.4 mm (-21.4 – 6.1 mm), -5.5 mm (-18.6 – 13.3 mm) in the left-right (LR), anterior-posterior (AP) and superior-inferior (SI) directions, respectively. The mean (min – max) magnitude of the displacement was 12.3 mm (3.8 – 29.1 mm).

Figure 3-6 presents the mean PTV volume used for the strategies at planning and during the 5 weeks of treatment, considering each CBCT to generate a potentially new PTV. The mean weekly CTV decrease was 10.9 cc, resulting in mean PTV decreases of 19 cc and 23 cc for a 7 mm and 10 mm margin, respectively.

3.2.3.2 Evolutive library implementation

The right portion of Figure 3-7a presents the mean CTV coverage by the PTV achieved by increasing the DSC threshold value and, thus, the number of CBCTs added to the evolutive library (*i.e.* the number of replannings). The value of the DSC threshold, which provided a minimum mean CTV coverage over 95% for a 10 mm PTV margin, was 0.55. Using this threshold, the mean number of replannings per patient was 0.7 (range, 0 – 3). Eleven patients had no replannings; six patients had 1 replanning, while one patient had 2 replannings, and two patients had 3 replannings. The mean time from the beginning of treatment to per-treatment replanning was 17 days for patients with one replanning, 15 and 27 days for those with two replannings, and 11, 12, and 23 days for those with three replannings.

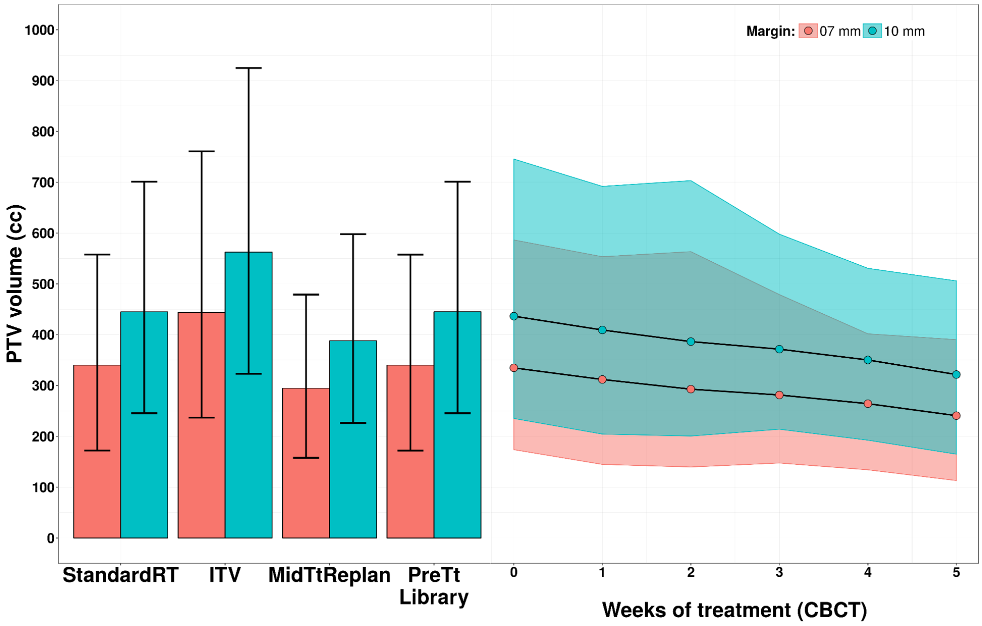

Figure 3-6 : PTV volume (in cc) for each strategy and its evolution during the 5 weeks of treatment (mean and range values)

For all strategies but the planning library, one PTV was considered per patient. For the planning library, three PTVs were included per patient. This figure shows a decreasing PTV volume during the 5 weeks of treatment and considers each CBCT as potentially generating a new PTV (included or not in the evolutive library). PTV: planning target volume; RT: radiotherapy; ITV: internal target volume based RT; MidTtReplan: mid-treatment replanning; PreTt Library: pretreatment library considering the planning CTs

3.2.3.3 Comparison of CTV geometric coverage for all strategies

Figure 3-7a and Table 3-1 represent the coverage of the CTV by the PTV for each strategy. Compared with standard RT, all strategies except the MidTtReplan significantly increased the CTV coverage. Compared with the evolutive library strategy, all others, except for the ITV-based RT, significantly decreased the CTV coverage. The mean (min – max) CTV coverage difference between the evolutive library and standard RT was 3.8% (0 – 26.1%). Five patients benefitted from an improved CTV coverage of more than 5%. Figure 3-8 shows that the CTV undercoverage was primarily located in the anterior and superior regions of the uterus and in the posterior region of the cervix and that the coverage of these regions was improved by the evolutive library-based strategy.

3.2.3.4 Comparison of OAR geometric coverage for all strategies

Figure 3-7bcd along with Table 3-1 represent the bladder, rectum, and bowel coverage by the PTV for each strategy, respectively. The ITV-based strategy significantly increased OAR coverage compared with standard RT. All except the ITV-based strategy significantly decreased the bowel coverage compared with the standard RT strategy. The pretreatment library-based and evolutive library-based strategies significantly increased the rectum coverage compared with the standard RT strategy. When using the evolutive library, eight patients had increased rectum coverage of more than 5% (up to 43.3% with 10 mm PTV margin). This rectum overcoverage correlated with the anterior-posterior ($r = -0.53$; $p < 0.02$) direction and with the magnitude of the vagina point displacement ($r = 0.76$; $p < 0.001$). However, eight patients had decreased bowel coverage of more than 2% (up to 6.7%). Seven patients had decreased bladder coverage of more than 5% (up to 27.5%). These OAR coverage differences were related to a better overlap between the CTV and the PTV, as illustrated in Figure 3-3b. The OAR overcoverage volumes were primarily those located close to the CTV and occurred in the same anatomic location in all RT strategies (Figure 3-8).

3.2.3.5 CTV and OAR dosimetric analysis for all strategies

Figure 3-9 represents the estimated cumulated DVH of the CTV and the OARs of each strategy and the two PTV margins (7 and 10 mm) for one patient only. Table 3-2 shows the dosimetric indices of the CTV and OAR with respect to each strategy. For the sake of comparison, Table 3-3 shows the corresponding geometric indices.

The highest CTV coverage was obtained with the evolutive library strategy. However, the dosimetric coverage of the bladder achieved with this strategy was higher than that obtained with other strategies. Considering a 10 mm (respectively, 7 mm) PTV margin, the coverage of the rectum using the evolutive library was higher (respectively, of the same order of magnitude) than that with the other strategies. For the bowel, dosimetric coverage was the lowest with the evolutive library.

Table 3-1 : CTV and OAR geometric coverage by the PTV for all strategies

These coverage values corresponded to the percentage of the volume of interest overlap with the PTV. A better strategy was defined as either increased CTV coverage or decreased OAR coverage, as evaluated using the signed-rank Wilcoxon test. PTV: planning target volume; CTV: clinical target volume; OAR: organ at risk; RT: radiotherapy; ITV: internal target volume

*** (respectively, **) indicates that the tested strategy provided a significantly better (respectively, worse) mean coverage across all patients compared with the standard RT strategy.**

° (respectively, °°) indicates that the tested strategy provided a significantly better (respectively, worse) mean coverage across all patients compared with the evolutive library strategy.

RT strategies	PTV margin (mm)	Coverage by the PTV (%) mean (min – max)			
		CTV	Bladder	Rectum	Bowel
Standard RT	7	90.7 °° (63.6 – 99.9)	20.6 (1.9 – 46.3)	22.4 ° (2.5 – 46.8)	6.99 °° (0.52 – 15.0)
	10	94.7 °° (70.9 – 100)	29.7 (6.8 – 60.5)	34.1 ° (5.0 – 69.8)	9.6 °° (1 – 18.9)
ITV-based RT	7	95.7 * ° (72.8 – 100)	30.8 ** °° (3.1 – 52.5)	38.3 ** °° (4.5 – 76.7)	9.9 ** °° (0.6 – 21.1)
	10	97.5 * (78.6 – 100)	41.1 ** °° (9.2 – 66.5)	50.6 ** °° (10.7 – 87.8)	12.8 ** °° (1.13 – 26.1)
MidTtReplan	7	92 °° (79.5 – 98.7)	19.7 (4.6 – 41.1)	22.7 (7.1 – 47.0)	5.6 * (0.77 – 13.4)
	10	95.7 °° (84.7 – 99.9)	28.9 (10.5 – 57.4)	37.2 (13.2 – 72.3)	7.9 * (1.3 – 17.9)
Pretreatment library	7	93.8 * °° (64.9 – 99.7)	19.9 (1.7 – 41.2)	24.6 ** (2.8 – 63.1)	6 * °° (0.4 – 13.5)
	10	96.6 * °° (72.4 – 100)	29.5 (6.1 – 55.7)	37.9 ** (7.9 – 75.1)	8.4 * °° (0.9 – 17.6)
Evolutive library	7	96.2 * (93.0 – 99.7)	19.3 (8.3 – 41.2)	26.5 ** (8 – 65.2)	5.2 * (0.4 – 10.2)
	10	98.5 * (96.4 – 100)	29.3 (15.4 – 55.7)	40.6 ** (16.4 – 76.8)	7.6 * (0.9 – 14.2)

Table 3-2 : Dosimetric indices of the CTV and the OAR stratified by strategy and the two PTV margins (7 and 10 mm) for one selected patient

The selected patient was the one with the worst coverage of the CTV by the PTV (lowest value) using the "standard RT" strategy. The mean and range values are displayed. For each volume of interest and strategy, dose indices were extracted from the estimated cumulated DVHs of the patient. The dosimetric objectives were ≥ 95% for the CTV, < 40% for the bladder and rectum and < 500cc for the bowel. Two approaches were considered to estimate the cumulated received doses: using deformable image registration for the rectum and the bladder and calculating the average value of the fraction doses for the CTV and the bowel. PTV: planning target volume; DVH: dose-volume histogram; CTV: clinical target volume; RT: radiotherapy; ITV: internal target volume

RT strategies	PTV margin (mm)	Dosimetric index of the strategy's DVH mean (min – max)			
		CTV (V42.75) (%)	Bladder (V40) (%)	Rectum (V40) (%)	Bowel (V35) (cc)
Standard RT	7	68 (50.6 – 87.5)	18.1 (7.8 – 76.8)	24.8 (1.2 – 45.7)	199.6 (166.6 – 231.8)
	10	71.2 (54.2 – 90.1)	23.1 (10 – 85.7)	39.4 (7.6 – 59.3)	213.1 (177.6 – 245.4)
ITV-based RT	7	75.4 (62 – 89.3)	22.1 (8.5 - 77.9)	34 (3.5 - 56.7)	206.7 (172.1 - 241.3)
	10	78.6 (64.5 – 92.7)	28.5 (18.7 – 87.2)	55.4 (16.8 – 73.6)	233.9 (200.5 – 271)
MidTtReplan	7	82.3 (52.8 – 99.9)	16.9 (3.1 - 41)	42.9 (14.1 – 73.5)	171.9 (104.4 – 219.5)
	10	84.9 (55.1 – 100)	23.7 (6.7 – 56.1)	58.2 (28.5 – 86.6)	199.4 (139.4 – 233.8)
Pretreatment library	7	67 (51.3 – 87.5)	9.5 (0 – 14.6)	20.8 (3.2 – 45.7)	205.8 (166.6 – 236.9)
	10	71.5 (58.2 – 90.1)	13 (0.4 – 20.5)	44.2 (14.2 – 70.2)	229.6 (177.6 – 265.5)
Evolutive library	7	94.9 (80.3 – 99.9)	23.2 (4.1 – 67.1)	33 (2.3 – 55.5)	164.6 (132.1 – 202.4)
	10	97.2 (83.1 – 100)	26.6 (2.4 – 78.8)	65.7 (34.4 – 87.7)	202.4 (177.6 – 246.7)

Table 3-3 : CTV and OAR geometric coverage by the 7 and 10 mm PTV for all strategies on the selected patient (Table 3-2)

This table presents the coverage of the volumes of interest (VOI) by the PTV (7 and 10 mm margins) for the patient selected for dosimetric analysis, presented symmetrically with Table 3-2. The mean value is calculated over all the fractions. The min and max values represent fraction coverage. PTV: planning target volume; RT: radiotherapy; CTV: clinical target volume; ITV: internal target volume; MidTtReplan: mid-treatment replanning

RT strategies	PTV margin (mm)	Geometric coverage of the selected patient (Table 3-2) mean (min – max)			
		CTV (%)	Bladder (%)	Rectum (%)	Bowel (cc)
Standard RT	7	63.6 (46.8 – 83.3)	15.5 (4.4 – 40)	12.7 (0.2 – 34.3)	51.5 (31.4 – 70.6)
	10	70.9 (54.2 – 89.8)	22.8 (9.5 – 51.6)	26.6 (2.3 – 51.2)	64.0 (40.5 – 86.4)
ITV-based RT	7	72.8 (60.3 – 86.5)	23.1 (5.5 – 43.5)	22.9 (1.3 – 49.3)	69.8 (46.3 – 92.5)
	10	78.6 (65.2 – 92.3)	30.8 (14.9 – 54)	41.6 (8.6 – 67.2)	81.7 (54.8 – 106.9)
MidTtReplan	7	79.5 (50 – 99.9)	16.4 (3.34 – 35.3)	27.4 (3.3 – 54.1)	36.8 (5.3 – 60.9)
	10	84.7 (54.6 – 100)	24.9 (9.5 – 46.9)	45.1 (10.8 – 74.9)	48.1 (10 – 74.5)
Pretreatment library	7	64.9 (50.6 – 83.2)	13.2 (0 – 22.8)	12 (0.3 – 34.3)	46.9 (31.4 – 65.5)
	10	72.4 (59.4 – 89.8)	18.8 (0.9 – 30.6)	25.1 (4.7 – 51.2)	58.4 (40.5 – 79.3)
Evolutive library	7	93.4 (76.6 – 99.9)	19 (0.4 – 58.4)	30.4 (0.1 – 65.1)	28.7 (6.7 – 54.5)
	10	97 (82.9 – 100)	27.4 (2.9 – 72.8)	49.1 (7 – 80.8)	41.3 (14.2 – 70.3)

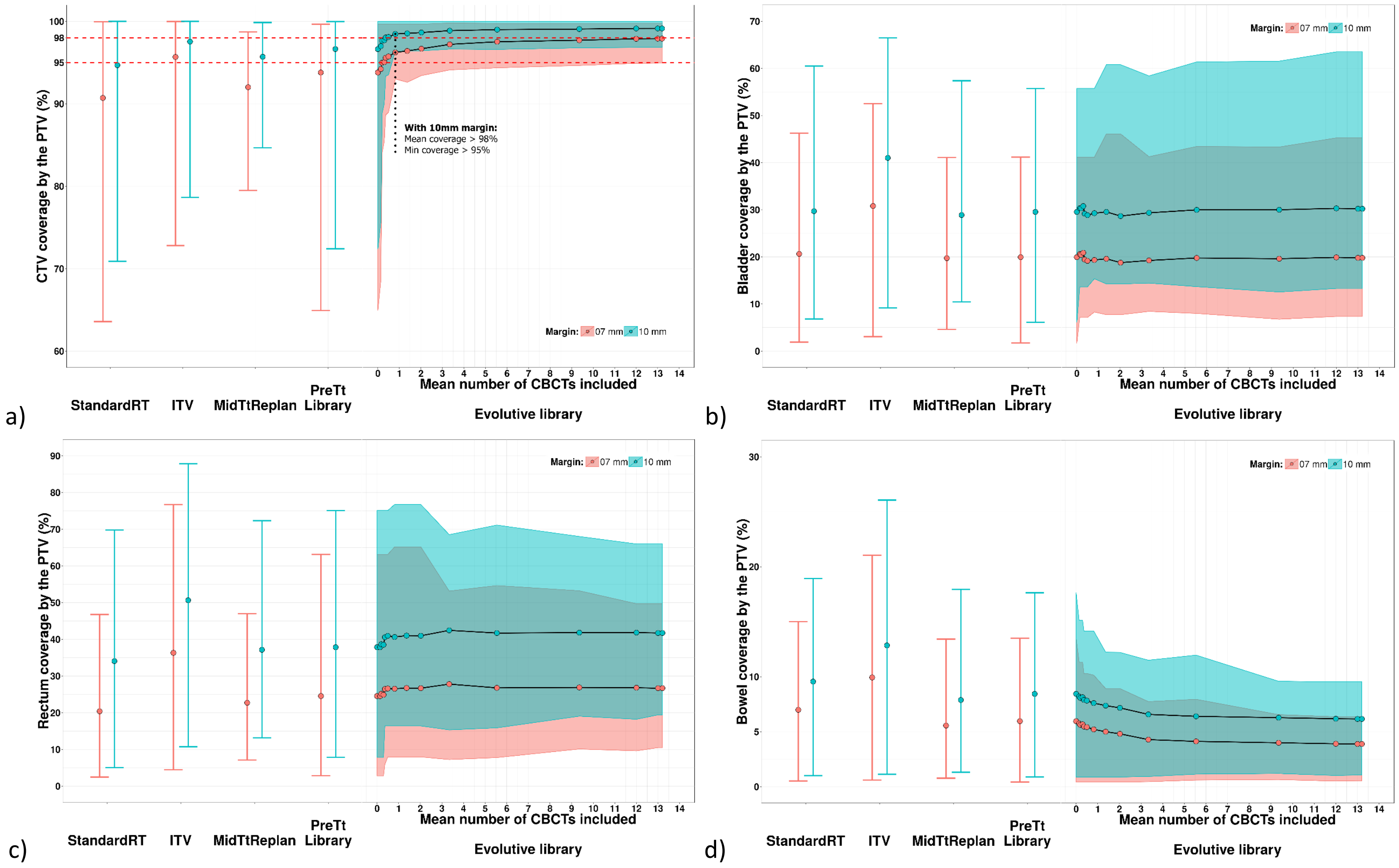

Figure 3-7 : CTV (a), bladder (b), rectum (c) and bowel (d) coverage by the PTV provided by each strategy

The mean coverage of the CTV and OAR by the PTV was calculated for each patient and strategy. The figure presents the distribution (mean and range values) of this coverage among all patients, with 7 mm (red) and 10 mm (blue) PTV margins. The right section represents, for the evolutive library, CTV and OAR coverage by the increasing the number of CBCTs that were included in the library, *i.e.* by increasing the DSC threshold. CTV: clinical target volume; PTV: planning target volume; MidTtReplan: mid-treatment replanning; ITV: internal target volume based RT; PreTt Library: pretreatment library; StandardRT: standard radiotherapy; CBCT: cone-beam CT

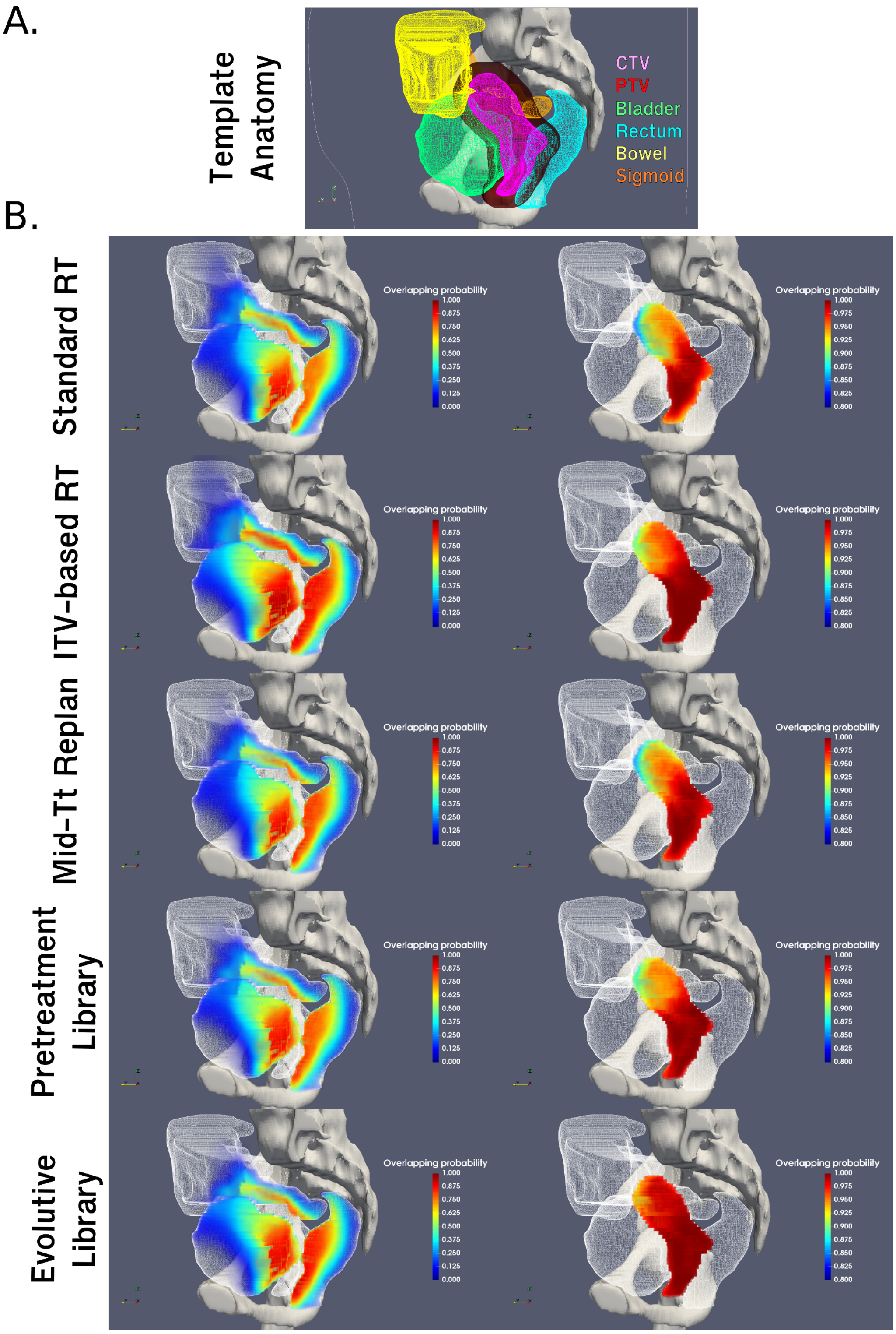

Figure 3-8 : Template anatomy with a 10 mm PTV margin (a) and maps that represent the probability of an overlap between the PTV and the OAR (left side) or the CTV (right side) for each strategy (b)

The represented OAR are the bladder, rectum and bowel. The method used to calculate the overlapping probability map is described in Figure 3-4. CTV: clinical target volume; PTV: planning target volume; Mid-Tt Replan: mid-treatment replanning; ITV-based RT: internal target volume based RT; Standard RT: standard radiotherapy

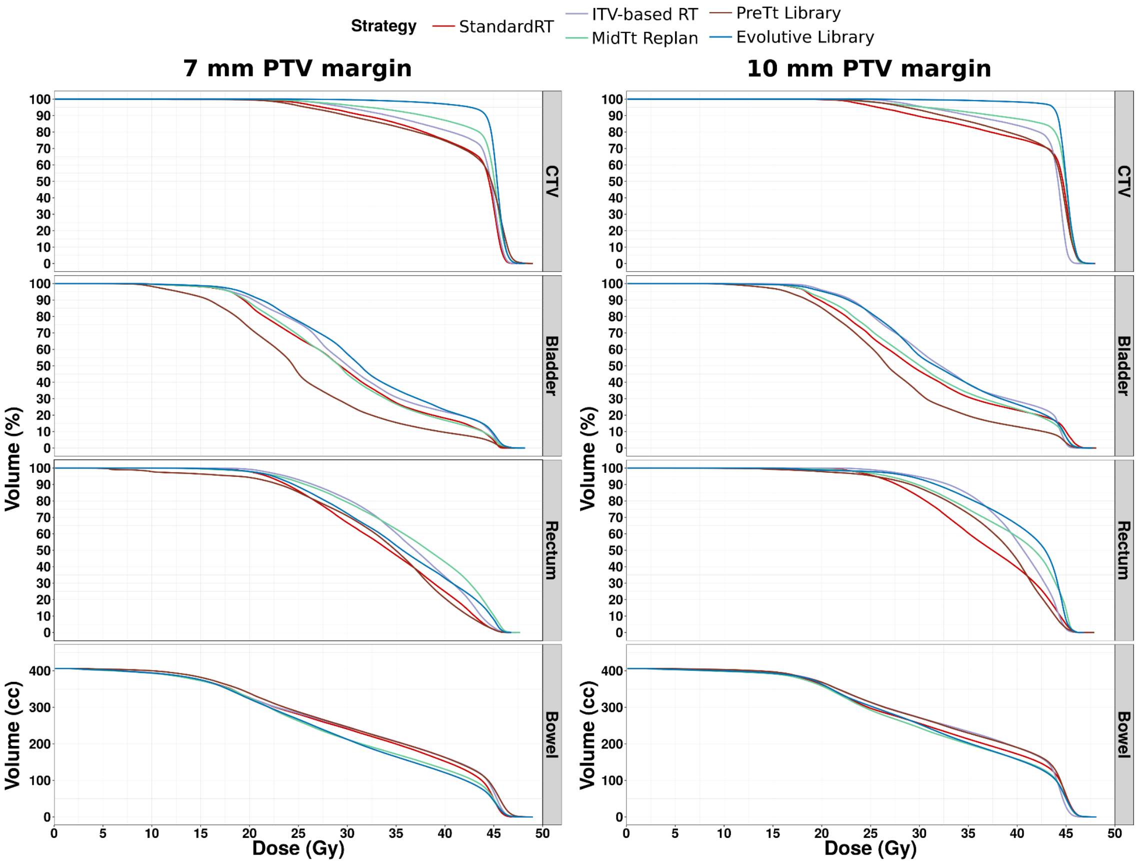

Figure 3-9 : Estimated cumulated DVH of the CTV and the OAR of each strategy and the two PTV margins (7 and 10 mm) for one patient only

Two approaches were considered in the estimation of the cumulated received doses: using deformable image registration for the rectum and the bladder and calculating the average value of the fraction doses for the CTV and the bowel. The selected patient was the one with the worst coverage of the CTV by the PTV (lowest value) with the “standard RT” strategy. StandardRT: standard radiotherapy (red); ITV-based RT: internal target volume based RT (purple); PreTt Library: pretreatment library (brown); MidTtReplan: mid-treatment replanning (green); Evolutive library (blue)

3.2.4 DISCUSSION

Using simulations, this study sought to compare five RT strategies, including an original evolutive library-based ART, in the context of LACC. The evolutive library strategy consisted of using a pretreatment library of three planning CT scans, enriched by at least one CBCT for half of the selected patients. This personalized strategy automatically triggered a replanning when the CBCT CTV differed from the CTVs in the planning library. Compared with the four other strategies, the enriched “evolutive library” offers significantly better target coverage with a reduced geometric coverage of the bowel. Indeed, due to anatomic variations, the standard RT approach indicated a relative undercoverage of the CTV by the PTV, involving mainly the uterus in its anterior and superior part and the cervix in its posterior part to a lesser extent (Figure 3-8). However, the rectum and the bladder are at risk of being more irradiated when using the evolutive library due to the movements of the uterus and the vagina towards these OARs, as illustrated in Figure 3-3 a, b. Combining the evolutive library with a moderately reduced PTV margin (7 mm) compared with standard RT with a standard margin (10 mm) permits an increased dose of CTV and decreased dose to OARs (Table 3-2).

Uterine motion has been reported to correlate with variations in bladder volume [11]. The most common method for defining the ITV and the pretreatment library in the literature is therefore based on planning CTs acquired at variable bladder volumes [11,15,26]. Our results demonstrate that the benefits of a bladder-based ITV and pretreatment library strategy were probably limited due to tumour fixation in the pelvis, as demonstrated by the absence of a correlation between the CTV angle and bladder volume prior to treatment. Furthermore, the pretreatment library strategy does not consider tumour shrinkage during the 5-week treatment (Figure 3-6). Moreover, the morphologic analysis suggests that cervical cancer patients can be separated into four groups as follows: those whose uterus is mobile or not during the planning stage, and those whose uterus is mobile or not during treatment. For example, a pretreatment planning library handles "mover / mover" (mover at the planning and mover during the treatment) patients well, while the evolutive library can also adapt to the "non-mover / mover" patients.

Simulations of RT strategies in cervical carcinoma patients can be achieved using geometric [27] or dosimetric endpoints [19,22-24,28,29]. The geometric criterion (coverage of the volumes of interest by the PTV) enables a large number of simulations to be performed that do not depend on a specific RT technique, with a drawback being a binary criterion that does not correspond with a dose gradient and thus, does not enable the prediction of toxicity or localized control. In our study, treatment strategies were compared among all patients using a geometric criterion, with dosimetric analysis performed for only one patient. The dosimetric evaluation produced results in accordance with the geometric analysis, as shown in Table 3-3.

Various ART strategies in cervical carcinoma patients have been reported in the literature, yet with only a limited number of patients per series (≤ 30 patients) and no clinical results. Authors have compared one replanning at mid-treatment to multiple replannings (up to three) triggered by dose accumulation using deformable image registration [22]. This dose-guided ART strategy has been proven to be the most effective in maintaining all patients with CTV coverage of up to 95%. Similar results were observed in our study when increasing the number of per-treatment replannings, from the mid-treatment replanning strategy to the evolutive library strategy (Table 3-1). This finding stresses the usefulness of the evolutive libraries. Both the evolutive library and mid-treatment replanning strategies aim to take into consideration tumour regression during treatment [19]. Moreover, a maximalist ART strategy with weekly replannings has also reported improved CTV coverage by ensuring that all patients benefit from over 95% of the prescription dose, although there were no overall dosimetric benefits for the OAR [23,24]. In our study, the evolutive library suggests that the best timing for a replanning may be in the third week after the start of treatment (11-16 fractions corresponding to 20-29 Gy). This finding is consistent with a study on tumour recurrence prediction showing that the third week of treatment (20-22 Gy) was the best timing from tissue perfusion analysis on MRI [41].

To our knowledge, our study is the first to quantify the benefits of using a planning library with numerous per-treatment replannings for this anatomic location. Heijkoop *et al* [26] described another original personalized strategy using a library that includes model-predicted internal target volumes (sub-ITV) in a cohort of 64 patients with daily CBCTs. A similar approach has been used on a cohort of 16 patients [42]. In both studies, when facing logistic trouble with implementing the planning library (*e.g.* image quality, OAR filling, tumour deformations), a backup plan was used. We did not evaluate this approach. This strategy appears to be complementary with the proposed evaluative library and could potentially be combined.

The sub-ITV library appears to also be an attractive option for avoiding the highest OAR coverage observed with the ITV strategy (Table 3-1). The use of a library based on sub-ITVs decreased the dose ($V_{40\ Gy}$) to the bladder, rectum and bowel in comparison with the ITV approach [28,42]. Recently, statistical shape modelling was also used to assess the dose coverage probability of 5 patients with weekly CTs [43]. That shape analysis appeared to be an excellent planning tool for modelling patient-specific deformations. However, no ART strategies were simulated using this method in this study.

The choice of PTV margin is crucial. Minimizing PTV margins permits a drastically decreased dose to the OARs, but risks CTV underdosing. In the literature, these margins are either isotropic, ranging from 3 to 15 mm [4,5,9,19,22-28,44-48], or anisotropic, ranging from 15 to 24 mm in the AP direction, 8 to 15 mm in the SI, and 10 to 20 mm in the LR [6,8,14,17,44,49]. Using a standard technique, the rational PTV margin ensuring 95% CTV coverage has been found to be 13 mm if isotropic and 20 mm and 10 mm in the AP and SI-LR directions, respectively, if anisotropic [50]. In our study, a 10 mm PTV margin was chosen as our standard because this value is widely reported in the literature [5,9,25,26,45,48]. A PTV margin moderately reduced to 7 mm was clearly inadequate at properly covering the CTV with a standard RT strategy. In this context, we found that ART permitted decreased PTV margins, while still maintaining satisfactory VOI coverage (Table 3-1; Figure 3-7 a, b, c, d). In the same perspective, a RT strategy based on two sub-ITVs with a reduced 7 mm margin enabled 90% of the patients to benefit from a CTV coverage higher than 95%, while this coverage was observed in only 64% of the patients who underwent standard RT with 16-mm margins [27].

A limitation of our evolutive library is that it is an off-line approach and therefore cannot correct for the current fraction in the event of significant new anatomic variations, which are consequently considered only for the following fractions. In these cases, another option is, as mentioned previously, to use a 3D conformal radiation therapy back-up plan, though this option carries the risk of increasing the dose to the OAR [25,26]. Moreover, our strategy does not consider intra-fraction anatomic variations. The amplitude of intra-fraction displacement has been reported to be on average between 0.1 and 4.2 mm for the cervix and between 1.1 and 3.1 mm for the uterus. These displacements were less than 5 mm in more than 97% of the cases [7,13]. Our reduced PTV margin (7 mm) therefore appears to include the vast majority of these intra-fraction displacements. Another limitation of our evolutive library strategy may be its complexity, making it difficult to implement in daily practice. Image processing tools must therefore be developed to guide the physician in choosing the right plan from the library for each day's fraction [25], as well as in updating the library with new anatomies. Such an implementation could be performed either through auto-segmentation [51] or with a non-rigid contour propagation with model constraint [52-54]. Moreover, delineation and dose calculation for replanning based on the CBCT is challenging due to limitations related to Hounsfield unit inconsistency, low image quality, and a limited field of view. In clinical practice, replanning could thus be performed by acquiring a new CT scan after treatment delivery. Magnetic resonance imaging-guided radiation therapy could also be employed instead of CBCT in the future.

Our study has several limitations. First, the study did not evaluate the impact of intra-fraction variation. Second, though this geometric analysis was performed on a series of 20 patients, only one had a dosimetric evaluation. Furthermore, with respect to dose calculation, all CBCT image densities were overridden, and the field of view was extended with the CT slices. The dose accumulation in the rectum and bladder was also subject to uncertainties related to dose warping, even if these have previously been shown to be limited [38]. Moreover, bi-weekly CBCTs provided limited image quality for contour delineation and ART guidance. Finally, the limited number of patients did not permit a subgroup analysis.

3.2.5 CONCLUSION

Evolutive library ART appears to be a personalized, original ART strategy that comprises a pretreatment planning library combined with one to three per-treatment replannings for half of patients. Based on the ratio between CTV and OAR coverage, the five RT strategies tested can be classified in the following order of decreasing performance: evolutive library; pretreatment library; ITV-based strategy; mid-treatment replanning; and standard RT. The evolutive library approach thus appears to be particularly attractive, as it also permits PTV margins to be reduced. Clinical studies must now be designed and conducted to confirm the feasibility and clinical benefits of this new ART strategy.

3.2.6 REFERENCES

1. Naik A, Gurjar O, Gupta K, Singh K, Nag P, Bhandari V. Comparison of dosimetric parameters and acute toxicity of intensity-modulated and three-dimensional radiotherapy in patients with cervix carcinoma: A randomized prospective study. *Cancer/Radiothérapie* 2016;20:370-376.
2. Vargo JA, Kim H, Choi S, Sukumvanich P, Olawaiye AB, Kelley JL, Edwards RP, Comerci JT, Beriwal S. Extended field intensity modulated radiation therapy with concomitant boost for lymph node–positive cervical cancer: Analysis of regional control and recurrence patterns in the positron emission tomography/computed tomography era. *International Journal of Radiation Oncology* Biology* Physics* 2014;90:1091-1098.
3. Gandhi AK, Sharma DN, Rath GK, Julka PK, Subramani V, Sharma S, Manigandan D, Laviraj M, Kumar S, Thulkar S. Early clinical outcomes and toxicity of intensity modulated versus conventional pelvic radiation therapy for locally advanced cervix carcinoma: A prospective randomized study. *International Journal of Radiation Oncology* Biology* Physics* 2013;87:542-548.
4. Han Y, Shin EH, Huh SJ, Lee JE, Park W. Interfractional dose variation during intensity-modulated radiation therapy for cervical cancer assessed by weekly ct evaluation. *International Journal of Radiation Oncology* Biology* Physics* 2006;65:617-623.
5. Buchali A, Koswig S, Dinges S, Rosenthal P, Salk J, Lackner G, Böhmer D, Schlenger L, Budach V. Impact of the filling status of the bladder and rectum on their integral dose distribution and the movement of the uterus in the treatment planning of gynaecological cancer. *Radiotherapy and oncology* 1999;52:29-34.
6. van de Bunt L, Jürgenliemk-Schulz IM, de Kort GA, Roesink JM, Tersteeg RJ, van der Heide UA. Motion and deformation of the target volumes during imrt for cervical cancer: What margins do we need? *Radiotherapy and Oncology* 2008;88:233-240.
7. Jadon R, Pembroke C, Hanna C, Palaniappan N, Evans M, Cleves A, Staffurth J. A systematic review of organ motion and image-guided strategies in external beam radiotherapy for cervical cancer. *Clinical Oncology* 2014;26:185-196.
8. Kaatee RS, Olofsen MJ, Verstraate MB, Quint S, Heijmen BJ. Detection of organ movement in cervix cancer patients using a fluoroscopic electronic portal imaging device and radiopaque markers. *International Journal of Radiation Oncology* Biology* Physics* 2002;54:576-583.
9. Huh SJ, Park W, Han Y. Interfractional variation in position of the uterus during radical radiotherapy for cervical cancer. *Radiotherapy and oncology* 2004;71:73-79.
10. Lee JE, Han Y, Huh SJ, Park W, Kang MG, Ahn YC, Lim DH. Interfractional variation of uterine position during radical rt: Weekly ct evaluation. *Gynecologic oncology* 2007;104:145-151.
11. Ahmad R, Hoogeman MS, Bondar M, Dhawtal V, Quint S, De Pree I, Mens JW, Heijmen BJ. Increasing treatment accuracy for cervical cancer patients using correlations between bladder-filling change and cervix–uterus displacements: Proof of principle. *Radiotherapy and oncology* 2011;98:340-346.
12. Chan P, Dinniwell R, Haider MA, Cho Y-B, Jaffray D, Lockwood G, Levin W, Manchul L, Fyles A, Milosevic M. Inter-and intrafractional tumor and organ movement in patients with cervical cancer undergoing radiotherapy: A cinematic-mri point-of-interest study. *Int J Radiat Oncol Biol Phys* 2008;70:1507-1515.
13. Heijkoop ST, Langerak TR, Quint S, Mens JWM, Zolnay AG, Heijmen BJ, Hoogeman MS. Quantification of intra-fraction changes during radiotherapy of cervical cancer assessed with pre-and post-fraction cone beam ct scans. *Radiotherapy and Oncology* 2015;117:536-541.
14. Taylor A, Powell ME. An assessment of interfractional uterine and cervical motion: Implications for radiotherapy target volume definition in gynaecological cancer. *Radiotherapy and Oncology* 2008;88:250-257.
15. Bondar L, Hoogeman M, Mens JW, Dhawtal G, De Pree I, Ahmad R, Quint S, Heijmen B. Toward an individualized target motion management for imrt of cervical cancer based on model-predicted cervix–uterus shape and position. *Radiotherapy and Oncology* 2011;99:240-245.

16. Haripotepornkul NH, Nath SK, Scanderbeg D, Saenz C, Yashar CM. Evaluation of intra-and inter-fraction movement of the cervix during intensity modulated radiation therapy. *Radiotherapy and Oncology* 2011;98:347-351.
17. Ahmad R, Hoogeman MS, Quint S, Mens JW, de Pree I, Heijmen BJ. Inter-fraction bladder filling variations and time trends for cervical cancer patients assessed with a portable 3-dimensional ultrasound bladder scanner. *Radiotherapy and oncology* 2008;89:172-179.
18. Eminowicz G, Motlib J, Khan S, Perna C, McCormack M. Pelvic organ motion during radiotherapy for cervical cancer: Understanding patterns and recommended patient preparation. *Clinical Oncology* 2016.
19. van de Bunt L, Van der Heide UA, Ketelaars M, de Kort GA, Jürgenliemk-Schulz IM. Conventional, conformal, and intensity-modulated radiation therapy treatment planning of external beam radiotherapy for cervical cancer: The impact of tumor regression. *International Journal of Radiation Oncology* Biology* Physics* 2006;64:189-196.
20. Lim K, Chan P, Dinniwell R, Fyles A, Haider M, Cho Y-B, Jaffray D, Manchul L, Levin W, Hill RP. Cervical cancer regression measured using weekly magnetic resonance imaging during fractionated radiotherapy: Radiobiologic modeling and correlation with tumor hypoxia. *International Journal of Radiation Oncology* Biology* Physics* 2008;70:126-133.
21. Beadle BM, Jhingran A, Salehpour M, Sam M, Iyer RB, Eifel PJ. Cervix regression and motion during the course of external beam chemoradiation for cervical cancer. *International Journal of Radiation Oncology* Biology* Physics* 2009;73:235-241.
22. Lim K, Stewart J, Kelly V, Xie J, Brock KK, Moseley J, Cho Y-B, Fyles A, Lundin A, Rehbinder H. Dosimetrically triggered adaptive intensity modulated radiation therapy for cervical cancer. *International Journal of Radiation Oncology* Biology* Physics* 2014;90:147-154.
23. Oh S, Stewart J, Moseley J, Kelly V, Lim K, Xie J, Fyles A, Brock KK, Lundin A, Rehbinder H, Milosevic M, Jaffray D, Cho YB. Hybrid adaptive radiotherapy with on-line mri in cervix cancer imrt. *Radiother Oncol* 2014;110:323-328.
24. Stewart J, Lim K, Kelly V, Xie J, Brock KK, Moseley J, Cho Y-B, Fyles A, Lundin A, Rehbinder H. Automated weekly replanning for intensity-modulated radiotherapy of cervix cancer. *International Journal of Radiation Oncology* Biology* Physics* 2010;78:350-358.
25. Langerak T, Heijkoop S, Quint S, Mens J-W, Heijmen B, Hoogeman M. Towards automatic plan selection for radiotherapy of cervical cancer by fast automatic segmentation of cone beam ct scans Medical image computing and computer-assisted intervention–miccai 2014: Springer; 2014. pp. 528-535.
26. Heijkoop ST, Langerak TR, Quint S, Bondar L, Mens JWM, Heijmen BJ, Hoogeman MS. Clinical implementation of an online adaptive plan-of-the-day protocol for nonrigid motion management in locally advanced cervical cancer imrt. *Int J Radiat Oncol Biol Phys* 2014;90:673-679.
27. Bondar M, Hoogeman M, Mens J, Quint S, Ahmad R, Dhawtal G, Heijmen B. Individualized nonadaptive and online-adaptive intensity-modulated radiotherapy treatment strategies for cervical cancer patients based on pretreatment acquired variable bladder filling computed tomography scans. *International Journal of Radiation Oncology* Biology* Physics* 2012;83:1617-1623.
28. Seppenwoolde Y, Stock M, Buschmann M, Georg D, Bauer-Novotny K-Y, Pötter R, Georg P. Impact of organ shape variations on margin concepts for cervix cancer art. *Radiotherapy and Oncology* 2016.
29. van de Schoot AJ, de Boer P, Visser J, Stalpers LJ, Rasch CR, Bel A. Dosimetric advantages of a clinical daily adaptive plan selection strategy compared with a non-adaptive strategy in cervical cancer radiation therapy. *Acta Oncologica* 2017;56:667-674.
30. Pecorelli S, Zigliani L, Odicino F. Revised figo staging for carcinoma of the cervix. *International Journal of Gynecology & Obstetrics* 2009;105:107-108.
31. Pötter R, Haie-Meder C, Van Limbergen E, Barillot I, De Brabandere M, Dimopoulos J, Dumas I, Erickson B, Lang S, Nulens A. Recommendations from gynaecological (gyn) gec estro working

group (ii): Concepts and terms in 3d image-based treatment planning in cervix cancer brachytherapy—3d dose volume parameters and aspects of 3d image-based anatomy, radiation physics, radiobiology. *Radiotherapy and Oncology* 2006;78:67-77.

32. Taylor A, Rockall AG, Reznek RH, Powell ME. Mapping pelvic lymph nodes: Guidelines for delineation in intensity-modulated radiotherapy. *International Journal of Radiation Oncology* Biology* Physics* 2005;63:1604-1612.
33. Dice LR. Measures of the amount of ecologic association between species. *Ecology* 1945;26:297-302.
34. Gobeli M, Simon A, Getain M, Leseur J, Lahlou E, Lafond C, Dardelet E, Williaume D, Rigaud B, de Crevoisier R. Benefit of a pretreatment planning library-based adaptive radiotherapy for cervix carcinoma? *Cancer radiotherapie* 2015;19:471-478.
35. Rigaud B, Simon A, Castelli J, Gobeli M, Ospina Arango JD, Cazoulat G, Henry O, Haigron P, De Crevoisier R. Evaluation of deformable image registration methods for dose monitoring in head and neck radiotherapy. *Biomed Res Int* 2015;2015:726268.
36. Cazoulat G, Simon A, Dumenil A, Gnep K, De Crevoisier R, Acosta O, Haigron P. Surface-constrained nonrigid registration for dose monitoring in prostate cancer radiotherapy. *IEEE Transactions on Medical Imaging* 2014;33:1464-1474.
37. Graves YJ, Smith A-A, Mcilvena D, Manilay Z, Lai YK, Rice R, Mell L, Jia X, Jiang SB, Cerviño L. A deformable head and neck phantom with in-vivo dosimetry for adaptive radiotherapy quality assurance. *Medical physics* 2015;42:1490-1497.
38. Nassef M, Simon A, Cazoulat G, Duménil A, Blay C, Lafond C, Acosta O, Balosso J, Haigron P, de Crevoisier R. Quantification of dose uncertainties in cumulated dose estimation compared to planned dose in prostate imrt. *Radiotherapy and Oncology* 2016;119:129-136.
39. Mencarelli A, van Kranen SR, Hamming-Vrieze O, van Beek S, Rasch CRN, van Herk M, Sonke J-J. Deformable image registration for adaptive radiation therapy of head and neck cancer: Accuracy and precision in the presence of tumor changes. *International Journal of Radiation Oncology* Biology* Physics* 2014;90:680-687.
40. Yeo U, Taylor M, Supple J, Smith R, Dunn L, Kron T, Franich R. Is it sensible to “deform” dose? 3d experimental validation of dose‐warping. *Medical physics* 2012;39:5065-5072.
41. Mayr NA, Yuh WT, Magnotta VA, Ehrhardt JC, Wheeler JA, Sorosky JI, Davis CS, Wen B-C, Martin DD, Pelsang RE. Tumor perfusion studies using fast magnetic resonance imaging technique in advanced cervical cancer: A new noninvasive predictive assay. *International Journal of Radiation Oncology* Biology* Physics* 1996;36:623-633.
42. Buschmann M, Majercakova K, Sturdza A, Smet S, Najjari D, Daniel M, Pötter R, Georg D, Seppenwoolde Y. Image guided adaptive external beam radiation therapy for cervix cancer: Evaluation of a clinically implemented plan-of-the-day technique. *Zeitschrift für Medizinische Physik* 2017.
43. Tilly D, van de Schoot AJ, Grusell E, Bel A, Ahnesjö A. Dose coverage calculation using a statistical shape model—applied to cervical cancer radiotherapy. *Physics in Medicine and Biology* 2017;62:4140.
44. Lim K, Kelly V, Stewart J, Xie J, Cho Y-B, Moseley J, Brock K, Fyles A, Lundin A, Rehbinder H. Pelvic radiotherapy for cancer of the cervix: Is what you plan actually what you deliver? *International Journal of Radiation Oncology* Biology* Physics* 2009;74:304-312.
45. Georg P, Georg D, Hillbrand M, Kirisits C, Pötter R. Factors influencing bowel sparing in intensity modulated whole pelvic radiotherapy for gynaecological malignancies. *Radiotherapy and oncology* 2006;80:19-26.
46. Taylor A, Powell M. Conformal and intensity-modulated radiotherapy for cervical cancer. *Clinical oncology* 2008;20:417-425.
47. Whelan B, Kumar S, Dowling J, Begg J, Lambert J, Lim K, Vinod SK, Greer PB, Holloway L. Utilising pseudo-ct data for dose calculation and plan optimization in adaptive radiotherapy. *Australasian Physical & Engineering Sciences in Medicine* 2015;38:561-568.

48. Nováková E, Heijkoop S, Quint S, Zolnay A, Mens J, Godart J, Heijmen B, Hoogeman M. What is the optimal number of library plans in art for locally advanced cervical cancer? *Radiotherapy and Oncology* 2017.
49. Lee CM, Shrieve DC, Gaffney DK. Rapid involution and mobility of carcinoma of the cervix. *International Journal of Radiation Oncology* Biology* Physics* 2004;58:625-630.
50. Khan A, Jensen LG, Sun S, Song WY, Yashar CM, Mundt AJ, Zhang F-q, Jiang SB, Mell LK. Optimized planning target volume for intact cervical cancer. *International Journal of Radiation Oncology* Biology* Physics* 2012;83:1500-1505.
51. Bondar ML, Hoogeman M, Schillemans W, Heijmen B. Intra-patient semi-automated segmentation of the cervix–uterus in ct-images for adaptive radiotherapy of cervical cancer. *Physics in medicine and biology* 2013;58:5317.
52. Zhang C, Christensen GE, Murphy MJ, Weiss E, Williamson JF. Non-rigid image registration with equally weighted assimilated surface constraint. International Workshop on Biomedical Image Registration. Springer. 2014. pp. 31-40.
53. Bondar L, Hoogeman MS, Osorio EMV, Heijmen BJ. A symmetric nonrigid registration method to handle large organ deformations in cervical cancer patients. *Medical physics* 2010;37:3760-3772.
54. Ghose S, Holloway L, Lim K, Chan P, Veera J, Vinod SK, Liney G, Greer PB, Dowling J. A review of segmentation and deformable registration methods applied to adaptive cervical cancer radiation therapy treatment planning. *Artificial intelligence in medicine* 2015;64:75-87.

3.3 DISCUSSION

Cette étude a montré les avantages et limites des stratégies proposées dans la littérature, pour une population hétérogène en termes de variabilité anatomique. Il a été montré que la stratégie standard était insuffisante pour assurer la couverture du CTV. En effet, avec une marge de PTV à 10 mm, la stratégie standard permet d'assurer une couverture du CTV supérieure à 98% uniquement pour 50% de la cohorte. Comparées à cette approche, les stratégies reposant sur l'ITV ou sur la replanification à 20 Gy permettent d'améliorer la couverture du CTV à l'échelle de la population (+2.8% pour l'ITV et +1% pour la replanification à mi-traitement). Cependant, la stratégie ITV résulte en une augmentation significative de la couverture de tous les OAR (+11.4% pour la vessie, +16.5% pour le rectum et +3.2% pour la cavité péritonéale). La replanification à mi-traitement permet une légère augmentation de la couverture du CTV, avec une épargne significative de la cavité péritonéale (-1.7%). La librairie de plans de traitement classique permet quant à elle d'améliorer la couverture du CTV (+2.1%) tout en réduisant faiblement la couverture des OAR (-0.2% pour la vessie et -1.2% pour la cavité péritonéale). Cette stratégie reste cependant limitée pour les patientes avec de faibles mouvements du CTV à la planification mais de larges mouvements pendant le traitement. La librairie évolutive, stratégie originale proposée dans cette étude, permet d'améliorer la couverture du CTV par l'enrichissement de la librairie avec de nouvelles anatomies, si ces dernières se présentent au cours du traitement. Cette librairie évolutive apporte la meilleure couverture du CTV (+3.8%) tout en épargnant la cavité péritonéale (+2%) et sans modifier la couverture de la vessie. La couverture du rectum est, quant à elle, légèrement dégradée.

Puisque les différentes stratégies ne sont pas adaptées à l'ensemble des patientes, la question de la définition de sous-groupes de patientes se pose. Dans l'étude de Heijkoop *et al* [6], la cohorte (*cf.* section 1.4.3.3) a été divisée en deux groupes, respectivement mobile à la planification (11 patientes) et non-mobile (29 patientes). Le critère utilisé, géométrique, était un seuillage de 2.5 cm sur le déplacement du fond utérin observé à la planification à partir des images TDM acquises avec une vessie pleine puis vide. A l'issue notre étude, quatre comportements (mobile ou non-mobile à la planification et mobile ou non-mobile pendant le traitement) permettent d'expliquer les performances des différentes stratégies. La Figure 3-10 et le Tableau 3-4 présentent les quatre groupes identifiés et la classification des stratégies pour chaque groupe de patientes. Il est à noter que, si la mobilité de l'utérus est aisément quantifiable à la planification, sa quantification pendant le traitement est faite *a posteriori* et ne permet donc pas de sélectionner une stratégie de traitement adaptée. Dans ce sens, la librairie évolutive, en ne déclenchant des replanifications qu'en cas de besoin, est un pas vers une meilleure personnalisation du traitement.

Ainsi, la librairie de plans de traitement résulte, pour 30% de notre cohorte, en une couverture moyenne du CTV par le PTV (marge de 10 mm) inférieure à 98% (respectivement 95% pour une marge à 7 mm). Dans le cas d'une patiente non-mobile à la planification et mobile pendant le traitement (identifiant 05, *cf.* Figure 3-10 et Figure 3-12), la couverture du CTV sur l'ensemble du traitement peut être très mauvaise, jusqu'à 72.4% de couverture du CTV (*cf.* Table 3-1). Pour cette patiente, la librairie évolutive permettait de corriger cette sous-couverture par l'ajout de 3 replanifications déclenchées en début de traitement, résultant en une augmentation de 20.6%.

Pour vérifier ces observations, le mouvement de l'utérus à la planification et pendant le traitement a été quantifié. Pour chaque patiente, à l'aide d'une méthode de recalage déformable de maillages (*cf.*

chapitre suivant, section 4.2.2.3), le déplacement du fond utérin a été estimé en utilisant l'anatomie issue de la TDM de planification à vessie intermédiaire comme référence.

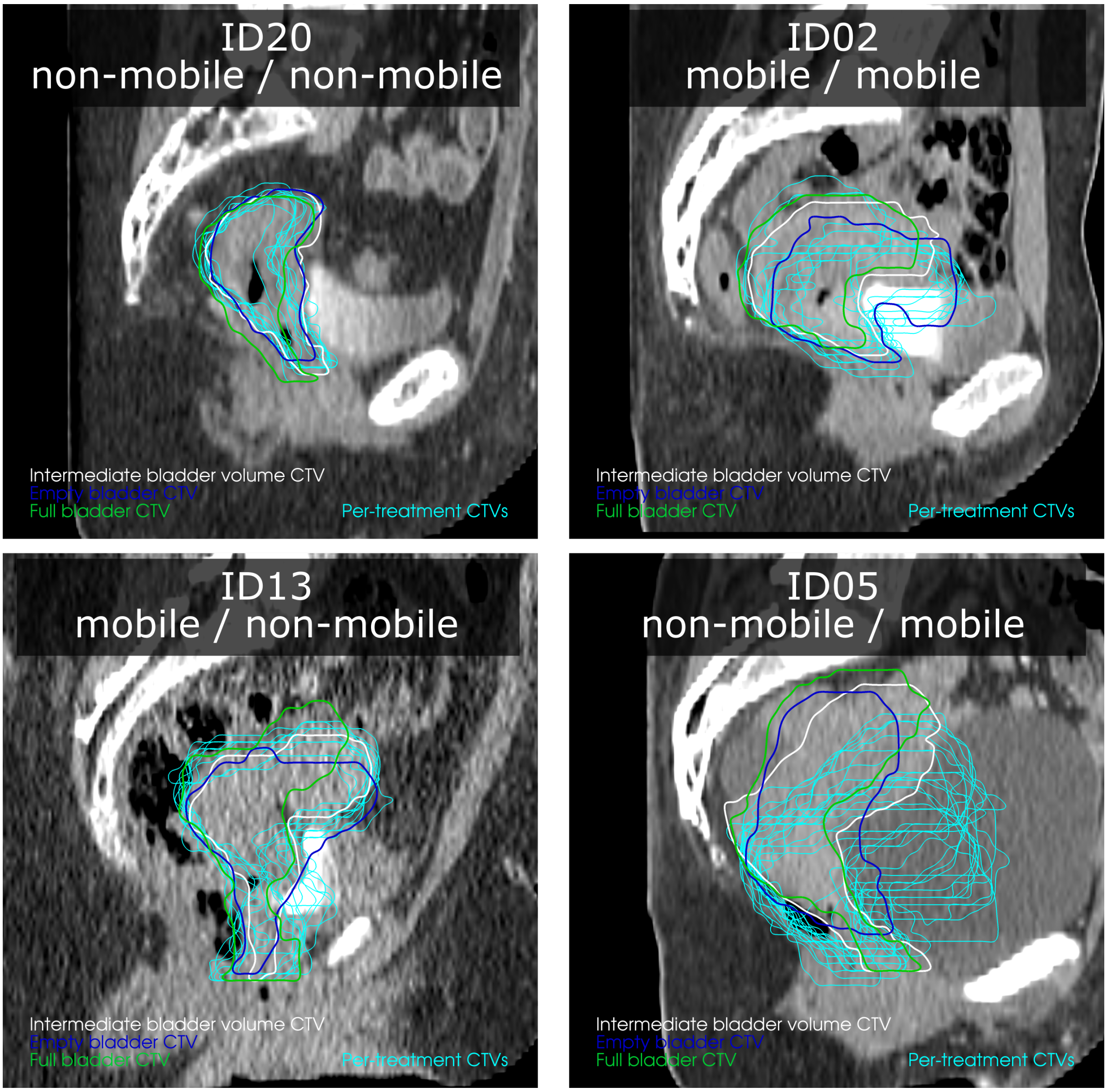

Figure 3-10 : Illustration de la classification en quatre groupes en fonction du mouvement de l'utérus à la planification et pendant le traitement

Chaque sous figure représente la TDM de planification avec vessie de volume intermédiaire. Chaque patiente est identifiée (20, 2, 13 et 5). Les délinéations des CTV de la librairie sont illustrées par les contours blanc, bleu foncé et vert pour le volume de vessie intermédiaire, vide et plein, respectivement. Les contours de chaque fraction, alignés par repositionnement osseux, sont représentés en bleu clair.

Tableau 3-4 : Classification qualitative des performances des stratégies pour les 4 groupes de patientes

Une case verte cochée indique la capacité de la stratégie à couvrir le CTV pour chaque groupe. Une case rouge indique une stratégie inefficace à couvrir le CTV.

Comportement planification/traitement	Stratégies				
	Standard	Replanification mi-traitement	ITV	Librairie plans de traitement	Librairie évolutive
Non-mobile/non-mobile	✓	✓	✓	✓	✓
Mobile/non-mobile	✓	✓	✓	✓	✓
Mobile/mobile	X	X	✓	✓	✓
Non-mobile/mobile	X	X	X	X	✓

La Figure 3-11 représente le déplacement du fond utérin pour chaque patiente de la cohorte. On peut remarquer que, pour certaines patientes, l’amplitude des mouvements supéro-inférieurs et antéro-postérieurs à la planification (lignes rouges), est similaire à l’amplitude observée au cours du traitement (par ex. les patientes 2, 9, 13 et 16). D’autres patientes ne montrent aucune déformation du CTV à la planification et au cours du traitement (par ex. les patientes 3 et 20). Pour ces deux groupes de patientes, une librairie de plans de traitement, voire une stratégie standard dans le deuxième cas, avec une marge de 10 mm semble appropriée. A contrario, certaines patientes montrent très peu de déformations du fond utérin à la planification et de larges déformations au cours du traitement (par ex. les patientes 4, 5, 12, 14 et 15). Pour ces patientes, la librairie évolutive est la seule stratégie testée qui soit efficace. Le Tableau 3-5 illustre le nombre de replanifications déclenchées par la librairie évolutive pour ce sous-groupe de patientes ainsi que la couverture du CTV avec une marge de 7 mm pour la stratégie standard, la librairie de plans de traitement et la librairie évolutive. Pour cette dernière, entre une et trois replanifications ont été déclenchées. Pour ces patientes, par rapport au standard, le gain moyen (min – max) en termes de couverture par le PTV apporté par la librairie évolutive est de 11.16% (2.24 – 30.16). Par rapport à la librairie de plans de traitement classique, le gain moyen (min – max) est de 7.95% (0.14 – 28.8).

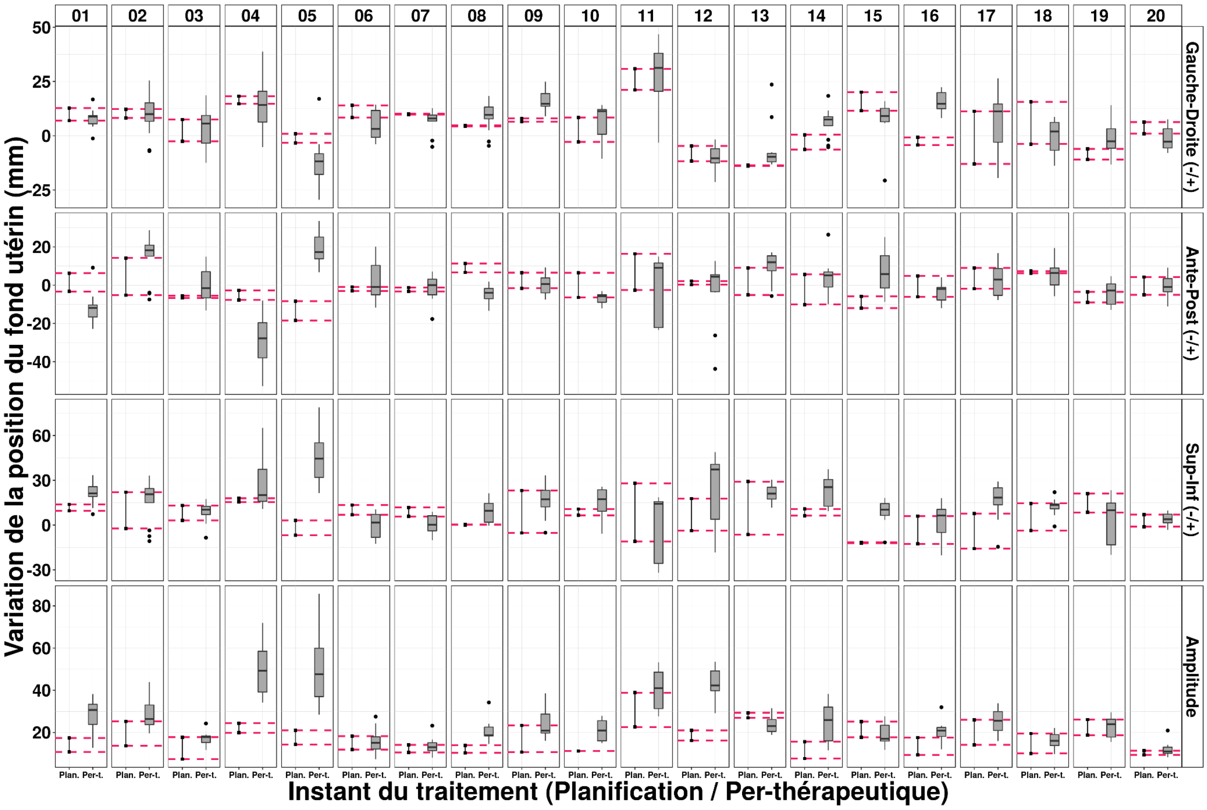

Figure 3-11 : Variation de la position du fond utérin

La figure représente la variation de la position du fond utérin, pour chaque patiente de la cohorte, entre l'anatomie de la TDM de planification avec volume de vessie intermédiaire et toutes les autres anatomies imagées (c'est-à-dire à la planification et pendant le traitement). Chaque ligne représente la direction du déplacement (*i.e.* gauche-droite, antérieure-postérieure, supérieure-inferieure, amplitude). Chaque colonne représente une patiente par son identifiant. Les lignes rouges représentent les déplacements à la planification.

Tableau 3-5 : Couverture du CTV par une marge de PTV à 7 mm pour un sous-groupe de patientes

Identifiant patiente	Nombre de replanifications (librairie évolutive)	Couverture moyenne du CTV (marge 7 mm) (%)		
		Standard RT	Librairie de plans de traitement	Librairie évolutive
04	2	82.85	85.81	93.01
05	3	63.58	64.94	93.74
12	1	83.80	91.25	93.43
14	1	93.54	97.05	97.19
15	1	93.70	94.50	95.94

Cependant, pour ces cinq patientes, trois ont un gain inférieur à 3% par rapport à la librairie de plans de traitement. Pour ces patientes, le gain apporté par l'unique replanification déclenchée par la librairie évolutive semble donc limité.

De plus, l'amélioration de la couverture du CTV peut engendrer de fortes variations de la couverture de certains OAR. Par exemple, comparant la stratégie standard à la librairie de plans de traitement avec une marge de 7 mm, la patiente 12 a une variation de la couverture de +23.97% pour le rectum. Cette sur-couverture du rectum résulte du déplacement antéro-postérieur du col de l'utérus (*cf.* section 3.2.3.4 et Figure 3-12). Pour la patiente 14, la librairie de plans de traitement avec une marge de PTV de 7 mm a entrainé une augmentation de 6.18% de la couverture de la vessie (et une diminution de 9.47% de celle du rectum). Similairement aux résultats de la littérature, à l'échelle de la population, une tendance en termes d'épargne aux OAR est difficilement identifiable. Par exemple, comparant la couverture de la vessie entre la stratégie standard et la librairie évolutive, 50% des patientes présentent un surdosage (5.7% en moyenne) ou une épargne (-9.7% en moyenne).

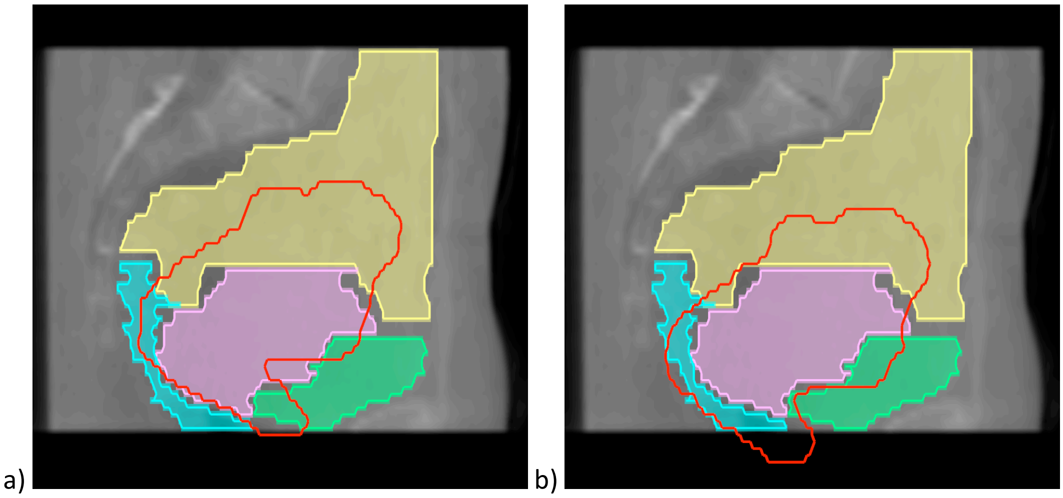

Figure 3-12 : Illustration de l'augmentation de la couverture du CTV et du rectum par une marge de PTV à 7 mm pour la patiente 12 entre les stratégies standard (plan vessie intermédiaire) (a) et de librairie de plans de traitement (plan vessie vide) (b)

Pour cette fraction de la patiente 12, l'utilisation du PTV de l'anatomie avec vessie vide entraine une amélioration de la couverture du CTV de 6.39% mais une dégradation de la couverture du rectum de 49.25%. Le CTV, le rectum, la vessie et la cavité péritonéale sont représentés par les contours pleins rose, bleu, vert et jaune, respectivement. Le PTV avec une marge à 7 mm est représenté par le contour rouge.

3.4 CONCLUSION

Ces travaux ont permis de définir une stratégie personnalisée, appelée librairie évolutive, qui repose sur une librairie de plans de traitement pouvant être enrichie des anatomies issues de l'imagerie per-thérapeutique. Par rapport aux stratégies de la littérature, cette approche est la seule à assurer, pour toutes les patientes, une bonne couverture du CTV tout en épargnant la vessie et la cavité péritonéale. Cette approche peut cependant s'avérer complexe à implémenter en routine clinique avec une charge de travail supplémentaire pour les patientes nécessitant de nombreuses replanifications.

3.5 RÉFÉRENCES

1. Ríos I, Vásquez I, Cuervo E, Garzón Ó, Burbano J. Problems and solutions in igrt for cervical cancer. *Reports of Practical Oncology & Radiotherapy* 2018.
2. Gobeli M, Simon A, Getain M, Leseur J, Lahlou E, Lafond C, Dardelet E, Williaume D, Rigaud B, de Crevoisier R. Benefit of a pretreatment planning library-based adaptive radiotherapy for cervix carcinoma? *Cancer radiotherapie* 2015;19:471-478.
3. Bondar M, Hoogeman M, Mens J, Quint S, Ahmad R, Dhawtal G, Heijmen B. Individualized nonadaptive and online-adaptive intensity-modulated radiotherapy treatment strategies for cervical cancer patients based on pretreatment acquired variable bladder filling computed tomography scans. *International Journal of Radiation Oncology* Biology* Physics* 2012;83:1617-1623.
4. Nassef M, Simon A, Cazoulat G, Duménil A, Blay C, Lafond C, Acosta O, Balosso J, Haigron P, de Crevoisier R. Quantification of dose uncertainties in cumulated dose estimation compared to planned dose in prostate imrt. *Radiotherapy and Oncology* 2016;119:129-136.
5. Cazoulat G, Simon A, Dumenil A, Gnep K, De Crevoisier R, Acosta O, Haigron P. Surface-constrained nonrigid registration for dose monitoring in prostate cancer radiotherapy. *IEEE Transactions on Medical Imaging* 2014;33:1464-1474.
6. Heijkoop ST, Langerak TR, Quint S, Bondar L, Mens JWM, Heijmen BJ, Hoogeman MS. Clinical implementation of an online adaptive plan-of-the-day protocol for nonrigid motion management in locally advanced cervical cancer imrt. *Int J Radiat Oncol Biol Phys* 2014;90:673-679.

4 MODELE STATISTIQUE DE FORME POUR LA MODELISATION D'UNE LIBRAIRIE DE PLANS DE TRAITEMENT

4 Modèle statistique de forme pour la modélisation d'une librairie de plans de traitement........138

4.1 Introduction........139

4.2 Article : "Statistical shape model to generate a planning library for cervical adaptive radiotherapy"........140

4.2.1 Introduction........141

4.2.2 Methods........143

4.2.3 Evaluation........150

4.2.4 Discussion and Conclusion........157

4.2.5 References........159

4.3 Discussion........162

4.3.1 Limites et perspectives........162

4.4 Extension au cancer de la vessie........164

4.5 Conclusion........168

4.6 Références........169

4.1 INTRODUCTION

L'étude décrite dans le chapitre 3 a montré que les stratégies proposées dans la littérature pouvaient être limitées pour assurer la couverture du CTV en toutes circonstances. Pour répondre à cette première problématique, la librairie évolutive a été proposée pour améliorer la couverture du CTV par le déclenchement de replanifications au cours du traitement. Cependant, plusieurs aspects limitent la projection de ce type de stratégie dans un contexte clinique. En effet, toutes les stratégies reposant sur une librairie de plans de traitement nécessitent l'acquisition de plusieurs scanners de planification avec des volumes de vessie variables, ce qui peut entraîner une irradiation supplémentaire de la patiente, une occupation plus longue des machines, une difficulté à acquérir des volumes de vessie précis et donc une augmentation de l'inconfort des patientes.

De plus, il existe différents groupes de patientes avec des comportements différents à la planification ou pendant le traitement (utérus non-mobile ou mobile). Pour les patientes non-mobiles à la planification, les librairies de plans de traitement ne reflètent pas forcément les déformations observées pendant le traitement. De ce fait, les résultats de ces stratégies peuvent être en deçà des attentes en terme de rapport coût/bénéfice [1]. Une approche intéressante pour résoudre cette problématique serait de simuler les déformations susceptibles de survenir pendant le traitement, au moment de la planification. Une analyse populationnelle, représentant les déformations de la cible clinique d'une population pendant le traitement, pourrait alors être utilisée. Cette approche passe par une mise en correspondance de l'ensemble col de l'utérus – utérus pour les patientes d'une population, puis par une analyse des formes pour extraire les déformations principales.

Pour la quantification des déformations, l'étude précédente repose sur l'utilisation du recalage déformable des Démons pour estimer un champ de déformation dense (défini en chaque voxel), soit en intra- soit en inter-patientes, à partir de cartes de distances représentant les organes délinéés. Cette méthode effectuant un compromis entre le recalage des surfaces et de l'intérieur des organes, elle reste limitée pour des applications de recalage de surfaces où des contraintes locales sont souhaitées pour générer des déformations plus complexes. Nous nous sommes donc orientés vers une autre approche permettant le recalage de maillages de surface.

Ce chapitre est dédié à la proposition et l'évaluation d'une librairie de plans de traitement modélisée, spécifique à chaque patiente, ne nécessitant l'acquisition que d'une TDM, et définie à partir d'une analyse populationnelle. Cette approche requiert l'analyse des déformations de la population dans un repère commun. De ce fait, une méthode de mise en correspondance anatomique intra- et inter-patientes est proposée. Afin de générer un modèle statistique de forme compact, représentant les déformations de la population, une Analyse en Composantes Principales (ACP ou *Principal Component Analysis, PCA*) a été utilisée. A partir de ce modèle standard, des modèles de forme d'ACP a posteriori, basés sur de contraintes représentant le mouvement du fond utérin, sont générées afin d'établir une librairie de plans de traitement. L'approche est comparée et évaluée géométriquement par rapport à la stratégie standard (c'est-à-dire considérant un unique CTV de planification) et à la librairie de plans de traitement classique (c'est-à-dire trois CTV de planification).

Ces travaux ont fait l'objet d'un article, intitulé « *Statistical shape model to generate a planning library for cervical adaptive radiotherapy* », publié dans le journal *IEEE Transactions on Medical Imaging* en 2018 et reproduit ci-dessous.

4.2 ARTICLE : “STATISTICAL SHAPE MODEL TO GENERATE A PLANNING LIBRARY FOR CERVICAL ADAPTIVE RADIOTHERAPY”

Bastien Rigaud *MSc* (1,2)*, Antoine Simon *PhD* (1,2), Maxime Gobeli *MD* (3), Julie Leseur *MD* (3), Loig Duvergé *MSc* (3), Danièle Williaume *MD* (3), Joël Castelli *MD, MSc* (1,2,3), Caroline Lafond *MD, PhD* (1, 3), Oscar Acosta *PhD* (1, 2),, Pascal Haigron *PhD* (1,2) and Renaud De Crevoisier *MD*, *PhD* (1,2,3)*

1. Université de Rennes 1, LTSI, Campus de Beaulieu, Rennes, F-35042
2. INSERM, U1099, Campus de Beaulieu, Rennes, F-35042
3. Centre Eugene Marquis, Radiotherapy Department, Rennes, F-35000

Abstract

External beam radiotherapy is extensively used to treat cervical carcinomas. A single planning CT scan enables the calculation of the dose distribution. The treatment is delivered over 5 weeks. Large per-treatment anatomical variations may hamper the dose delivery, with the potential of an organs at risk (OAR) overdose and a tumor underdose. To anticipate these deformations, a recent approach proposed three planning CTs with variable bladder volumes, which had the limitation of not covering all per-treatment anatomical variations. An original patient-specific population-based library has been proposed. It consisted of generating two representative anatomies, in addition to the standard planning CT anatomy. First, the cervix and bladder meshes of a population of 20 patients (314 images) were registered to an anatomical template, using a deformable mesh registration. An iterative point-matching algorithm was developed based on local shape context (histogram of polar or cylindrical coordinates and geodesic distance to the base) and on a topology constraint filter. Second, a standard principal component analysis (PCA) model of the cervix and bladder was generated to extract the dominant deformation modes. Finally, specific deformations were obtained using posterior PCA models, with a constraint representing the top of the uterus deformation. For a new patient, the cervix-uterus and bladder were registered to the template, and the patient’s modeled planning library was built according to the model deformations. This method was applied following a leave-one-patient-out cross-validation. The performances of the modeled library were compared to those of the three-CT-based library and showing an improvement in both target coverage and OAR sparing.

4.2.1 INTRODUCTION

External beam radiotherapy (EBRT) with chemotherapy, followed by brachytherapy, is the reference treatment for locally advanced cervical carcinomas. EBRT is based on the acquisition of a single planning CT scan on which anatomical structures are manually delineated and from which the dose distribution is calculated. The clinical target volume (CTV) is defined as the cervical tumor, uterus, parametria and vagina according to initial staging, and pelvic lymph nodes. A planning target volume (PTV) is defined, corresponding to the CTV, with a fixed margin (generally of 10 mm). The organs at risk (OAR) are the bladder, rectum, and bowel, with the latter including the sigmoid. The dose distribution is then optimized to deliver the prescribed dose to the PTV, while sparing as much as possible of the OAR. The treatment is delivered in daily fractions, over 5 weeks. On-board imaging, such as cone-beam CT (CBCT), enables the visualization of anatomical structures (*cf.* Figure 4-1). However, large anatomical variations may occur over treatment, such as bladder and rectum filling or tumor regression. The position of the uterus has been shown to be related to bladder volume: an empty bladder results in an anteriorly tipped uterus and a full bladder results in a vertical uterus [1,2]. These deformations may, consequently, hamper the precision of the dose delivery since the per-treatment anatomy does not correspond to the planning anatomy (*cf.* Figure 4-2). The patient may be exposed to both tumor underdose and OAR overdose [3-5].

Several strategies have previously been proposed to account for these anatomical variations. The simplest solution is to increase the size of the PTV by increasing the CTV-to-PTV margin. Another option is to define an internal target volume (ITV) that corresponds to the union of different CTVs from planning CT acquired with various bladder volumes. These two solutions limit the risk of CTV underdosage, yet carry the major drawback of increasing the dose delivered to the OAR [6-8]. Thus, recently, more sophisticated strategies, known as adaptive radiation therapy (ART), have been proposed. ART considers not only one treatment plan but multiple treatment plans, adapted to different anatomical configurations that anticipate per-treatment organ deformations. In EBRT for cervical cancer, the main ART strategy relies on the generation of a treatment planning library [7,8]. This treatment planning library is composed of multiple treatment plans based on different anatomies (*i.e.* CTV shape) resulting from planning CTs acquired with different bladder volumes (*cf.* Figure 4-1b). The "classic" CT-based library is generally based on two or three anatomies (empty, intermediate and full bladder volume) in order to provide adequate coverage, while limiting the workload of the treatment plan optimization (one for each CT). At each treatment fraction, CBCT images enable the optimal treatment plan to be chosen among those of the library ("plan-of-the-day"). This strategy appears to be adequate to compensate for uterine motions [9-11]. However, such a library does not handle per-treatment deformations that are not represented in the planning CTs. In particular, this strategy is inefficient for patients with no motion at the planning and motion during treatment (*cf.* Figure 4-2) [8]. Furthermore, compared to the standard treatment, the workload required to acquire and delineate the CT images is relatively heavy (*i.e.* 1 hour instead of 20 minutes for the whole acquisition procedure, and 1 hour 30 minutes instead of 30 minutes for manual segmentation) while causing more discomfort to the patient (i.e. bladder filling protocol).

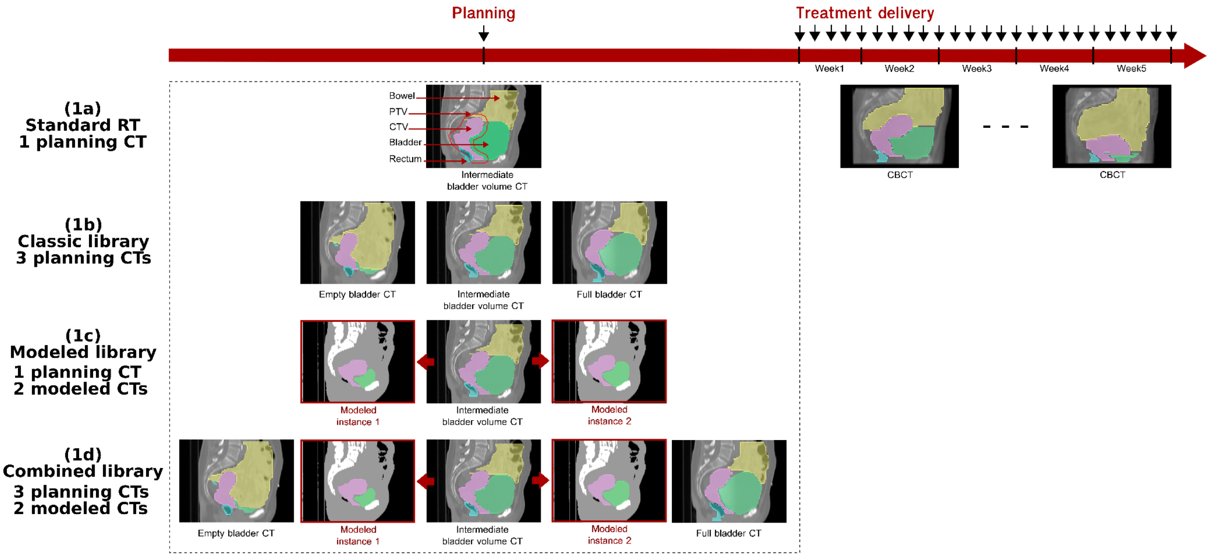

Figure 4-1: Radiotherapy strategies for locally advanced cervical cancer

In the standard RT approach (1a), the dose distribution is calculated based on one planning CT, generally with intermediate bladder volume, and the treatment is delivered in 25th fractions over 5 weeks. However, large per-treatment anatomical deformations, mainly due to the bladder filling and tumor shrinking, can be observed. These deformations may not be taken into account on the single planning CT, thereby exposing the patient to tumor underdose and organ at risk overdose. Three alternative strategies are represented: (1b) a classic library-based RT with three planning CTs (variable bladder volumes); (1c) the proposed modeled planning library based on the population analysis; and (1d) the combined library using (1b) and (1c). RT: Radiation therapy; PTV: Planning target volume; CTV: Clinical target volume

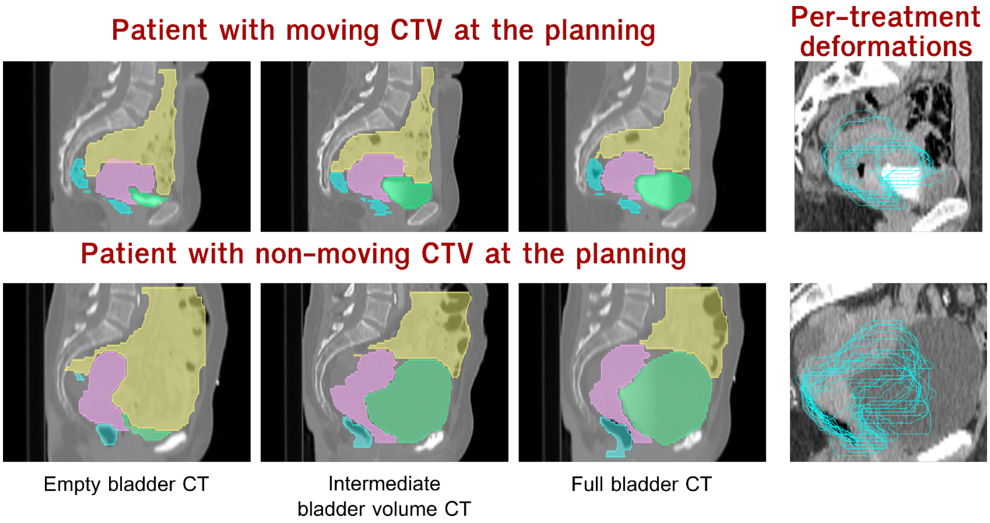

Figure 4-2: Classic CT-based planning library limitations

Two patients are illustrated. One patient had a moving CTV at the planning and during the treatment. The classic library appears to be adapted. Another patient had a non-moving CTV at the planning and a moving CTV during treatment, resulting in tumor underdose and OAR overdose when using the classic library. The CTV (cervix-uterus) is in pink. The rectum, bladder and bowel are in blue, green and yellow, respectively. The per-treatment CTV contours are in light blue. CTV: Clinical target volume; OAR: Organ at risk

One way to overcome these limitations would be to simulate the most likely deformations of the patient's anatomy in order to improve the coverage of the target. For this purpose, a population analysis can be used to identify the main deformations. This population analysis needs the cervix-uterus of the different patients to be registered. This registration step is challenging due to the large intra-patient and all the more inter-patient variations. To our knowledge, only one study analyzed both intra and inter-patient deformations of the cervix-uterus anatomy in the context of EBRT [12]. Based on CT images, the proposed approach used deformable registration and principal component analysis (PCA) to quantify the delivered dose uncertainties.

The aim of this study was thus, based on a population analysis, to generate a patient-specific planning library (CTV and bladder) using a single CT scan of the considered patient (*cf.* Figure 4-1c). First, a deformable mesh registration (DMR) method was used to quantify the population deformations within a template space. This DMR was based on the shape context descriptors using an iterative and multiscale approach. Second, standard and posterior principal component analysis (sPCA and pPCA) were used to build a statistical shape model (SSM) in the template space. By using different motion constraints associated with the top of the uterus, deformation vector fields (DVF) between the mean sPCA and pPCA models were generated. Finally, the DVFs were used to deform the patient CTV and bladder, thereby, generating the different shapes of the patient-specific library. This paper first describes the proposed workflow, including the DMR method, the sPCA and pPCA approaches and the method used to model a patient-specific library. This approach was then evaluated by comparing it with the standard RT and a three-CT-based planning library (*i.e.* "classic" library). The endpoints were the geometric coverages of the CTV and OAR by the PTV throughout the whole treatment.

4.2.2 METHODS

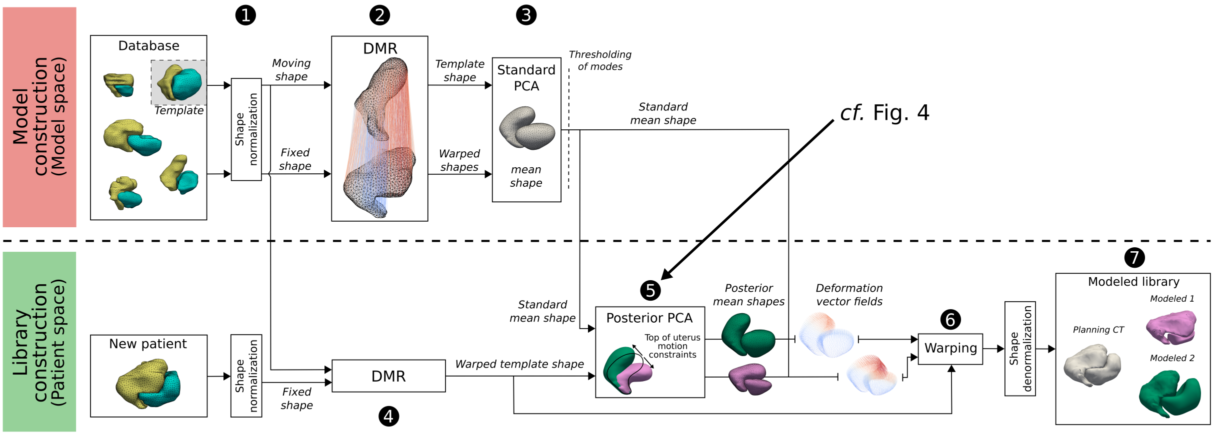

Figure 4-3: Model workflow used to generate the modeled library

The first step is the model construction: (1) the organ shapes are normalized to limit the observations to the uterus movement; (2) the DMR method is used to compute the correspondence fields between the template and the population shapes; and (3) the standard PCA is built over the shapes in correspondences to represent the dominant deformations. The second step is the library construction to apply the model to a new patient: (4) the organ shapes are propagated in the model space by means of the DMR method; (5) a posterior PCA is built to extract the desired deformation corresponding to the tipping of the uterus; (6) the shapes are then warped by the deformation vector fields of the model; and (7) the warped shapes are denormalized to define the modeled planning library in the patient space. DMR: deformable mesh registration; PCA: principal component analysis

4.2.2.1 Proposed workflow

The workflow of the model construction is presented in Figure 4-3. The first step was the population model construction. First, the meshes of the cervix-uterus (*i.e.* CTV) and the bladders of the patient population were aligned and normalized according to an anatomical template. Second, DVF between the template and the inter- and intra-patient shapes were obtained using DMR. Third, the sPCA was built over these shapes in correspondence to generate a SSM. Then, for a new patient's shapes (CTV and bladder), normalization and DMR correspondences with the anatomical template were computed. According to the CTV shape of the new patient, motion constraints were generated over the top of the uterus of the sPCA mean shape in order to obtain the pPCA models. Finally, the new patient planning shapes (CTV and bladder) were deformed by means of the DVF between the standard and posterior mean shapes. This enabled the definition of several instances around the patient CTV and bladder shapes, which formed the planning library.

Each of these steps is described here-after.

4.2.2.2 Template selection and shape normalization

A template shape (S_{temp}) was selected as the CTV, having the median volume of the database. To analyze the patients in a common space (*i.e.* scale and position), a shape normalization was first applied:

$$S_{norm}(x,y,z) = \frac{\max\{GeoD[S_{temp}(x,y,z)]\} \times [S(x,y,z) - C_{centroid}(x,y,z)]}{\max\{GeoD[S(x,y,z)]\}} \tag{4-1}$$

Each patient's CTV shapes, $S(x, y, z)$, were size- and position-normalized. The size-normalization was based on the maximum of the geodesic distance (*GeoD*) to the base centroid of the planning CTV. The position-normalization was related to the CTV base centroid coordinates ($C_{centroid}(x, y, z)$). Finally, each patient's CTV shapes were size-normalized by the maximum *GeoD* of the template CTV. The maximum of the *GeoD* to the cervix centroid was also used to identify the position of the top of the uterus (ToU). The bladder shapes were normalized using the same transformations.

4.2.2.3 Iterative deformable mesh registration based on Shape Context

To quantify the population deformations, point-to-point correspondences of organ shapes had to be estimated. Shapes can be represented in a common domain using skeletal representation [13] or spherical harmonic decomposition [14,15], which can be limited for complex shapes.

More commonly, DMR methods have been introduced to estimate a DVF between two meshes. The DVF is generally estimated using local correspondences estimated by morphological descriptors. Shape context descriptors have been shown to be efficient for this purpose [16]. This method has been enriched with a depth feature [17] or filtered by a geodesic distance-based topology criterion [18] to improve its robustness. However, DMR based on a shape context descriptor still remains highly sensitive to point mismatch when computed in one step. Filtering and regularization may, therefore, be required to constrain the transformation and to ensure more realistic behavior [19]. Iterative DMR methods have been developed, such as surface-based algorithms, thin plate spline robust-point matching (TPS-RPM) [20-23] and coherent point drift (CPD) [24]. Nevertheless, these algorithms rely on point-to-point distances to drive the DVF. They are, thus, dependent on the alignment of the shapes and ultimately may lead to uncertainties in inter-patient soft tissue matching when large deformations have to be estimated, without complex parametrization.

The proposed DMR aims to estimate the forward DVF, representing the elastic transformation T between the fixed (*i.e.* the template) and the moving shapes (S_{fixed}, S_{moving}). The considered shapes are the cervix-uterus and the bladder, which are highly deformable organs. This iterative process is expressed by the following equations:

$$DVF = DVF + G(\mu \times DVF_{step}) \tag{4-2}$$

$$S_{warped} = T(S_{moving}, DVF) \tag{4-3}$$

At each iteration, the S_{moving} shape is warped (S_{warped}) by the DVF, which is updated by means of the DVF_{step}. The DVF_{step} is computed, at each iteration, between S_{fixed} and S_{warped} using a shape context descriptor [16] and the normalized geodesic distance to the centroid of the organ base, as described below. DVF_{step} is then interpolated and regularized by a thin plate spline (TPS) transformation and a Gaussian kernel (G), respectively, and is weighted by $\mu \in]0, 1]$ ($\mu=1$ at the last iteration).

The descriptors are calculated on S_{fixed} and S_{moving}, with each shape being represented by N points. For each point p_i, a normalized histogram, h_i, is defined, representing the spherical (resp. cylindrical) coordinate difference between this point and the remaining $N-1$ points of the shape. Thus, for each point of the bladder (resp. CTV), $\beta \times \gamma \times \delta = Nbins$, histogram bins are defined, with $\beta=5$ for the radial distance (resp. x-y distance), $\gamma=12$ for the azimuth angle and $\delta=6$ for the elevation angle (resp. z signed distance) with a range of $[0, 100]$, $[-180, 180]$, and $[0, 180]$ (resp. $[-100, 100]$). The similarities between the points of S_{fixed} and S_{moving} are computed over a cost matrix, C_{hist}, defined with the χ^2 test statistic:

$$C_{hist}(p_i, q_j) = \frac{1}{2} \sum_{b=1}^{Nbins} \frac{\left[h_i(b) - h_j(b)\right]^2}{h_i(b) + h_j(b)} \tag{4-4}$$

where $h_i(b)$ (resp. $h_j(b)$) represents the bin b of the histogram of point p_i (resp. q_j) of S_{fixed} (resp. S_{moving}).

The geodesic cost matrix C_{geo} is also computed:

$$C_{geo}(p_i, q_j) = \left|GeoD_{fixed}(p_i) - GeoD_{moving}(q_j)\right| \tag{4-5}$$

where $GeoD_{fixed}(p_i)$ (resp. $GeoD_{moving}(q_j)$) represents the geodesic distance between p_i (resp. q_j) and the centroid of the base of S_{fixed} (resp. S_{moving}).

A global cost matrix *C* is computed with the two weighted normalized cost matrices:

$$C_{\varphi_{norm}}(p_i, q_j) = \frac{C_{\varphi}(p_i, q_j) - \min[C_{\varphi}(p_i, q_j)]}{\max[C_{\varphi}(p_i, q_j)] - \min[C_{\varphi}(p_i, q_j)]} \quad (4\text{-}6)$$

where ϕ is either *hist* or *geo to compute* $Chist_{norm}(p_i,q_j)$ *or* $Cgeo_{norm}(p_i,q_j)$, respectively.

$$C(p_i, q_j) = \alpha \times C_{hist_{norm}}(p_i, q_j) + (1-\alpha) \times C_{geo_{norm}}(p_i, q_j) \\ \alpha \in [0,1] \quad (4\text{-}7)$$

To obtain the point-to-point correspondences between S_{fixed} and S_{moving}, the Hungarian optimization method was used on the *C* matrix [25]. The correspondences represent the vectors between S_{fixed} and S_{moving}, with the minimal cost value in terms of the histogram and geodesic descriptors. Similar to the method implemented by Xiao *et al* [18], in order to reduce the sensitivity of the shape descriptors, the correspondences that did not respect the following topological constraint were removed:

$$\left|\sum_{h=1}^{Nneighb} D(p_i, p_h) - \sum_{h=1}^{Nneighb} D[T(p_i), T(p_h)]\right| < \tau \times \sum_{h=1}^{Nneighb} D(p_i, p_h) \quad (4\text{-}8)$$

where $D(p_i,p_h)$ (resp. $D[T(p_i),T(p_h)]$) represents the Euclidean distance between the tested point p_i and its neighbor p_h (resp. the correspondences of the tested point p_i and of its neighbor p_h), over a total of $Nneighb=8$ points. This constraint enables the avoidance of large matching irregularities. The parameter τ is used as a relaxation factor to enable an increase in the number of correspondences driving the deformations.

During the iterative process, S_{warped} becomes progressively closer to S_{fixed}, thus, the number of correspondences, as well as the non-linearity of the DVF, increase during the process. To improve the optimization, a multiresolution scheme is used that considers different factors of the Taubin filter [26]. For each resolution, Gaussian sigma and topological constraint thresholds (τ) can be defined. The process is stopped if the mean correspondence cost is greater than the previous one or if the DVF_{step} mean displacement difference between two iterations is less than a convergence threshold.

4.2.2.4 Standard principal component analysis

Standard PCA (sPCA) enables the compression of large observations and the organization of the dominant information [27,28]. Most studies expressed the dominant deformations of an organ by a compact sPCA model based on few eigenmodes. New samples can then be generated by a weighted sum of these eigenmodes [29,30]. Following this, the generated shapes representing the dominant deformations can be combined to define an ITV [31] or to propose a model-generated PTV [32]. Recent studies used the ability of the model to generate random or systematic deformations prior to the treatment according to the training set observation. For example, random treatment planning scenarios have been generated to assess the dose coverage probability in cervical cancer [12]. The patient-specific per-treatment bladder deformations have been predicted in a prostate cancer population [14]. Using early per-treatment images of a patient, regularized PCA-based methods have also been proposed to anticipate systematic deformations [33].

PCA-based models have, thus, been widely used for different applications; however, no study has proposed the use of PCA models to anticipate the clinical target deformations of a new patient in the emergent plan-of-the-day strategy for adaptive RT.

sPCA was used to build a SSM and observe the dominant deformations of the population. A mean shape (S_{mean}) was computed from the *Nshapes* input shapes (S_i):

$$S_{mean} = \frac{1}{Nshapes} \sum_{i=1}^{Nshapes} S_i \tag{4-9}$$

The S_i shapes represent the inter- and intra-patient CTVs and bladders deformed toward the template anatomy by the DMR. The covariance matrix was computed to represent the linear combination of the shapes:

$$\Sigma = \frac{1}{Nshapes} \sum_{i=1}^{Nshapes} (S_{mean} - S_i)(S_{mean} - S_i)^T \tag{4-10}$$

The covariance matrix was decomposed to extract the eigenvectors and the eigenvalues, which represent the dominant deformations and their variance, respectively:

$$\Sigma = UD^2U^T \tag{4-11}$$

where U and D^2 represent the orthogonal eigenvectors and the corresponding eigenvalues, respectively. Each of the L modes can be scanned independently according to their variance (eigenvalue λ_l) in a range of $\pm 3\sigma$, from the larger deformations to the noisier.

Any shape S_η can be expressed by the ranked model of l modes ($l < L$) with the following linear combination, following a normal law ($\mathcal{N}(S_{mean}, \Sigma)$):

$$S_\eta = S_{mean} + UD_l \tag{4-12}$$

Every generated shape S_η has the same point indices than S_{mean}, thus, a DVF can be computed by the difference of their coordinates.

4.2.2.5 Patient specific modeled planning library

The SSM, built by the sPCA over the population, was used to generate potential anatomies for a new patient, based on a single observation. For this purpose, posterior PCA were computed to apply constraints (displacement of the ToU) on the planning anatomy of the new patient. The resulting deformations were applied on this anatomy to build the modeled library, prior to treatment.

4.2.2.5.1 Posterior principal component analysis

SSM has been used for shape reconstructions from partial information [34,35]. The SSM was fitted on the known part of the shape and, thus, the missing part of the shape was reconstructed according to the instance of the model. Furthermore, posterior PCA has been introduced to represent a subset of sPCA with constraints on the known part of a given shape [36].

From the compact sPCA model (S_{mean}, UD_l), a pPCA model was generated based on a given constraint, C_g. The resulting pPCA, using Gaussian regression, represents the S_{Cg} mean shape and the submatrix $U_{Cg}D_{Cg}$. The S_{Cg} represents a new shape, that satisfies the local constraint C_g and with its remaining points interpolated. The submatrix $U_{Cg}D_{Cg}$ represents the residual eigenvectors and the corresponding eigenvalues, which are not related to C_g. To express the uncertainty of C_g, a Gaussian noise (ε) is added.

The pPCA formula to express any shape S_η, following a normal law ($\mathcal{N}(S_{Cg}, \Sigma_{Cg})$), is then:

$$\begin{gathered} S_\eta = S_{Cg} + \left(U_{Cg}D_{Cg}\right)_l + \varepsilon \\ \varepsilon \sim \mathcal{N}(0, \sigma^2) \end{gathered} \tag{4-13}$$

More detailed calculus and justifications are present in the study conducted by the Scalismo team [36], an open-access library for statistical shape analysis used for this study.

4.2.2.5.2 Generation of the patient-specific constraint

To generate two new shapes from the new patient's anatomy using the pPCA, two constraints have to be defined. They were made of two vectors (V_{C1} and V_{C2} in mm) applied to the ToU. The ToU point was automatically localized using the geodesic distance to the base centroid *(cf.* equation (4-1*).* Each constraint was defined according to the signed z-axis distance between the ToU positions of the new patient (ToU_{new}) and of the mean shape of the sPCA (ToU_{Smean}):

$$D = ToU_{new}(z) - ToU_{S_{mean}}(z) \tag{4-14}$$

The CTV deformations were analyzed, inside the sPCA space, by a clinical expert to define the mean cervix-uterus shape in a vertical (head direction) and horizontal position (foot direction). From this analysis, the resulting constraint amplitude of the ToU$_{Smean}$, was defined by: $\gamma = \langle 0, 15, 15\rangle$ mm. Considering the position of ToU$_{new}$ relatively to ToU$_{Smean}$, three cases were considered, based on *D*, to generate V_{C1} and V_{C2} (*cf.* Figure 4-4):

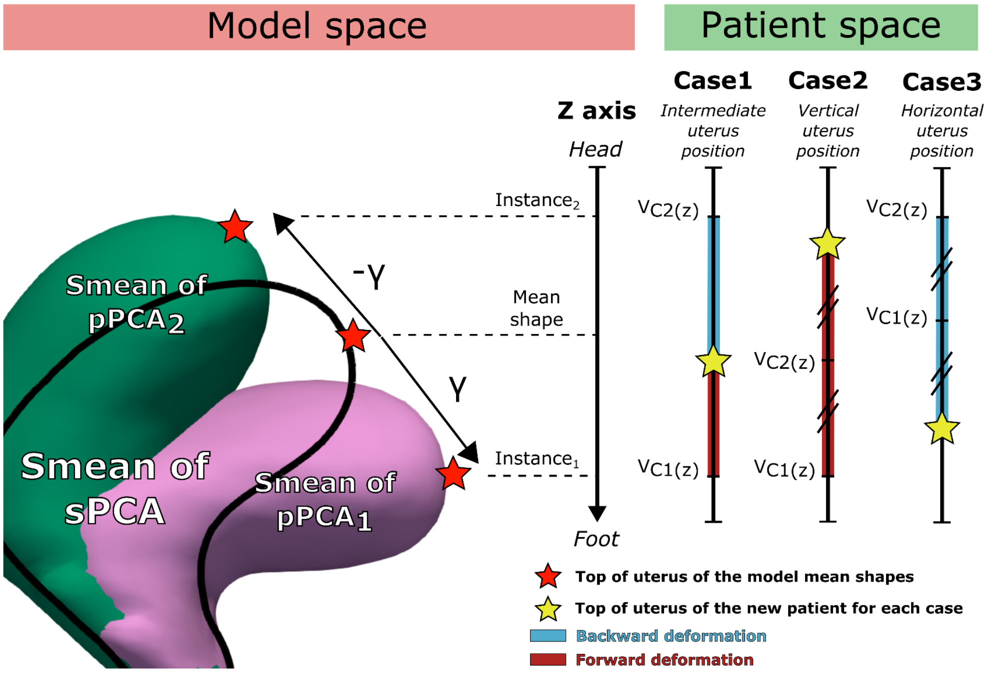

Figure 4-4: pPCA constraint definition

The decision process involved in computing the pPCA mean shapes (Smean) of the new patient is illustrated for different cases. VC1 and VC2 represent the resulting constraint vectors. The constraint vectors length and direction are dependent of the considered case. The cases are explained section 4.2.2.5.2. The z-axis is pointing to the foot direction. sPCA: standard principal component analysis; pPCA: posterior PCA

Case 1, $if\ \frac{-\gamma(z)}{2} < D < \frac{\gamma(z)}{2}$

$$then \begin{cases} V_{C1}(x,y,z) = \langle 0, \gamma(y), \gamma(z) - D\rangle \\ V_{C2}(x,y,z) = \langle 0, -\gamma(y), -\gamma(z) - D\rangle \end{cases} \tag{4-15}$$

Case 2, $if\ D < \frac{-\gamma(z)}{2}$

$$then \begin{cases} V_{C1}(x,y,z) = \langle 0, \gamma(y), \gamma(z) - D\rangle \\ V_{C2}(x,y,z) = \dfrac{V_{C1}(x,y,z)}{2} \end{cases} \tag{4-16}$$

Case 3, $if\ D > \frac{\gamma(z)}{2}$

$$then \begin{cases} V_{C2}(x,y,z) = \langle 0, -\gamma(y), -\gamma(z) - D\rangle \\ V_{C1}(x,y,z) = \dfrac{V_{C2}(x,y,z)}{2} \end{cases} \tag{4-17}$$

The two defined constraints enabled the computation of two pPCA mean shapes and their eigenvectors (*cf*. section 4.2.2.5.1*)*. The two DVFs between each pPCA and the sPCA on the CTV and bladder mean shapes were extracted. Finally, the new patient's planning CTV and bladder were deformed by these DVFs.

Due to the difference in the bladder shapes and volumes among the patients, a basic representation of the bladder mean shape of the population may lead to unsatisfying bladder DVFs. Indeed, the initial bladder of the patient may be larger or smaller than the population mean bladder. Thus, the bladder DVF from the model can be improper in term of amplitude (*i.e.* resulting in uterus-bladder overlap for large initial bladder or unrealistic deformations for small initial bladder). To correct this, a ratio was applied on the DVF amplitude corresponding to the difference between the position of the top of the bladder of each shape (patient and sPCA bladder shapes). Moreover, the deformed bladder was iteratively smoothed and deflated, where the local uterus-bladder overlap occurs, following the inverse of the vertex normal.

After the denormalization of the deformed shapes, the pretreatment library, containing the two modeled CTVs and bladders shapes and the patient original planning CT anatomy, was obtained.

4.2.3 EVALUATION

4.2.3.1 Dataset

The method was evaluated on a total of 20 subjects. Each underwent three planning CTs with different bladder volumes (empty, intermediate, and full) and, at least, bi-weekly CBCTs during the 5 weeks of treatment (total 314 images). The CTV, including the cervix and uterus, and the OARs (rectum, bladder, and bowel) were delineated by the same expert on CT and CBCT images. The surfaces of the delineations were smoothed using Taubin filter [26], decimated and remeshed using the approximated centroidal Voronoi diagrams (ACVD) method [37], resulting in smooth meshes of 1500 equidistant points.

The experiments were performed following a leave-one-patient-out cross-validation. A PCA-based model was defined for each patient using the 19 other patients for the training set.

Considering the iterative DMR, the following parameters were empirically selected: 3 resolutions of smoothing (Taubin filter passband=[0.01, 0.1, 1]); cost matrix weight factor $\alpha=0.5$; Gaussian sigma $\sigma=[4,2,1]$; step update factor $\mu=0.25$; and topology constraint threshold $\tau=[0.25, 0.5, 1]$.

In order to keep the dominant information from the training set and to filter out the noisy deformations (*i.e.* resulting from DMR uncertainties or intra-observer delineation variations), a rank threshold of 10% was therefore considered for the sPCA (*cf.* section 4.2.3.5). Thus, the pPCA models were defined on 10% of the sPCA first modes.

The proposed DMR method was developed using the VTK library. Statistical shape analysis was performed using the Scalismo library. A non-parametric test (paired Wilcoxon test) was used to compare the performance of the strategies and to assess if a strategy was statistically different from another. The R software was used for this purpose.

4.2.3.2 Simulation of Treatment Delivery

As considered in clinical routine, for each CTV (either resulting from the CTs segmentation or from the model), a PTV was generated by adding an isotropic margin. To simulate patient positioning during treatment delivery, all the CBCTs were bone-registered with the planning CT (intermediate bladder). For the standard RT, only the PTV with intermediate bladder volume was used to simulate the treatment. For the library-based strategies, multiple PTV (3 or 5, *cf*. Figure 4-1) were available for each treatment fraction. The PTV selected for each CBCT was the one providing the maximum coverage with the CTV delineated on the CBCT. In the event of equal overlap by multiple PTVs, the PTV with the lowest volume was selected.

The modeled planning library was evaluated and compared against the standard RT (based on the intermediate bladder volume CT) and the three-CT-based planning library, including, for each patient, the shapes of the three planning CTs (empty, intermediate and full bladder volumes). A combined library, including the three-CT-based and modeled library shapes, totaling 5 shapes, was also evaluated (*cf.* Figure 4-1d).

4.2.3.3 Evaluation of the Treatment Strategies

The criterion used to assess the best strategy was the coverage of the volumes of interest (CTV and OAR) by the PTV. The “coverage of the organ by the PTV” was computed as the intersection between the selected PTV and the structure delineation, normalized according to the structure volume. This coverage criterion represented the ability of the considered strategy to cover the target or to spare the organs at risk for each treatment fraction and, thus, of its ability to anticipate the deformations. For each patient, the coverages of the volumes of interest were averaged by the number of fractions (*i.e.* CBCTs) to represent the whole treatment.

All the strategies were tested with 0 mm, 7 mm and 10 mm PTV margins (*i.e.* isotropic dilatation of the CTV to generate the PTV). The 0 mm PTV margin, if clinically unrealistic, was considered to assess the coverage of the organs provided by the geometrical model only.

4.2.3.4 Deformable mesh registration performance

Figure 4-5 illustrates two cases of estimated deformation, namely simple and difficult, based on the similarity between the template and a patient. Figure 4-6 represents the mean nearest neighbor distance (MNND) on the template shapes after DMR. The largest errors were located on the salient local regions of the CTV and on the top part of the bladder.

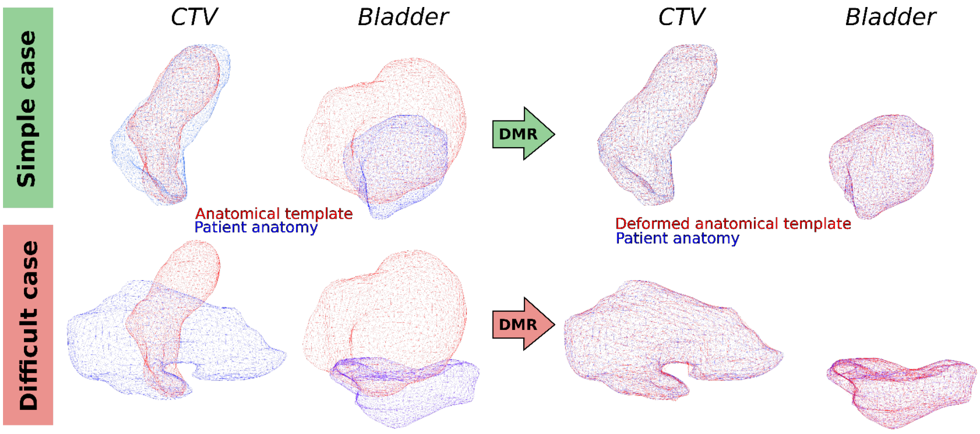

Figure 4-5: DMR examples

Two different cases are illustrated. One simple case with similar CTV shapes and small deformations (except for the volume of the bladder) and one difficult case with different CTV shapes and large deformations. In both cases, the proposed DMR method generates a deformation vector field that warps the template shapes to the target patient shapes. CTV: Clinical target volume; DMR: deformable mesh registration

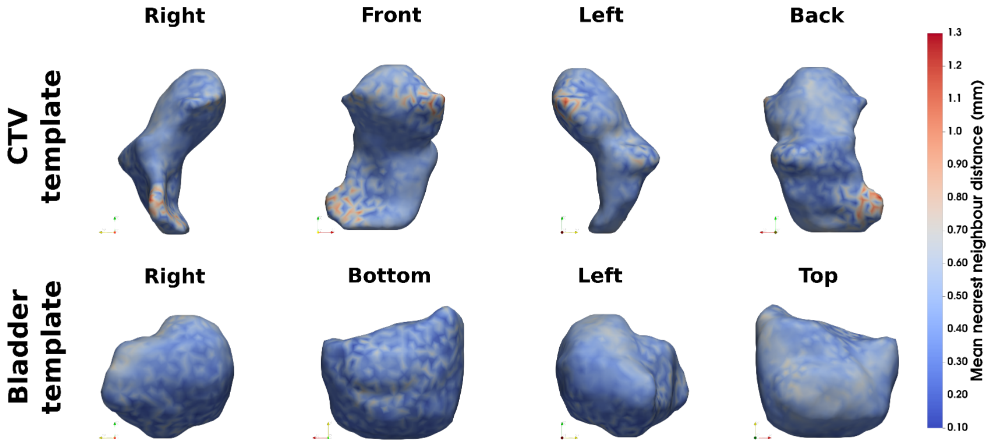

Figure 4-6: Illustration of DMR MNND on the template shapes

The MNND is illustrated on the anatomical template showing larger error on the salient local regions of the CTV and larger error on the top part of the bladder. CTV: Clinical target volume, MNND: mean nearest neighbor distance, DMR: deformable mesh registration

Table 4-1 represents the rigid registration (RR, *cf.* section 4.2.2.2), and DMR performances using the following metrics: MNND, Hausdorff distance (HD), Dice similarity coefficient (DSC) and inverse consistency error (ICE). Compared to the RR, the DMR performances were significantly better.

Table 4-1: Rigid registration and DMR performances for the CTV and bladder.

The table represents the mean (min – max) values over all patients for each method and organ. * indicates a p-value < 0.001 for the Wilcoxon test comparing DMR with RR. MNND: Mean nearest neighbor distance; HD: Hausdorff distance; DSC: Dice similarity coefficient; ICE: inverse consistency error; CTV: Clinical target volume

Metric	**Methods**			
	RR		DMR	
	CTV	Bladder	CTV	Bladder
MNND (mm)	12.1 (5.5 – 22.3)	9.5 (6.6 – 13.4)	0.5 * (0.3 – 0.7)	0.5 * (0.3 – 0.8)
HD (mm)	41.1 (19 – 64.6)	51.6 (31.2 – 70.6)	3.2 * (2.5 – 4.2)	3.1 * (2.1 – 4.4)
DSC	0.39 (0.22 – 0.67)	0.39 (0.16 – 0.67)	0.98 * (0.94 – 0.99)	0.99 * (0.97 – 1.0)
ICE (mm)	/	/	5.7 (3.2 – 7.7)	3.8 (1.9 – 6.3)

4.2.3.5 Principal component analysis

The sPCA-based model was cross-validated using a leave-one-patient-out procedure across the 20 subjects. Figure 4-7 represents the three main modes of deformation of the cervix-uterus/bladder sPCA. The first mode can be interpreted as the tipping of the uterus according to the bladder filling. The second and third modes correspond to an ante-posterior shrinking and a left-right rotation on the Y-axis of the shapes, respectively.

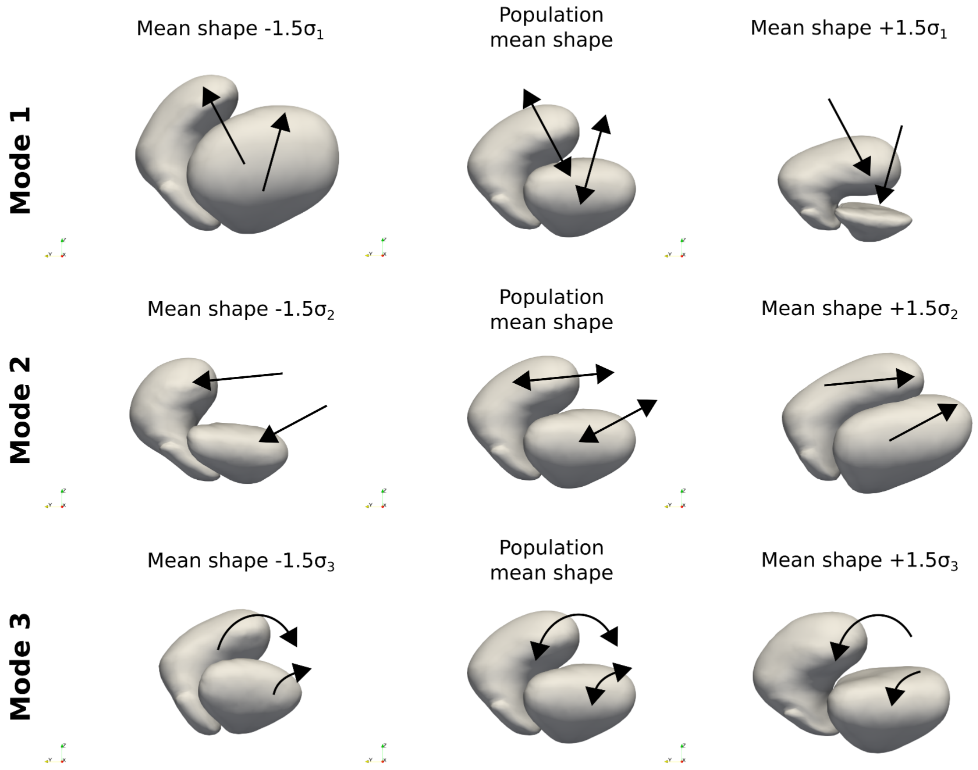

Figure 4-7: Three main modes of deformation of the standard principal components analysis

The three main modes of deformation of the cervix-uterus/bladder population sPCA are represented. Mode 1 can be interpreted as a superior/inferior deformation of the uterus with a large variation in the bladder volume. Modes 2 and 3 correspond to an ante-posterior shrinking and a left-right rotation on the Y-axis of the anatomical structures, respectively. PCA: principal component analysis; σ2x: variance of the xth mode (eigenvalue)

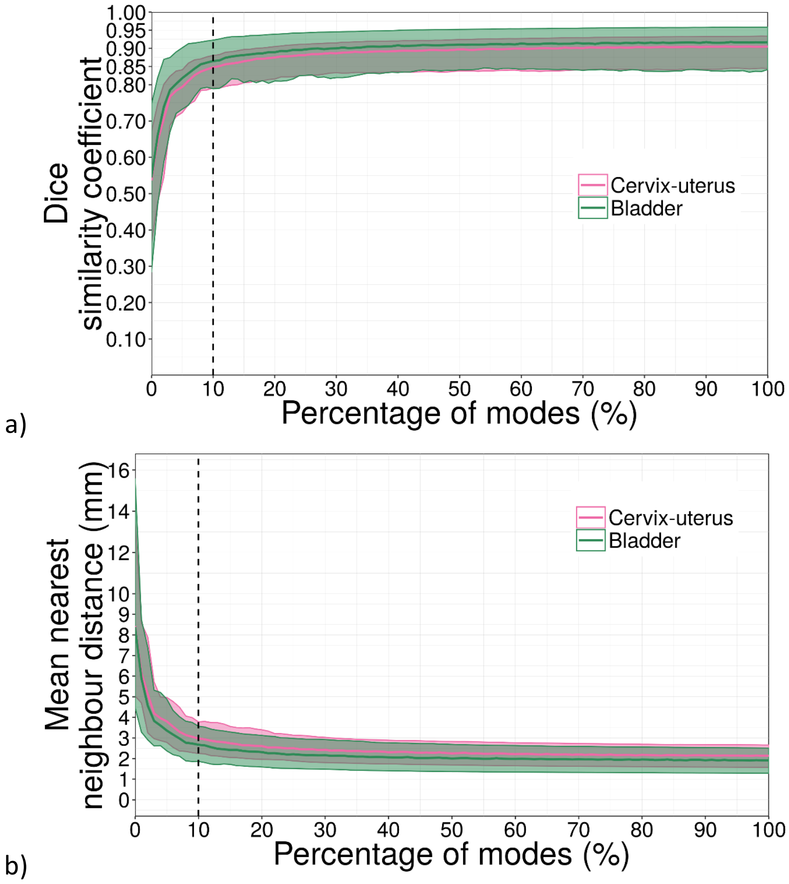

Figure 4-8: Standard PCA performance of the two shapes in all ranks by considering: (a) the DSC and (b) the MNND

The multi-organ PCA performances are illustrated for all tested modes using leave-one-patient-out cross-validation. PCA: Principal component analysis; DSC: Dice similarity coefficient; MNND: Mean nearest neighbor distance

Figure 4-8ab represents the DSC and MNND for each organ as a function of the sPCA modes, and thus, the ability of the sPCA to explain the inter- and intra-patient variation with a given number of modes. The Figure 4-8ab illustrates, thus, the generalization ability of the models to represent unseen shapes in the training set (*i.e.* following leave-one-patient-out cross validation) [38]. At a 10% rank, the DSC and MNND were 0.85 (0.79 - 0.88) and 3.0 mm (2.2 – 3.8) for the cervix-uterus and 0.86 (0.79 - 0.92) and 2.7 mm (1.9 – 3.6) for the bladder, respectively. At this rank, 90% of the maximum DSC was reached for each organ.

4.2.3.6 Modeled library

Figure 4-9 represents the strategy performances in terms of the CTV and OAR coverage by the PTV, for each margin value.

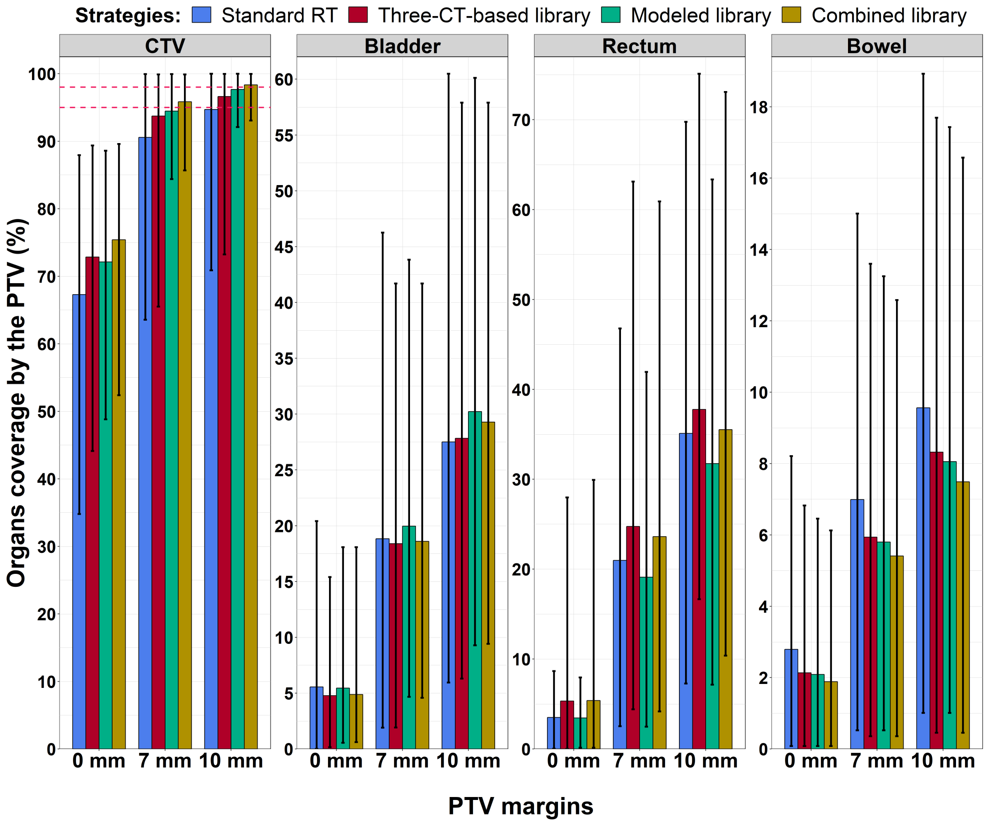

Figure 4-9: CTV and OAR coverage by the PTV across various margins and all strategies

The colours represent the RT strategies, and the x-axis represents the PTV margins (0, 7, and 10 mm). The filled bars represent the mean values of the population (with one value per patient, corresponding to the mean coverage over the treatment), and the black lines represent the min and max values. The optimal treatment corresponds to a high CTV coverage and a low OAR coverage. The red dashed lines represent 95% and 98% CTV coverage by the PTV, respectively. CTV: Clinical target volume; OAR: Organs at risk (bladder, rectum and bowel); PTV: Planning target volume; RT: Radiation therapy

Considering the CTV coverage by the PTV, compared to the standard RT, all strategies significantly increased the coverage (p<0.001). Compared the standard RT, the modeled library was beneficial for 75% of the patients (with no impact for the other). The modeled library had similar performances compared to the three-CT-based library (p=0.95).

Importantly, considering a 10 mm PTV margin, the minimal value of the CTV coverage increased from 73.2% with the three-CT-based library to 92.1% with the modeled libraries. Also, the combined library significantly increased the CTV coverage, compared to all strategies: +3.6% compared to the standard RT (p<0.001); +1.7% compared to the three-CT-based library (p<0.001) and +0.7% compared to the modeled library (p<0.001).

Comparing the modeled library with the classic library at 10 mm PTV margin, 20% of the patients had an increase of CTV coverage superior to 1% (up to 21.3%) while 10% had a decrease superior to 1% (up to 4%). By combining the two libraries, 25% of the patients had an increase of the CTV coverage superior to 1% (up to 21.3%) and none had a decrease.

Considering the OAR coverage by the PTV, the modeled library significantly increased the sparing of the rectum (-6%, p<0.001) compared to the three-CT-based library. The modeled and combined libraries increased the sparing of the bowel (-0.3% and -0.8% [*eq.* 1.2 cc and 2.4 cc], p=0.08 and p<0.001). However, the modeled and combined library significantly over-covered the bladder (+2.4% and +1.5%; p<0.001).

Considering the impact of the PTV margins on CTV coverage, an improvement of approximately 25% was observed by increasing the margin from 0 to 7 mm and of 5% from 7 to 10 mm. Concerning the impact of the PTV margins on the OAR, an impairment of 15% was observed by increasing the margin from 0 to 7 mm and of 10% from 7 to 10 mm for the rectum and bladder. In total, if the use of adaptive strategies will enable to reduce the margins, their choice remains crucial.

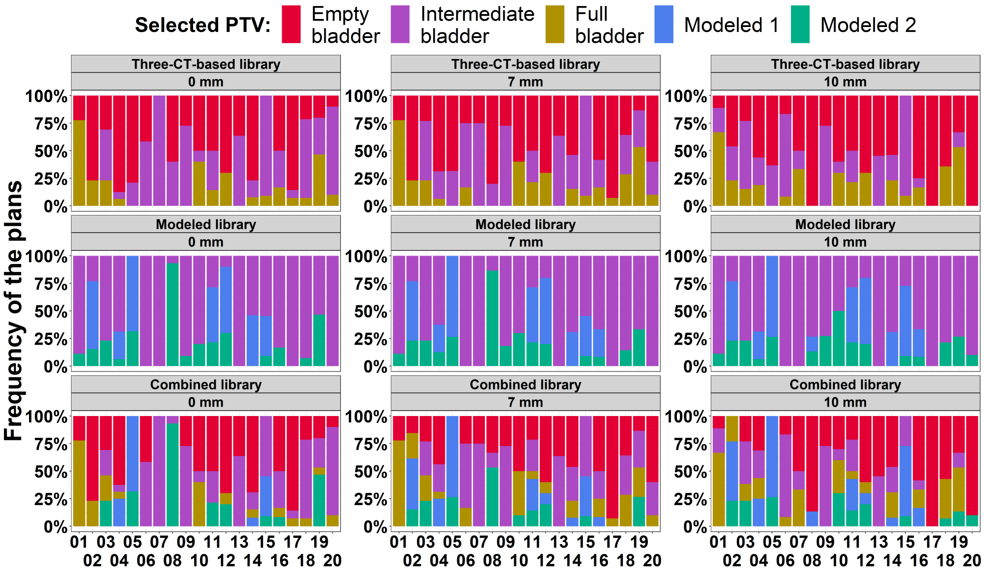

Figure 4-10: Selected PTV during the treatment of each patient.

The y-axis represents the frequency of the PTV selected during the treatment simulations. The colors represent the different PTV. The x-axis represents the patient identifiers. Each facet represents a strategy with a PTV margin (0, 7, and 10 mm). PTV: Planning target volume;

Figure 4-10 represents the frequency of fractions for which the plans were used, according to the strategy and for each individual. Considering the modeled library, the modeled plans were used at least once for 75% of the patients. Considering all the available plans using the combined library, the modeled plans were used at least once for 60% of the patients.

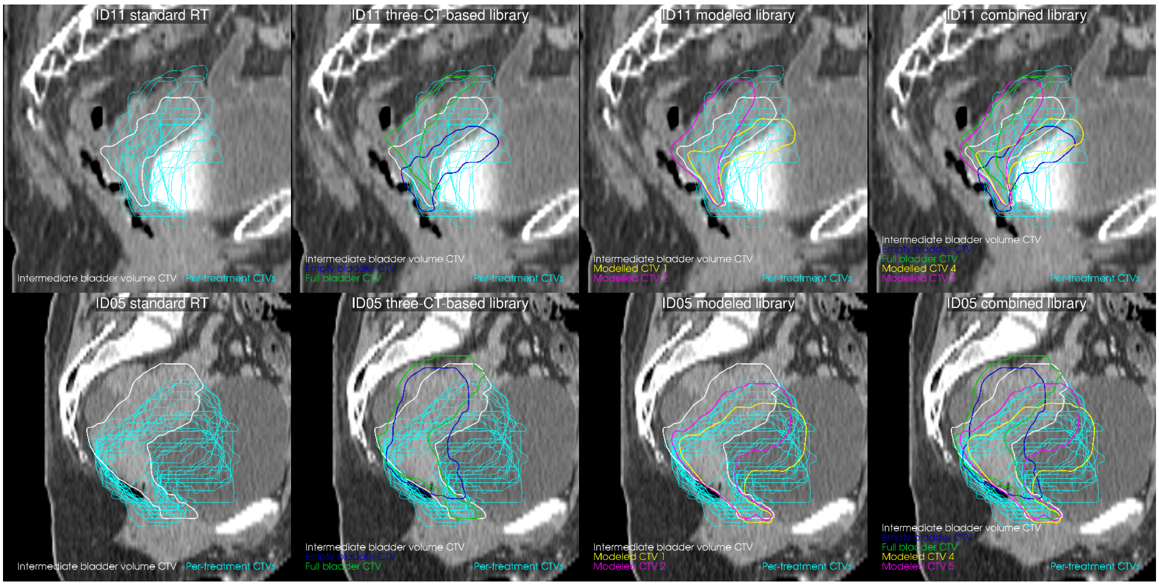

Figure 4-11: Example of the RT strategies used for two different patients

The patient on the first row has a moving uterus prior to and during the treatment. The patient on the second row has a non-moving uterus prior to the treatment and moving uterus during the treatment. For the latter, the modeled planning library has the ability to anticipate per-treatment deformations, while the three-CT-based library shows low uterus movements. The four strategies are illustrated. The standard RT CTV (first column) is in white. The CTVs of the "classic" three-CT-based library (second column) are in white, dark blue and green. The CTVs of the patient-specific modeled library (third column) are in white, pink and yellow. The CTVs of the combined library (fourth column) are in white, dark blue, green, yellow and pink. The per-treatment CTV contours are in light blue. In this particular order, the CTV coverages by the 10 mm PTV of the patient of the first row were 84.8%, 92.0%, 92.1% and 93.1%. The CTV coverages by the 10 mm PTV of the patient of the second row were 70.9%, 73.2%, 94.5% and 94.5%. CTV: Clinical target volume

Figure 4-11 illustrates each strategy for two different patients: the first one (upper row), had a moving uterus at the planning and during the treatment; the second one had a non-moving uterus at the planning, which became mover during the treatment. For the first patient, both libraries performed similarly. However, for the second patient, the modeled library better anticipated the deformations than the three-CT-based library. Indeed, before treatment, the tumor may prevent the uterus from moving, whereas during treatment, the tumor shrinks and then lets the uterus move.

In terms of computation time, the proposed approach simulates the two modeled CTs in less than 3 minutes per patient (approximately 1 minute per organ for the DMR and 1 minute for the pPCA-based models). Compared to the three-CT-based library, only the combined library would increase the workload in term of treatment plan optimization.

4.2.4 DISCUSSION AND CONCLUSION

We have proposed a workflow that models a planning library by taking into account population deformations. This workflow relies on two steps. First, a DMR method was proposed to compute the inter-patient cervix-uterus and bladder correspondences. Second, a SSM was built to deform the specific-patient anatomy to generate a modeled library.

This study has several limitations. First, the DMR performance was only evaluated considering geometric metrics and not using fiducial markers or manually placed landmarks. Landmark positioning appears, however, difficult on pelvic anatomy, and a numerical phantom could have been used as reported when considering prostate cancer [39]. The ICE were larger than the ones reported in the literature using symmetric registration methods [12,20] due to the fact that our method computes the DVF in only one direction (*i.e.* forward). Still, the proposed method provides the smallest reported ICE of the non-symmetrical registration method [20] (*cf.* Table 4-1).

Second, the statistical shape analysis was done by mixing both intra- and inter-patient deformations, without taking the patient's deformations among the population specifically into account. One proposed solution would be to consider the inter-fractions average shape per patient [40]. To overcome this shortcoming, the population was normalized according to a common space, limiting the deformation analysis on the uterus. Moreover, the model deformation vector fields were applied on the specific patient's planning anatomy.

Finally, the modeled planning library performance was assessed using only a geometric criterion, instead of dosimetric criteria that are more important in a clinical perspective. The workload implied by dose optimization and calculation prevent the exhaustive dosimetric evaluation of new strategies. Moreover, a previous study has shown a good agreement between geometric and dosimetric criteria for cervical cancer patients [8]. In the end, the clinical benefits of such complex strategies will have to be evaluated on a larger cohort.

The modeled and combined libraries performed similarly or better than a standard RT or classic CT-based library. In particular, the coverage of the target was largely improved for patients with non-moving CTV at the planning. Moreover, the proposed modeled approach reduces the need for the heavy three-CT-acquisition protocol. The use of the proposed combined library, including the modeled shapes, would increase the workload of the physicist at the planning (2h per plan optimization). However, the need for adaptive strategies, based on the generation of multiple treatment plans, is largely accepted and some clinical tools, such as automatic planning tools [41], may ease their clinical implementation. Two ongoing clinical trials based on the use of the planning library showed that 3 to 15 min is required to select the plan-of-the-day at each treatment fraction [10,42].

The perspective of this work is to compute planning doses with the modeled shapes on a water-air-bone pseudo-CT to dosimetrically confirm the results. The proposed method can be derived to evaluate similar adaptive strategies for bladder and rectal cancers.

4.2.5 REFERENCES

1. Jadon R, Pembroke C, Hanna C, Palaniappan N, Evans M, Cleves A, Staffurth J. A systematic review of organ motion and image-guided strategies in external beam radiotherapy for cervical cancer. *Clinical Oncology* 2014;26:185-196.
2. Ahmad R, Hoogeman MS, Bondar M, Dhawtal V, Quint S, De Pree I, Mens JW, Heijmen BJ. Increasing treatment accuracy for cervical cancer patients using correlations between bladder-filling change and cervix–uterus displacements: Proof of principle. *Radiotherapy and oncology* 2011;98:340-346.
3. Han Y, Shin EH, Huh SJ, Lee JE, Park W. Interfractional dose variation during intensity-modulated radiation therapy for cervical cancer assessed by weekly ct evaluation. *International Journal of Radiation Oncology* Biology* Physics* 2006;65:617-623.
4. Buchali A, Koswig S, Dinges S, Rosenthal P, Salk J, Lackner G, Böhmer D, Schlenger L, Budach V. Impact of the filling status of the bladder and rectum on their integral dose distribution and the movement of the uterus in the treatment planning of gynaecological cancer. *Radiotherapy and oncology* 1999;52:29-34.
5. van de Bunt L, Jürgenliemk-Schulz IM, de Kort GA, Roesink JM, Tersteeg RJ, van der Heide UA. Motion and deformation of the target volumes during imrt for cervical cancer: What margins do we need? *Radiotherapy and Oncology* 2008;88:233-240.
6. Seppenwoolde Y, Stock M, Buschmann M, Georg D, Bauer-Novotny K-Y, Pötter R, Georg P. Impact of organ shape variations on margin concepts for cervix cancer art. *Radiotherapy and Oncology* 2016.
7. Bondar M, Hoogeman M, Mens J, Quint S, Ahmad R, Dhawtal G, Heijmen B. Individualized nonadaptive and online-adaptive intensity-modulated radiotherapy treatment strategies for cervical cancer patients based on pretreatment acquired variable bladder filling computed tomography scans. *International Journal of Radiation Oncology* Biology* Physics* 2012;83:1617-1623.
8. Rigaud B, Simon A, Gobeli M, Lafond C, Leseur J, Barateau A, Jaksic N, Castelli J, Williaume D, Haigron P, De Crevoisier R. Cbct-guided evolutive library for cervical adaptive imrt. *Medical Physics* 2018.
9. Gobeli M, Simon A, Getain M, Leseur J, Lahlou E, Lafond C, Dardelet E, Williaume D, Rigaud B, de Crevoisier R. Benefit of a pretreatment planning library-based adaptive radiotherapy for cervix carcinoma? *Cancer radiotherapie* 2015;19:471-478.
10. Heijkoop ST, Langerak TR, Quint S, Bondar L, Mens JWM, Heijmen BJ, Hoogeman MS. Clinical implementation of an online adaptive plan-of-the-day protocol for nonrigid motion management in locally advanced cervical cancer imrt. *Int J Radiat Oncol Biol Phys* 2014;90:673-679.
11. van de Schoot AJ, de Boer P, Visser J, Stalpers LJ, Rasch CR, Bel A. Dosimetric advantages of a clinical daily adaptive plan selection strategy compared with a non-adaptive strategy in cervical cancer radiation therapy. *Acta Oncologica* 2017;56:667-674.
12. Tilly D, van de Schoot AJ, Grusell E, Bel A, Ahnesjö A. Dose coverage calculation using a statistical shape model—applied to cervical cancer radiotherapy. *Physics in Medicine and Biology* 2017;62:4140.
13. Tu L, Styner M, Vicory J, Elhabian S, Wang R, Hong J, Paniagua B, Prieto JC, Yang D, Whitaker R, Pizer SM. Skeletal shape correspondence through entropy. *IEEE Transactions on Medical Imaging* 2018;37:1-11.
14. Rios R, De Crevoisier R, Ospina JD, Commandeur F, Lafond C, Simon A, Haigron P, Espinosa J, Acosta O. Population model of bladder motion and deformation based on dominant eigenmodes and mixed-effects models in prostate cancer radiotherapy. *Medical image analysis* 2017;38:133-149.
15. Kelemen A, Székely G, Gerig G. Elastic model-based segmentation of 3-d neuroradiological data sets. *IEEE Transactions on medical imaging* 1999;18:828-839.

16. Belongie S, Malik J, Puzicha J. Shape matching and object recognition using shape contexts. *IEEE transactions on pattern analysis and machine intelligence* 2002;24:509-522.
17. Acosta O, Fripp J, Doré V, Bourgeat P, Favreau J-M, Chételat G, Rueda A, Villemagne VL, Szoeke C, Ames D. Cortical surface mapping using topology correction, partial flattening and 3d shape context-based non-rigid registration for use in quantifying atrophy in alzheimer's disease. *Journal of Neuroscience Methods* 2012;205:96-109.
18. Xiao D, Zahra D, Bourgeat P, Berghofer P, Tamayo OA, Wimberley C, Gregoire MC, Salvado O. An improved 3d shape context based non-rigid registration method and its application to small animal skeletons registration. *Computerized Medical Imaging and Graphics* 2010;34:321-332.
19. Ruhaak J, Polzin T, Heldmann S, Simpson I, Handels H, Modersitzki J, Heinrich MP. Estimation of large motion in lung ct by integrating regularized keypoint correspondences into dense deformable registration. *IEEE Transactions on Medical Imaging* 2017.
20. Bondar L, Hoogeman MS, Osorio EMV, Heijmen BJ. A symmetric nonrigid registration method to handle large organ deformations in cervical cancer patients. *Medical physics* 2010;37:3760-3772.
21. Yang J. The thin plate spline robust point matching (tps-rpm) algorithm: A revisit. *Pattern Recognition Letters* 2011;32:910-918.
22. Chui H, Rangarajan A. A new point matching algorithm for non-rigid registration. *Computer Vision and Image Understanding* 2003;89:114-141.
23. Vásquez Osorio EM, Kolkman-Deurloo IKK, Schuring-Pereira M, Zolnay A, Heijmen BJ, Hoogeman MS. Improving anatomical mapping of complexly deformed anatomy for external beam radiotherapy and brachytherapy dose accumulation in cervical cancer. *Medical physics* 2015;42:206-220.
24. Myronenko A, Song X. Point set registration: Coherent point drift. *IEEE transactions on pattern analysis and machine intelligence* 2010;32:2262-2275.
25. Jonker R, Volgenant A. A shortest augmenting path algorithm for dense and sparse linear assignment problems. *Computing* 1987;38:325-340.
26. Taubin G, Zhang T, Golub G. Optimal surface smoothing as filter design. *Computer Vision—ECCV'96* 1996:283-292.
27. Jackson JE. A user's guide to principal components: John Wiley & Sons; 2005.
28. Cerrolaza JJ, Summers RM, Linguraru MG. Soft multi-organ shape models via generalized pca: A general framework. International Conference on Medical Image Computing and Computer-Assisted Intervention. Springer. 2016. pp. 219-228.
29. Söhn M, Birkner M, Yan D, Alber M. Modelling individual geometric variation based on dominant eigenmodes of organ deformation: Implementation and evaluation. *Physics in Medicine and Biology* 2005;50:5893.
30. Brion E, Richterb C, Macqa B, Stützerb K, Exnerb F, Troostb E, Hölscherb T, Bondara L. Modeling patterns of anatomical deformations in prostate patients undergoing radiation therapy with an endorectal balloon. SPIE Medical Imaging. International Society for Optics and Photonics. 2017. pp. 1013506-1013506-1013509.
31. Thörnqvist S, Hysing LB, Zolnay AG, Söhn M, Hoogeman MS, Muren LP, Heijmen BJ. Adaptive radiotherapy in locally advanced prostate cancer using a statistical deformable motion model. *Acta Oncologica* 2013;52:1423-1429.
32. Bondar L, Intven M, Burbach JM, Budiarto E, Kleijnen J-P, Philippens M, van Asselen B, Seravalli E, Reerink O, Raaymakers B. Statistical modeling of ctv motion and deformation for imrt of early-stage rectal cancer. *International Journal of Radiation Oncology* Biology* Physics* 2014;90:664-672.
33. Chetvertkov MA, Siddiqui F, Kim J, Chetty I, Kumarasiri A, Liu C, Gordon JJ. Use of regularized principal component analysis to model anatomical changes during head and neck radiation therapy for treatment adaptation and response assessment. *Medical physics* 2016;43:5307-5319.

34. Buchaillard SI, Ong SH, Payan Y, Foong K. 3d statistical models for tooth surface reconstruction. *Computers in Biology and Medicine* 2007;37:1461-1471.
35. Poltaretskyi S, Chaoui J, Mayya M, Hamitouche C, Bercik M, Boileau P, Walch G. Prediction of the pre-morbid 3d anatomy of the proximal humerus based on statistical shape modelling. *Bone Joint J* 2017;99:927-933.
36. Albrecht T, Lüthi M, Gerig T, Vetter T. Posterior shape models. *Medical image analysis* 2013;17:959-973.
37. Valette S, Chassery JM, Prost R. Generic remeshing of 3d triangular meshes with metric-dependent discrete voronoi diagrams. *IEEE Transactions on Visualization and Computer Graphics* 2008;14:369-381.
38. Styner MA, Rajamani KT, Nolte L-P, Zsemlye G, Székely G, Taylor CJ, Davies RH. Evaluation of 3d correspondence methods for model building. Biennial International Conference on Information Processing in Medical Imaging. Springer. 2003. pp. 63-75.
39. Cazoulat G, Simon A, Dumenil A, Gnep K, De Crevoisier R, Acosta O, Haigron P. Surface-constrained nonrigid registration for dose monitoring in prostate cancer radiotherapy. *IEEE Transactions on Medical Imaging* 2014;33:1464-1474.
40. Budiarto E, Keijzer M, Storchi P, Hoogeman M, Bondar L, Mutanga T, de Boer H, Heemink A. A population-based model to describe geometrical uncertainties in radiotherapy: Applied to prostate cases. *Physics in medicine and biology* 2011;56:1045.
41. Sharfo AWM, Breedveld S, Voet PW, Heijkoop ST, Mens J-WM, Hoogeman MS, Heijmen BJ. Validation of fully automated vmat plan generation for library-based plan-of-the-day cervical cancer radiotherapy. *PloS one* 2016;11:e0169202.
42. Buschmann M, Majercakova K, Sturdza A, Smet S, Najjari D, Daniel M, Pötter R, Georg D, Seppenwoolde Y. Image guided adaptive external beam radiation therapy for cervix cancer: Evaluation of a clinically implemented plan-of-the-day technique. *Zeitschrift für Medizinische Physik* 2017.

4.3 DISCUSSION

4.3.1 LIMITES ET PERSPECTIVES

4.3.1.1 Recalage déformable de maillage

Si l'approche DMR est plus appropriée que la méthode des Démons pour la mise en correspondance de surfaces, elle reste sujette à des limites.

La limite principale est la sensibilité des résultats aux métriques utilisées pour guider les correspondances. De manière générale, la méthode *Shape Context (SC)* [2] peut être sensible pour certaines applications et typiquement les études proposent de filtrer 20% des correspondances avec le coût le plus élevé [3]. Pour répondre à cette problématique, la méthode a été enrichie de plusieurs aspects. Dans un premier temps, la distance géodésique a été utilisée comme deuxième métrique [4]. Ensuite, une résolution itérative par pondération du DVF a été considérée afin de pouvoir mettre à jour les métriques au cours du processus. Cette résolution itérative permet d'appliquer des étapes de régularisation afin de guider les régions sans correspondance par les correspondances de leurs voisins. De plus, à chaque itération, un filtre topologique a été implémenté pour supprimer les correspondances qui ne respectaient pas une contrainte locale. Enfin, une régularisation par TPS permet d'interpoler les points d'ancrage restant, pour définir une transformation globale. Finalement, afin d'améliorer la régularisation du DVF, un filtrage gaussien à chaque itération et une approche multi-résolutions (lissage de forme) sont intégrés à la méthode. La combinaison et le paramétrage de ces différentes étapes a permis la mise en correspondance de formes complexes.

Néanmoins, malgré ces contraintes et étapes de régularisation, des incertitudes peuvent persister. Si la méthode proposée permet de mettre en correspondance deux maillages sans initialisation rigide, puisqu'elle n'est pas dépendante de la distance euclidienne, elle peut montrer des mises en correspondance « glissées » en cas de rotation globale d'une surface. De plus, certaines irrégularités peuvent être présentes dans les zones homogène (surface plane) puisque plusieurs points peuvent avoir les mêmes métriques. Ce comportement non souhaité de l'algorithme se traduit par une augmentation de l'*Inverse Consistency Error* (ICE, *cf.* section 4.2.3.4), représentant la variabilité des correspondances en fonction du choix des surfaces fixe et mobile. Ces incertitudes peuvent être réduites en modifiant les paramètres de convergence (distance point à point souhaitée), de la régularisation et des facteurs de préservation de topologie.

Afin de comparer la méthode DMR aux méthodes de la littérature, la méthode *Coherent Point Drift* (*CPD*) [5] a été utilisée pour mettre en correspondance la cohorte vers le patient modèle. Cette approche repose sur une transformation non-rigide régularisée par une gaussienne et représentant les nuages de points à mettre en correspondance comme des modèles de mélange gaussien. Les paramètres de régularisation, λ et β, de la méthode CPD ont été définis empiriquement pour obtenir des déformations réalistes (λ=1 et β=2 pour le CTV et λ=3 et β=3 pour la vessie). Le Tableau 4-2 résume les performances géométriques des deux méthodes. La méthode CPD offre de bonnes correspondances globales mais reste limitée pour quantifier des déformations complexes sans engendrer une instabilité (par ex. un retournement de la paroi vésicale).

Tableau 4-2 : Comparaison des performance des méthodes CPD et DMR

Le tableau représente les performances en terme de valeurs moyennes (min – max) pour les méthodes CPD et DMR pour la cohorte de patientes. * indique une p-value < 0.001 pour le test de Wilcoxon permettant de montrer une différence entre la méthode CPD et DMR. ***MNND: Mean nearest neighbor distance; HD: Hausdorff Distance; DSC: Dice Similarity Coefficient;***

Métrique	**Méthode**			
	CPD		DMR	
	CTV	Vessie	CTV	Vessie
MNND (mm)	2 (1.4 – 2.7)	1.8 (1.1 – 2.4)	0.3 * (0.18 – 0.50)	0.22 * (0.15 – 0.37)
HD (mm)	7.7 (5.6 – 10.4)	6.3 (3.5 - 10)	1.87 * (1.4 – 2.9)	2.4 * (1.8 – 3.9)
DSC	0.91 (0.85 – 0.95)	0.93 (0.85 – 0.96)	0.99 * (0.97 – 1)	0.99 * (0.99 – 1)

Les perspectives de la méthode DMR sont l'évaluation des correspondances par rapport à une vérité terrain par l'usage d'un fantôme numérique anatomique complexe [6-9] ou la définition de marqueurs anatomiques (*landmark*) [10,11], notamment grâce à des images IRM.

4.3.1.2 Modèle statistique de forme

Dans cette étude, un modèle statistique de forme (*Statistical Shape Model*, SSM) a été défini à partir des anatomies intra- et inter-patientes de la cohorte mises en correspondance vers une patiente modèle. A partir de ce SSM standard, des modèles a posteriori peuvent être générés en fonction de contraintes définies [12]. Chaque contrainte, représentant une déformation existante dans le modèle, permet la définition d'un autre sous-modèle par régression gaussienne. Cette approche a permis de définir une librairie de prétraitement spécifique à chaque patiente en fonction des déformations d'une population. La définition de la librairie repose sur une contrainte sur la position du fond utérin.

Cette méthode a plusieurs limites. Premièrement, le SSM a été généré sans distinction des données intra- et inter-patientes. Ceci ne prend donc pas en compte plusieurs aspects comme la variabilité anatomique intra-patiente, un nombre plus important d'instances pour certaines patientes et la réponse au traitement. Cependant, l'objectif de cette étude était d'extraire la tendance d'une population pour l'appliquer à une nouvelle patiente. Pour ce faire, la cohorte a été standardisée pour supprimer les variations volumiques et concentrer l'observation du modèle sur le mouvement de l'utérus. Le modèle a ensuite été limité par un seuil pour garder les déformations dominantes et filtrer les déformations à faibles variances. La généralisation du modèle, par validation croisée *leave-one-patient-out* (*cf*. section 4.2.3.5), n'a pas montré l'existence de patientes non représentées (*outliers).* Une approche reposant sur un modèle à effets mixtes pourrait être une perspective intéressante pour séparer les informations intra- et inter-patientes [13]. Une telle méthode, appliquée sur une cohorte plus importante, pourrait permettre l'identification de sous-groupes de patientes suivant des critères de forme.

Deuxièmement, les contraintes appliquées pour la définition des différents modèles ACP à posteriori peuvent être considérées comme arbitraires. Dans le cas de cette étude, une première étape d'observation et d'analyse a été menée afin de déterminer une amplitude réaliste des déformations de l'utérus. Cette analyse a permis de définir des contraintes avec une amplitude maximale du déplacement du fond utérin de 15 mm dans la direction supéro-inférieure et antéro-postérieure. Une déformation moyenne du fond utérin supérieure à 14 mm a aussi été rapportée dans d'autres études [14]. Afin de personnaliser la contrainte, elle a été définie en prenant en compte la différence entre la position du fond utérin de l'anatomie au scanner de planification et celle de la structure du CTV représentant la forme moyenne du SSM (*cf.* section 4.2.2.5.2). Une perspective intéressante pourrait être de définir des conditions limites sur la position de l'utérus à partir de la position de la colonne vertébrale et de l'os pubien de chaque patiente.

Par rapport aux performances de la librairie évolutive, l'approche par librairie modélisée obtient une couverture moyenne du CTV légèrement inférieure (moyenne (min – max) : 97.7% (92.1 – 100.0) contre 98.5% (96.4 – 100.0)) avec une marge de PTV de 10 mm. Si l'on compare la librairie évolutive et la librairie modélisée combinée, qui sont toutes deux une extension de la librairie classique (à trois plans), la différence résulte de l'utilisation des replanifications per-thérapeutiques contre celle des instances modélisées. Sur l'ensemble de la population, cette différence est relativement faible, avec +0.2% en moyenne en faveur des replanifications. Cette différence peut cependant atteindre 5% pour le traitement de la patiente là moins bien prise en compte par le modèle. Pour les OAR, la librairie modélisée permet une réduction de la couverture du rectum de 9% (31.7% contre 40.6%) en moyenne par rapport à la librairie évolutive, sans changement pour la vessie et la cavité péritonéale.

De plus, par rapport à la stratégie standard (c'est-à-dire un unique CTV à la planification) ou à la librairie de plans de traitement classique (c'est-à-dire 3 CTV à la planification), les deux stratégies adaptatives proposées dans ces travaux de thèse permettent d'augmenter la couverture du CTV pour une patiente avec un utérus très mobile pendant le traitement de 71% – 72% à 92% – 96%. Une confirmation avec des résultats dosimétriques est indispensable afin de quantifier la différence concrète entre la librairie modélisée et la librairie évolutive (4% d'écart pour une patiente). Une perspective intéressante serait de combiner les principes de ces deux approches.

4.4 EXTENSION AU CANCER DE LA VESSIE

L'approche présentée pour les patientes atteintes d'un cancer du col de l'utérus peut être appliquée à d'autres localisations anatomiques. La littérature offre déjà de nombreuses études proposant des librairies de plans de traitement pour l'anatomie pelvienne [15], notamment pour la vessie [16]. Parmi les approches considérées, la plus simple est la généreration d'une librairie par la dilatation du volume de la vessie de planification, suivant une marge de PTV isotropique (5 – 30 mm) [17] ou anisotropique [18]. Une autre approche, similaire à la librairie de plans de traitement cervico-utérine, consiste à générer une librairie à partir de plusieurs scanners de planification (jusqu'à 4) avec un remplissage de vessie variable [19]. En suivant la méthode proposée par [20], une interpolation entre les volumes de vessie de deux scanners de planification (vessie vide et pleine) permet de générer une librairie jusqu'à 6 formes [21,22]. Certaines études ont proposé d'exploiter aussi les CBCT de la première semaine de traitement [23,24].

La majorité de ces études montrent une amélioration de la couverture du CTV par rapport à une approche standard. Il paraît alors intéressant de dériver la méthode proposée dans ce chapitre de thèse pour cette localisation. Dans cet objectif et en collaboration avec Loïg Duvergé, radiothérapeute au Centre Eugene Marquis, un projet de librairie modélisée pour la vessie a été initié dans le cadre de ses travaux de Master 2 Signaux Images en Biologie et Médecine (SIBM). Le principe de ces travaux repose sur la création de deux modèles statistiques de forme, un modèle pour les femmes (vessie/utérus) et un modèle pour les hommes (vessie/prostate). Pour le modèle féminin, les données de l'étude de ce chapitre seront réutilisées. Pour le modèle masculin, les simulations ont été réalisées sur une cohorte de 48 patients traités pour un cancer de la prostate au centre Eugène Marquis. Tous les patients ont eu un scanner de planification et une imagerie perthérapeutique pendant les 8 semaines du traitement. Parmi ces patients, 25 patients ont eu des CBCT hebdomadaires, 20 patients ont eu des CT hebdomadaires et 3 patients ont eu des CBCT quotidiens, représentant en tout 540 images.

Dans les deux cas, l'approche repose sur les étapes qui sont présentées dans ce chapitre (*cf*. sections 4.2.2.3 et 4.2.2.4) afin de générer un modèle dans un espace commun qui est une anatomie avec l'organe reproducteur médian. Puisque quelques différences existent entre les deux sexes en termes de déformations de la vessie et de relations entre les organes, les repères géométriques considérés diffèrent par rapport à l'approche initiale. Pour le sexe masculin, la vessie étant directement reliée et placée sur la prostate, cette dernière sert de repère anatomique pour aligner rigidement, par translation des centroïdes, l'ensemble de la cohorte sur le patient modèle. De plus, la contrainte permettant de modéliser les déformations est placée sur le point de la vessie le plus éloigné de la prostate. Cette contrainte représente un vecteur qui pointe dans la direction supéro-antérieure. Pour le modèle féminin, la contrainte est un vecteur placé sur le dôme de la vessie évoluant dans la direction supérieure-inférieure. Afin de définir les instances de la librairie des deux sexes, une approche itérative a été utilisée. Cette approche repose sur la variation du vecteur de contrainte, pas à pas, pour générer un ensemble de vessies. Le modèle permet de générer un total de 30 instances de vessie d'un volume de 75 cc jusqu'à 800 cc par pas de 25 cc. Des résultats préliminaires sont illustrés ci-dessous.

La Figure 4-12 montre la mise en correspondance du patient modèle vers plusieurs anatomies complexes. Le Tableau 4-3 montre les performances de la méthode RR et DMR en terme de distance moyenne entre les points (*Mean Nearest Neighbor Distance, MNND*), distance de Hausdorff (*Hausdorff Distance, HD*) et coefficient de similarité Dice (*Dice Similarity Coefficient, DSC*).

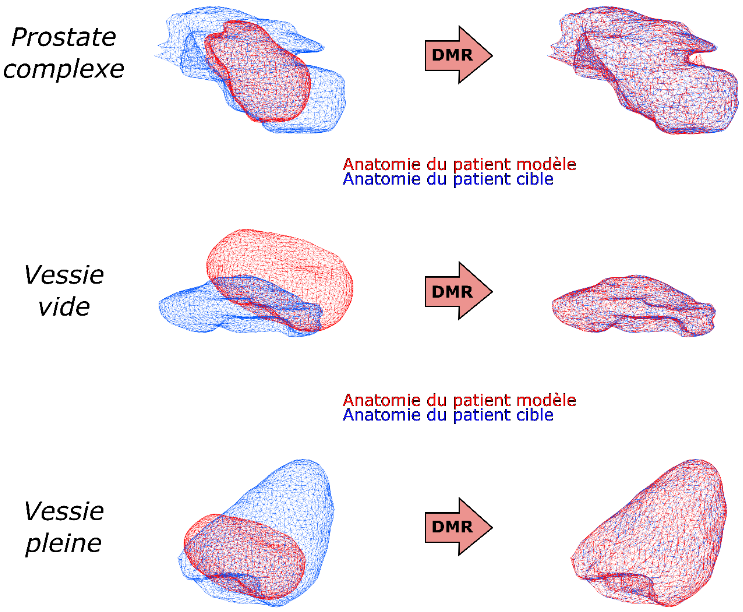

Figure 4-12 : Exemples du DMR pour l'anatomie masculine

Trois cas sont illustrés. La première ligne représente la mise en correspondance de la prostate du patient modèle (rouge) vers une prostate à la forme plus irrégulière (bleu). Les deux dernières lignes représentent la mise en correspondance de la vessie du patient modèle (rouge) vers une vessie vide plate et une vessie remplie pointue (bleu). ***DMR : Deformable Mesh Registration***

Tableau 4-3 : Performance des méthodes RR et DMR pour la mise en correspondance de la cohorte de sexe masculin

Le tableau représente les performances en terme de valeurs moyennes (min – max) pour les méthodes rigide et déformable pour la population de patients masculins. * indique une p-value < 0.001 pour le test de Wilcoxon permettant de montrer une différence entre la méthode RR et DMR. ***MNND: Mean Nearest Neighbor Distance; HD: Hausdorff Distance; DSC: Dice Similarity Coefficient;***

Métrique	**Méthode**			
	RR		DMR	
	Prostate	Vessie	Prostate	Vessie
MNND (mm)	4.1 (1.5 – 8.1)	9.35 (4.9 – 17.5)	0.3 * (0.18 – 0.50)	0.22 * (0.15 – 0.37)
HD (mm)	12.3 (3.7 – 6.3)	33.7 (16.3 – 54.8)	1.87 * (1.4 – 2.9)	2.4 * (1.8 – 3.9)
DSC	0.72 (0.51 – 0.92)	0.52 (0.25 – 0.80)	0.99 * (0.97 – 1)	0.99 * (0.99 – 1)

L'approche ACP a été validée en utilisant la méthode *leave-one-patient-out* respectivement sur les 20 patientes de sexe féminin et sur les 48 patients de sexe masculin. Similairement au résultat de l'approche initiale, un seuil de 10% permettait de représenter plus de 90% de la variabilité en termes de DSC. Les trois modes principaux du modèle ACP pour les patients de sexe masculin sont illustrés Figure 4-13. La Figure 4-14 représente la variation anatomie de la vessie pendant le traitement et les instances modélisées pour un patient de sexe masculin et une patiente de sexe féminin. Pour ces deux exemples on peut observer que les instances modélisées par contraintes conservent la topologie de la vessie du scanner de planification.

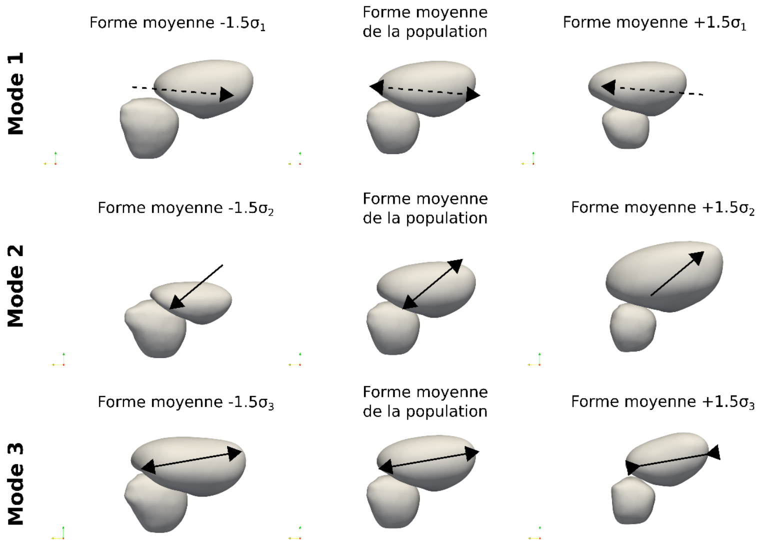

Figure 4-13 : Trois modes principaux de déformation de l'ACP standard masculin

Les trois principaux modes de déformations du modèle vessie/prostate montrent un déplacement de la vessie autour de la coiffe de la prostate (mode 1), un remplissage de la vessie dans la direction antéro-supérieure (mode 2) et un remplissage de la vessie dans la direction antéro-postérieure (mode 3). Le mode 1 peut être expliqué par la forte variation inter-patient présente au sein du modèle puisque la position de la vessie par rapport à la prostate dépend de chaque patient. Les modes 2 et 3 représentent le remplissage de la vessie dans des directions orthogonales. Les 3 modes montrent une forte variation de la prostate en terme de forme et de volume, illustrant la variabilité inter-patient.

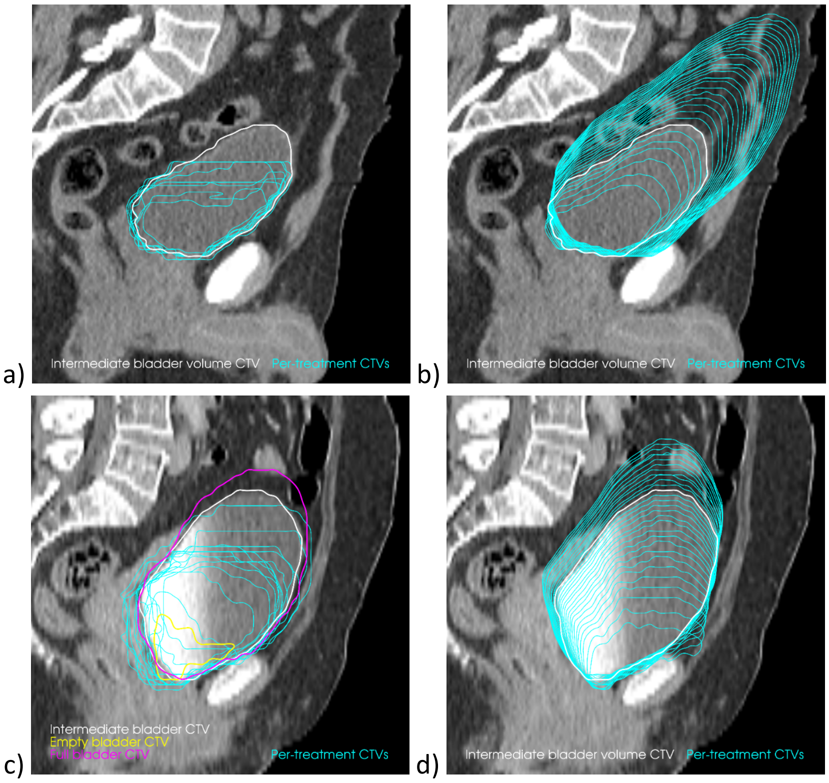

Figure 4-14 : Exemple des instances de vessie modélisées pour un patient de sexe masculin, comparées à une vessie intermédiaire (1ere ligne) et de sexe féminin, comparées à une librairie de plan de traitement (2eme ligne).

Chaque ligne représente la variabilité du volume vésical durant le traitement (a et c) et les instances modélisées de 75 cc à 800 cc par pas de 25 cc (b et d).

L’objectif ces travaux était de générer une librairie de plans de traitement composée d’un large nombre d’instances de vessie. Nous avons montré qu’un modèle statistique de forme était possible pour la vessie du sexe féminin et masculin. Ces deux modèles permettent la génération de vessies avec des volumes différents. Ce matériel pourra servir à la définition d’une librairie de plans de traitement optimale en termes de marge de PTV et de taille de librairie pour chaque sexe.

4.5 CONCLUSION

A partir d’une analyse populationnelle, ces travaux ont permis de définir une librairie de plan de traitement modélisée à la planification pour l’ensemble de la cohorte. Par rapport à la librairie de plans de traitement classique, cette approche permettait d’améliorer la couverture du CTV pour les patientes montrant de faibles déformations à la planification et d’importantes déformations pendant le traitement.

4.6 RÉFÉRENCES

1. Fiorino C, Cozzarini C, Passoni P. The promise of adaptive radiotherapy for pelvic tumors:“Too high cost for too little result” or “a low cost for a significant result”? In: Editor, editor^editors. Book The promise of adaptive radiotherapy for pelvic tumors:“Too high cost for too little result” or “a low cost for a significant result”?: Taylor & Francis; 2016.
2. Belongie S, Malik J, Puzicha J. Shape matching and object recognition using shape contexts. *IEEE transactions on pattern analysis and machine intelligence* 2002;24:509-522.
3. Xiao D, Zahra D, Bourgeat P, Berghofer P, Tamayo OA, Wimberley C, Gregoire MC, Salvado O. An improved 3d shape context based non-rigid registration method and its application to small animal skeletons registration. *Computerized Medical Imaging and Graphics* 2010;34:321-332.
4. Acosta O, Fripp J, Doré V, Bourgeat P, Favreau J-M, Chételat G, Rueda A, Villemagne VL, Szoeke C, Ames D. Cortical surface mapping using topology correction, partial flattening and 3d shape context-based non-rigid registration for use in quantifying atrophy in alzheimer's disease. *Journal of Neuroscience Methods* 2012;205:96-109.
5. Myronenko A, Song X. Point set registration: Coherent point drift. *IEEE transactions on pattern analysis and machine intelligence* 2010;32:2262-2275.
6. Cazoulat G, Simon A, Dumenil A, Gnep K, De Crevoisier R, Acosta O, Haigron P. Surface-constrained nonrigid registration for dose monitoring in prostate cancer radiotherapy. *IEEE Transactions on Medical Imaging* 2014;33:1464-1474.
7. Rubeaux M, Cazoulat G, Duménil A, Lafond C, Acosta O, De Crevoisier R, Simon A, Haigron P. Numerical phantom generation to evaluate non-rigid ct/cbct registration algorithms for prostate cancer radiotherapy. *Image-Guidance and Multimodal Dose Planning in Radiation Therapy* 2012:74.
8. Wognum S, Bondar L, Zolnay A, Chai X, Hulshof M, Hoogeman M, Bel A. Control over structure-specific flexibility improves anatomical accuracy for point-based deformable registration in bladder cancer radiotherapy. *Medical physics* 2013;40.
9. Wognum S, Heethuis S, Rosario T, Hoogeman M, Bel A. Validation of deformable image registration algorithms on ct images of ex vivo porcine bladders with fiducial markers. *Medical physics* 2014;41.
10. Rigaud B, Simon A, Castelli J, Gobeli M, Ospina Arango JD, Cazoulat G, Henry O, Haigron P, De Crevoisier R. Evaluation of deformable image registration methods for dose monitoring in head and neck radiotherapy. *Biomed Res Int* 2015;2015:726268.
11. Mencarelli A, van Kranen SR, Hamming-Vrieze O, van Beek S, Rasch CRN, van Herk M, Sonke J-J. Deformable image registration for adaptive radiation therapy of head and neck cancer: Accuracy and precision in the presence of tumor changes. *International Journal of Radiation Oncology* Biology* Physics* 2014;90:680-687.
12. Albrecht T, Lüthi M, Gerig T, Vetter T. Posterior shape models. *Medical image analysis* 2013;17:959-973.
13. Rios R, De Crevoisier R, Ospina JD, Commandeur F, Lafond C, Simon A, Haigron P, Espinosa J, Acosta O. Population model of bladder motion and deformation based on dominant eigenmodes and mixed-effects models in prostate cancer radiotherapy. *Medical image analysis* 2017;38:133-149.
14. Jadon R, Pembroke C, Hanna C, Palaniappan N, Evans M, Cleves A, Staffurth J. A systematic review of organ motion and image-guided strategies in external beam radiotherapy for cervical cancer. *Clinical Oncology* 2014;26:185-196.
15. Thörnqvist S, Hysing LB, Tuomikoski L, Vestergaard A, Tanderup K, Muren LP, Heijmen BJ. Adaptive radiotherapy strategies for pelvic tumors–a systematic review of clinical implementations. *Acta Oncologica* 2016;55:943-958.
16. Collins SD, Leech MM. A review of plan library approaches in adaptive radiotherapy of bladder cancer. *Acta Oncologica* 2018;57:566-573.

17. Murthy V, Master Z, Adurkar P, Mallick I, Mahantshetty U, Bakshi G, Tongaonkar H, Shrivastava S. ‘Plan of the day’adaptive radiotherapy for bladder cancer using helical tomotherapy. *Radiotherapy and Oncology* 2011;99:55-60.
18. Murthy V, Masodkar R, Kalyani N, Mahantshetty U, Bakshi G, Prakash G, Joshi A, Prabhash K, Ghonge S, Shrivastava S. Clinical outcomes with dose-escalated adaptive radiation therapy for urinary bladder cancer: A prospective study. *International Journal of Radiation Oncology* Biology* Physics* 2016;94:60-66.
19. Tuomikoski L, Collan J, Keyriläinen J, Visapää H, Saarilahti K, Tenhunen M. Adaptive radiotherapy in muscle invasive urinary bladder cancer–an effective method to reduce the irradiated bowel volume. *Radiotherapy and Oncology* 2011;99:61-66.
20. Bondar M, Hoogeman M, Mens J, Quint S, Ahmad R, Dhawtal G, Heijmen B. Individualized nonadaptive and online-adaptive intensity-modulated radiotherapy treatment strategies for cervical cancer patients based on pretreatment acquired variable bladder filling computed tomography scans. *International Journal of Radiation Oncology* Biology* Physics* 2012;83:1617-1623.
21. Meijer GJ, van der Toorn P-P, Bal M, Schuring D, Weterings J, de Wildt M. High precision bladder cancer irradiation by integrating a library planning procedure of 6 prospectively generated sib imrt plans with image guidance using lipiodol markers. *Radiotherapy and Oncology* 2012;105:174-179.
22. Lutkenhaus LJ, Visser J, de Jong R, Hulshof MC, Bel A. Evaluation of delivered dose for a clinical daily adaptive plan selection strategy for bladder cancer radiotherapy. *Radiotherapy and Oncology* 2015;116:51-56.
23. Tuomikoski L, Valli A, Tenhunen M, Muren L, Vestergaard A. A comparison between two clinically applied plan library strategies in adaptive radiotherapy of bladder cancer. *Radiotherapy and Oncology* 2015;117:448-452.
24. Wright P, Redpath AT, Høyer M, Muren LP. A method to individualize adaptive planning target volumes for deformable targets. *Physics in Medicine & Biology* 2009;54:7121.

5 RECALAGE DEFORMABLE BIOMECANIQUE POUR LA CURIETHERAPIE DES CANCERS DU COL UTERIN

5 Recalage déformable biomécanique pour la curiethérapie des cancers du col utérin 172

- 5.1 Introduction 172
  - 5.1.1 Principe de base des modèles biomécaniques 174
  - 5.1.2 Méthode des éléments finis 175
- 5.2 Article : “Technical Note: Biomechanical model-based deformable image registration to solve extreme position variation in a commercial treatment planning system” 177
  - 5.2.1 Introduction 179
  - 5.2.2 Materials and methods 179
  - 5.2.3 Registration methods description 181
  - 5.2.4 Registration methods evaluation 182
  - 5.2.5 Results 182
  - 5.2.6 Discussion 186
  - 5.2.7 Conclusion 186
  - 5.2.8 References 187
- 5.3 Article : “Deformable image registration for dose mapping between external beam radiotherapy and brachytherapy for cervical cancer” 188
  - 5.3.1 Introduction 189
  - 5.3.2 Materials and methods 191
  - 5.3.3 Results 198
  - 5.3.4 Discussion 208
  - 5.3.5 Conclusion 210
  - 5.3.6 References 211
- 5.4 Discussion 216
- 5.5 Conclusion 217
- 5.6 Références 218

5.1 INTRODUCTION

Les travaux de ce chapitre prennent place dans le contexte de la curiethérapie, la deuxième partie du traitement recommandé pour les cancers du col de l'utérus localement avancés. La planification de ce traitement nécessite l'insertion d'un applicateur, comprenant un moule, un guide, un anneau ou des ovoïdes et un tandem, afin de permettre la délivrance de la dose. De plus, un ballon de Foley est inséré dans la vessie afin de contrôler son volume. L'insertion de ces dispositifs engendre alors de très forts déplacement et déformation de la cible clinique et des organes à risque. Ces variations anatomiques entre les traitements compliquent l'estimation précise de la dose totale délivrée localement par la radiothérapie externe et la curiethérapie. La question se pose donc de proposer une méthode de recalage déformable qui puisse estimer les déformations induites par ces dispositifs afin de propager les doses de curiethérapie vers une anatomie sans dispositif.

Comme abordé dans le chapitre 2 (*cf*. section 2.3.2.4), différentes approches ont été proposées pour ce type d'application [1-3]. Elles reposent sur des méthodes permettant d'estimer des déformations importantes, soit par l'usage des contours soit par une assistance manuelle, et sur des méthodes de régularisation permettant les discontinuités. Ces discontinuités doivent permettre de simuler l'interface entre les organes présentant des déformations indépendantes, et donc des glissements, ce qui est difficilement modélisable avec des approches de régularisation classiques (par ex. la méthode des Démons) ou de simuler la disparition d'éléments entre deux images (par ex. l'applicateur de curiethérapie). Ces approches n'ont cependant jamais été exploitées pour des applications dosimétriques.

Dans le contexte de la curiethérapie des cancers du col utérin, ce chapitre porte sur l'utilisation d'un modèle biomécanique pour générer des déformations réalistes pour deux applications différentes. Ces travaux ont été réalisés au sein de l'hôpital *MD Anderson Cancer Center, The University of Texas, Houston* au sein de l'équipe *Morfeus Lab* dirigée par Dr. Kristy Brock sous le tutorat du Dr. Guillaume Cazoulat dans le cadre d'une mobilité de thèse de 5 mois financée par Rennes Métropole.

Le premier travail de ce chapitre porte sur l'évaluation de méthodes de recalage (rigide et déformable), disponibles dans un système clinique, afin d'estimer les déformations entre une image acquise lors de la radiothérapie externe, sans matelas, et une image acquise pour la curiethérapie, avec un matelas. La présence du matelas engendre des déplacements osseux importants qui génèrent des déformations majeures des organes du pelvis. Cette étude a été menée sur les données d'une patiente montrant des déformations de grande amplitude. Les différentes approches de recalage déformables considérées sont basées intensité, hybride ou biomécanique. Dans le cas des approches hybride et biomécanique, seuls les contours des os et du corps sont utilisés pour assister l'estimation de la déformation. Une évaluation géométrique est menée, reposant sur : (i) l'évaluation des correspondances des délinéations propagées, notamment celles correspondant aux tissus mous, non utilisés en entrée du modèle ; (ii) l'évaluation de la topologie du champ de déformation par l'intermédiaire du déterminant du Jacobien.

Le deuxième travail porte sur la définition et l'évaluation de méthodes de recalage déformable pour la quantification des déformations induites par l'insertion de l'applicateur de curiethérapie, sur une cohorte de 20 patientes. Pour cette application, la méthode de recalage déformable reposant sur un modèle biomécanique est particulièrement considérée, notamment à travers l'utilisation de différentes conditions aux limites. Ces dernières résultent de variantes de la méthode DMR (section

4.2.2.3). Les différentes méthodes biomécaniques sont comparées, géométriquement puis dosimétriquement (en termes de dose propagée), à la méthode des Démons et à un outil commercial.

Ces travaux ont permis la soumission d'une *technical note*, intitulée *« Technical note: biomechanical model-based deformable image registration to solve extreme position variation in a commercial treatment planning system »,* au journal *Medical Physics* et d'un article, intitulé « *Deformable image registration for dose mapping between external beam radiotherapy and brachytherapy for cervical cancer* », au journal *Physics in Medicine and Biology*. Après une présentation des grands principes des modèles biomécaniques, ils sont tous deux reproduits dans la suite de ce chapitre.

5.1.1 PRINCIPE DE BASE DES MODELES BIOMECANIQUES

Les modèles biomécaniques permettent de simuler le comportement biomécanique des tissus biologiques (organes) par un modèle simplifié. L'application d'une force sur une structure engendre la déformation de celle-ci. La variation d'état de la structure s'exprime par la déformation (ϵ, *strain*) qui est définie par la variation de la longueur de la structure *ΔL* divisée par sa longueur originale *L* ($\epsilon = \Delta L/L$, 5-1). Cette déformation engendre alors des forces internes au sein de la structure, que l'on appelle contraintes (σ, *stress*), qui sont définies comme une force *F* par unité de surface *S* ($\sigma = F/S$, 5-2). Les termes étirement (*stretching*) et compression représentent respectivement une déformation positive et négative. Deux lois de comportement sont utilisées pour modéliser les déformations et les contraintes associées à un objet : la loi d'élasticité linéaire (Loi de Hooke) et la loi d'élasticité non-linéaire (hyperélasticité). Il a été montré que le choix du modèle devait être défini en fonction de l'application. Un modèle linéaire peut être suffisant pour modéliser des déformations limitées [4]. Ce chapitre abordera uniquement cette loi d'élasticité linéaire.

La loi de Hooke modélise donc le comportement élastique d'une structure lorsque cette dernière est soumise à des contraintes (forces ou déplacements). Cette loi est dite linéaire car elle stipule que la déformation de la structure, par exemple l'étirement, est proportionnelle à la force appliquée :

$$\sigma = \mathrm{C} \cdot \epsilon \tag{5-3}$$

Le symbole C est une matrice symétrique de dimension 6x6 décrivant le comportement élastique du matériau. Les symboles σ et ϵ représentent respectivement les tenseurs de contraintes et de déformations.

Si on considère un matériau élastique homogène (isotropique), alors la matrice C peut s'exprimer uniquement en fonction du module de Young (*E*, *Young's modulus*) et du coefficient de Poisson (ν*, Poisson's ratio*). Le module de Young, qui mesure la déformation d'une structure sous contrainte, représente la rigidité d'un matériau en kilo Pascal (KPa). Le coefficient de Poisson caractérise le rapport entre la déformation latérale et la déformation axiale. Il représente donc la compressibilité d'une structure en cas d'étirement ou de compression, avec conservation de son volume. Ce dernier est compris entre 0 et 0.5, sans unité, pour définir un matériau compressible à incompressible.

5.1.2 METHODE DES ELEMENTS FINIS

La méthode des éléments finis (*Finite Element Model,* FEM) repose sur la représentation d'un objet d'intérêt en sous-éléments simples et l'assignation de propriétés mécaniques afin de résoudre numériquement un problème mécanique. La modélisation en éléments finis peut être divisée en deux étapes. Dans un premier temps le FEM est construit, ce qui correspond à définir la représentation géométrique et à assimiler les propriétés matérielles de chaque composante du modèle (par ex. chaque organe). Dans un second temps, l'analyse des éléments finis (*Finite Element Analysis,* FEA) est faite, où les contraintes internes du FEM sont résolues à partir de conditions aux limites imposées.

5.1.2.1 Génération du modèle d'éléments finis

La représentation géométrique des structures d'intérêt doit être définie afin de pouvoir résoudre numériquement le modèle. Pour ce faire, un FEM est construit avec une ou plusieurs structures d'intérêts où chaque structure est représentée par un maillage. Chaque maillage est alors divisé en plusieurs géométries simples (*cf.* Figure 5-1). Ces géométries simples sont communément des éléments tétraédriques linéaires constitués de 4 nœuds et de 6 éléments les joignant. D'autres géométries sont envisageables permettant de modéliser des comportements plus complexes (par ex. les géométries quadratiques ou cubiques), au prix d'un temps de calcul plus élevé.

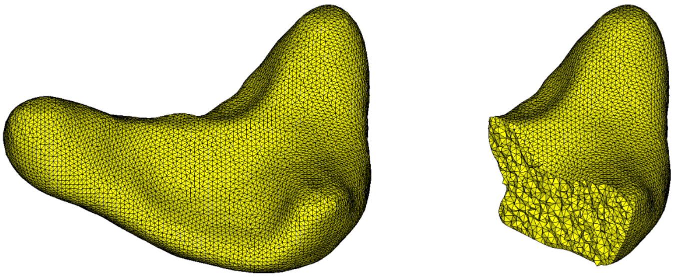

Figure 5-1: Exemple d'un maillage en éléments finis tétraédriques d'une vessie comprenant 31 000 nœuds

Chaque composante du modèle est alors représentée par son propre maillage éléments finis. Un maillage « englobant » (par ex. le corps de la patiente) peut aussi être défini pour modéliser l'environnement et l'interface entre chaque composante du modèle.

Une fois la géométrie du modèle définie, les propriétés matérielles sont assignées à chaque composante. Suivant la loi de Hooke, représentant le comportement élastique linéaire dans un milieu isotrope, un module de Young et un coefficient de Poisson sont assignés à chaque composante du modèle pour représenter sa rigidité et sa compressibilité, respectivement.

5.1.2.2 Analyse du modèle d'éléments finis

L'analyse du modèle d'éléments finis repose sur une première étape primordiale, la définition des conditions aux limites et des chargements (loads) qui définissent respectivement l'environnement et les interactions dans l'environnement et les forces qui ont engendré les déformations des composantes du FEM. Ces chargements sont appliqués indépendamment à chaque composante du FEM et représentent les déplacements des points de la surface du maillage entre les deux instances.

La résolution du modèle d'éléments finis permet ensuite de définir l'étape d'équilibre du FEM après l'application des conditions aux limites (comprenant les chargements). En d'autres termes, pour chaque composante, les conditions aux limites, de type déplacement, représentent des forces extérieures qui engendrent des déformations internes. Dans un contexte de comportement élastique linéaire homogène, l'énergie de la déformation (Σ) d'un matériau par un déplacement externe peut être exprimé de la façon suivante [5] :

$$\Sigma = \frac{1}{2}\int_{\Omega} \sigma^T \epsilon d\Omega + \int_{\Omega} F^T u d\Omega \qquad (5\text{-}4)$$

Où *F* représente les forces appliquées à la surface de la structure (conditions aux limites), *u* les déformations internes de la structure que l'on souhaite estimer, Ω représente le domaine (l'espace du maillage éléments finis), σ et ϵ respectivement le vecteur de contrainte et de déformation (*cf.* section 5.1.1).

La déformation interne de la structure *u* est le champ de déformations qui minimise l'énergie Σ. Finalement, le problème peut être écrit comme un système linéaire permettant d'estimer le déplacement de chaque nœud interne de la structure en fonction des conditions aux limites imposées :

$$Ku = -F \qquad (5\text{-}5)$$

$$u = K^{-1}F \qquad (5\text{-}6)$$

Ou K représente la matrice de rigidité de la structure qui est composée de constantes intégrant les paramètres *E* et ν. La résolution de cette équation permet l'obtention des déplacements internes du FEM tout en respectant les conditions aux limites.

Les études qui sont présentées dans la suite font l'hypothèse que la majorité des incertitudes de la modélisation biomécanique sont dues à la méthode de définition des conditions aux limites et du coefficient de Poisson des composantes du FEM. Cette hypothèse a été vérifiée dans le cadre de la modélisation biomécanique de la compression du sein [6]. Les conditions aux limites seront définies comme un déplacement imposé, estimé à partir de la méthode de recalage déformable de maillage (*Deformable Mesh Registration*, DMR) présentée dans la section 4.2.2.3. Ce type d'approche est simple car il permet d'imposer une contrainte globale sur la structure sans devoir investiguer les forces qui ont entraîné la déformation de la structure vers cette configuration [7].

5.2 ARTICLE : "TECHNICAL NOTE: BIOMECHANICAL MODEL-BASED DEFORMABLE IMAGE REGISTRATION TO SOLVE EXTREME POSITION VARIATION IN A COMMERCIAL TREATMENT PLANNING SYSTEM"

B. Rigaud *MSc* (1, 2) *, A. Klopp *MD, PhD* (3), A. Simon *PhD* (1), S. Vedam *PhD* (4), A. Venkatesan *MD, PhD* (5), P. Haigron *PhD* (1), N. Taku *MD, MSc* (3), R. De Crevoisier *MD, PhD* (1), KK. Brock *PhD* (2), G. Cazoulat *PhD* (2) *

1. Univ Rennes, CLCC Eugène Marquis, Inserm, LTSI – UMR 1099, F-35000 Rennes, France
2. Department of Imaging Physics, The University of Texas MD Anderson Cancer Center, Houston, TX 77030, USA
3. Department of Radiation Oncology, The University of Texas MD Anderson Cancer Center, Houston, TX 77030, USA
4. Department of Radiation Physics, The University of Texas MD Anderson Cancer Center, Houston, TX 77030, USA
5. Department of Diagnostic Radiology, The University of Texas MD Anderson Cancer Center, Houston, TX 77030, USA

Abstract

Purpose

During multi-modality and fractionated cancer treatments, consistent patient positioning for imaging cannot always be ensured. This technical note aims to demonstrate how biomechanical model-based registration, integrated into a clinical treatment planning system, can be used to align images presenting large deformations due to patient positioning variations.

Methods

For one patient who underwent concomitant chemoradiation with brachytherapy for a locally advanced cervical cancer, four commercially available image alignment methods were compared to manage large bone displacements due to positioning variation: (1) rigid registration of the bones and body; (2) intensity-based deformable image registration (DIR); (3) hybrid DIR and (4) biomechanical model-based DIR. The hybrid and biomechanical model-based DIR methods used the bones and body contours as boundary conditions. The performance of all methods was evaluated based on the centroid alignment, Dice similarity coefficient (DSC), Hausforff distance and distance to agreement of the manually contoured pelvic organs. The Jacobian determinant values were reported for the DIR methods.

Results

Rigid registration resulted in poor vertebrae and pelvic bones alignment with DSC of 0.38 and 0.59, respectively, and in DSC of 0.31, 0.07, 0.26, 0.39, and 0.35 for the bladder, cervix, rectum, uterus, and vagina, respectively. DIR methods improved the vertebrae and pelvic bone alignment, with DSC of 0.92 and 0.95 for the intensity-based, 0.98 and 0.98 for the hybrid, and 0.99 and 0.99 for the biomechanical

model-based. The biomechanical model-based DIR improved the soft tissues contour alignment with DSC of 0.56, 0.48, 0.55, 0.51, and 0.41 for the bladder, cervix, rectum, uterus, and vagina, respectively. The min – max and 0.02% quantile range of the Jacobian determinants were 0.97 – 1.86 and 0.30 – 1.00 for the intensity-based, 0.99 – 1.53 and 0.22 – 0.96 for the hybrid, and 1.00 – 1.33 and 0.71 – 1.12 for the biomechanical model-based DIR method.

Conclusions

Compared to standard DIR methods, the biomechanical model-based DIR with boundary conditions on the bones and body contours improved the matching of the soft tissue contours. Also, the resulting deformation provided the most stable Jacobian determinants and organ volumes. This method opens perspectives for multimodal image registration.

5.2.1 INTRODUCTION

Deformable image registration (DIR) is increasingly used in the field of radiation therapy (RT) to manage body and organ deformations. One of the main applications in RT is the fusion of one image to another at different times during treatment. This reduces the workload from manual segmentation and can assist in the contouring of the tumor by taking advantage of different image modalities [1-3]. During fractioned treatments, organ deformations can occur due to patient motion, breathing, weight loss, tumor shrinkage and organ at risk filling. Deformations can also be observed between images acquired in different positions (*e.g.* supine, prone or decubitus position), for example from different treatment procedures or different clinical centers. Position variation can induce external body deformation and independent bone displacement (*e.g.* vertebrae/coccyx and pelvic bones for the pelvis) that can impact the soft tissues position. In this case, the large deformations can motivate the clinical team to acquire a new image in a different position, thus increasing the overall treatment billing [4].

Classic rigid registration (*i.e.* translation only or translation and rotation) may fail to take into account such complex displacements, thus requiring more sophisticated methods like DIR. Biomechanical model-based DIR has the ability to simulate independent displacements, such as sliding for lung patients [5,6]. Recently, a biomechanical model-based DIR algorithm has been integrated and validated into a treatment planning system (TPS) [7]. Such implementation enables its use in different clinical applications involving multiple imaging modalities [8]. Indeed, intensity-based or hybrid DIR methods (*i.e.* using both intensity and contour information to drive the deformation) may estimate unrealistic deformations when intensity variability is observed between the images [9]. Hybrid DIR has previously shown to degrade the target registration error compared to the biomechanical approach while having a better average distance between organ surfaces [7]. The consequences of patient position variation were observed for breast surgery, in which context a finite element model has been proposed to align the patient anatomy [10]. Other biomechanical model-based methods have been developed to take in account large bone displacements such as arm position [11] and head and neck posture [12].

In this technical note, one patient treated for a locally advanced cervical cancer has been selected in order to demonstrate the potential of biomechanical model-based DIR using commercially available tools. The patient showed large bone displacements due to the presence of a mattress on the table at the time of pulsed dose rate brachytherapy (PDR-BT). The patient had one computed tomography (CT) scan in supine position prior to BT treatment and one CT in supine position with a mattress on the table for BT planning. The presence of a BT applicator on the BT image complicates the task for standard intensity-based DIR methods. However, the main challenge in fusing the images for this patient lied in the presence of the mattress which induced large bone displacements compared to the images acquired with a flat table only.

The aim of this technical note was to evaluate the performance of different DIR methods available in a TPS to transform the patient anatomy with extreme bone displacements and to demonstrate in this context the advantages of biomechanical model-based DIR. The endpoint was to provide indication for managing these uncommon cases for which most of the anatomical deformation is caused by patient posture change. For this purpose, the BT CT (with applicator and the mattress) was registered toward the pre-CT (without applicator and flat table).

5.2.2 MATERIALS AND METHODS

5.2.2.1 Patient information

This technical note is based on images of one patient, 43 years old, treated for a squamous cervical carcinoma with an extension to the upper node (stage IIIB of the FIGO classification [13]). The treatment consisted of a combination of external beam radiation therapy (EBRT) with chemotherapy and BT.

The EBRT was delivered using step and shoot intensity-modulated RT planned using the Pinnacle TPS v9.4. The dose constraints to the tumor were 47.25 Gy to the isocenter of the pelvis using four 18 MV beams and a mean dose of 52.99 Gy to the nodal gross tumor volume (GTV) using nine 6 MV beams.

The chemotherapy was delivered using cisplatin at 40 mg/m^2. The PDR-BT was used to deliver 19.67-20.43 Gy at the points A.

The images used for this technical note were the following (*cf.* Figure 5-2):

- One body CT-scan in supine position (from the thorax to the femoral heads) at the time of the EBRT boost planning (“pre-BT CT”)
- One MRI of the pelvis in supine position (from L5 to the femoral heads) for the first PDR-BT fraction with applicator inserted (10 days after the pre-BT CT) (“BT MRI”). This image was used to help the delineation task only.
- One CT-scan of the pelvis in supine position with a mattress on the table (from L4 to the femoral heads) with the PDR-BT applicator inserted for planning (1 hour after the BT MRI) (“BT CT”)

5.2.2.2 Organ delineation

The organs were manually delineated by the same observer on the pre-BT CT, BT MRI and BT CT using a commercial TPS (RayStation v7, RaySearch Laboratories, Stockholm, Sweden). The BT MRI was used to assist the delineation of the soft tissues on the BT CT.

The following organs were considered (*cf.* Figure 5-2):

- Pelvic bone
- Vertebrae, from the L4 vertebra to the coccyx
- Corpus of the uterus, starting from the uterus isthmus to the fundus of the uterus
- Cervix:
    - With applicator: starting from the end of the ovoid to the start of the uterus isthmus
    - Without applicator: from the uterus isthmus with respect to the BT MRI cervix volume
- Vagina, from the cervix to 1 cm below the pubic bone
- Bladder, encompassing the bladder urethra until the bladder base is visible
- Rectum, from the sigmoid bend to the end of the anal canal

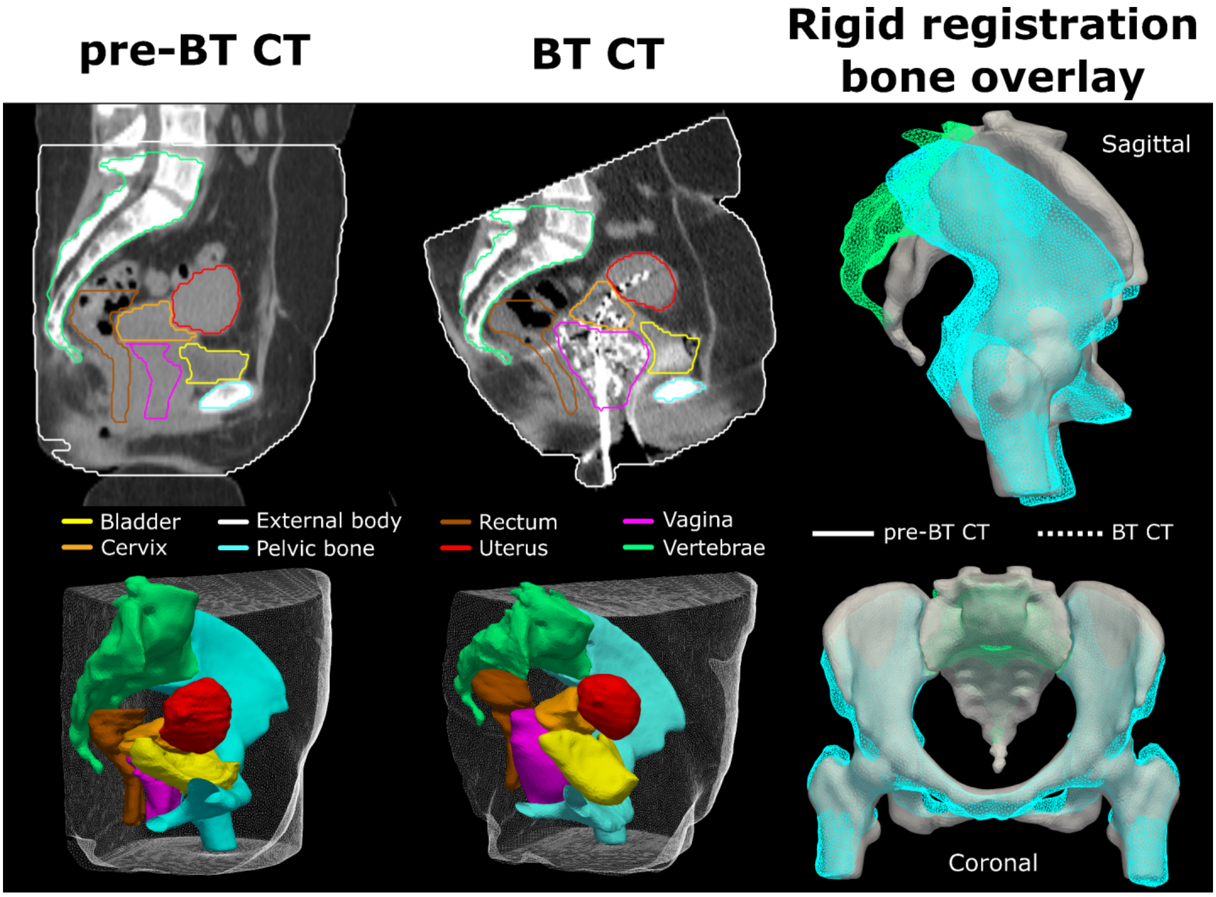

Figure 5-2: Organ delineations on the pre-BT CT without mattress (left) and BT CT with mattress (right), both in supine position

The organ meshes are represented under their corresponding image. The bone displacements between the anatomy without and with mattress (full and wireframe meshes, respectively), after rigid registration, is represented on the right part of the figure. The controlling structures used for the hybrid and biomechanical methods were the external body, vertebrae and pelvic bones. BT: brachytherapy; CT: computed tomography;

5.2.3 REGISTRATION METHODS DESCRIPTION

Four registration methods, available in the TPS, were compared in this study:

The rigid registration algorithm allows alignment of two images using 6 degrees of freedom (3 translations and 3 rotations) with a focus on the external body contour and the bones intensity.

The integrated DIR algorithm in the TPS, ANACONDA [14], generates a dense deformation vector field (DVF) between the reference and the moving image. The optimization process of this method, to estimate the DVF, relies on the correlation coefficient between the image intensities with a regularization term influenced by the determinant of the Jacobian. Two methods can be defined based on this algorithm. The intensity-based DIR uses only the intensity information of the considered images. The hybrid DIR uses “controlling structures” as constraints in order to add a priori information into the optimization process. The controlling structures are thus matched by deforming their respective distance maps. The hybrid DIR takes advantage of both the intensity and delineation between the images to estimate the DVF.

The biomechanical model-based DIR algorithm, an implementation of the Morfeus algorithm into the TPS [15], generates a dense DVF from the reference image to the moving image coordinates. This approach can be used indifferently with multimodal images as it does not rely on image intensity. However, this approach requires contouring of corresponding regions of interests to drive the DVF. First, the surface meshes of the considered structures are generated in order to compute the boundary conditions that will be used as the constraints. For this purpose, the TPS uses a model-based segmentation method to deform the moving surface meshes toward the reference image delineations. The triangular surface meshes are converted in volumetric tetrahedral meshes with homogeneous material properties. Finally, based on the boundary conditions, the finite element analysis solves the internal displacements of the model in order to generate a dense DVF. The default material properties proposed by the TPS were used including a Poisson's ratio of 0.48 for all structures.

The pre-BT CT was registered to the BT CT using these different registration methods. For the hybrid and biomechanical model-based DIR methods, the controlling structures were the external body, vertebrae and pelvic bones. The soft tissues were not used as controlling structures. The structures propagated using the resulting transformations were the bladder, cervix, rectum, uterus, and vagina.

5.2.4 REGISTRATION METHODS EVALUATION

The rigid transformation and DVF obtained for each evaluated method were exported from RayStation using available scripting functions and the analysis of the exported DVF were performed with an in-house software. Using the resulting transformation for each method, all structures were propagated from the reference image space toward the moving image space following the vectors direction.

The methods were compared using delineation and DVF criteria. The delineation criteria were the centroid difference, Dice similarity coefficient (DSC) [16], Hausdorff distance (HD) [17] and distance to agreement (DTA), between the reference and propagated organ surfaces. The DVF criteria were statistics (mean, min, max and 0.02% quantile) of the Jacobian determinant values of each organ volume, on the reference image space (following the inverse transformation). The determinant of the Jacobian testifies to the voxel-wise volumetric change according to the DVF. A determinant value superior (respectively inferior) to one represents a volume expansion (respectively a compression). A determinant value equal or below zero represents a discontinuity in the DVF. In this application, a good registration method should result to good delineation criteria while keeping the determinant of the Jacobian around one. An improper anatomy correspondence would be detected by poor delineation criteria with large variations of the determinant of the Jacobian.

5.2.5 RESULTS

Figure 5-3 represents the reference image as well as the transformed images for each method in the sagittal and coronal views. While the rigid registration failed to correctly align the bones, the deformable methods improved their correspondence.

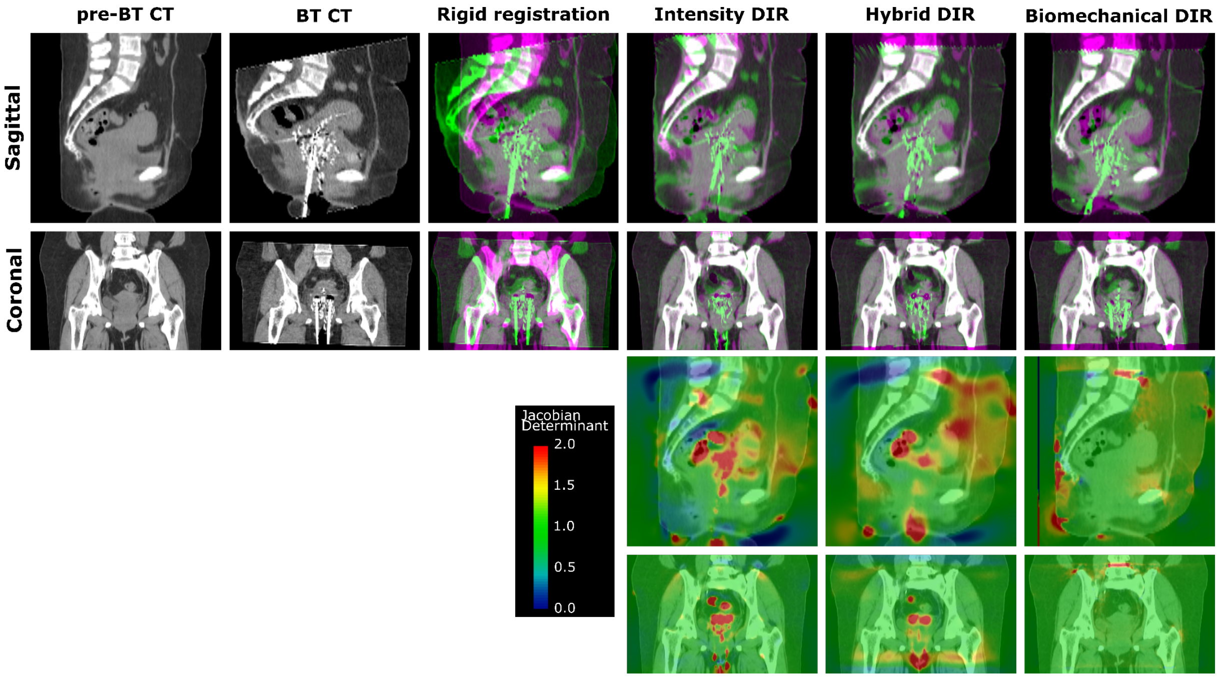

Figure 5-3: Comparison between the reference and the transformed moving images according to the different methods (top) and Jacobian determinant for the deformable methods (bottom right)

The rigid registration does not align the vertebrae well due to an independent displacement and deformation according to the pelvic bone. The deformable methods improve the alignment of bony structures. The intensity-based methods are deforming the gas inside the rectum, the applicator and the uterus. Comparing the Jacobian determinant, the biomechanical approach generates a more consistent and realistic deformation.

5.2.5.1 Delineation evaluation

The deformed delineations correspond to the reference delineations following the DVF direction (reference to moving space). Table 5-1 represents the volumes of the delineations on the reference, moving and deformed images.

Compared with the biomechanical model-based approach, the DIR methods using the intensity information have larger volume variation as they were trying the match the pelvic soft tissues. Except for the bladder, the biomechanical approach was the method providing the lowest volume changes while deforming the bones and body.

Figure 5-4 represents the delineation evaluation of the four tested methods, for each considered organ. The rigid registration failed to align both the vertebrae and pelvic bones with a DSC of 0.38 and 0.59, respectively. Before DIR, the position variation led to a Hausdorff distance for the vertebrae and pelvic bones of 33 mm and 27 mm, respectively. The biomechanical model-based DIR method improved the DSC and Hausdorf distance to 0.99 and 3 mm, respectively, for the two bony structures.

Compared to the intensity-based and hybrid DIR methods, the biomechanical model-based approach showed better delineation scores of the considered organs, except for the rectum. A better rectum alignment was achieved by the intensity-based methods due to a larger DVF smoothing around the anterior part of the vertebrae-coccyx. Poor alignment of the cervix was obtained by the rigid and intensity-based DIR methods.

Table 5-1: Organ volumes on each image and for each method

The organ shapes are deformed following the DVF direction (reference towards moving). An ideal method should provide the volumes of the moving contours. The soft tissue volumes are reported in cc and the increase relative to the reference volumes. DIR: deformable image registration; DVF: deformation vector field

Methods	Organ volumes in cc (increasing relative to reference)							
	External contour	Pelvic bone	Vertebrae	Cervix	Uterus	Vagina	Bladder	Rectum
Pre-BT CT	16515.4	935.9	312.6	58.1	109.3	45.4	66.8	63.6
BT CT	18612.3	953.6	312.1	52.6	70.8	187.5	80.0	70.8
Intensity DIR	15997.7 (-3%)	940.0 (0.4%)	320.1 (2%)	107.8 (86%)	159.7 (46%)	54.8 (21%)	81.5 (22%)	79.7 (25%)
Hybrid DIR	18208.7 (10%)	956.1 (2%)	309.9 (-0.8%)	88.3 (52%)	148.3 (36%)	52.7 (16%)	75.6 (13%)	73.2 (15%)
Biomechanical DIR	18584.2 (13%)	960.8 (3%)	313.5 (0.2%)	63.1 (9%)	131.9 (21%)	50.2 (11%)	88.9 (33%)	64.1 (1%)

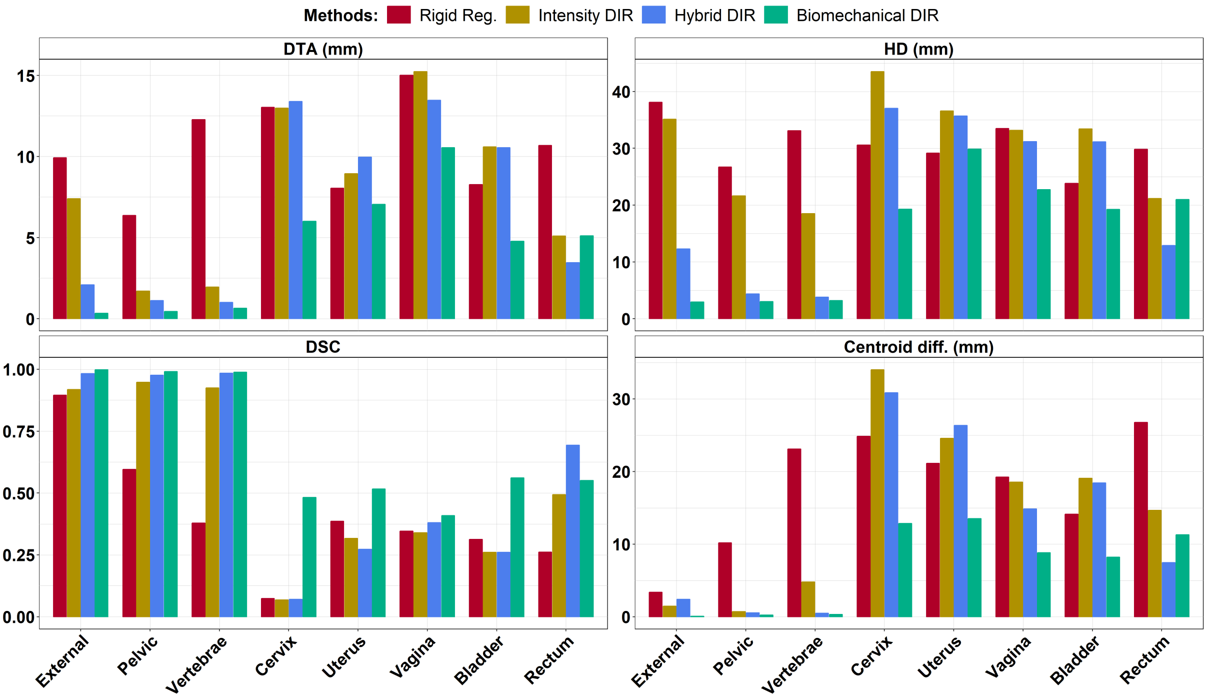

Figure 5-4: Delineation scores of the considered methods for each organ surface

The external body, vertebrae and pelvic bones were used as controlling structures for the hybrid and biomechanical model-based DIR methods. Better delineation criteria of these structures should be expected for these methods compared to the intensity-based only approach. Each bar represents the value of a metric comparing the reference and the transformed organs. A lower value means a better registration for the DTA, HD and centroid difference metrics. A higher value means a better registration for the DSC. Each color represents a method. The organ shapes are deformed following the DVF direction. DSC: Dice similarity coefficient; DTA: distance to agreement; DIR: deformable image registration; DVF: deformation vector field; HD: Hausdorff distance

5.2.5.2 Deformation vector field comparison

Figure 5-5 represents the mean, min, max and 0.02% quantile of the determinant of the Jacobian of each organ volume for each deformable registration method.

Compared to the intensity-based and hybrid DIR methods, the biomechanical model-based method provided a more consistent deformation inside the body as shown by the mean Jacobian determinant value around 1 for each structure (*cf.* bottom right part of Figure 5-3).

For the intensity-based method, maximum values of the Jacobian determinant were observed at 13.1, 17.1, 16.7 and 14.2 for the cervix, external body, rectum and uterus, respectively. These values were decreased to 4.5, 6.2, 5.8 and 4 considering the hybrid DIR method.

A negative minimal Jacobian value was observed inside the body contour for the biomechanical model-based method in the posterior part of the coccyx. This can be expected since biomechanical model-based DIR methods allow DVF discontinuities at the interface of the controlling structures. However, the 0.02% quantile shows a Jacobian determinant value closer to 1 for the biomechanical DIR.

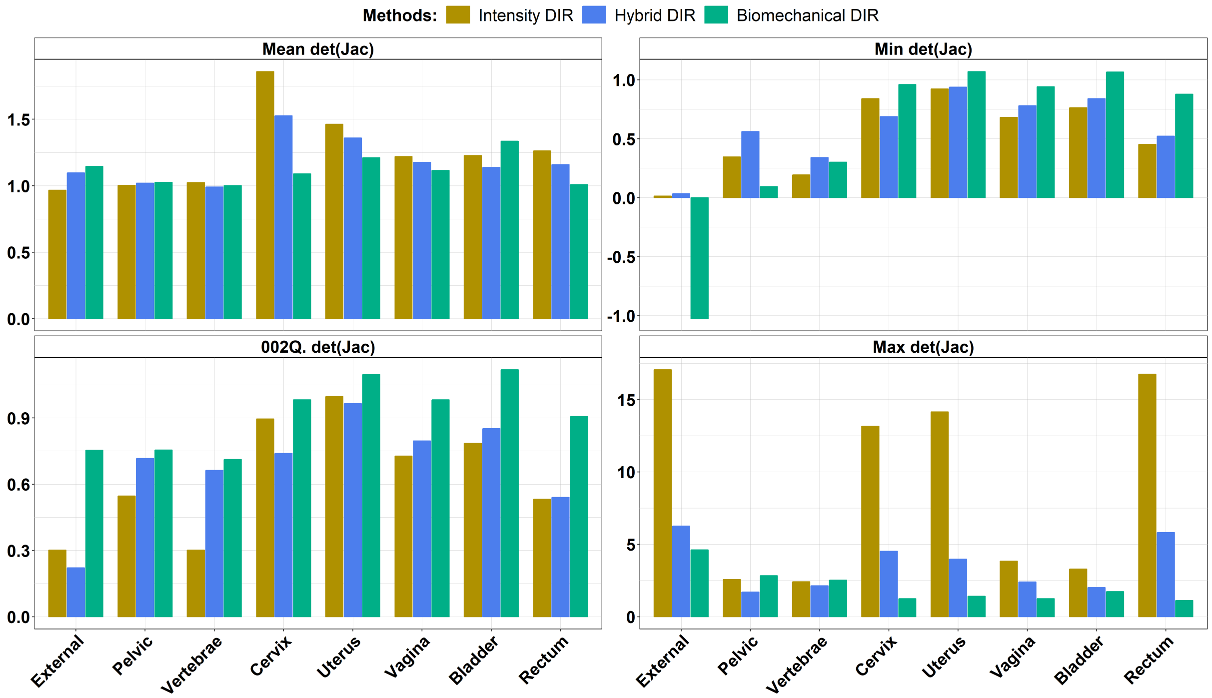

Figure 5-5: Jacobian determinant evaluation of the deformable methods for each organ volume

Each bar represents a value of the Jacobian determinant of the DVF for each organ volume in the reference space (following the following the inverse transformation). Each color represents a DIR method. DIR: deformable image registration; DVF: deformation vector field

5.2.6 DISCUSSION

This technical note described the use of DIR methods available in a commercial TPS to deform the anatomy of a patient when large bone displacements are observed due to posture change. To manage the complex deformations, the methods based on constrained deformation (hybrid and biomechanical) were the preferred approaches. The biomechanical model-based DIR method provided the most realistic deformations as it was not influenced by intensity, noise or bowel gas. As shown by the determinant of the Jacobian, it enabled the alignment of the patient anatomy in a more consistent way compared to the two intensity-based DIR methods. This resulted in an improvement of the soft tissue contours alignment as well.

The rigid registration was not able to match the independent bone displacements and, thus, the soft tissue deformations resulting from this position variation. The intensity-based and hybrid DIR methods managed to deform the bony structures to match them but were influenced by intensity inconsistency (*i.e.* due to the presence of the BT applicator). Compared to the rigid registration and intensity-based DIR, the constrained methods (hybrid and biomechanical) improved the registration results in this complex application, while requiring pre-processing to extract the segmentation. This task may increase the workload. For this case, automatic tools available in the TPS, have been used to improve efficiency. Manual corrections may be required to correct the auto-segmentation and model-based segmentation mapping methods to remove small artifacts and organs overlapping.

There is a need for documentation, training and evaluation to encourage the use of DIR in a clinical context [18]. This technical note aimed to provide indications to motivate the clinical teams to use biomechanical DIR methods, available in the TPS to manage uncommon large bone displacement. In a first step, this approach can be used to reduce the contouring workload either at the planning (*i.e.* to propagate the GTV from one modality to the planning image) or during the treatment (*i.e.* to propagate contours toward numerous fraction images). Such an approach will reduce uncertainties in the interpretation of fused images and potentially avoid the need to acquire a new image when large displacements are observed leading toward reduced treatment billing for the patient.

5.2.7 CONCLUSION

Compared to standard DIR methods, biomechanical model-based DIR can manage large bone displacements while providing a consistent DVF inside the body. Such a tool is already commercially available and could be used clinically in the context of image alignment to assist the manual gesture of organ contouring when extreme posture changes are observed.

5.2.8 REFERENCES

1. Zhong H, Wen N, Gordon JJ, Elshaikh MA, Movsas B, Chetty IJ. An adaptive mr-ct registration method for mri-guided prostate cancer radiotherapy. *Physics in medicine and biology* 2015;60:2837.
2. Chuter R, Prestwich R, Bird D, Scarsbrook A, Sykes J, Wilson D, Speight R. The use of deformable image registration to integrate diagnostic mri into the radiotherapy planning pathway for head and neck cancer. *Radiotherapy and Oncology* 2017;122:229-235.
3. Lu C, Chelikani S, Jaffray D, Milosevic MF, Staib LH, Duncan JS. Simultaneous nonrigid registration, segmentation, and tumor detection in mri guided cervical cancer radiation therapy. *Medical Imaging, IEEE Transactions on* 2012;31:1213-1227.
4. Dinan MA, Curtis LH, Hammill BG, Patz EF, Abernethy AP, Shea AM, Schulman KA. Changes in the use and costs of diagnostic imaging among medicare beneficiaries with cancer, 1999-2006. *Jama* 2010;303:1625-1631.
5. Al-Mayah A, Moseley J, Brock K. Contact surface and material nonlinearity modeling of human lungs. *Physics in Medicine & Biology* 2007;53:305.
6. Cazoulat G, Owen D, Matuszak MM, Balter JM, Brock KK. Biomechanical deformable image registration of longitudinal lung ct images using vessel information. *Physics in medicine and biology* 2016;61:4826-4839.
7. Velec M, Moseley JL, Svensson S, Hårdemark B, Jaffray DA, Brock KK. Validation of biomechanical deformable image registration in the abdomen, thorax and pelvis in a commercial radiotherapy treatment planning system. *Medical physics* 2017.
8. Voroney J-P, Brock KK, Eccles C, Haider M, Dawson LA. Prospective comparison of computed tomography and magnetic resonance imaging for liver cancer delineation using deformable image registration. *International Journal of Radiation Oncology• Biology• Physics* 2006;66:780-791.
9. Cazoulat G, Simon A, Dumenil A, Gnep K, De Crevoisier R, Acosta O, Haigron P. Surface-constrained nonrigid registration for dose monitoring in prostate cancer radiotherapy. *IEEE Transactions on Medical Imaging* 2014;33:1464-1474.
10. Han L, Hipwell JH, Eiben B, Barratt D, Modat M, Ourselin S, Hawkes DJ. A nonlinear biomechanical model based registration method for aligning prone and supine mr breast images. *IEEE transactions on medical imaging* 2014;33:682-694.
11. Teske H, Bartelheimer K, Bendl R, Stoiber EM, Giske K. Handling images of patient postures in arms up and arms down position using a biomechanical skeleton model. *Current Directions in Biomedical Engineering* 2017;3:469-472.
12. Teske H, Bartelheimer K, Meis J, Bendl R, Stoiber EM, Giske K. Construction of a biomechanical head and neck motion model as a guide to evaluation of deformable image registration. *Physics in Medicine & Biology* 2017;62:N271.
13. Pecorelli S, Zigliani L, Odicino F. Revised figo staging for carcinoma of the cervix. *International Journal of Gynecology & Obstetrics* 2009;105:107-108.
14. Weistrand O, Svensson S. The anaconda algorithm for deformable image registration in radiotherapy. *Medical physics* 2015;42:40-53.
15. Brock K, Sharpe M, Dawson L, Kim S, Jaffray D. Accuracy of finite element model-based multi-organ deformable image registration. *Medical physics* 2005;32:1647-1659.
16. Dice LR. Measures of the amount of ecologic association between species. *Ecology* 1945;26:297-302.
17. Huttenlocher DP, Klanderman G, Rucklidge WJ. Comparing images using the hausdorff distance. *Pattern Analysis and Machine Intelligence, IEEE Transactions on* 1993;15:850-863.
18. Brock KK, Mutic S, McNutt TR, Li H, Kessler ML. Use of image registration and fusion algorithms and techniques in radiotherapy: Report of the aapm radiation therapy committee task group no. 132. *Medical Physics* 2017.

5.3 ARTICLE : "DEFORMABLE IMAGE REGISTRATION FOR DOSE MAPPING BETWEEN EXTERNAL BEAM RADIOTHERAPY AND BRACHYTHERAPY FOR CERVICAL CANCER"

B. Rigaud *MSc* (1, 2) *, A. Klopp *MD, PhD* (3), S. Vedam *PhD* (4), A. Venkatesan *MD, PhD* (5), N. Taku, *MD, MSc* (3), A. Simon *PhD* (1), P. Haigron *PhD* (1), R. De Crevoisier *MD, PhD* (1), KK. Brock *PhD* (2), G. Cazoulat *PhD* (2) *

6. Univ Rennes, CLCC Eugène Marquis, Inserm, LTSI – UMR 1099, F-35000 Rennes, France
7. Department of Imaging Physics, The University of Texas MD Anderson Cancer Center, Houston, TX 77030, USA
8. Department of Radiation Oncology, The University of Texas MD Anderson Cancer Center, Houston, TX 77030, USA
9. Department of Radiation Physics, The University of Texas MD Anderson Cancer Center, Houston, TX 77030, USA
10. Department of Diagnostic Radiology, The University of Texas MD Anderson Cancer Center, Houston, TX 77030, USA

Abstract

For locally advanced cervical cancer (LACC), anatomy correspondence with and without applicator needs to be quantified to merge the delivered doses of external beam radiation therapy (EBRT) and brachytherapy (BT). This study proposed and evaluated different deformable image registration (DIR) methods for this application.

A total of 20 patients who underwent EBRT and BT for LACC were retrospectively analyzed. Each patient had a pre-BT CT at the EBRT boost planning (without BT applicator) and a CT and MRI for one BT fraction (with BT applicator). The DIR methods evaluated included the diffeomorphic Demons, commercial intensity and hybrid methods, and three different biomechanical models. The three biomechanical models considered different boundary conditions. The impact of the BT devices insertion on the anatomy was quantified. DIR method performances were quantified using geometric criteria between the original and deformed contours. The BT dose was deformed toward the pre-CT BT by each DIR methods. The impact of the boundary condition to drive the biomechanical model was evaluated based on the deformation vector field and dose differences. The GEC-ESTRO guideline dose indices were also reported.

Large organ displacements, deformations, and volume variations were observed between the pre-BT and BT anatomies. Rigid registration and intensity-based DIR methods resulted in poor geometric accuracy. Biomechanical models provided mean DSC of 0.96 for all the organs. By considering the cervix-uterus as one single structure, biomechanical models provided mean DSC of 0.88 and 0.94 for the cervix and uterus, respectively. The deformed doses were represented for each DIR method.

Standard DIR methods should not be used for this application. The biomechanical model-based approach which modeled the cervix-uterus as one structure provided the most realistic deformations to propagate the BT dose toward the EBRT boost anatomy.

5.3.1 INTRODUCTION

The standard treatment of locally advanced cervical cancer (LACC) is based on a combination of chemo-radiotherapy and brachytherapy. External beam radiation therapy (EBRT) with chemotherapy represents the first step with the aim to deliver a prescribed dose to the planning target volume (PTV) encompassing the cervix-uterus, nodes and vagina depending on the international federation of gynecology and obstetrics (FIGO) classification. The brachytherapy (BT) represents the second part of the treatment with the aim to locally irradiate the residual tumor using an inserted applicator, from one to multiple fractions.

Large organ deformations are known to occur during the course of treatment, leading to uncertainties in the total delivered dose distribution. During EBRT, the large number of daily treatment fractions increases the risk of facing different anatomical configurations. Target displacements and deformations have been reported to be possibly superior to 20 mm for the cervix [1,2] and be up to 48 mm for the uterus [3,4]. The causes of these anatomical deformations have been clearly defined. Uterine motion is mostly related to bladder filling, while vagina and cervix motion is linked to rectum filling [5-11]. Tumor shrinking, due to EBRT treatment response, has also been reported with a mean decrease of 63% (up to 87%) of the cervix volume at the end of EBRT [12-15]. Those anatomical variations during EBRT increase the risk of tumor underdosage and organ at risk overdosage. For this purpose, different strategies have been proposed, from the definition of an internal target volume to planning libraries [16-26].

During BT, less organ displacements and deformations are expected due to the reduced number of fractions and strict recommendations in patient preparation, *e.g.* applicator insertion or control of the bladder filling with a Foley balloon. Moreover, a new treatment plan is often developed at each fraction in case of applicator re-insertion [27]. Still, the consequences of these anatomical deformations in a context of steep-dose gradients are not fully identified. A multicenter study highlighted the impact of organ and target deformation during and between BT fractions for 120 patients [28]. The endpoint of the study was the variation of the maximum dose in a 2 cc volume (D2cc). In average the deviation was found to be inferior to 5% but large uncertainties were observed for individuals with a standard deviation superior to 20%. Such D2cc deviations can mainly be explained by organ filling variation between BT insertions and applicator position [29,30]. For fractionated BT delivery, investigations are still ongoing to determine the necessity and accuracy of deformable image registration (DIR) to estimate the delivered dose in comparison with the state-of-the-art direct dose addition (DDA) of the dose volume histogram (DVH) indexes [31-38]. The majority of the studies demonstrate an overestimation of the deviation by the DDA of the DVH compared to DIR.

DIR methods have also been proposed to map the EBRT planning dose to the anatomy of the first BT fraction, for planning purpose and toxicity prediction. The recommended approach is to consider the EBRT dose to the organ at risk (OAR) as uniform and thus to add the EBRT prescribed dose to the BT prescribed dose [39]. However, some studies showed the ability of DIR to propagate the planning EBRT dose onto the BT anatomy to estimate more accurately the local dose to the OAR and thus guide the BT planning procedure [37,40]. The clinical impact of DIR for this application still needs to be investigated, especially in case of planning with nodal boost [41] or highly conformal strategy.

The quantification of the total delivered dose, after EBRT and BT, needs to be investigated for LACC in order to better understand and predict OAR toxicity risks [42]. For this, tissue deformations induced by the applicator insertion and the Foley balloon need to be correctly modeled by the DIR method. Registration of images with and without applicator is challenging for standard DIR algorithms because of image content differences but also because of complex inter-organ motion such as sliding which creates discontinuities in the actual deformation vector field (DVF). A limited number of methods have been proposed for the registration of such images [37,40,43-45]. Christensen *et al* proposed the first study to investigate the use of DIR to estimate the deformation between CT with and without BT applicator. In this study, a fluid-based DIR method with an optional landmark-based initialization was proposed to register the labeled images. Vásquez Osorio *et al* proposed another workflow to map the anatomy of the planning MRI before RT onto the first MRI of the BT. In their study, each organ was independently aligned using the thin plate spline robust point matching (TPS-RPM) method [46,47]. A dense DVF was then defined by merging the organs DVF using a thin plate spline transformation that allows discontinuities resulting from sliding organs. Berendsen *et al* proposed and evaluated the use of a free-form deformation DIR method with a penalty term to simulate the applicator removal between pairs of MRI. Kim *et al* used a commercially available B-spline-based DIR with mutual information to match the planning CT of EBRT to each BT MRI. van Heerden *et al* used the TPS-RPM method to deform the rectum and bladder from the EBRT anatomy to the BT anatomy.

Few details were reported in the above mentioned studies about the impact of the BT applicator and Foley balloon insertion on the anatomy. In addition, the deformations were computed between the anatomies at the time of planning of each subpart of the treatment (EBRT and BT) and therefore included tumor shrinking resulting from the treatment response. Considering an image acquired closer to the time of BT should yield to a better model of the anatomical deformations caused by the BT applicator insertion. In our knowledge, no study has showed the results of deforming a BT dose toward an anatomy without applicator. Also, no study evaluated the ability of the DIR method to separately quantify the deformation of the cervix and uterus which is of high interest in a context of highly conformal radiation treatment.

This study though to provide a quantitative analysis of the deformation of the cervical cancer anatomy (target organ and OAR) induced by the BT applicator and Foley balloon insertion. For this purpose, the anatomies on CT scans with and without BT applicator were put in correspondence with DIR. Different DIR methods were considered and evaluated. In particular, a biomechanical model-based DIR approach is proposed and different surface projection methods are investigated for the determination of boundary conditions. Finally, the use of each DIR method for the mapping of the BT dose onto a CT without applicator is illustrated. Figure 5-6 depicts the workflow of the study.

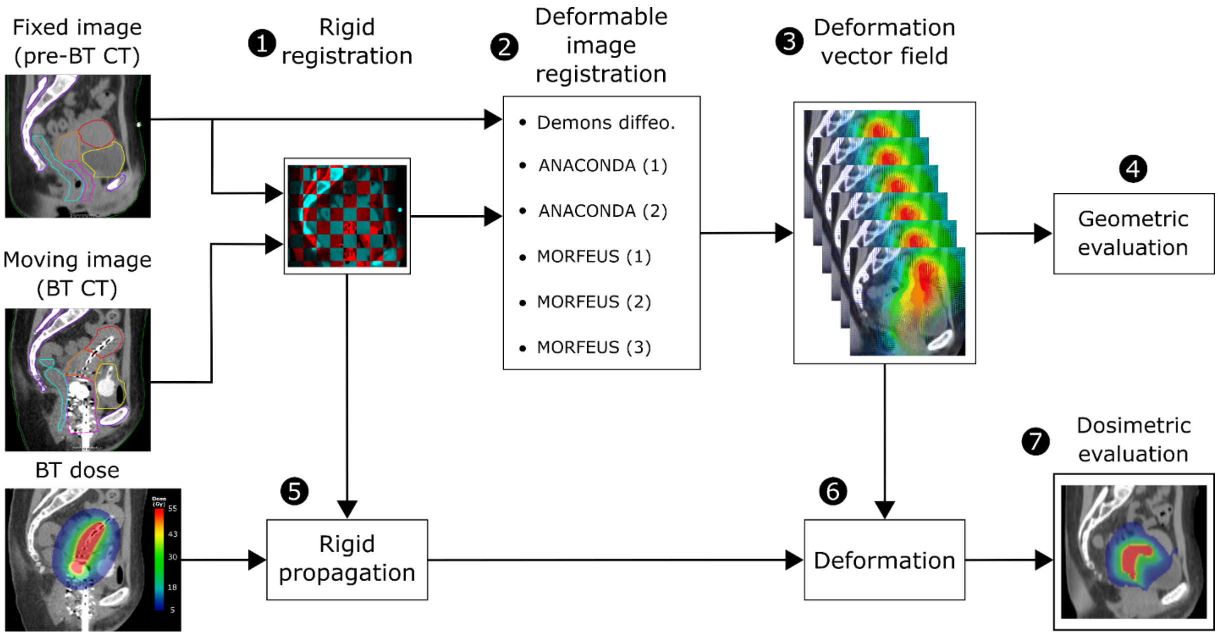

Figure 5-6: Workflow of the study

For each patient, the BT CT is aligned on the pre-BT CT using bone-based rigid registration (1). Different DIR methods (2) are used to estimate the DVF (3) that allow to deform the BT CT toward the pre-BT CT. A geometric evaluation on the volume of interests is done to quantify the geometric performances of the DIR methods (4). The BT dose, optimized on the BT CT, is then rigidly propagated (5) and deformed (6) on the pre-BT CT thanks to the rigid transformation and the DVF. Dosimetric uncertainties can be observed by comparing the different deformed doses according to each DIR method (7). CT: computed tomography; BT: brachytherapy; MRI: magnetic resonance imaging;

5.3.2 MATERIALS AND METHODS

5.3.2.1 Patients, tumors, and treatment

20 patients treated for LACC between 2013 and 2018 were retrospectively analyzed. Stage distribution, according to the FIGO classification [48], was as follows: IB1-2, n= 4; IIA-B, n= 7; IIIA-B-C, n= 6; and IVA-B, n= 3. All patients were treated with a combination of EBRT, chemotherapy and pulse-dose-rate (PDR) BT. The EBRT corresponded to a step & shoot IMRT planned using a commercial treatment planning system (TPS) (Pinnacle 9.4, Philips Medical Systems, Cleveland, OH). The dose constraints to the tumor were 47.25 Gy to the isocenter of the pelvis using four 18 MV beams and a mean dose of 53 Gy to the nodal gross tumor volume (GTV) using nine 6 MV beams when a nodal boost was prescribed. The pulsed dose rate (PDR) BT was planned using the Oncentra TPS and varied between 13 – 25 Gy at the points A. Patients were treated with an ovoid/tandem (N=15) or cylinder/tandem applicator (N=5). Each BT 3D dose array was multiplied by the number of pulses (range: 40 – 60) to represent the BT prescription. The chemotherapy was delivered using cisplatin at 40 mg/m^2.

5.3.2.2 Patient imaging

For each patient, a CT scan was acquired in the supine position from the thorax to the femoral heads at the time of the EBRT boost planning or after the EBRT, named “pre-BT CT”. At the considered fraction of the PDR-BT, the patients had a MRI and a CT scan (“BT MRI” and “BT CT”) with the BT applicator inserted. The BT MRI was acquired in the supine position from the L5 vertebrae to the femoral heads on average 9 days after the pre-BT CT (range: 1 – 25 days). The BT CT was acquired in the supine position from the L4 vertebrae to the femoral heads for BT planning 1 hour after the BT MRI. Because the MRIs were not always available for the first BT fraction, the first BT fraction was used for 14 patients and the second BT fraction was used for 6 patients. The BT planning dose distributions were collected for 16 patients only as software compatibility issues were encountered for the 4 other patients.

5.3.2.3 Organs contouring

The organs were manually delineated by the same observer on the pre-BT CT and on the BT images using a commercial TPS (RayStation v7, RaySearch Laboratories, Stockholm, Sweden). All contours were first delineated on the BT MRI (with applicator) which presents the best definition of organ boundaries. The resulting contours were rigidly aligned according to the bony anatomy on the BT CT (with applicator) using the integrated semi-automatic rigid registration available on the TPS. Minor contour edits were made according to anatomy changes between the image acquisitions. The contours were then delineated on the pre-BT CT (without applicator) with the help of the BT MRI in order to be consistent between anatomical delimitations.

The following organs were considered: the corpus of the uterus, from the uterus isthmus to the fundus of the uterus; the cervix, from the uterus isthmus to the superior part of the applicator ovoids on the images with the applicator; the vagina, from the cervix to 1 cm bellow the pubic bone if applicable; the bladder encompassing the start of the urethra; the rectum from the anal canal to the sigmoid bend; the visible bony structures (pelvic bone and vertebrae body); the external body. Figure 5-7 represents the images and contours for one patient.

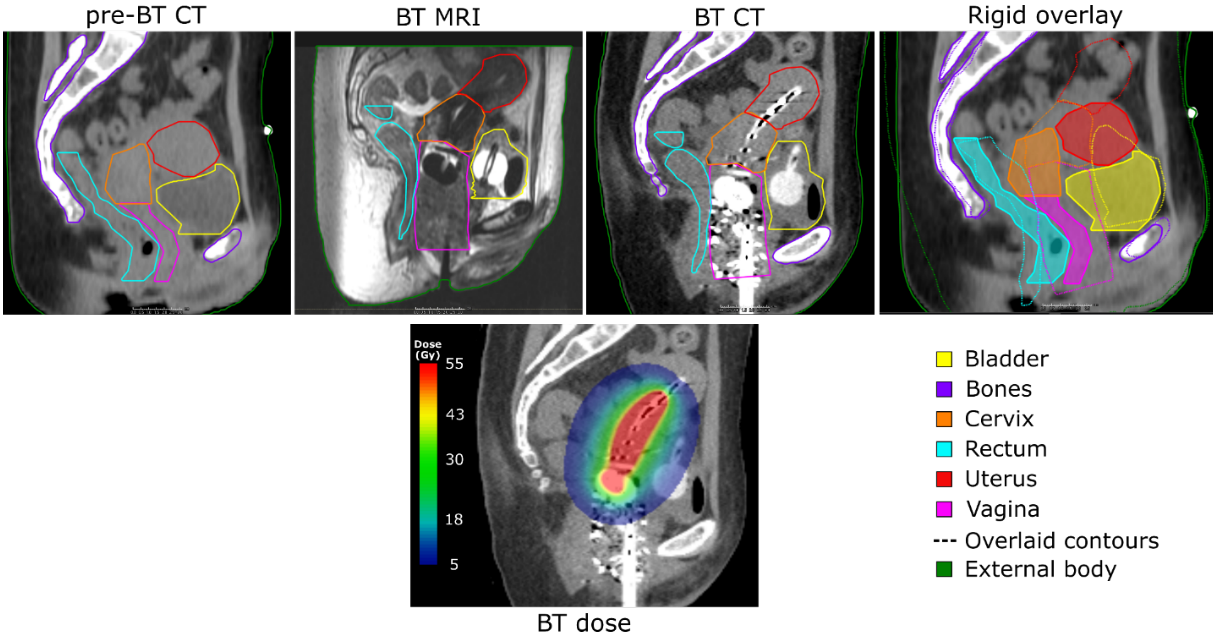

Figure 5-7: Example of the images (sagittal slices) and organ delineations for one patient of the study

The anatomy of the patient prior and at the time of BT is represented on the pre-BT CT, BT MRI and BT CT. An example of the deformation induced by the applicator insertion is represented by the overlay of the anatomy after rigid registration. For this patient, could be observed: a deformation of the uterus in the superior direction, a rotational deformation of the cervix, an increase of the volume of the vagina, a flatten rectum toward the posterior direction and a shifted bladder in the anterior direction. These deformations are due to the BT applicator and Foley balloon insertion. CT: computed tomography; BT: brachytherapy; MRI: magnetic resonance imaging;

5.3.2.4 Rigid registration

The rigid registration was performed to align the bones of the BT CT anatomy to the bones of the pre-BT CT anatomy using 6 degrees of freedom: 3 translations and 3 rotations parameters. Two rigid registrations were used in this study: one outside the TPS for the initialization of the in-house DIR methods and the one integrated on the TPS to help the delineation procedure and initialize the DIR methods of the TPS. The two rigid registration algorithms provided similar alignments. Considering the algorithm outside the TPS, bone structures were automatically segmented using a fixed threshold and were used for the estimation of the rigid transformation. The algorithm used the sum of square difference (SSD) as metric and the optimal transformation was defined through gradient descent using the ITK library.

5.3.2.5 Intensity-based DIR algorithm

5.3.2.5.1 Demons registration

The Demons algorithm was considered as one intensity-based DIR method [49]. In this study, the diffeomorphic variant was used with the SSD metric, a Gaussian sigma of 2 mm and 3 resolutions with 25, 20 and 15 iterations [50]. This method allowed a quick estimate of an invertible DVF.

5.3.2.5.2 ANACONDA registration

The ANAtomically CONstrained Deformation Algorithm (ANACONDA) method was also considered in this study as intensity-based and hybrid-based (*i.e.* intensity and contour-based method) method [51]. The ANACONDA method generates a smooth DVF optimized by the quasi-Newton algorithm and guided by the correlation coefficient between the images. The DVF is regularized by the weighted Dirichlet energy, automatically influenced by the determinant of the Jacobian. The DIR method is considered hybrid when constrained by organ contours, delineated on both images prior to the DIR process. Each organ contour deformation is computed using its signed distance map. In the following, the ANACONDA (1) method stands for the intensity-based only method and the ANACONDA (2) stands for the hybrid method with constraints on all the contours. These registrations were performed in the TPS (RayStation v7, RaySearch Laboratories, Stockholm, Sweden) using the default settings.

5.3.2.6 MORFEUS, a biomechanical model-based DIR

The biomechanical model-based DIR algorithm, MORFEUS [52], which relies on contours only, allows the generation of a dense DVF from the reference image to the moving image coordinates. First, triangular surface meshes of the organ delineations are generated and a deformable mesh registration method is used to determine boundary conditions. Then, a tetrahedral finite-element model (FEM) including all the structures of interest is built and a finite element analysis (FEA) is performed (Radioss, HyperWorks, Altair Engineering, Troy, MI) to solve the displacements of all the volumetric mesh nodes in order to generate a dense DVF. The implemented MORFEUS workflow is depicted in Figure 5-8 and detailed below.

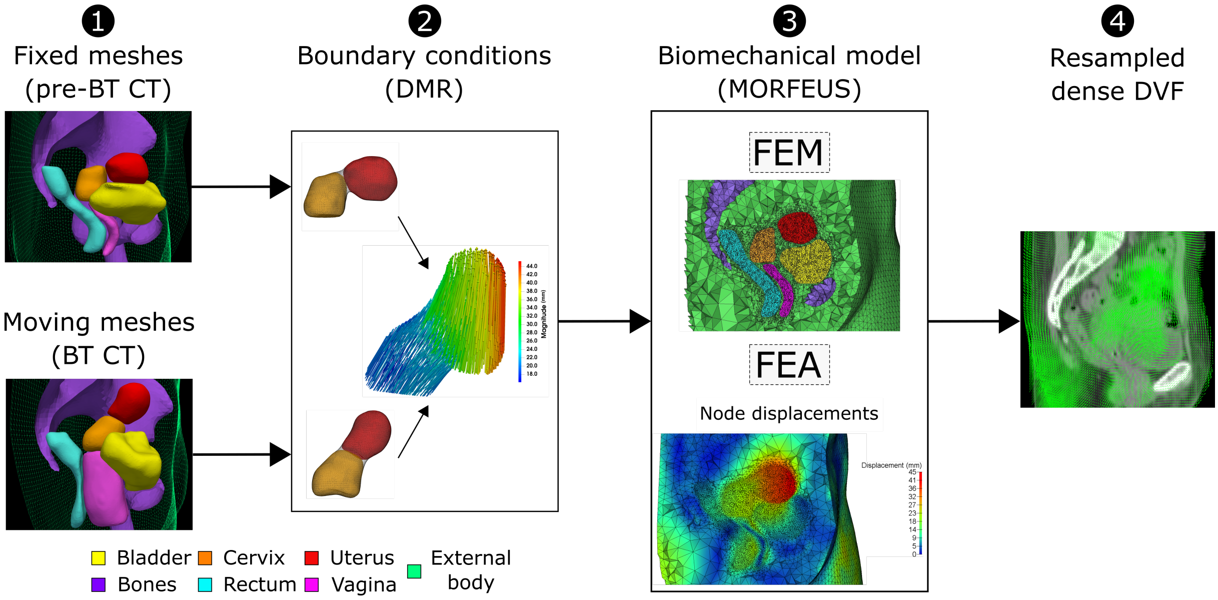

Figure 5-8: Workflow for the biomechanical model-based DIR using DMR and MORFEUS

For each patient after rigid registration alignment, triangle meshes of the organ delineations on the pre-BT and at the BT anatomies are defined (1). For each organ mesh, the boundary conditions are estimated using the DMR method (section 5.3.2.6.2.2) (2). Using the organ meshes and their respective boundary conditions, the biomechanical model can be defined (section 5.3.2.6.3) (3). After optimization, the node displacements of the model can be resampled on the pre-BT CT to define the DVF (4). CT: computed tomography; BT: brachytherapy; MRI: magnetic resonance imaging; DMR: deformable mesh registration; FEM: finite element model; FEA: finite element analysis; DVF: deformation vector field;

5.3.2.6.1 Organ triangle meshes

The organ contours have been represented as triangular surfaces. For this purpose, the binary masks were converted to meshes using an edge detection method [53]. The dense triangular surfaces were then smoothed using Taubin filter [54], “shrink-wrapped” using a commercial finite element modeling software (HyperMesh v11, Altair HyperWorks, Altair Engineering Inc., Troy, MI), decimated and re-meshed using approximated centroidal Voronoi diagrams method [55]. The resulting triangular surfaces represent the volumes of interest as smooth meshes with an arbitrary chosen number of equidistant points (*cf.* Table 5-2).

5.3.2.6.2 Determination of boundary conditions

5.3.2.6.2.1 Centerline initialization

Considering the large deformations and displacements of the organs due to applicator insertion, the use of the centerline of the organs was investigated to define a first alignment and gross deformation estimation. First, the centerlines of each fixed and moving meshes were defined by a spline of 50 points. Second, a thin plate spline transformation was computed by using the paired spline centerline points as anchor points. Finally, the transformation was used to align and deform the moving mesh toward the fixed mesh. This pre-deformed mesh was then used as initialization for more complex surface projection approaches.

The organ centerlines were automatically defined as follow:

Vagina: a spline was defined between the basis centroid, volume centroid and the centroid of the closest points of the cervix; cervix: a spline was defined between the centroid of the closest points of the vagina, the volume centroid and the centroid of the closest points of the uterus; uterus: a spline was defined between the centroid of the closest points of the cervix and the fundus of the uterus; rectum: a spline was defined using the contour centroids every 10 mm slices, the border centroids were attached to the closest point of the mesh.

5.3.2.6.2.2 Deformable mesh registration

The organ mesh deformations were estimated independently and served as boundary conditions for the biomechanical model-based DIR. This step is done by using the deformable mesh registration (DMR) method [26] in order to estimate a non-rigid transformation represented by a point-to-point correspondence. The DMR method aims to estimate the forward DVF, representing the elastic transformation *T* between the fixed and the moving shapes (S_{fixed}, S_{moving}). This iterative process is expressed by the following equations:

$$DVF = DVF + G(\mu \times DVF_{step}) \tag{5-7}$$

$$S_{warped} = T(S_{moving}, DVF) \tag{5-8}$$

At each iteration, the S_{moving} shape is warped (S_{warped}) by the *DVF*, which is updated by means of the DVF_{step}. A point-to-point correspondence is estimated at each iteration, between S_{fixed} and S_{warped}, using a shape context descriptor [56] and a normalized geodesic distance metric [57]. The geodesic distance, according to a source point (*cf. 5.3.2.6.2.3*), enables to add a priori information to drive the correspondences. The DVF_{step} is computed with a thin plate spline transformation to interpolate the point-to-point correspondences. The DVF_{step} is then smoothed by a Gaussian kernel (*G*) and weighted by the factor $\mu \in]0, 1]$ ($\mu = 1$ at the last iteration). At each iteration, the shape descriptors are computed on both meshes and a global cost matrix is computed with each descriptor's weighted normalized cost matrix. The symmetric point-to-point correspondences between S_{fixed} and S_{moving} were obtained by the Hungarian optimization method on the global cost matrix [58]. A topological constraint filter, relying on the Euclidean distances between the neighbors of each point with and without the correspondence, was used to remove unrealistic matching. The method was also implemented following a multiresolution scheme that considered different factors of the Taubin filter [54].

5.3.2.6.2.3 Deformable mesh registration parameters

Table 5-2 reports the different parameters used to define the methods to compute the boundary conditions (BC) for the biomechanical model (MORFEUS). A total of three DMR methods were defined depending on the organs (*e.g.* cervix and uterus combined), the descriptors (*e.g.* geodesic distance) or the initialization (*e.g.* centerline):

DMR (1) for MORFEUS (1): the geodesic distance was considered for the vagina, cervix and uterus. For the vagina the source point was the basis centroid. For the cervix and the uterus, the source point was the centroid of the closest points of the vagina and cervix, respectively. No centerline initializations were performed.

DMR (2) for MORFEUS (2): no geodesic distance was used. The centerlines of the rectum, vagina, cervix and uterus were used to deform the moving meshes as an initialization.

DMR (3) for MORFEUS (3): no geodesic distance was used. The cervix and the uterus were combined as one single mesh. The centerlines of the rectum, vagina, and cervix-uterus were used to deform the moving meshes as an initialization.

For each organ of each patient, three DVF were estimated to derive boundary conditions in three biomechanical models (MORFEUS (1), MORFEUS (2) and MORFEUS (3)). For the body, bones and bladder, the boundary conditions where the same for all methods (*i.e.* DMR with the shape context descriptor and without geodesic distance).

Table 5-2: Definition of the different DMR for each organ's boundary condition. DMR: deformable mesh registration; Y: Yes; N: No;

DMR parameters	Organs						
	Body	Bones	Bladder	Cervix	Rectum	Uterus	Vagina
Number of points	5000	5000	2000	2000	2000	2000	2000
Resolution*iteration	2*10	2*10	3*20	3*20	3*20	3*20	3*20
Geodesic distance	No	No	No	DMR (1): Y DMR (2,3): N	No	DMR (1): Y DMR (2,3): N	DMR (1): Y DMR (2,3): N
Ponderation factor (α)	1	1	1	DMR (1): 0.5 DMR (2,3): 1	1	DMR (1): 0.5 DMR (2,3): 1	DMR (1): 0.5 DMR (2,3): 1
Gaussian kernel (σ)	[8;4]	[8;4]	[8;4;2]	[8;4;2]	[8;4;2]	[8;4;2]	[8;4;2]
Update factor (μ)	0.50	0.50	0.20	0.20	0.20	0.20	0.20
Topological constraint factor (τ)	[0.25;0.5]	[0.25;0.5]	[0.25;0.5;1]	[0.25;0.5;1]	[0.25;0.5;1]	[0.25;0.5;1]	[0.25;0.5;1]
Taubin filter passband	[0.01;1]	[0.01;1]	[0.01;0.1;1]	[0.01;0.1;1]	[0.01;0.1;1]	[0.01;0.1;1]	[0.01;0.1;1]
Centerline initialization	No	No	No	DMR (1): N DMR (2,3): Y	DMR (1): N DMR (2,3): Y	DMR (1): N DMR (2,3): Y	DMR (1): N DMR (2,3): Y

5.3.2.6.3 *Finite element model*

For each patient a FEM was defined considering the body, bones (pelvic bones and vertebrae body), bladder, rectum, vagina, cervix and uterus. The FEM considered seven triangular surfaces for MORFEUS (1) and (2) and six triangular surfaces for MORFEUS (3), since the cervix and uterus were combined for the latter. The overlapping and intersections between surfaces were removed by using an in-house method that deformed one of the surfaces to add a 2 mm margin between the organs. The organs with highest priority were those which were part of the clinical target volume (*i.e.* CTV: vagina, cervix and uterus) and the organs with the lowest priority were the bones and body surfaces. Each triangular surfaces were converted into four-node tetrahedral mesh volumes.

A linear elastic material model was used to characterize the FEM. The material properties were homogeneously assigned to the elements of each organ in the four-node tetrahedral FEM. The properties of each organ are shown in the Table 5-3 and were selected based on observations and from the literature [59-61].

Table 5-3: Linear elastic material properties of the organs for the biomechanical models

The Young's modulus is the ratio of stress to strain describing the ability of the material to be stretched or compressed in its longitudinal direction (*i.e.* stiffness). The Poisson's ratio is the ratio of transverse contraction strain to longitudinal extension strain in the direction of stretching force. A Poisson's ratio of 0.5 represents an incompressible material.

Organ	Density (ton/m^3)	Young's modulus (E) (KPa)	Poisson's ratio (ν)
Body	1.050	15	0.400
Bones	1.920	10e6	0.499
Bladder	1.030	10	0.490
Cervix	1.030	5	0.470
Rectum	1.030	10	0.450
Uterus	1.030	5	0.470
Vagina	1.030	5	0.430

5.3.2.6.4 *Finite element analysis*

The boundary conditions of each triangular surface were computed using the different DMR methods (*cf.* section 5.3.2.6.2.3). The FEA was then performed with Radioss (Altair HyperWorks v11.0, Altair Engineering Inc., Troy, MI) to compute the node displacements of each tetrahedral mesh volume. The discontinuities between neighbor organs should allow to simulate the peritoneum, recto-uterine pouch and vesico-uterine pouch behaviors, which are membranes and gap between soft tissues in the pelvic area. The node displacements were resampled on an image grid. Two DVF were defined for each biomechanical model-based DIR: one resampled to 1.25 mm slice thickness for dense triangular surface deformation and one resampled to the 2.5 mm slice thickness of the pre-BT CT for dose deformation.

5.3.2.7 Morphological Analysis and Evaluation

5.3.2.7.1 Geometric evaluation

The impact of the BT applicator and Foley balloon insertion in term of soft tissue deformation was analyzed by reporting the volume variation and the centroid displacement between the pre-BT CT and BT CT contours. The centroid displacement was thus reported relatively to the bone-based rigid registration. The geometric criteria to assess the performances of the DIR methods were the Dice similarity coefficient (DSC) [62], the Hausdorff distance (HD) [63] and the distance to agreement (DTA) (*i.e.* average distance between surface points), between the reference and propagated organ surfaces. The two most distinct biomechanical model-based DIR methods (MORFEUS (1) and MORFEUS (3)) were compared in term of the average magnitude of their DVF difference.

5.3.2.7.2 Dosimetric analysis

For each tested method, the mean doses were reported for the planning dose on the BT CT and for the deformed dose on the pre-BT CT, for each organ. The GEC-ESTRO guidelines DVH indices were reported for the BT planning dose and the deformed dose by one selected DIR method [39,64]. The indices were the D100% and D90% for the vagina, cervix and uterus (DX% defining the minimum dose delivered to X% of the volume) and the D2cc and D1cc for the bladder and rectum (DXcc meaning the minimal received dose by X cc of the volume). The deformed doses by the two most distinct biomechanical model-based DIR methods (MORFEUS (1) and MORFEUS (3)) were compared in term of the absolute mean and median differences and the absolute mean and max DVH differences. The DVH of the vagina, cervix and uterus were computed considering the volume of the BT device (*i.e.* applicator, mold, cylinder, tandem, and ring). The dose indices and metrics were reported for 16 cases.

5.3.2.7.3 Statistical analysis

The geometric parameters were compared using the non-parametric Wilcoxon signed-rank test. This test allows to compare both paired and unpaired observations. The result of the test enables to define if a method provide a significant improvement compared to another method. A test was considered significant if the resulting p-value was inferior to 0.05. The data analysis was done using R software.

5.3.3 RESULTS

5.3.3.1 Deformation analysis

Table 5-4 represents the mean (min – max) volumes of the organs of interest prior to the BT and at the time of the BT. The difference of volume induced by the applicator insertion and BT protocol is also represented relatively to the anatomy without applicator. The vagina volume was significantly larger when the applicator was inserted. The Foley balloon induced a reduction of the bladder size of 15.8%.

Table 5-4: Volume of the organs of interest

The mean (min – max) volumes of each organ are reported prior and at the time of BT. The volume differences are reported relatively to the volume prior to BT. The * indicates a significant difference (p-value< 0.001, two-sided Wilcoxon test). BT: brachytherapy

Organ	Mean (min – max) volume		
	Prior to BT (cc)	At BT (cc)	BT - prior (%)
Rectum	54.2 (22.5 – 136)	47.2 (24.7 – 95.8)	4.2 (-67.4 – 98.1)
Bladder	102.6 (31.9 – 218.2)	86.9 (62.6 – 152.8)	15.8 (-68.9 – 379.0)
Vagina	24.4 (6.7 – 123.0)	116.8 (36.2 – 219.9)	552.6 (1.5 – 1561.6) *
Cervix	32.2 (10.8 – 59.2)	31.0 (10.4 – 55.9)	-1.4 (-29.4 – 17.8)
Uterus	67.6 (9.3 – 172.8)	63.4 (11.4 – 146.5)	-2.2 (-34.3 – 21.6)

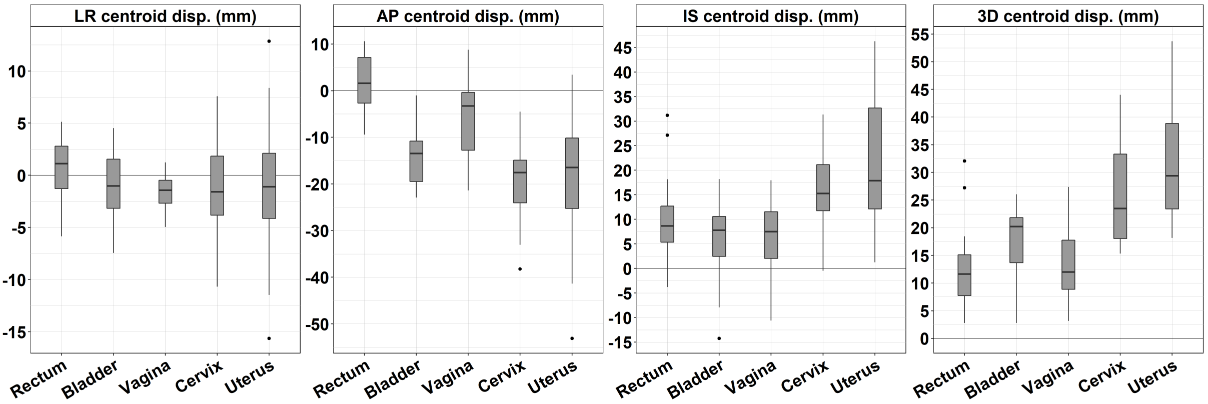

Figure 5-9: Centroid displacement of the volume of interests

The displacements of the centroid from the pre-BT to the BT anatomy of each organ are reported using the bone-based rigid registration. The displacements are reported in mm in the left-right (LR), anterior-posterior (AP), inferior-superior (IS) directions and 3D magnitude as negative-positive. The boxplots are computed on 20 values. The bold line represents the median, the boxes represent the 25th and 75th percentiles and the whiskers represent the larger values no further than the length of the box. Individual points are considered as outliers.

Figure 5-9 represents the centroid displacement in the left-right (LR), anterior-posterior (AP), inferior-superior (IS) directions and 3D amplitude of each organ of the cohort as boxplots. The applicator insertion induced the largest mean (min – max) 3D centroid displacement for the uterus and cervix of 32.5 mm (18.2 – 53.7) and 26.5 mm (15.3 – 44.0), respectively. Considering the impact of both the applicator and Foley balloon on the bladder, a mean (min – max) centroid displacement of 14.3 mm (1.0 – 22.9) in the anterior direction was also observed.

No statistical differences were observed for the centroid displacements between the groups with ovoid/tandem and cylinder/tandem applicator. Patients treated with ovoid/tandem applicator (n= 15) had a mean (min – max) increase of the vagina volume of 626.5% (1.6 – 1561.6) while patients treated with cylinder/tandem applicator (n= 5) had an increase of 331% (164.0 – 745.0). This volume difference was, however, not statistically significant (unpaired Wilcoxon test, p= 0.058). The difference was mainly explained by the presence of the mold inside the vagina to reduce applicator motion. In addition, the difference may be patient dependent since the size of the applicator was defined according to the patient anatomy.

5.3.3.2 Geometric comparison

5.3.3.2.1 DMR for boundary conditions

Figure 5-10 represents the geometric performances of the DMR for each organ in term of distance to agreement (DTA), Hausdorff distance (HD) and Dice similarity coefficient (DSC). Compared to the MORFEUS BC (1), the MORFEUS BC (2) and (3) which both included an initialization with the centerline provided a significant improvement for the DSC and DTA of the rectum and vagina, respectively. The initialization with the centerline also allowed to significantly improve the cervix metrics and DTA of the uterus. However, all DMR provided surface matching metrics considered as excellent. The mean (min – max) DSC for the boundary conditions of the body and the bones were 0.99 (0.99 – 0.99) and 0.99 (0.98 – 0.99), respectively.

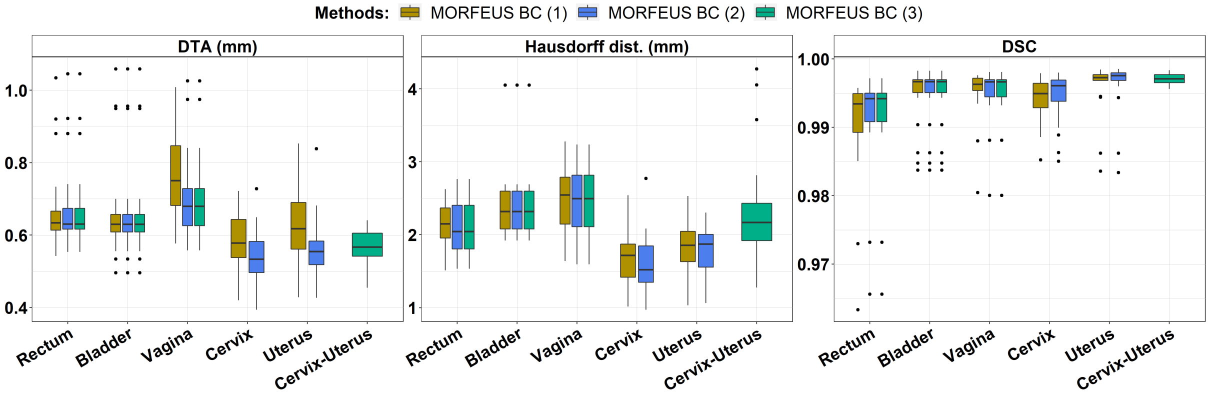

Figure 5-10: DMR performances to compute the boundary conditions for the biomechanical model-based DIR

Each facet represents a metric with its value on the y-axis and the considered organ on the x-axis. Each color represents a DMR method. The three DMR methods were the same for the bladder. For the DTA and Hausdorff distance, a lower value means a better correspondence. For the DSC, a higher value means a better correspondence. The boxplots are computed on 20 values. The bold line represents the median, the boxes represent the 25th and 75th percentiles and the whiskers represent the larger values no further than the length of the box. Individual points are considered as outliers. DTA: distance to agreement; DSC: Dice similarity coefficient; DMR: deformable mesh registration; BC: boundary condition

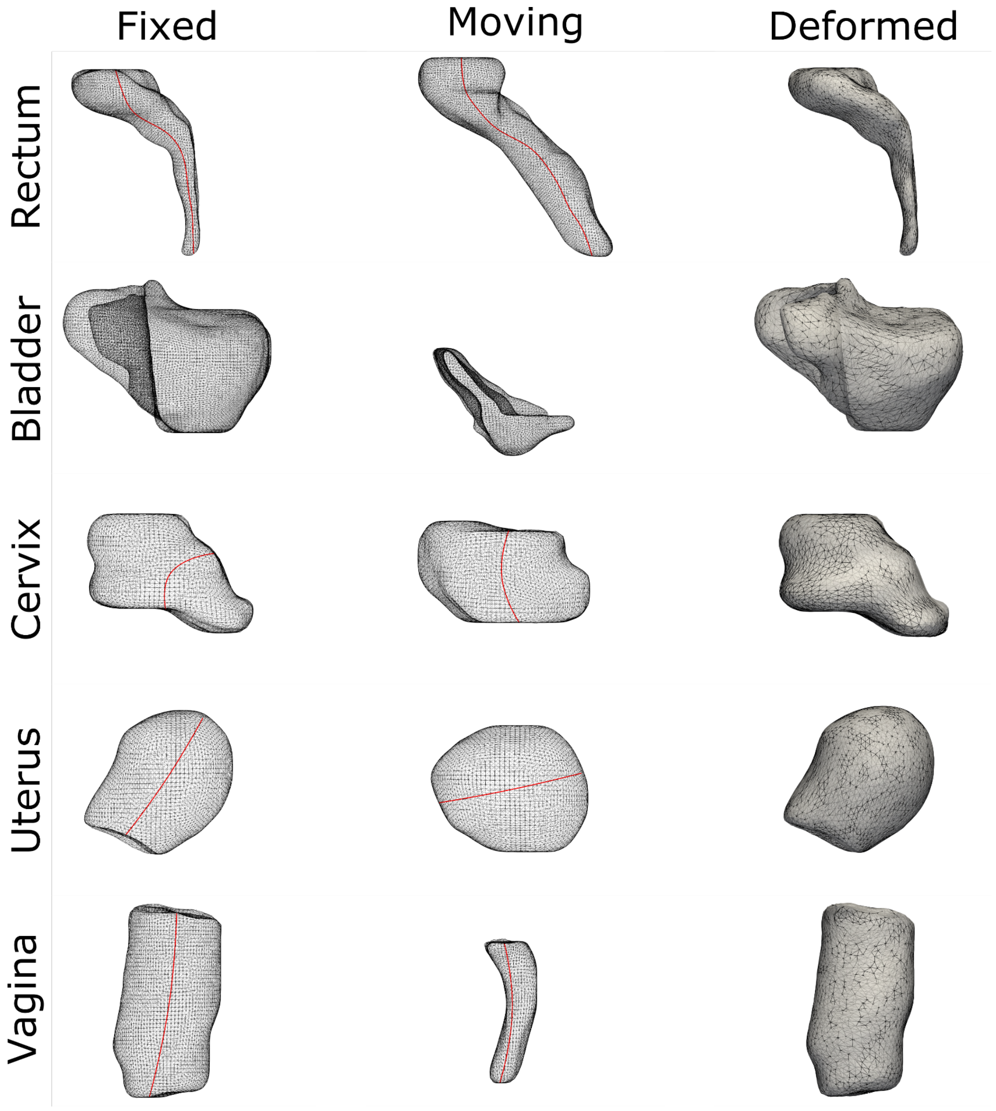

Figure 5-11: Example of DMR results

To obtain the inverse transformation, the fixed and moving images used for the DMR are the BT CT and pre-BT CT anatomy, respectively. The left column represents the organ surfaces of the fixed image (with applicator). The middle column represents the corresponding organ surfaces of the moving image (without applicator). The right column displays the overlay of the fixed surfaces and the wireframe of the deformed moving surfaces. The rectum and the vagina examples are computed with MORFEUS BC (3). The cervix and the uterus examples are computed with MORFEUS BC (2). The bladder is the same regardless of the MORFEUS BC. The red lines represent the centerlines.

Figure 5-11 represents examples of DMR results with the best method for each organ demonstrating the ability of the DMR methods to match organ surfaces presenting extreme deformations.

5.3.3.2.2 Methods comparison

Figure 5-12 represents the geometric evaluation of the DIR methods to propagate the organ meshes in term of DTA, HD and DSC. The bone-based rigid registration provided a mean DSC of 0.41 for the bladder, 0.41 for the rectum, 0.16 for the cervix, 0.21 for the uterus and 0.26 for the vagina. Compared to the rigid registration, ANACONDA (1), which is only based on image intensities, significantly improved only the DTA and DSC of the bladder, vagina and uterus, and the DSC of the cervix. ANACONDA (2) significantly improved all the metrics compared to rigid registration except the HD of the rectum and the vagina. All other DIR methods improved all the geometric metrics compared to rigid registration. The diffeomorphic Demons significantly improved all metrics for all organs compared to ANACONDA (1). This difference can be explained as the diffeomorphic Demons estimated higher non-linear deformation inside the body while ANACONDA (1) was more conservative.

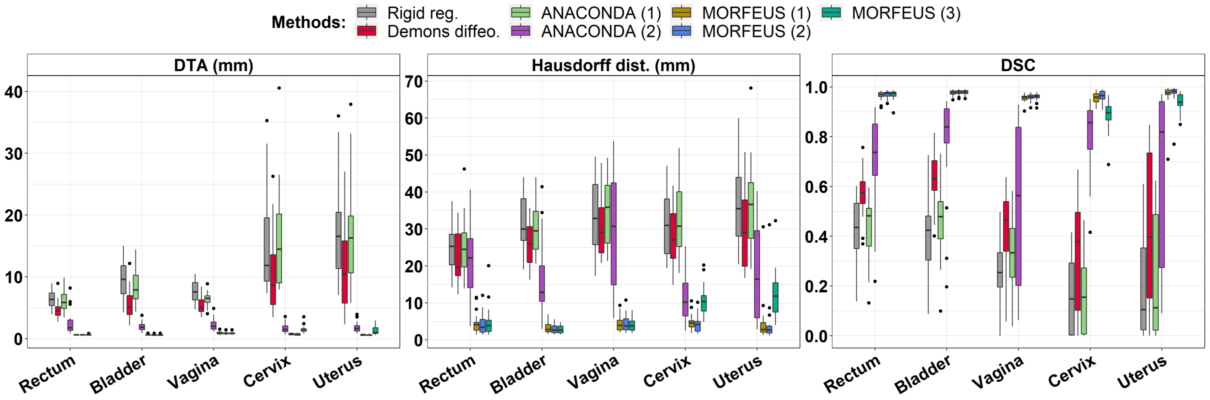

Figure 5-12: Geometric evaluation of the DIR methods

Each facet represents a metric with its value on the y-axis and the considered organ on the x-axis. Each color represents a DIR method. For the DTA and Hausdorff distance, a lower value means a better correspondence. For the DSC, a higher value means a better correspondence. The boxplots are computed on 20 values. The bold line represents the median, the boxes represent the 25th and 75th percentiles and the whiskers represent the larger values no further than the length of the box. Individual points are considered as outliers. DTA: distance to agreement; DSC: Dice similarity coefficient; DIR: deformable image registration;

Considering the biomechanical model-based DIR methods, only the DTA and HD were not significantly better for the cervix and uterus when comparing ANACONDA (2) and MORFEUS (3). Otherwise, all biomechanical model-based DIR methods significantly performed better than other DIR methods. The MORFEUS (3) methods, which combined the cervix-uterus, significantly performed worse than the two other biomechanical model-based DIR methods for the cervix and uterus because of the non-inclusion in the model of the separation surface between those two structures. However, for the MORFEUS (3), the resulting DSC of the cervix and uterus were still very high with values of 0.88 (0.69 – 0.97) and 0.94 (0.85 – 0.98), respectively.

Table 5-5 represents the comparison between the MORFEUS (1) and the MORFEUS (3) methods considering the mean (min – max) DVF difference for the rectum, cervix, uterus and vagina. It illustrates that even when different DMR perform similarly in term of geometric accuracy (*cf*. Figure 5-10), the resulted internal DVF could present different directions and magnitudes.

Table 5-5: DVF and dose differences between the MORFEUS (1) and the MORFEUS (3)

The mean (min – max) values of each metric for each organ are reported. Comparing MORFEUS (1) with MORFEUS (3), the considered metrics are the mean magnitude of the subtraction of two DVF, the mean and median values of the absolute difference of the two deformed doses and the mean value of the absolute difference between the deformed doses DVH. The dose metrics were reported for 16 individuals. The DVF difference metric is reported for 20 individuals since no significant difference was observed with the 16 individuals (unpaired two-sided Wilcoxon test). DVH: dose volume histogram; DVF: deformation vector field; Abs: absolute

Organs	Mean (min – max) metric values			
	DVF difference (mm) (n= 20)	Abs. mean dose difference (Gy) (n= 16)	Abs. median dose difference (Gy) (n= 16)	Abs. DVH difference (% of volume) (n= 16)
Rectum	3.3 (0.63 – 5.7)	0.53 (0.08 – 1.2)	0.18 (0.00 – 0.72)	0.16 (0.04 – 0.30)
Cervix	4.2 (1.7 – 8.9)	7.1 (0.10 – 14.2)	2.9 (0.06 – 6.1)	1.7 (0.05 – 6.7)
Uterus	3.8 (1.6 – 7.9)	3.9 (0.05 – 9.3)	1.6 (0.02 – 3.3)	0.87 (0.02 – 2.2)
Vagina	4.6 (1.8 – 7.6)	4.9 (1.8 – 8.9)	1.6 (0.54 – 4.2)	1.5 (0.26 – 4.7)

5.3.3.3 Dosimetric comparison

Figure 5-13 illustrates the variability of the mean dose considering the deformed doses toward the pre-BT CT according to each method and compared to the BT planned dose. The intensity-based approaches showed large deviations compared to the planning dose. This deviation was in accordance with the geometric inaccuracy as illustrated in Figure 5-12. Thus, only the biomechanical model-based DIR methods were considered for the evaluation of the local deformed dose.

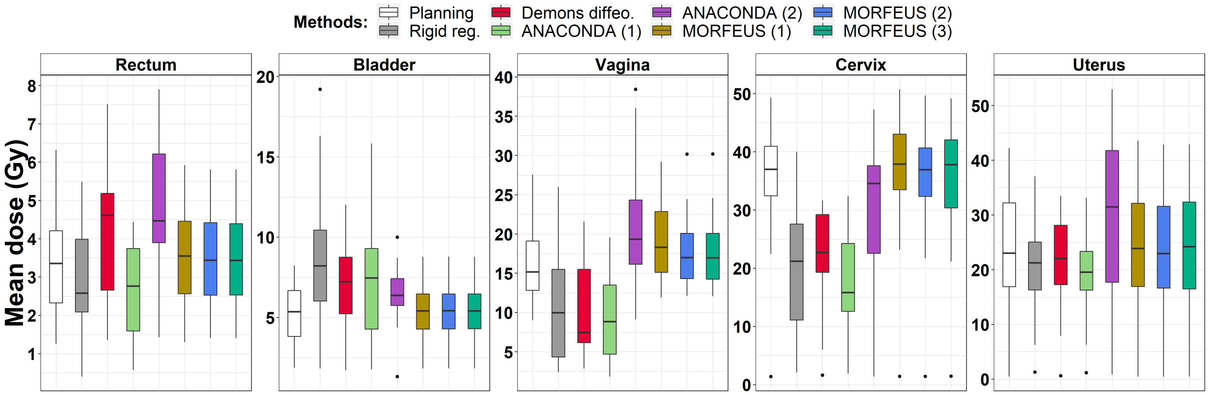

Figure 5-13: Mean dose variability between the planned and deformed doses by each method for each organ

Each facet represents an organ. The mean doses are reported for each organ. The white boxplots represent the mean planning dose for each organ. Each color represents a DIR method. The boxplots allow to compare the deviations between the planned dose on the BT anatomy (with BT applicator) and the deformed doses on the pre-BT anatomy (without BT applicator). The boxplots are computed on 16 values. The bold line represents the median, the boxes represent the 25th and 75th percentiles and the whiskers represent the larger values no further than the length of the box. Individual points are considered as outliers.

Differences between the two most distinct biomechanical models were investigated. Table 5-5 represents the comparison between the deformed doses by MORFEUS (1) and MORFEUS (3) methods considering the mean (min – max) absolute mean dose difference, absolute median dose difference and absolute mean DVH difference. The dose metrics, between the deformed doses by the two biomechanical method, showed important local absolute dose differences and low average DVH differences. Comparing MORFEUS (1) and MORFEUS (3) in term of the maximum absolute volume difference between the deformed doses DVH, the difference was superior to 4% for 38% of the cervix, superior to 4% for 19% of the rectum, superior to 3% for 44% of the uterus and superior to 3% for 75% of the vagina.

Table 5-6ab reports the GEC-ESTRO guideline DVH indices of the planning BT dose on the BT CT and the deformed dose on the pre-BT CT by MORFEUS (3), for each organ. Low differences were observed for the D1cc, D2cc and D90% indices. Slightly higher differences were observed for the D100% index for the cervix, uterus and vagina. However, larger differences per patient were observed for some individuals. The table suggests that the MORFEUS (3) approach was able to deform the planning BT dose on a different anatomy, without applicator, while keeping the topology of the dose gradients. Figure 5-14 illustrates the topology of the deformed doses, by each method, for one patient showing large displacements and deformations (*cf.* Figure 5-7). The MORFEUS (3) method provided the most realistic deformed doses. Figure 5-15 depicts the planning and deformed doses with MORFEUS (3) for 5 cases.

Table 5-6: GEC-ESTRO guidelines DVH indices of the planning dose on the BT CT and of the deformed dose on the pre-BT CT with the MORFEUS (3) method for each organ

The mean (min – max) D1cc and D2cc indices are reported for the bladder and rectum (a). The mean (min – max) D90% and D100% indices are reported for the cervix, uterus and vagina. The indices are reported using the planned dose at the time of BT on the BT CT with applicator and on an anatomy without applicator by considering the deformed dose by the MORFEUS (3) method. The doses were reported for 16 individuals. Depending on the applicator, some patients can have a planned D90% and D100% of 0 Gy. DX defining the minimum dose delivered to X% of the volume; DXcc meaning the minimal received dose by X cc of the volume; DVH: Dose volume histogram; MORFEUS (3) is the biomechanical approach with the combined cervix-uterus, centerline initialization and DMR with spherical coordinate descriptor.

a)

Methods	Mean (min – max) DVH indices (n= 16)			
	D1cc (Gy)		D2cc (Gy)	
	Bladder	Rectum	Bladder	Rectum
Planning	14.5 (7.6 – 23.5)	10.3 (5.1 – 16.4)	13.2 (6.1 – 21.4)	9.3 (4.5 – 14.5)
MORFEUS (3)	14.6 (9.3 – 23.2)	10.4 (5.6 – 17.2)	13.2 (8.0 – 21.1)	9.2 (5.3 – 14.1)
Difference	1.4 (0.26 – 5.3)	1.4 (0.03 – 3.6)	1.3 (0.15 – 4.7)	1.0 (0.10 – 2.9)

b)

Methods	Mean (min – max) DVH indices (n= 16)					
	D90% (Gy)			D100% (Gy)		
	Cervix	Uterus	Vagina	Cervix	Uterus	Vagina
Planning	17.4 (0.89 – 28.2)	7.9 (0 – 17.9)	2.2 (0 – 10.9)	8.2 (0.0 – 16.5)	3.7 (0 – 12.1)	1.1 (0 – 4.9)
MORFEUS (3)	17.7 (0.93 – 28.8)	8.1 (0 – 18.6)	2.4 (0 – 11.6)	6.3 (0 – 14.4)	2.5 (0 – 8.4)	0.55 (0 – 5.0)
Difference	0.34 (0.04 – 0.78)	0.21 (0 – 0.79)	0.24 (0 – 2.0)	4.8 (0 – 16.5)	2.4 (0 – 12.1)	0.60 (0 – 4.2)

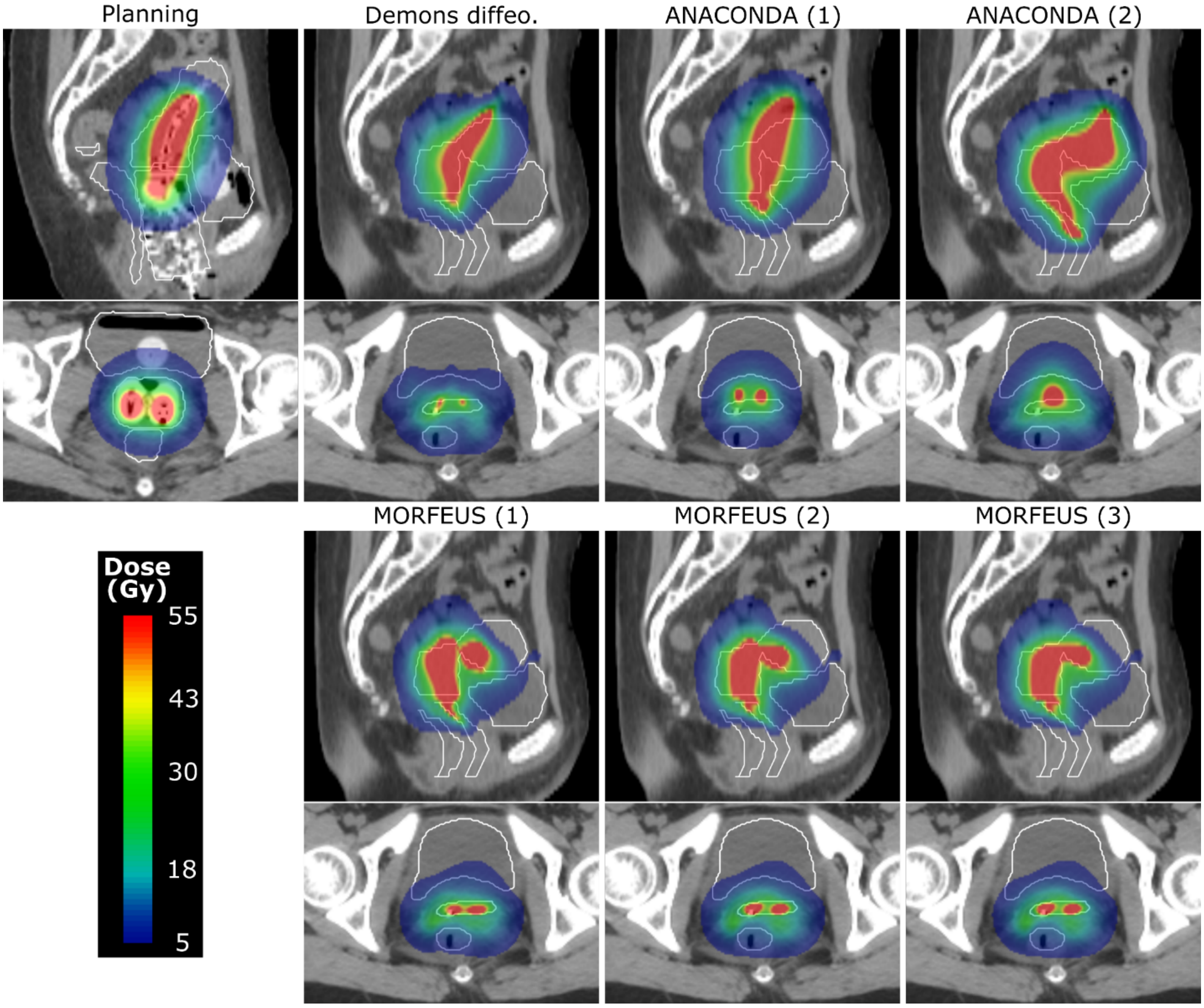

Figure 5-14: Example of the deformed doses by each DIR method for one patient with large deformations

The left group of images represents a sagittal and axial slice of the planning BT dose on the BT CT anatomy (with applicator). The six groups of images on the right part of the figure represent a sagittal and axial slice of the deformed BT doses on the pre-BT CT (without applicator) according to each DIR method. The light white contours represent the organs on the pre-BT CT. The color map (threshold= 5 Gy, level= 30 Gy and window= 50 Gy) is the same for all the doses to ease comparison. Considering the intensity-based DIR methods only (*i.e.* Demons diffeo. and ANACONDA (1)), the deformed doses are not matching the anatomy due to poor geometric correspondence. Considering the hybrid-based DIR method (*i.e.* ANACONDA (2)), the deformed dose was smoother but did not perfectly match the anatomy. The planned dose inside the tandem has been deformed toward the fundus of the uterus, contrary to initial planning. Considering the biomechanical model-based DIR (MORFEUS (1), (2) and (3)), the third method provided a more realistic deformation, especially in term of dose consistency between the cervix and the uterus (sagittal slice) and inside the vagina (axial slice).

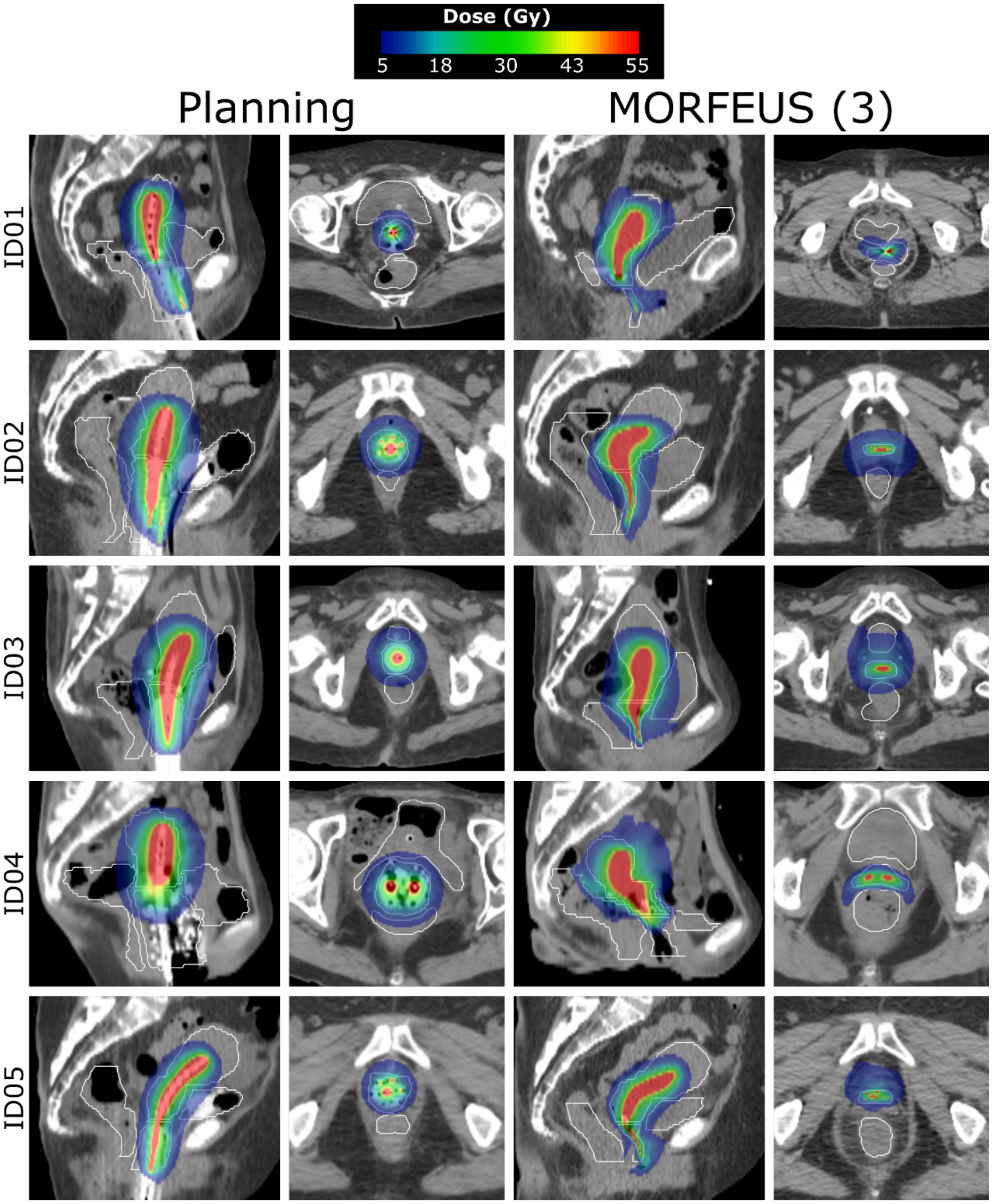

Figure 5-15: Example of the planning and deformed doses with MORFEUS (3) for 5 patients

Each row represents a patient images. The first and second columns represent the sagittal and axial views of the planned dose on the BT CT (with applicator), respectively. The third and fourth columns represent the sagittal and axial views of the deformed dose on the pre-BT CT (without applicator) by the biomechanical model MORFEUS (3), respectively. For each patient, the impact of the volume variation of the vagina and the rotational deformation of the cervix on the dose can be observed. The light white contours represent the rectum, bladder, cervix-uterus and vagina delineations. The color map (threshold= 5 Gy, level= 30 Gy and window= 50 Gy) is the same for all the doses to ease comparison. BT: brachytherapy; CT: computed tomography

5.3.4 DISCUSSION

General discussion

This study quantified the organ motion induced by the applicator insertion for 20 patients. Large displacements and deformations were observed for all the patients. Different DIR methods were used to estimate these deformations. The geometric evaluation suggested that the classic intensity-based DIR methods were inadequate to quantify such complex and independent deformations. The ANACONDA (2) approach, even by taking advantage of the intensity and organ contours, was not able to quantify the deformations. The reason might be that, due to the large and independent deformations of the modeled organs, much less regularization of the DVF is required than when considering the more classical applications in radiation oncology ANACONDA has been designed for. As illustrated by the Figure 5-14, this geometric inaccuracy was also observed on the deformed doses. The biomechanical model-based approaches were the only methods to match the organs delineations and thus deforming the dose in a more consistent way.

Boundary conditions comparison

Multiple parameters of the DMR to drive the surface displacement, and thus influence the FEM internal node displacements, were also investigated. Comparing the different DMR in term of classic geometric evaluation, only low differences were observed. The MORFEUS BC (1) and (2) used either the geodesic distance or the centerline, respectively, to estimate the deformation and displacement of the cervix. The complexity to estimate the rotational deformation underwent by the cervix motivated the use of a combined cervix-uterus delineation to let the biomechanical model solve the internal deformations. Even with an impairment of the cervix and uterus geometric correspondence, the MORFEUS BC (3) was considered to estimate the most realistic deformations.

DIR methods comparison

The diffeomorphic Demons methods was not appropriate for such complex application since it relies on the intensity information only. The performances of ANACONDA (1) and (2) were surprisingly lower than in the literature [65-67]. The method insures high regularization with constraint over the determinant of the Jacobian to obtain a smooth continuous DVF. The default parameters were used in our study, but no significant changes were observed by changing the regularization or convergence parameters. Kadoya *et al* evaluated the performance of ANACONDA (2) on a 3D printed phantom representing a CT pelvic anatomy with and without BT applicator. In this study, they observed a systematic improvement of the geometric evaluation by considering more contours to drive the DVF. While the average DSC were high for the uterus and bladder, large landmark errors were still reported. In our study, the ANACONDA methods did not reach such accuracy. This may be explained by the larger number of contours used to drive the DVF with independent deformation directions. In addition, the centroid displacements were found important with the bone-based rigid alignment contrary to Kadayo *et al* who used a rigid registration to match the uterine structure prior to DIR.

A biomechanical model-based DIR method for complex clinical application is also available in the RayStation TPS. This method computes the boundary condition using model-based segmentation projection between the fixed and moving contours. This approach was not considered in this study since it required too many manual interventions to remove all existing contour intersections that can appear after rigid registration and boundary condition computation (*cf.* section 5.3.2.6.3). However, the implementation of the research version of MORFEUS inside the RayStation TPS has been evaluated, showing similar results for different anatomical localizations [66]. Similar results should be expected for cervical application.

Dose mapping

Considering the dose deformed by the intensity-based DIR methods, the deviation of the mean dose compared to the planning dose was in accordance with the observed geometric inaccuracies. Considering the biomechanical model-based approaches, the choice of the boundary conditions had a large impact on the deformed dose (*cf.* Figure 5-14). The cervix deformation showed complex rotational deformation, which was difficult to quantify using mesh registration approaches. For this application, the MORFEUS (3) was the only method able to keep the relation between the cervix and the uterus, thus, realistically deforming the tandem dose (*cf.* Figure 5-15). Indeed, DIR methods showing similar geometric coverage can have large differences in term of DVF. Small displacement differences can have a large impact in term of local dose differences while not being detectable by comparing the deformed dose DVH (*cf.* Table 5-5). The MORFEUS (3) was showing similar DVH indices for the organs on the anatomy without applicator compared to the planning dose (*cf.* Table 5-6ab). However, the ability to propagate the hotspot positions from one anatomy to another remains the most interesting feature to estimate the total delivered dose (EBRT and BT). The analysis of the relationship between the estimated total delivered dose and tissues toxicity is still to be done for the cervical cancer patients [64,68].

Study limitations

The biomechanical model-based DIR considered the bones and the body to simulate the discontinuities modeled as a thin body part between the soft tissues. Only the accuracy of the considered organs was reported and the displacement of the body (soft tissues between the organs) and bones nodes were not considered in this study. The displacements of the body nodes (representing internal displacement and discontinuities) decreased the geometric accuracy compared to the initial boundary condition, as illustrated by the increase of the HD in Figure 5-12. This can be explained by the different resolutions between the fixed image and the FEM and by the linear interpolation to deform the meshes. More complex biomechanical models still need to be investigated to simulate more complex behavior such as sliding, applicator insertion/removal, and, sigmoid and bowel deformations.

In the study of [45], the applicator removal was simulated by allowing image folding inside the vagina. The impact on the dose of such deformable method needs to be evaluated. In our study overlapping inside the structures were not allowed and the vagina was not considered as a hollow surface. Indeed, FEA needs high quality meshes and defining a small hollow structure may be difficult with 2.5 mm slice thickness images. It is still interesting to mention that the deformation of the biomechanical model can be larger in the border than inside of the vagina (*cf.* Figure 5-8). However, simulating the impact of the applicator insertion and removal on the patient anatomy could be an interesting solution.

The determinants of the Jacobian were not reported in the results. However, the map of the determinant of the Jacobian for each method were controlled during the study to insure that no unrealistic deformations were present inside the considered organs. Report of the determinant of the Jacobian for the biomechanical model-based DIR was difficult due to negative values on the border of the contours caused by the discontinuity at the interface of each organs.

The geometric evaluation was limited by the difficulty to identify corresponding anatomical landmarks in the images which prevented the measure of target registration error. Another source of uncertainties in this study corresponds to delineation variability that may exist especially on the pre-BT CT scan without the guidance of an MRI. For this purpose, volume and delineation consistency were checked for every images. The sigmoid was not analyzed in this study since its delineation is subject to high inter-observer variability.

Future works should focus on increasing the realism of the FEM by considering more structures (*e.g.* GTV, sigmoid, bowel, separated bones), hollow structures (*e.g.* bladder, rectum, sigmoid) and organ interface (*e.g.* bowel and body). Finally, uncertainties of the biomechanical model can be present because of the use of simple linear elastic FEM and uncertainties in the materiel properties definition. Indeed, we found the biomechanical deformations of the vagina to look more realistic when allowing much higher compressibility by reducing the Poisson’s ratio to 0.43. Future works should investigate the sensitivity of the materiel properties in the context of such large deformations.

5.3.5 CONCLUSION

Large displacements and complex deformations due to the insertion of BT applicator and Foley balloon were observed and reported between the anatomies prior and at the time of BT for 20 patients. Standard DIR methods appeared inadequate to estimate such deformations. For this purpose, a biomechanical model-based DIR method was proposed and demonstrated to be able to deform the dose from the BT anatomy toward an anatomy without applicator in a realistic way. Further evaluation, using phantom-based approaches should be conducted to confirm the potential of the proposed method to perform such dose mapping between images with and without BT devices.

5.3.6 REFERENCES

1. Jadon R, Pembroke C, Hanna C, Palaniappan N, Evans M, Cleves A, Staffurth J. A systematic review of organ motion and image-guided strategies in external beam radiotherapy for cervical cancer. *Clinical Oncology* 2014;26:185-196.
2. Kaatee RS, Olofsen MJ, Verstraate MB, Quint S, Heijmen BJ. Detection of organ movement in cervix cancer patients using a fluoroscopic electronic portal imaging device and radiopaque markers. *International Journal of Radiation Oncology* Biology* Physics* 2002;54:576-583.
3. Huh SJ, Park W, Han Y. Interfractional variation in position of the uterus during radical radiotherapy for cervical cancer. *Radiotherapy and oncology* 2004;71:73-79.
4. Lee JE, Han Y, Huh SJ, Park W, Kang MG, Ahn YC, Lim DH. Interfractional variation of uterine position during radical rt: Weekly ct evaluation. *Gynecologic oncology* 2007;104:145-151.
5. Ahmad R, Hoogeman MS, Bondar M, Dhawtal V, Quint S, De Pree I, Mens JW, Heijmen BJ. Increasing treatment accuracy for cervical cancer patients using correlations between bladder-filling change and cervix–uterus displacements: Proof of principle. *Radiotherapy and oncology* 2011;98:340-346.
6. Chan P, Dinniwell R, Haider MA, Cho Y-B, Jaffray D, Lockwood G, Levin W, Manchul L, Fyles A, Milosevic M. Inter-and intrafractional tumor and organ movement in patients with cervical cancer undergoing radiotherapy: A cinematic-mri point-of-interest study. *Int J Radiat Oncol Biol Phys* 2008;70:1507-1515.
7. Heijkoop ST, Langerak TR, Quint S, Mens JWM, Zolnay AG, Heijmen BJ, Hoogeman MS. Quantification of intra-fraction changes during radiotherapy of cervical cancer assessed with pre-and post-fraction cone beam ct scans. *Radiotherapy and Oncology* 2015;117:536-541.
8. Taylor A, Powell ME. An assessment of interfractional uterine and cervical motion: Implications for radiotherapy target volume definition in gynaecological cancer. *Radiotherapy and Oncology* 2008;88:250-257.
9. Buchali A, Koswig S, Dinges S, Rosenthal P, Salk J, Lackner G, Böhmer D, Schlenger L, Budach V. Impact of the filling status of the bladder and rectum on their integral dose distribution and the movement of the uterus in the treatment planning of gynaecological cancer. *Radiotherapy and oncology* 1999;52:29-34.
10. Haripotepornkul NH, Nath SK, Scanderbeg D, Saenz C, Yashar CM. Evaluation of intra-and inter-fraction movement of the cervix during intensity modulated radiation therapy. *Radiotherapy and Oncology* 2011;98:347-351.
11. Jhingran A, Salehpour M, Sam M, Levy L, Eifel PJ. Vaginal motion and bladder and rectal volumes during pelvic intensity-modulated radiation therapy after hysterectomy. *International Journal of Radiation Oncology* Biology* Physics* 2012;82:256-262.
12. van de Bunt L, Van der Heide UA, Ketelaars M, de Kort GA, Jürgenliemk-Schulz IM. Conventional, conformal, and intensity-modulated radiation therapy treatment planning of external beam radiotherapy for cervical cancer: The impact of tumor regression. *International Journal of Radiation Oncology* Biology* Physics* 2006;64:189-196.
13. Lim K, Chan P, Dinniwell R, Fyles A, Haider M, Cho Y-B, Jaffray D, Manchul L, Levin W, Hill RP. Cervical cancer regression measured using weekly magnetic resonance imaging during fractionated radiotherapy: Radiobiologic modeling and correlation with tumor hypoxia. *International Journal of Radiation Oncology* Biology* Physics* 2008;70:126-133.
14. Beadle BM, Jhingran A, Salehpour M, Sam M, Iyer RB, Eifel PJ. Cervix regression and motion during the course of external beam chemoradiation for cervical cancer. *International Journal of Radiation Oncology* Biology* Physics* 2009;73:235-241.
15. Chen W, Bai P, Pan J, Xu Y, Chen K. Changes in tumor volumes and spatial locations relative to normal tissues during cervical cancer radiotherapy assessed by cone beam computed tomography. *Technology in cancer research & treatment* 2017;16:246-252.

16. Lim K, Stewart J, Kelly V, Xie J, Brock KK, Moseley J, Cho Y-B, Fyles A, Lundin A, Rehbinder H. Dosimetrically triggered adaptive intensity modulated radiation therapy for cervical cancer. *International Journal of Radiation Oncology* Biology* Physics* 2014;90:147-154.
17. Oh S, Stewart J, Moseley J, Kelly V, Lim K, Xie J, Fyles A, Brock KK, Lundin A, Rehbinder H, Milosevic M, Jaffray D, Cho YB. Hybrid adaptive radiotherapy with on-line mri in cervix cancer imrt. *Radiother Oncol* 2014;110:323-328.
18. Stewart J, Lim K, Kelly V, Xie J, Brock KK, Moseley J, Cho Y-B, Fyles A, Lundin A, Rehbinder H. Automated weekly replanning for intensity-modulated radiotherapy of cervix cancer. *International Journal of Radiation Oncology* Biology* Physics* 2010;78:350-358.
19. Bondar L, Hoogeman M, Mens JW, Dhawtal G, De Pree I, Ahmad R, Quint S, Heijmen B. Toward an individualized target motion management for imrt of cervical cancer based on model-predicted cervix–uterus shape and position. *Radiotherapy and Oncology* 2011;99:240-245.
20. Langerak T, Heijkoop S, Quint S, Mens J-W, Heijmen B, Hoogeman M. Towards automatic plan selection for radiotherapy of cervical cancer by fast automatic segmentation of cone beam ct scans Medical image computing and computer-assisted intervention–miccai 2014: Springer; 2014. pp. 528-535.
21. Heijkoop ST, Langerak TR, Quint S, Bondar L, Mens JWM, Heijmen BJ, Hoogeman MS. Clinical implementation of an online adaptive plan-of-the-day protocol for nonrigid motion management in locally advanced cervical cancer imrt. *Int J Radiat Oncol Biol Phys* 2014;90:673-679.
22. Bondar M, Hoogeman M, Mens J, Quint S, Ahmad R, Dhawtal G, Heijmen B. Individualized nonadaptive and online-adaptive intensity-modulated radiotherapy treatment strategies for cervical cancer patients based on pretreatment acquired variable bladder filling computed tomography scans. *International Journal of Radiation Oncology* Biology* Physics* 2012;83:1617-1623.
23. Seppenwoolde Y, Stock M, Buschmann M, Georg D, Bauer-Novotny K-Y, Pötter R, Georg P. Impact of organ shape variations on margin concepts for cervix cancer art. *Radiotherapy and Oncology* 2016.
24. van de Schoot AJ, de Boer P, Visser J, Stalpers LJ, Rasch CR, Bel A. Dosimetric advantages of a clinical daily adaptive plan selection strategy compared with a non-adaptive strategy in cervical cancer radiation therapy. *Acta Oncologica* 2017;56:667-674.
25. Rigaud B, Simon A, Gobeli M, Lafond C, Leseur J, Barateau A, Jaksic N, Castelli J, Williaume D, Haigron P, De Crevoisier R. Cbct-guided evolutive library for cervical adaptive imrt. *Medical Physics* 2018.
26. Rigaud B, Simon A, Gobeli M, Leseur J, Duvergé L, Williaume D, Castelli J, Lafond C, Acosta O, Haigron P, Crevoisier RD. Statistical shape model to generate a planning library for cervical adaptive radiotherapy. *IEEE Transactions on Medical Imaging* 2018:1-1.
27. Hoskin P, Cook M, Bouscale D, Cansdale J. Changes in applicator position with fractionated high dose rate gynaecological brachytherapy. *Radiotherapy and oncology* 1996;40:59-62.
28. Nesvacil N, Tanderup K, Hellebust TP, De Leeuw A, Lang S, Mohamed S, Jamema SV, Anderson C, Pötter R, Kirisits C. A multicentre comparison of the dosimetric impact of inter-and intra-fractional anatomical variations in fractionated cervix cancer brachytherapy. *Radiotherapy and Oncology* 2013;107:20-25.
29. Rangarajan R. Interfraction variations in organ filling and their impact on dosimetry in ct image based hdr intracavitary brachytherapy. *Journal of medical physics* 2018;43:23.
30. Chakraborty S, Patel FD, Patil VM, Oinam AS, Sharma SC. Magnitude and implications of interfraction variations in organ doses during high dose rate brachytherapy of cervix cancer: A ct based planning study. *ISRN oncology* 2014;2014.
31. Noe KØ, Tanderup K, Sørensen TS. Surface membrane based bladder registration for evaluation of accumulated dose during brachytherapy in cervical cancer. Biomedical Imaging: From Nano to Macro, 2011 IEEE International Symposium on. IEEE. 2011. pp. 1253-1256.

32. Andersen ES, Noe KØ, Sørensen TS, Nielsen SK, Fokdal L, Paludan M, Lindegaard JC, Tanderup K. Simple dvh parameter addition as compared to deformable registration for bladder dose accumulation in cervix cancer brachytherapy. *Radiotherapy and Oncology* 2013;107:52-57.
33. Jamema SV, Mahantshetty U, Andersen E, Noe KØ, Sørensen TS, Kallehauge JF, Shrivastava SK, Deshpande DD, Tanderup K. Uncertainties of deformable image registration for dose accumulation of high-dose regions in bladder and rectum in locally advanced cervical cancer. *Brachytherapy* 2015;14:953-962.
34. Kobayashi K, Murakami N, Wakita A, Nakamura S, Okamoto H, Umezawa R, Takahashi K, Inaba K, Igaki H, Ito Y. Dosimetric variations due to interfraction organ deformation in cervical cancer brachytherapy. *Radiotherapy and Oncology* 2015;117:555-558.
35. Hayashi K, Isohashi F, Akino Y, Wakai N, Mabuchi S, Suzuki O, Seo Y, Ootani Y, Sumida I, Yoshioka Y. Estimation of the total rectal dose of radical external beam and intracavitary radiotherapy for uterine cervical cancer using the deformable image registration method. *Journal of radiation research* 2015;56:546-552.
36. Teo B-K, Millar LPB, Ding X, Lin LL. Assessment of cumulative external beam and intracavitary brachytherapy organ doses in gynecologic cancers using deformable dose summation. *Radiotherapy and Oncology* 2015;115:195-202.
37. van Heerden LE, Houweling AC, Koedooder K, van Kesteren Z, van Wieringen N, Rasch CR, Pieters BR, Bel A. Structure-based deformable image registration: Added value for dose accumulation of external beam radiotherapy and brachytherapy in cervical cancer. *Radiotherapy and Oncology* 2017;123:319-324.
38. van Heerden LE, van Wieringen N, Koedooder K, Rasch CR, Pieters BR, Bel A. Dose warping uncertainties for the accumulated rectal wall dose in cervical cancer brachytherapy. *Brachytherapy* 2017.
39. Pötter R, Haie-Meder C, Van Limbergen E, Barillot I, De Brabandere M, Dimopoulos J, Dumas I, Erickson B, Lang S, Nulens A. Recommendations from gynaecological (gyn) gec estro working group (ii): Concepts and terms in 3d image-based treatment planning in cervix cancer brachytherapy—3d dose volume parameters and aspects of 3d image-based anatomy, radiation physics, radiobiology. *Radiotherapy and Oncology* 2006;78:67-77.
40. Kim H, Huq MS, Houser C, Beriwal S, Michalski D. Mapping of dose distribution from imrt onto mri-guided high dose rate brachytherapy using deformable image registration for cervical cancer treatments: Preliminary study with commercially available software. *Journal of contemporary brachytherapy* 2014;6:178.
41. Van de Kamer JB, De Leeuw AA, Moerland MA, Jürgenliemk-Schulz I-M. Determining dvh parameters for combined external beam and brachytherapy treatment: 3d biological dose adding for patients with cervical cancer. *Radiotherapy and Oncology* 2010;94:248-253.
42. Chen J, Chen H, Zhong Z, Wang Z, Hrycushko B, Zhou L, Jiang S, Albuquerque K, Gu X, Zhen X. Investigating rectal toxicity associated dosimetric features with deformable accumulated rectal surface dose maps for cervical cancer radiotherapy. *Radiation Oncology* 2018;13:125.
43. Christensen GE, Carlson B, Chao KC, Yin P, Grigsby PW, Nguyen K, Dempsey JF, Lerma FA, Bae KT, Vannier MW. Image-based dose planning of intracavitary brachytherapy: Registration of serial-imaging studies using deformable anatomic templates. *International Journal of Radiation Oncology• Biology• Physics* 2001;51:227-243.
44. Vásquez Osorio EM, Kolkman-Deurloo IKK, Schuring-Pereira M, Zolnay A, Heijmen BJ, Hoogeman MS. Improving anatomical mapping of complexly deformed anatomy for external beam radiotherapy and brachytherapy dose accumulation in cervical cancer. *Medical physics* 2015;42:206-220.
45. Berendsen F, Kotte A, de Leeuw A, Jürgenliemk-Schulz I, Viergever M, Pluim J. Registration of structurally dissimilar images in mri-based brachytherapy. *Physics in Medicine & Biology* 2014;59:4033.

46. Osorio EMV, Hoogeman MS, Bondar L, Levendag PC, Heijmen BJ. A novel flexible framework with automatic feature correspondence optimization for nonrigid registration in radiotherapy. *Medical physics* 2009;36:2848-2859.
47. Bondar L, Hoogeman MS, Osorio EMV, Heijmen BJ. A symmetric nonrigid registration method to handle large organ deformations in cervical cancer patients. *Medical physics* 2010;37:3760-3772.
48. Pecorelli S, Zigliani L, Odicino F. Revised figo staging for carcinoma of the cervix. *International Journal of Gynecology & Obstetrics* 2009;105:107-108.
49. Thirion J-P. Image matching as a diffusion process: An analogy with maxwell's demons. *Medical image analysis* 1998;2:243-260.
50. Vercauteren T, Pennec X, Perchant A, Ayache N. Diffeomorphic demons: Efficient non-parametric image registration. *NeuroImage* 2009;45:S61-S72.
51. Weistrand O, Svensson S. The anaconda algorithm for deformable image registration in radiotherapy. *Medical physics* 2015;42:40-53.
52. Brock K, Sharpe M, Dawson L, Kim S, Jaffray D. Accuracy of finite element model-based multi-organ deformable image registration. *Medical physics* 2005;32:1647-1659.
53. Schroeder WJ, Lorensen B, Martin K. The visualization toolkit: An object-oriented approach to 3d graphics: Kitware; 2004.
54. Taubin G, Zhang T, Golub G. Optimal surface smoothing as filter design. *Computer Vision—ECCV'96* 1996:283-292.
55. Valette S, Chassery JM, Prost R. Generic remeshing of 3d triangular meshes with metric-dependent discrete voronoi diagrams. *IEEE Transactions on Visualization and Computer Graphics* 2008;14:369-381.
56. Belongie S, Malik J, Puzicha J. Shape matching and object recognition using shape contexts. *IEEE transactions on pattern analysis and machine intelligence* 2002;24:509-522.
57. Acosta O, Fripp J, Doré V, Bourgeat P, Favreau J-M, Chételat G, Rueda A, Villemagne VL, Szoeke C, Ames D. Cortical surface mapping using topology correction, partial flattening and 3d shape context-based non-rigid registration for use in quantifying atrophy in alzheimer's disease. *Journal of Neuroscience Methods* 2012;205:96-109.
58. Jonker R, Volgenant A. A shortest augmenting path algorithm for dense and sparse linear assignment problems. *Computing* 1987;38:325-340.
59. Chai X, van Herk M, van de Kamer JB, Hulshof MC, Remeijer P, Lotz HT, Bel A. Finite element based bladder modeling for image-guided radiotherapy of bladder cancer. *Medical physics* 2011;38:142-150.
60. Baah-Dwomoh A, McGuire J, Tan T, De Vita R. Mechanical properties of female reproductive organs and supporting connective tissues: A review of the current state of knowledge. *Applied Mechanics Reviews* 2016;68:060801.
61. Dias N, Peng Y, Khavari R, Nakib NA, Sweet RM, Timm GW, Erdman AG, Boone TB, Zhang Y. Pelvic floor dynamics during high-impact athletic activities: A computational modeling study. *Clinical Biomechanics* 2017;41:20-27.
62. Dice LR. Measures of the amount of ecologic association between species. *Ecology* 1945;26:297-302.
63. Huttenlocher DP, Klanderman G, Rucklidge WJ. Comparing images using the hausdorff distance. *Pattern Analysis and Machine Intelligence, IEEE Transactions on* 1993;15:850-863.
64. Georg P, Pötter R, Georg D, Lang S, Dimopoulos JC, Sturdza AE, Berger D, Kirisits C, Dörr W. Dose effect relationship for late side effects of the rectum and urinary bladder in magnetic resonance image-guided adaptive cervix cancer brachytherapy. *International Journal of Radiation Oncology• Biology• Physics* 2012;82:653-657.
65. Kadoya N, Miyasaka Y, Nakajima Y, Kuroda Y, Ito K, Chiba M, Sato K, Dobashi S, Yamamoto T, Takahashi N. Evaluation of deformable image registration between external beam radiotherapy and hdr brachytherapy for cervical cancer with a 3d-printed deformable pelvis phantom. *Medical physics* 2017;44:1445-1455.

66. Velec M, Moseley JL, Svensson S, Hårdemark B, Jaffray DA, Brock KK. Validation of biomechanical deformable image registration in the abdomen, thorax and pelvis in a commercial radiotherapy treatment planning system. *Medical physics* 2017.
67. Takayama Y, Kadoya N, Yamamoto T, Ito K, Chiba M, Fujiwara K, Miyasaka Y, Dobashi S, Sato K, Takeda K. Evaluation of the performance of deformable image registration between planning ct and cbct images for the pelvic region: Comparison between hybrid and intensity-based dir. *Journal of radiation research* 2017;58:567-571.
68. Zakariaee R, Hamarneh G, Brown CJ, Gaudet M, Aquino-Parsons C, Spadinger I. Bladder accumulated dose in image-guided high-dose-rate brachytherapy for locally advanced cervical cancer and its relation to urinary toxicity. *Physics in Medicine & Biology* 2016;61:8408.

5.4 DISCUSSION

Ces deux études ont permis de mettre en avant deux applications différentes utilisant une approche de recalage déformable basé sur un modèle biomécanique.

La première étude montre qu'un modèle biomécanique peut être utilisé avec un nombre de conditions aux limites restreint afin de simuler de larges déplacements et déformations pour améliorer l'alignement des tissus mous d'une patiente. Ce type d'outil, intégré dans un système commercial pour applications cliniques, peut trouver sa place auprès des cliniciens qui font face à des difficultés délinéer des patientes avec des fortes déformations dû à la présence d'un matelas. L'approche biomécanique était adéquate pour ce type d'application car résultait en une amélioration de l'alignement des tissus mous par rapport aux méthodes basées intensité tout en générant un champ dense non influencé par la présence de l'applicateur de curiethérapie.

La deuxième étude montre cependant un usage plus complexe qui utilise un modèle reposant sur 6 à 7 composantes afin d'estimer un champ de déformations dense comprenant les déformations indépendantes de chaque organe. Elle a alors montré que de fortes déformations anatomiques étaient engendrées par l'insertion de l'applicateur et du ballon de Foley. Cette insertion engendre des déplacements 3D moyens du centroïde du col de l'utérus et de l'utérus de 26.5 mm et 32.5 mm en moyenne et jusqu'à 44 mm et 53.7 mm, respectivement, principalement dans la direction antéro-supérieure. Ces déformations doivent être estimées afin de permettre l'accumulation des doses. L'estimation de cette dose délivrée permettrait alors la quantification d'une éventuelle dérive de dose, par rapport à la planification, et d'étudier l'impact de cette dérive sur le contrôle de la tumeur et le risque de toxicité aux OAR. Ces travaux se sont focalisés sur l'approche de recalage déformable entre l'anatomie avec et sans applicateur, afin de pouvoir propager la dose de curiethérapie vers l'anatomie de radiothérapie externe. Afin de réduire l'impact de la fonte tumorale, une image acquise à un instant proche de la curiethérapie a été sélectionnée, la TDM de planification du *boost* de dose aux extensions ganglionnaires.

Nos travaux ont montré que les méthodes classiques de la littérature ou d'outils commerciaux n'étaient pas adéquates pour cette application. Une méthode déformable reposant sur un modèle biomécanique dont les conditions aux limites sont définies par la méthode DMR avec le col utérin et l'utérus combinés ainsi que l'initialisation des déformations par la ligne centrale a montré les meilleurs résultats. Cette méthode a permis une propagation réaliste de la dose, évaluée visuellement et en termes de conservation des indices des HDV.

Cette étude a plusieurs limites et perspectives.

Premièrement, l'évaluation géométrique des méthodes de recalage déformable est limitée à l'utilisation des critères classiques (DSC, DTA et HD). L'utilisation de marqueurs géométriques (*landmarks*) permettrait de la préciser. Pour cette cohorte de patientes, plusieurs marqueurs potentiels ont pu être identifiés, comme des grains d'or dans le GTV servant au guidage de l'IMRT ou des fibromes utérins. Cependant, le suivi de ces marqueurs reste complexe puisque ces derniers peuvent se déplacer indépendamment de la déformation de l'organe. De plus, le scanner de planification au moment de la curiethérapie est fortement dégradé par la présence du dispositif (par ex. bruits, artefacts et distorsions), augmentant l'incertitude pour le suivi de marqueurs anatomiques. Un fantôme anatomique (physique, numérique ou synthétiquement généré à partir d'une patiente) permettrait de s'abstenir de cette difficulté mais reste cependant lui aussi complexe à mettre en place pour simuler des déformations réalistes. Un fantôme permettrait de quantifier l'impact des déformations estimées par les méthodes de recalage déformable de surface [8] sur la solution du modèle biomécanique.

Deuxièmement, le modèle biomécanique défini dans cette étude assume que les déformations suivent un comportement élastique linéaire. Cette approche peut entrainer des incertitudes lorsque de fortes déformations doivent être estimées. Pour limiter ces incertitudes, les conditions aux limites sont définies par la méthode DMR. La solution du modèle biomécanique est alors imposée par les conditions aux limites et les propriétés mécaniques des organes.

Cela soulève une autre limite. La solution des contraintes est influençable par les propriétés mécaniques des organes. En effet, le coefficient de Poisson a été ajusté pour la vessie et le vagin, en prenant en compte la littérature, afin d'obtenir une déformation interne réaliste (déterminant du Jacobien strictement positif). Cependant, l'ajustement du coefficient de Poisson pour satisfaire ce critère soulève la question de la compressibilité de certains organes lors de fortes déformations (par ex. variation du volume de la vessie). Une perspective pour surmonter cette limite serait de simuler la vessie, le rectum et le vagin comme des parois.

De plus, toujours dans l'intérêt d'améliorer le réalisme du FEM, le masque binaire de la tumeur pourrait être ajouté dans le contour considérant le vagin, le col utérin et l'utérus afin de définir des propriétés mécaniques hétérogènes et influencer les déplacements des nœuds internes du modèle. Une autre perspective serait de simuler l'insertion de l'applicateur et du ballon de Foley pour déformer ou initialiser l'anatomie de la radiothérapie externe pour la faire correspondre à celle de la curiethérapie. Cette approche, bien plus complexe, ne nécessiterait plus de méthode de recalage déformable de maillage pour la définition des conditions aux limites.

5.5 CONCLUSION

Ces travaux ont permis la proposition et l'évaluation d'une méthode de recalage déformable reposant sur la méthode DMR et sur le modèle biomécanique MORFEUS et permettant d'estimer les déformations importantes induites par l'insertion de l'applicateur de curiethérapie. Cette approche, comparée aux méthodes de la littérature, était la seule à permettre une bonne correspondance géométrique des organes et donc de déformer la dose de la curiethérapie d'une manière réaliste. Cette approche nécessite cependant une évaluation complémentaire, notamment à travers l'utilisation de marqueurs anatomiques.

5.6 RÉFÉRENCES

1. Berendsen F, Kotte A, de Leeuw A, Jürgenliemk-Schulz I, Viergever M, Pluim J. Registration of structurally dissimilar images in mri-based brachytherapy. *Physics in Medicine & Biology* 2014;59:4033.
2. Christensen GE, Carlson B, Chao KC, Yin P, Grigsby PW, Nguyen K, Dempsey JF, Lerma FA, Bae KT, Vannier MW. Image-based dose planning of intracavitary brachytherapy: Registration of serial-imaging studies using deformable anatomic templates. *International Journal of Radiation Oncology• Biology• Physics* 2001;51:227-243.
3. Vásquez Osorio EM, Kolkman-Deurloo IKK, Schuring-Pereira M, Zolnay A, Heijmen BJ, Hoogeman MS. Improving anatomical mapping of complexly deformed anatomy for external beam radiotherapy and brachytherapy dose accumulation in cervical cancer. *Medical physics* 2015;42:206-220.
4. Chabanas M, Payan Y, Marécaux C, Swider P, Boutault F. Comparison of linear and non-linear soft tissue models with post-operative ct scan in maxillofacial surgery Medical simulation: Springer; 2004. pp. 19-27.
5. Warfield SK, Haker SJ, Talos I-F, Kemper CA, Weisenfeld N, Mewes AU, Goldberg-Zimring D, Zou KH, Westin C-F, Wells WM. Capturing intraoperative deformations: Research experience at brigham and women’s hospital. *Medical image analysis* 2005;9:145-162.
6. Tanner C, Schnabel JA, Hill DL, Hawkes DJ, Leach MO, Hose DR. Factors influencing the accuracy of biomechanical breast models. *Medical physics* 2006;33:1758-1769.
7. Wittek A, Miller K, Kikinis R, Warfield SK. Patient-specific model of brain deformation: Application to medical image registration. *Journal of biomechanics* 2007;40:919-929.
8. Zakariaee R, Hamarneh G, Brown CJ, Spadinger I. Validation of non-rigid point-set registration methods using a porcine bladder pelvic phantom. *Physics in Medicine & Biology* 2016;61:825.

SYNTHESE ET CONCLUSION

Les travaux présentés dans cette thèse s'inscrivent dans le cadre du traitement par radiothérapie des cancers du col de l'utérus localement avancés et de la problématique majeure de la prise en compte des incertitudes géométriques. Concernant la radiothérapie externe, ces incertitudes comprennent notamment les déplacements et déformations de l'utérus liés aux modifications de volume de la vessie et du rectum, mais aussi la fonte tumorale due à la réponse au traitement. Ces incertitudes ont un impact dosimétrique et peuvent ainsi augmenter les risques de récidive et de toxicité. Concernant la curiethérapie, les variations anatomiques sont notamment dues à l'insertion des dispositifs de traitement (applicateur et ballon de Foley), limitant la quantification de la dose totale délivrée par les deux traitements. L'objectif de ces travaux était donc de proposer et d'évaluer des stratégies permettant d'améliorer la prise en compte des incertitudes géométriques survenant en cours de traitement.

Deux stratégies de radiothérapie externe ont été proposées pour améliorer la personnalisation du traitement. Elles font partie des approches dites de radiothérapie adaptative puisqu'elles remplacent le plan de traitement unique de l'approche standard par plusieurs plans de traitement adaptés à différentes configurations anatomiques. L'objectif est d'améliorer la stratégie adaptative la plus utilisée pour le col de l'utérus, la librairie de plans de traitement, qui repose sur l'optimisation de plusieurs balistiques de traitement suivant différents volumes de vessie puis sur le choix, à chaque séance de traitement, du plan le plus adapté. La première stratégie proposée, la librairie évolutive, exploite les images CBCT acquises pendant le traitement pour mettre à jour la librairie [1]. En effet, une limite de la librairie classique est liée, pour certaines patientes, à une mauvaise représentation des anatomies rencontrées pendant le traitement. C'est notamment le cas pour les patientes avec un utérus non-mobile à la planification qui devient mobile lors du traitement. La librairie évolutive repose sur l'évaluation, à chaque séance, de la représentation de l'anatomie du jour dans la librairie. Un critère géométrique est utilisé, associé à un seuil, pour déclencher l'ajout de l'anatomie du jour dans la librairie, ce qui en pratique nécessiterait une replanification. La valeur du seuil a été sélectionnée suivant un compromis entre le nombre de replanifications, et donc la charge supplémentaire, et la couverture de la cible. Le point fort de cette approche est qu'il ne déclenche des replanifications que si nécessaire. Ainsi, aucune replanification n'est déclenchée pour les patientes pour lesquelles la librairie initiale est performante (55% de notre cohorte). A l'inverse, jusqu'à 3 replanifications sont déclenchées pour les patientes dont la librairie initiale n'est pas adaptée. L'évaluation, géométrique pour 20 patientes et dosimétrique pour une patiente, montre que cette stratégie est la seule assurant la couverture de la cible pour toutes les patientes, même avec une marge réduite à 7 mm ce qui permet d'améliorer l'épargne des organes à risque de façon conséquente.

La seconde stratégie proposée, la librairie modélisée, repose sur une analyse populationnelle pour simuler les configurations anatomiques les plus probables [2]. A partir de la quantification des déformations intra- et inter-patientes, cette analyse conduit à la génération d'un modèle statistique de forme reposant sur une analyse en composantes principales (ACP). Le modèle compact généré représente les déformations dominantes du CTV et de la vessie. Une ACP a posteriori est ensuite utilisée pour simuler, pour une nouvelle patiente, les configurations anatomiques les plus probables suivant le modèle et une contrainte de déplacement du fond utérin. L'évaluation a montré que, comparée à la librairie classique, si l'approche proposée n'apporte pas de gain systématique pour toutes les patientes, elle permet de corriger de façon importante la couverture de la cible pour des patientes pour lesquelles la librairie standard n'est pas adaptée, tout en ne nécessitant l'acquisition que d'un unique scanner de planification. Comparée à la librairie évolutive, si les résultats de couverture sont légèrement moins bons, son implémentation pratique serait beaucoup plus simple, ne nécessitant pas de replanification en cours de traitement.

Au niveau méthodologique, ces travaux reposent notamment sur des méthodes de recalage déformable utilisées pour estimer les déformations des organes d'intérêt, en intra- et inter-patientes. Une revue de la littérature a tout d'abord montré que, de par les très fortes déformations rencontrées, les méthodes standard (FFD, Démons) n'exploitant que les intensités des images sont inadaptées. Les travaux se sont donc tournés vers l'exploitation d'informations complémentaires, points de référence ou contours, pour guider le recalage. Des modèles en éléments finis ont aussi été proposés pour améliorer le réalisme des déformations estimées. Dans ce sens, dans nos travaux, suivant les applications considérées, différentes méthodes ont été exploitées. Pour la librairie évolutive, le recalage déformable n'est utilisé que pour l'analyse des résultats, de façon à rapporter l'ensemble des couvertures géométrique ou dosimétrique vers une anatomie commune. La méthode des Démons difféomorphiques appliquée à des cartes de distance a été utilisée. A l'opposé, le recalage occupe une place centrale pour la génération de la librairie modélisée, puisque qu'il estime les déformations analysées par l'ACP. Une méthode de recalage déformable de maillages (DMR) a permis de mettre en correspondance les anatomies inter-patientes vers l'anatomie d'une patiente modèle. Cette approche itérative repose sur la combinaison du *shape context* et de la distance géodésique afin d'estimer des déformations complexes et de fortes amplitudes (par ex. bascule de l'utérus). Enfin, dans le contexte de la curiethérapie, nos travaux ont porté sur l'évaluation des méthodes de recalage pour la mise en correspondance d'anatomies avec et sans applicateur. Des méthodes standard et hybride, issues de la littérature et d'un outil commercial, ont été considérées, ainsi qu'une méthode reposant sur un modèle biomécanique, MORFEUS, combiné avec l'approche DMR. L'évaluation géométrique a montré les limites des méthodes standard et hybride. Pour les modèles biomécaniques, l'évaluation a montré l'impact des différentes conditions aux limites sur les déformations estimées et la dose déformée. Ces travaux ont permis la proposition d'une méthode capable de déformer la dose de curiethérapie vers une anatomie sans applicateur.

L'évaluation de ces méthodes de recalage déformable s'est limitée à des critères géométriques simples qui ne permettent pas d'assurer une réelle correspondance locale des tissus considérés. Une évaluation plus approfondie des méthodes serait donc à mener [3]. Celle-ci pourrait passer par la sélection de repères anatomiques, cependant très difficiles à identifier sur images TDM ou CBCT, nécessitant donc l'utilisation d'IRM. Elle pourrait aussi reposer sur un fantôme physique, probablement complexe à fabriquer, ou numérique, à l'image du fantôme de pelvis masculin développé dans l'équipe [4].

Plus généralement, différentes perspectives de ces travaux peuvent être envisagées.

Les stratégies par librairie évolutive et modélisée ont été principalement évaluées suivant des critères géométriques. Bien que confirmé, pour l'approche évolutive, dosimétriquement pour une patiente, une analyse dosimétrique plus large doit être menée. Celle-ci passera par la génération de plans de traitement à partir des CBCT ou des anatomies simulées. En ce sens, les travaux menés dans l'équipe sur le calcul de dose à partir d'images CBCT montrent la faisabilité de l'approche [5].

Concernant les stratégies proposées, de nouvelles approches pourraient être envisagées. Par exemple, la librairie évolutive ne permettant pas d'utiliser un nouveau plan de traitement dès le déclenchement de la replanification (approche *offline*), l'apport d'un plan de secours (type RC3D) pour assurer la couverture du CTV pourrait être quantifié. Par ailleurs, pour la librairie classique (qui est utilisée pour la librairie évolutive et pour la librairie « combinée », intégrant les librairies classique et modélisée), les trois TDM à volume de vessie variable sont systématiquement considérés. Puisque, pour certaines patientes, l'utérus n'est pas mobile à la planification, cette exploitation systématique est probablement sous-optimale. L'exploitation de critères géométriques pour sélectionner au mieux les images pertinentes pourrait permettre de limiter la charge de planification de ces stratégies. Enfin, la combinaison des deux stratégies proposées, les librairies évolutive et modélisée, pourrait permettre d'améliorer encore le compromis entre l'efficacité du traitement et la charge liée aux replanifications. Plus généralement, la question du choix du plan de traitement adapté à chaque séance se pose pour toutes les stratégies intégrant une librairie de plans [6,7]. Des outils reposant sur des méthodes de segmentation, d'identification de points d'intérêt (par ex. le fond utérin ou le dôme de la vessie) pourraient permettre d'assister cette étape cruciale.

Les méthodes développées pourraient aussi probablement être améliorées. Ainsi, la méthode DMR pourrait bénéficier de traitements des correspondances, reposant sur le déterminant du Jacobien, pendant ou après l'estimation du champ de déformation. Le modèle statistique de forme utilisé considère sans distinction les variations intra- et inter-patientes. Une perspective serait de considérer les variations intra-patientes au sein du modèle par un modèle à effets mixtes [8]. Cette méthode, appliquée à une cohorte plus large, pourrait aussi peut-être permettre, dès la planification, la classification des patientes mobile/non-mobile pendant le traitement. Les contraintes pour le modèle d'analyse en composantes principales a posteriori ont été définies empiriquement afin de générer une librairie modélisée réaliste pour l'ensemble de la cohorte. Une perspective pourrait être de définir une contrainte spécifique à chaque patiente suivant des caractéristiques morphologiques (par ex. la position des os). Le choix des contraintes pourrait être proposé dans un outil semi-automatique, intégré au système de planification. Le radiothérapeute pourrait alors définir lui-même les contraintes permettant de modéliser la librairie de la patiente considérée.

Pour la modélisation des déformations induites par l'insertion de l'applicateur de curiethérapie, différentes perspectives sont envisageables. Premièrement, il est nécessaire de quantifier l'impact de la complexité du modèle en éléments finis sur le champ de déformation estimé. Par exemple, il serait intéressant de modéliser les déformations avec un modèle hyperélastique ou d'enrichir l'hétérogénéité du modèle à l'aide de masques (par ex. GTV, air, applicateur).

D'une façon générale, les approches proposées sont très dépendantes des délinéations, à la fois des TDM et des CBCT. Ceci peut générer de la variabilité mais surtout, de par la charge de travail très conséquente, limite ce type d'études à des cohortes restreintes (20 patientes dans notre cas). Des méthodes de segmentation automatique, par exemple à base d'apprentissage, pourraient permettre d'étendre ces études. Enfin, l'intégration de l'IRM aux accélérateurs linéaires ouvre de nouvelles perspectives pour ces stratégies adaptatives, que ce soit en termes de précision de définition de la cible tumorale ou d'estimation et de compensation des incertitudes intra-fraction [9].

En conclusion, ces travaux de thèse représentent une contribution pour la prise en compte des variations anatomiques survenant entre les fractions de radiothérapie et au moment de la curiethérapie. Deux stratégies de radiothérapie adaptative ont été proposées, la librairie évolutive et la libraire modélisée. Les principes de ces stratégies ne sont pas limités au col de l’utérus mais pourraient permettre de répondre à des problématiques pour le traitement d’autres cancers, par exemple le cancer de la vessie ou du rectum. Ces travaux ont aussi permis la définition d’une approche de recalage déformable reposant sur un modèle biomécanique afin d’estimer les déformations complexes induites par l’insertion des dispositifs de planification de la curiethérapie, permettant donc d’envisager l’estimation de la dose totale délivrée par l’ensemble du traitement. D’une façon générale, ces travaux de thèse ouvrent donc la voie à des études permettant, grâce à l’amélioration de la personnalisation du traitement, d’améliorer le ciblage de la tumeur, et donc le contrôle local, tout en limitant les effets secondaires.

REFERENCES

1. Rigaud B, Simon A, Gobeli M, Lafond C, Leseur J, Barateau A, Jaksic N, Castelli J, Williaume D, Haigron P, De Crevoisier R. Cbct-guided evolutive library for cervical adaptive imrt. *Medical Physics* 2018.
2. Rigaud B, Simon A, Gobeli M, Leseur J, Duvergé L, Williaume D, Castelli J, Lafond C, Acosta O, Haigron P, Crevoisier RD. Statistical shape model to generate a planning library for cervical adaptive radiotherapy. *IEEE Transactions on Medical Imaging* 2018:1-1.
3. Paganelli C, Meschini G, Molinelli S, Riboldi M, Baroni G. Patient-specific validation of deformable image registration in radiation therapy: Overview and caveats. *Medical physics* 2018.
4. Nassef M, Simon A, Cazoulat G, Duménil A, Blay C, Lafond C, Acosta O, Balosso J, Haigron P, de Crevoisier R. Quantification of dose uncertainties in cumulated dose estimation compared to planned dose in prostate imrt. *Radiotherapy and Oncology* 2016;119:129-136.
5. Barateau A, Celeste M, Lafond C, Henry O, Couespel S, Simon A, Acosta O, Périchon N. External beam radiotherapy cone beam-computed tomography-based dose calculation. *Cancer radiotherapie: journal de la Societe francaise de radiotherapie oncologique* 2017.
6. Gobeli M, Rigaud B, Charra-Brunaud C, Renard S, De Rauglaudre G, Beneyton V, Racadot S, Peignaux K, Leseur J, Williaume D. Po-1078: Cbct guided adaptive radiotherapy for cervix cancer: Uncertainty of the choice of the plan of the day. *Radiotherapy and Oncology* 2018;127:S606-S607.
7. van Beek S, Betgen A, Buijs M, Stam J, Hartgring L, van Triest B, Remeijer P. Pre-clinical experience of an adaptive plan library strategy in radiotherapy of rectal cancer: An inter-observer study. *Physics and Imaging in Radiation Oncology* 2018;6:89-93.
8. Rios R, De Crevoisier R, Ospina JD, Commandeur F, Lafond C, Simon A, Haigron P, Espinosa J, Acosta O. Population model of bladder motion and deformation based on dominant eigenmodes and mixed-effects models in prostate cancer radiotherapy. *Medical image analysis* 2017;38:133-149.
9. Cree A, Livsey J, Barraclough L, Dubec M, Hambrock T, Van Herk M, Choudhury A, McWilliam A. The potential value of mri in external-beam radiotherapy for cervical cancer. *Clinical Oncology* 2018.

LISTE DES PUBLICATIONS

JOURNAUX

B. Rigaud, A. Klopp, A. Venkatesan, S. Vedam, A. Simon, P. Haigron, N. Taku, R. De Crevoisier, KK. Brock, G. Cazoulat, "Deformable image registration for dose mapping between external beam radiotherapy and brachytherapy for cervical cancer", Physics in Medicine & Biology **(SOUMIS)**

B. Rigaud, A. Klopp, A. Venkatesan, S. Vedam, N. Taku, A. Simon, P. Haigron, R. De Crevoisier, KK. Brock, G. Cazoulat, "Technical Note: Biomechanical model-based deformable image registration to solve extreme position variation in a commercial treatment plan system", Medical Physics **(SOUMIS)**

MM. McCulloch, B. Anderson, G. Cazoulat, AS. Mohamed, S. Volpe, H. Elhalawani, H. Bahig, **B. Rigaud**, JB. King, A. Ford, C. Fuller, KK. Brock, “Biomechanical Modeling of Neck Flexion for Deformable Alignment of the Salivary Glands in Head and Neck Cancer Images” Physics in Medicine & Biology **(SOUMIS)**

B. Rigaud, A. Simon, J. Castelli, C. Lafond, O. Acosta, P. Haigron, R. De Crevoisier, "Deformable image registration for radiation therapy: principle, methods, applications and evaluation", Acta Oncologica. **(REVISION)**

B. Rigaud, A. Simon, M. Gobeli, J. Leseur, L. Duvergé, D. Williaume, J. Castelli, C. Lafond, O. Acosta, P. Haigron, R. De Crevoisier, "Statistical shape model to generate a planning library for cervical adaptive radiotherapy", IEEE Transactions on Medical Imaging (2018).

J. Castelli, A. Simon, C. Lafond, N. Perichon, **B. Rigaud**, E. Chajon, J. Bourhis, R. De Crevoisier, "Adaptive radiotherapy for head and neck cancer", Acta Oncologica (2018).

J. Castelli, A. Simon, **B. Rigaud**, E. Chajon, J. Thariat, K. Benezery, E. Vauleon, F. Jegoux, O. Henry, C. Lafond, R. de Crevoisier, "Adaptive radiotherapy in head and neck cancer is required to avoid tumor underdose", Acta Oncologica (2018).

B. Rigaud, A. Simon, M. Gobeli, C. Lafond, J. Leseur, A. Barateau, N. Jaksic, J. Castelli, D. Williaume, P. Haigron, R. De Crevoisier, "A CBCT-guided evolutive library for cervix adaptive IMRT", Medical Physics (2018).

O. Acosta, E. Mylona, M. Le Dain, C. Voisin, T. Lizee, **B. Rigaud**, C. Lafond, K. Gnep, R. De Crevoisier, "Atlas-based segmentation of prostatic urethra in the planning CT of prostate cancer", Radiotherapy and Oncology (2017).

A. Simon, A. Le Maitre, M. Nassef, **B. Rigaud**, J. Castelli, O. Acosta, P. Haigron, C. Lafond, R. De Crevoisier, "Is dose deformation-invariance hypothesis verified in prostate IGRT?", International Journal of Radiation Oncology & Biology & Physics (2017).

P. Zhang, A. Simon, **B. Rigaud**, J. Castelli, J.D. Ospina Arango, M. Nassef, O. Henry, P. Haigron, B. Li, H. Shu, R. De Crevoisier, "Optimal adaptive radiotherapy strategy in head and neck to spare the parotid gland", Radiotherapy and Oncology (2016).

J. Castelli, A. Simon, **B. Rigaud**, C. Lafond, E. Chajon, J.D. Ospina Arango, P. Haigron, B. Laguerre, A. Ru-er Loubiere, K. Benezery, R. de Crevoisier, "A nomogram to predict parotid gland overdose in head and neck IMRT", Radiation Oncology (2016).

B. Rigaud, A. Simon, J. Castelli, M. Gobeli, J.D. Ospina Arango, G. Cazoulat, O. Henry, P. Haigron, R. De Crevoisier, "Evaluation of deformable image registration methods for dose monitoring in head and neck radiotherapy", BioMed Research International, Oncology (2015).

M. Gobeli, A. Simon, M. Getain, J. Leseur, E. Lahlou, C. Lafond, E. Dardelet, D. Williaume, **B. Rigaud**, R. De Crevoisier, "Bénéfice de la radiothérapie adaptative par librairie de plans de traitement dans les cancers du col utérin ?", Journal officiel de la Société Française de Radiothérapie Oncologique (SFRO) (2015).

CONFERENCES

B. Rigaud, A. Simon, M. Gobeli, J. Leseur, D. Williaume, C. Lafond, O. Acosta, P. Haigron, R. De Crevoisier, "Planning library based on population shape analysis for cervical adaptive radiotherapy", Oral communication, European Society of Radiotherapy and Oncology (ESTRO) (2018).

M. Gobeli, **B. Rigaud**, A. Simon, C. Charra-Brunaud, S. Renard, G. De Rauglaudre, V. Beneyton, S. Racadot, K. Peignaux, N. Rannou, J. Leseur, D. Williaume, N. Jaksic, F. George Riet, K. Gnep, I. Pougnet, C. Herve, C. Lafond, R. De Crevoisier, "CBCT guided adaptive radiotherapy for cervix cancer: Uncertainty of the choice of the plan of the day", Poster, European Society of Radiotherapy and Oncology (ESTRO) (2018).

J. Castelli, A. Simon, **B. Rigaud**, C. Lafond, O. Henry, E. Chajon, F. Jegoux, E. Vauleon, R. De Crevoisier, "Adaptive radiotherapy in head and neck cancer to correct tumor underdose and parotid gland overdose", Poster discussion, European Society of Radiotherapy and Oncology (ESTRO) (2018).

B. Rigaud, A. Simon, M. Gobeli, J. Leseur, D. Williaume, C. Lafond, O. Acosta, P. Haigron, R. De Crevoisier, "Treatment plan library based on population shape analysis for cervical adaptive radiotherapy", Poster discussion, SPIE Medical Imaging (2018).

B. Rigaud, A. Simon, M. Gobeli, J. Leseur, D. Williaume, C. Lafond, O. Acosta, P. Haigron, R. De Crevoisier, "Treatment plan library based on population shape analysis for cervical adaptive radiotherapy", Oral communication, Surgetica (2017).

J. Castelli, A. Simon, **B. Rigaud**, C. Lafond, O. Henry, E. Chajon, F. Jegoux, E. Vauleon, R. De Crevoisier, "Radiothérapie adaptive des cancers ORL : Bénéfice sur la couverture du volume tumoral", Poster, Congrès de la Société Française de Radiothérapie Oncologique (SFRO) (2017).

M. Nassef, A. Simon, L. Duverné, **B. Rigaud**, C. Lafond, J-Y Giraud, P. Haigron, R. De Crevoisier, "Vers une radiothérapie adaptative guidée par la dose dans les cancers de prostate pour corriger les surdosages dans les organes à risque", Poster, Congrès de la Société Française de Radiothérapie Oncologique (SFRO) (2017).

M. Nassef, A. Simon, **B. Rigaud**, L. Duverné, C. Lafond, J-Y Giraud, P. Haigron, R. De Crevoisier, "Prostate cancer dose guided adaptive radiotherapy based on cumulated dose in the rectum and bladder", Poster, European Society of Radiotherapy and Oncology (ESTRO) (2017).

O. Acosta, M. Le Dain, C. Voisin, **B. Rigaud**, C. Lafond, K. Gnep, R. De Crevoisier, "Atlas-based segmentation of prostatic urethra in the planning CT of prostate cancer", Oral communication, European Society of Radiotherapy and Oncology (ESTRO) (2017).

B. Rigaud, A. Simon, M. Gobeli, C. Lafond, D. Williaume, J. Leseur, J. Castelli, P. Haigron, R. De Crevoisier, "CBCT-guided evolutive library for cervix adaptive IMRT", Oral communication, European Society of Radiotherapy and Oncology (ESTRO) (2017).

M. Gobeli, A. Simon, **B. Rigaud**, J. Leseur, D. Williaume, C. Lafond, R. de Crevoisier, "ITV versus RTA par librairie de plan de traitement dans les cancers du col utérin", Poster, Congrès de la Société Française de Radiothérapie Oncologique (SFRO) (2016).

J. Castelli, P. Zhang, A. Simon, **B. Rigaud**, J.D. Ospina Arango, M. Nassef, C. Lafond, O. Henry, P. Haigron, B. Li, H. Shu, R. De Crevoisier, "Optimal adaptive radiotherapy strategy in head and neck to spare the parotid glands", Poster, European Society of Radiotherapy and Oncology (ESTRO) (2016).

M. Gobeli, A. Simon, M. Getain, J. Leseur, E. Lahlou, C. Lafond, E. Dardelet, D. Williaume, **B. Rigaud**, R. De Crevoisier, "Bénéfice de la radiothérapie adaptative par librairie de plans de traitement dans les cancers du col utérin ?", Oral communication, Congrès de la Société Française de Radiothérapie Oncologique (SFRO) (2015).

A. Simon, M. Nassef, **B. Rigaud**, G. Cazoulat, J. Castelli, C. Lafond, O. Acosta, P. Haigron, R. De Crevoisier, "Roles of Deformable Image Registration in Adaptive RT: from Contour Propagation to Dose Monitoring", Oral communication, Annual International Conference of the IEEE Engineering in Medicine and Biology Society (EMBC) (2015).

J. Castelli, A. Simon, P. Zhang, **B. Rigaud**, J.D. Ospina Arango, M. Nassef, O. Henry, P. Haigron, B. Li, H. Shu, R. De Crevoisier, "Stratégie optimale de radiothérapie adaptative dans les cancers ORL localement avancés", Oral communication, Congrès National de la Société Française de Radiothérapie Oncologique (SFRO) (2015).

J. Castelli, A. Simon, O. Henry, **B. Rigaud**, C. Lafond, E. Chajon, J.D. Ospina Arango, P. Haigron, B Laguerre, K. Benezery, R. De Crevoisier, "Nomogramme pour prédire le surdosage parotidien au cours d'une RCMI pour cancers ORL", Poster, Congrès National de la Société Française de Radiothérapie Oncologique (SFRO) (2015).

B. Rigaud, A. Simon, J. Castelli, M. Gobeli, J.D. Ospina Arango, G. Cazoulat, O. Henry, P. Haigron, R. De Crevoisier "Evaluation of deformable image registration methods for dose monitoring in head and neck adaptive radiotherapy", Poster, European Society of Radiotherapy and Oncology (ESTRO) (2015).

J. Castelli, A. Simon, **B. Rigaud**, O. Henry, E. Chajon, P. Haigron, J.D. Ospina Arango, E. Vauleon, K. Benezery, R. De Crevoisier, "Nomograms to assess the parotid gland dose in Head & Neck IMRT based on anatomical markers", Poster, European Society of Radiotherapy and Oncology (ESTRO) (2015).

J. Castelli, A. Simon, **B. Rigaud**, O. Henry, G. Louvel, E. Chajon, M. Nassef, P. Haigron, G. Cazoulat, J.D. Ospina et R. De Crevoisier, "Une radiothérapie adaptative permet-elle de diminuer la xérostomie lors d'une irradiation ORL ?", Oral communication, Congrès de la Société Française de Radiothérapie Oncologique (2014).

G. Dréan, O. Acosta, J.D. Ospina, C. Voisin, **B. Rigaud**, A. Simon, P. Haigron, R. De Crevoisier. "How to identify rectal sub-regions likely involved in rectal bleeding in prostate cancer radiotherapy", Proc. SPIE, IX International Seminar on Medical Information Processing and Analysis (2013).

UNIVERSITE
BRETAGNE
LOIRE / MATHSTIC

UNIVERSITÉ DE
RENNES 1

Titre : Radiothérapie adaptative guidée par l'imagerie anatomique...

Mots clés : Col de l'utérus, radiothérapie adaptative, recalage déformable, modèle statistique

Résumé : Le traitement standard des cancers du col de l'utérus localement avancés repose sur une radiothérapie en parallèle à une chimiothérapie, suivie d'une curiethérapie. La radiothérapie externe comporte une phase de planification du traitement faite à partir d'une unique acquisition scanner et une phase de délivrance. Cependant, la position et la forme de la cible clinique varient fortement durant le traitement, avec des conséquences en termes de contrôle de la tumeur et de toxicité. L'objectif de cette thèse est donc de développer des stratégies optimisées de radiothérapie adaptative personnalisées permettant de prendre en compte et de compenser l'incidence de ces déformations anatomiques. Les images acquises lors de la planification et de la délivrance du traitement jouant alors un rôle central, ceci passe par le développement de méthodes de recalage, de fusion et d'analyse d'images ainsi que d'outils d'aide à la décision.

Les travaux de thèse ont permis la définition de deux nouvelles stratégies de traitement : (1) une stratégie reposant sur une librairie évolutive permettant d'exploiter l'anatomie de la patiente en cours de traitement pour enrichir une librairie préexistante ; (2) une stratégie de librairie modélisée à partir d'un scanner de planification unique reposant sur l'analyse des déformations d'une population. Pour la mise en correspondance des anatomies des deux traitements par radiothérapie (avec et sans applicateur), une méthode de recalage déformable basée sur un modèle biomécanique est proposée et évaluée par rapport aux méthodes classiques et à un outil commercial. Les résultats, reposant notamment sur des critères géométriques, montrent que les approches proposées permettent d'assurer, pour toutes les patientes, une bonne couverture de la cible, tout en limitant l'irradiation des organes sains et donc, à terme, des meilleurs résultats cliniques.

Title: Adaptive radiotherapy using anatomical imaging..

Keywords: Cervix, adaptive radiotherapy, deformable image registration, statistical shape model

Abstract: The reference treatment for locally advanced cervical carcinomas relies on chemoradiotherapy and brachytherapy (BT). The radiotherapy (RT) is based on a planning made on a single scanner and on the delivery of the treatment. During the treatment, the clinical target volume (CTV) position may change and hamper the precision of the dose delivery, thus, increasing the risk of recurrence and toxicity. The aim of the thesis is the development of new adaptive radiation therapy (ART) strategies in order to take in account the per-treatment anatomical deformations. These approches will have to rely on image processing tools such as deformable image registration (DIR) and data mining to extract the information from the images acquired at the planning and during the treatment.

The work of this thesis has led to the definition of two new ART strategies: (1) an evolutive planning library that can be enriched by new per-treatment anatomies; (2) a modeled library based on a population analysis at the time of planning. Finally, in the context of delivered dose estimation, a biomechanical based DIR method is proposed to map the anatomy of the BT, with applicator, toward the anatomy of RT, without applicator. This method is compared to open access and commercially available DIR methods. The geometrical evaluation, show that the proposed adaptive strategies allow to insure a good coverage of the CTV for all the patients while limiting the irradiation of the healthy organs. Such strategies may improve the clinical outcome of the patients.